FERMILAB-THESIS-1999-27

Mass and Width Measurements of Σ_c Baryons

by

Eric W. Vaandering

B.S., Valparaiso University, 1993

M.S., University of Colorado, 1995

A thesis submitted to the

Faculty of the Graduate School of the

University of Colorado

in partial fulfillment of the requirements for the degree

Doctor of Philosophy

Department of Physics

2000

This thesis entitled:
Mass and Width Measurements of Σ_c Baryons
written by Eric W. Vaandering
has been approved for the Department of Physics

John P. Cumalat

William T. Ford

Date

The final copy of this thesis has been examined by the signatories, and we find that both the content and the form meet acceptable presentation standards of scholarly work in the above mentioned discipline.

Vaandering, Eric Wayne (Ph.D., Physics)

Mass and Width Measurements of Σ_c Baryons

Thesis directed by Professor John P. Cumalat

Analyses of several charmed baryons decaying to Λ_c^+ are presented. The data for these analyses were collected by FOCUS, Fermilab Experiment E831. FOCUS is a high statistics charm photoproduction experiment and accumulated data during the 1996–1997 Fermilab Fixed Target run.

In an analysis of the decays $\Sigma_c \to \Lambda_c^+\pi^\pm$ we measure the $\Sigma_c - \Lambda_c^+$, $\Sigma_c^{++} - \Sigma_c^0$, and $\Sigma_c^+ - \Sigma_c^0$ mass differences. We find $m_{\Sigma_c^0} - m_{\Lambda_c^+} = 167.54 \pm 0.19 \pm 0.34$ MeV/c^2, $m_{\Sigma_c^{++}} - m_{\Lambda_c^+} = 167.59 \pm 0.20 \pm 0.27$ MeV/c^2, and $m_{\Sigma_c^{++}} - m_{\Sigma_c^0} = 0.05 \pm 0.28 \pm 0.09$ MeV/c^2. In an analysis of the decay $\Sigma_c^+ \to \Lambda_c^+\pi^0$ we find $m_{\Sigma_c^+} - m_{\Lambda_c^+} = 168.03 \pm 1.01 \pm 0.30$ MeV/c^2 and $m_{\Sigma_c^+} - m_{\Sigma_c^0} = 0.49 \pm 1.03 \pm 0.45$ MeV/c^2. These results are obtained with a sample of 362 ± 36 $\Sigma_c^0 \to \Lambda_c^+\pi^-$ decays, 118 ± 40 $\Sigma_c^+ \to \Lambda_c^+\pi^0$ decays, and 487 ± 41 $\Sigma_c^{++} \to \Lambda_c^+\pi^+$ decays. The results with charged pions are improvements on the best available measurements

Using a cleaner analysis of $\Sigma_c \to \Lambda_c^+\pi^\pm$ decays, we measure the widths of Σ_c^0 and Σ_c^{++}. We find $\Gamma(\Sigma_c^0) = 2.58 \pm 0.79^{+0.51}_{-0.55}$ MeV/c^2 and $\Gamma(\Sigma_c^{++}) = 2.53 \pm 0.77^{+0.51}_{-0.56}$ MeV/c^2. These results are obtained with a sample of 425 ± 55 $\Sigma_c^0 \to \Lambda_c^+\pi^-$ decays and 540 ± 59 $\Sigma_c^{++} \to \Lambda_c^+\pi^+$ decays. There are no published measurements of the Σ_c widths.

We also report on the observation of two excited charm baryon resonances decaying to $\Lambda_c^+\pi^\pm$. These states are interpreted as the Σ_c^{*0} and Σ_c^{*++} with $I(J^P) = 1(\frac{3}{2}^+)$. We obtain preliminary measurements of the properties of these states of $m_{\Sigma_c^{*0}} - m_{\Lambda_c^+} = 232.7 \pm 1.2$ MeV/c^2, $\Gamma(\Sigma_c^{*0}) = 9.4 \pm 3.7$ MeV/c^2, $m_{\Sigma_c^{*++}} - m_{\Lambda_c^+} = 234.2 \pm 1.5$ MeV/c^2, and $\Gamma(\Sigma_c^{*0}) = 23.6 \pm 4.5$ MeV/c^2. These measurements are compatible with the only previous observation, but no attempt is made to optimize statistical errors or determine systematic errors.

Finally, we report on a search for the doubly charmed baryons Ξ_{cc}^+ and Ξ_{cc}^{++} in the decay modes $\Xi_{cc} \to \Lambda_c^+ K^- n\pi$. No compelling evidence for the existence of doubly charmed baryon states is observed.

For Mom and Dad

Acknowledgments

A high energy physics experiment of the magnitude of FOCUS is an accomplishment which is shared by many, many people. For this reason, any acknowledgments section would be remiss in not first thanking each and every member of the FOCUS collaboration as well as the many engineers, technicians, and students who have worked on the experiment. The FOCUS collaboration is truly a unique group of people: hard working, intelligent, personable, and fun loving.

Within this collaboration, numerous people must be singled out for their particular accomplishments, without which FOCUS may well have failed.

First, thank you to everyone who built detectors. Special thanks to those who built the IE. Eric Erdos, John "the sander man" Cumalat, Luca Cinquini, and Brian O'Reilly. Thanks also to everyone who helped us pull the RG-8 cables: Iuri Pepe, Luis Méndez, Hasaan Mourad, Carlos Rivera, Enrique Montiel, David Olaya, and the many others whom I've forgotten. Whose great idea was that, anyway? Finally, thanks to Roy Justice who was always willing to help anyone (and to tell jokes that would make the Venus de Milo blush).

Thanks to Francesco Prelz who tirelessly kept the DAQ running like a champ.

Thanks to Joel Butler for writing and developing the Pass1 software. Thanks also to Irwin Gaines, Alberto Sanchez, and especially Jon "Bad Cop" Link for being "Pass1 Czars" along with me. It was too big of a job for Jon and me; you saved our sanity. Thanks, too, to the collaborators who ran Pass1 shifts, especially those who *didn't* page me at 6:00 am.

Thanks to Matt Nehring and Luca Cinquini for spear-heading the Skim1 project. These guys stepped into a project no one was even thinking about and made it a reality. Thanks also to John Cumalat, Brian O'Reilly, Eduardo Ramírez, David Olaya, and all the Vandy guys for running Skim1 shifts.

Thanks to everyone who developed and ran Skim2 and copied tapes, but special thanks to Harry Cheung. He coordinated, started first, finished first, and he processed *my* data.

Thanks also to those who have helped me along this final path of analysis with suggestions, encouragement, and enlightening discussions. Jim Wiss, Paul Sheldon, Phil "The Million Mile Man" Yager, Harry Cheung, Will Johns, and Kevin Stenson.

Special thanks to the two people who (in addition to John) have written letters of recommendation: Joel Butler and Jim Wiss.

Working with such a great group of people, it's impossible not to form meaningful and (I hope) long lasting friendships.

- Jon Link, for being willing to conspire with me on just about anything and for being an good person to bounce ideas off of.

- Brian O'Reilly, for among other things, taking care of me the famous Messrs. V, W, X, Y, and Z night. (I won't mention that is was partly his fault that I was in that condition to begin with.)

- Will Johns, for being a great and thoughtful housemate and for giving all of us an ideal to look to.

- Harry Cheung, who is always willing to include the new arrivals in social activities.

- Kevin "I don't even know 'er" Stenson, for being an all around great friend and an excellent travel agent/partner.

Outside of our collaboration, there are many people at Fermilab who deserve a recognition too. Thank you to the Farms group of the Computing Division, especially Tanya Levshina, Marilyn Schweitzer, and Mike Wolbers for helping us through the process and always being willing to throw a couple thousand more MIPS our way. Thanks also to the engineering staff for designing detector supports that could hold an elephant.

Being uprooted from "home" and sent off to the far off land of the Fermilab village can be a traumatic experience. Fortunately there were plenty of people who befriended me and made the process easier. The Users Center gang was crucial to my survival those two years on the prairie. Forest, Renee, Rich, and Chuck (or Chuck and Rich) thank you. And special thanks to Nancy Joyce for being a barkeep who was equally willing to talk as to listen, for always being willing to give a poor grad student a break, and for showing up bearing gifts whenever a party was running low on beer in the wee hours of the morning.

Of course, I had many friends during my two stints in Boulder too.

First, I want to thank both sets of housemates I've had. Kim King, Heather Robinson, and Sarah Simpson-Parks saw me through my difficult second year of grad school and understood (or at least pretended to) when I came home from taking comps and just wanted to "sit." Thanks also to my current housemates, Greg Rakness (who's spent just as many days on "the frontier of knowledge" as I have), Orion Poplawski, and Marc Welliver. They have been quite understanding this last year.

Thanks also to all my fellow classmates, my support network during the first year or two of graduate school, especially Keith, Jim, Darren, Kristan, and Sarah. We suffered together and we made it, each in our own way.

Thanks to Kerstin Kirschenbaum for sharing with me the love of the solitude of the wilderness and for being a wonderful backpacking partner.

Thanks to my friend Brian King for making me realize, in an indirect sort of way, that life ain't so bad.

Away from Boulder, special thanks go to Jennifer Johnson. First for being a constant and special friend. Second, for helping me to not take myself too seriously. And finally, for providing a welcome and important diversion right at the end of my writing.

Of course, the list of people who have helped me and guided along my educational and personal path didn't begin with my graduate school experiences.

While my earliest memories are somewhat hazy, I do remember that my 2nd grade teacher, Jean Portenga was one of the first to encourage my scientific predispositions, giving her own time to challenge a young mind.

While I had many excellent teachers in high school, two stand out above the crowd. Arley Bouwma, for impressing on me that science isn't just important, it can also be fun. And Dave VerMerris for being so many things: a marvelous teacher, a cheerful man who always had a smile on his face, a motivator, and above all a role model.

My college experiences at Valparaiso University were no different. I was again guided by many wonderful professors who must be thanked. Malcolm Reynolds for his methodical and thorough (read "lots of homework") way of giving me a foundation in calculus and differential equations. Stan Zygmunt, for his clarity and energy. Donald Koetke for his excellent teaching and for encouraging my interest in research. Robert Manweiler for taking me under his wing and for being a confidant and mentor. And both Bob and Bruce Hrivnak for adopting me into their families, so to speak. Thank you, all of you.

Also during my undergraduate years, I spent three summers and two semesters working with people at Argonne National Laboratory. While everyone I met there was wonderful, two people deserve special recognition. Thanks to Hal Spinka for advising me and teaching me to believe in myself. And thanks to David Grosnick for doing the same and being another of my mentors and an all around great guy. My experiences at Argonne, more than anything else, helped me realize that I wanted to be a research physicist.

Of course, formal education is just one set of influences. Many other people have made substantial contributions to get me to this point.

First, my childhood neighbor, Percy Dowell, comes to mind. He was an uneducated man, who always told me "You just keep going to school. Once you learn something, no one can take that away from you." Of course, I may have followed his advice to the extreme.

Second, my grandmother, Liz Huizenga, has had an enormous influence, not only on me but on our entire family. Because she was needed on the family farm, my grandmother never attended school past the eighth grade. That didn't stop her from continuing to learn new things all through her long life, and becoming, in a way, one of the most educated people I've ever known. It also didn't stop her from passing on to her children and grandchildren a love of learning unparalleled in my experience. My deepest regret is that she is not alive to see the first of her descendants receive a Ph.D.

To my parents, I owe everything. Throughout my life, they have encouraged me in everything I ever wanted to do. At great hardship to themselves, they made sure I had every opportunity they could possibly give me. They have made sacrifices that I can never fully understand or appreciate. And they never questioned my choices. Who I am is a direct result of who they are, what they have done, and what they believe in. Thank you.

Finally, to my advisor John Cumalat, I owe my deepest appreciation and admiration. John has always been a fount of ideas: many of them good, all of them interesting. He has also trusted my instincts and tried to guide rather than direct me. And he's done all this with an energy I can scarcely imagine. I couldn't imagine a better advisor. I feel very fortunate to count him, not only among my collaborators, but among my friends.

Contents

List of Tables

List of Figures

Chapter 1

Introduction

1.1 Scope of the Thesis

This thesis presents measurements of the masses and widths of the Σ_c baryons. Mass measurements for all three Σ_c states (Σ_c^0, Σ_c^+, and Σ_c^{++}) are given while width measurements are given for only the Σ_c^0 and Σ_c^{++}. An observation of the decays $\Sigma_c^* \to \Lambda_c^+ \pi^\pm$ without a detailed analysis is also presented. Finally, a search for decays of doubly charmed baryons in the decay modes $\Xi_{cc} \to \Lambda_c^+ K + n\pi$ is also discussed. These analyses are based on data from the FOCUS[1] experiment, a high statistics charm photoproduction experiment at Fermi National Accelerator Laboratory (Fermilab).

This introductory chapter is an overview of the Standard Model of elementary particle physics, the theory which describes the nature of matter and its interactions. The theory governing weak interactions and properties of charmed particles, especially baryons is also covered. More detailed theoretical models, calculations, and predictions relating to the topics of this thesis are presented in the relevant chapters.

In Chapter 2 the Fermilab Tevatron accelerator complex and the production of high energy photons for use by the FOCUS experiment is described in some detail.

Chapter 3 describes the FOCUS experimental apparatus in detail. The individual detector elements are covered, with special emphasis on those most important to the analyses presented in this thesis. Chapter 3 also contains information on the data acquisition system used to collect detector information.

In Chapter 4 the reconstruction algorithms used by the experiment are explained.

[1] Fotoproduction (sic) Of Charm with an Upgraded Spectrometer

These algorithms transform raw detector information into tracking information, particle identification, and calorimetry information. The processing and reduction of data into summary sets suitable for individual analyses is also explained.

Chapter 5 covers the methods used to select $\Lambda_c^+ \to pK^-\pi^+$ candidates[2] used in later analyses. In addition, the analysis techniques common to the other analyses are described and many cuts used later are defined.

Chapter 6 is concerned with measurements of the masses of Σ_c baryons. We present $\Sigma_c - \Lambda_c^+$ mass difference measurements for each of the three Σ_c states. These mass differences are found to be $m_{\Sigma_c^0} - m_{\Lambda_c^+} = 167.54 \pm 0.19 \pm 0.34$ MeV/c^2, $m_{\Sigma_c^+} - m_{\Lambda_c^+} = 168.03 \pm 1.01 \pm 0.30$ MeV/c^2, and $m_{\Sigma_c^{++}} - m_{\Lambda_c^+} = 167.59 \pm 0.20 \pm 0.27$ MeV/c^2. (The first errors are statistical, the second are systematic.) We also determine mass differences between the Σ_c states, which are especially sensitive probes of the various theoretical models. The measurements of the $\Sigma_c^0 - \Lambda_c^+$, $\Sigma_c^{++} - \Lambda_c^+$, and $\Sigma_c^0 - \Sigma_c^{++}$ mass differences represent improvements on the world's current best measurements.

Chapter 7 details the measurement of the natural widths of the Σ_c^0 and Σ_c^{++} baryons. In this analysis we determine that $\Gamma(\Sigma_c^0) = 2.58 \pm 0.79^{+0.51}_{-0.55}$ MeV/c^2 and $\Gamma(\Sigma_c^{++}) = 2.53 \pm 0.77^{+0.51}_{-0.56}$ MeV/c^2. This analysis is challenging due to limited statistics and because the natural width is narrow compared to the experimental resolution.

Chapter 8 presents an observation of two broad states decaying to $\Lambda_c^+\pi^\pm$ which are interpreted as Σ_c^* states. The measured properties of these states are found to be $m_{\Sigma_c^{*0}} - m_{\Lambda_c^+} = 232.7 \pm 1.2$ MeV/c^2, $\Gamma(\Sigma_c^{*0}) = 9.4 \pm 3.7$ MeV/c^2, $m_{\Sigma_c^{*++}} - m_{\Lambda_c^+} = 234.2 \pm 1.5$ MeV/c^2, and $\Gamma(\Sigma_c^{*0}) = 23.6 \pm 4.5$ MeV/c^2, but a detailed analysis is not performed. As a consequence, the statistical errors are not optimized and no systematic error is determined.

In Chapter 9 a search for the doubly charmed baryons Ξ_{cc}^+ and Ξ_{cc}^{++} is described. No doubly charmed baryons have been observed to date, but they are needed to complete the spectrum of charmed baryons. We do not observe any evidence for doubly charmed baryon production in FOCUS.

Several appendices are also included. Appendix A presents a study of low momentum, or "soft," π^0 reconstruction methods which bears on the Σ_c^+ mass difference analysis. Appendix B describes the methods used to calculate systematic errors in all the analyses. Appendix C is a glossary of terms used throughout the thesis.

[2]Unless explicitly stated otherwise, charge conjugate states are always implied.

1.2 The Standard Model

The "Standard Model" is the current description of elementary particles and their interactions, a model which is not inconsistent with current experimental measurements. However, because the Standard Model requires a large number of input parameters, and does not unify all the observed forces, we believe it must be incomplete.

The Standard Model separates all of the known elementary particles into two classes: fermions (matter particles) and gauge bosons (force carrying particles). The fermions are further divided into two categories, quarks and leptons.

1.2.1 Quarks

Quarks were simultaneously proposed by Gell-Mann [1] and Zweig [2] in 1964 as a useful mathematical technique to give order to what was quickly becoming a "particle zoo." The initial quark models required three types, or flavors, of quarks which were labeled *up*, *down*, and *strange* (denoted as u, d, and s). By combining the quarks in various ways, one could form all the hadrons known at the time.

Today, not only do we know that quarks are actually real objects, but we have also added three more: *charm*, *bottom*, and *top*. These additional quarks are denoted by the symbols c, b, and t. The properties of the quarks are summarized in Table 1.1. The quarks are naturally grouped into three families. Each family contains two quarks (for instance the u and the d) with charges $+\frac{2}{3}$ and $-\frac{1}{3}$. Between families the quarks differ only in their masses.

Table 1.1: Properties of the quarks [4].

Quark	Mass (MeV/c^2)	Charge (e)
d	3–9	$-\frac{1}{3}$
u	1.5–5	$+\frac{2}{3}$
s	60–170	$-\frac{1}{3}$
c	1100–1400	$+\frac{2}{3}$
b	4100–4400	$-\frac{1}{3}$
t	$173.8 \pm 5.2 \times 10^3$	$+\frac{2}{3}$

All known hadrons are composed of three quarks (baryons) or a quark and an anti-quark (mesons). No free quarks have been observed. In order to explain this grouping, quantum chromodynamics postulates the existence of another quantum number, the *color* charge. Each quark carries one of the three colors (called red, blue, or green) while each anti-quark carries one of the three anti-colors. Composite states are required to be "color neutral;" baryons must have one quark of each color while mesons

must have two quarks with opposite colors. Hadrons are bound together by gluons which act on the color charge, as described in Section 1.2.3.

1.2.2 Leptons

The leptons exhibit the same familial structure as the quarks. Each lepton family contains a unit charged, massive lepton and a neutral, nearly massless[3] neutrino. The first family of leptons consists of the *electron* (e) and the *electron-neutrino* (ν_e). As with the quarks, there are three families of leptons, named electron, muon, and tau (e, μ, and τ). Each quark family and lepton family are related through symmetry. The ν_τ remains unobserved to date,[4] but its existence is not seriously doubted. The properties of the leptons are summarized in Table 1.2.

Table 1.2: Properties of the three families of leptons [4].

	Mass (MeV/c^2)		Mass
e	0.5110	ν_e	< 15 eV/c^2
μ	105.66	ν_μ	< 0.17 MeV/c^2
τ	1777.1	ν_τ	< 18.2 MeV/c^2

Combining the families, or generations, of quarks and leptons, the generations of matter can be represented by

$$\begin{pmatrix} u \\ d \end{pmatrix} \quad \begin{pmatrix} c \\ s \end{pmatrix} \quad \begin{pmatrix} t \\ b \end{pmatrix}$$
$$\begin{pmatrix} \nu_e \\ e \end{pmatrix} \quad \begin{pmatrix} \nu_\mu \\ \mu \end{pmatrix} \quad \begin{pmatrix} \nu_\tau \\ \tau \end{pmatrix} \tag{1.1}$$

where the particles in each row differ only in mass.

1.2.3 Force mediating bosons

Within the Standard Model there are four fundamental forces. *Gravity*, *electromagnetism*, the *strong* nuclear force, and the *weak* nuclear force. Gravity and electromag-

[3]Recent results [5] suggest that neutrinos, in a method similar to that described below for quarks, change flavor. This implies that some neutrinos have masses, however small.

[4]The experimental problem is very difficult since one looks for the appearance and subsequent decay of a τ lepton.

netism have been known, if not understood, since ancient times. The nuclear forces were only discovered in this century.

In the Standard Model each force is mediated by elementary particles called "gauge bosons." The electromagnetic force is mediated by the familiar photon (γ). The strong force is mediated between quarks by the massless gluons (g). The weak force is mediated by the massive $W^{\pm}$ and Z^0 bosons. Gravity is mediated by the postulated, but undiscovered, *graviton*. The Standard Model does not include a description of gravity; at the energy and distance scales of today's particle physics experiments, gravity is irrelevant. The properties of the gauge bosons are summarized in Table 1.3.

Table 1.3: Properties of the gauge bosons [4]. The properties of the graviton are only postulates.

Boson(s)	Force	Mass (GeV/c^2)	Spin
γ	Electromagnetic	0	1
$W^{\pm}(Z^0)$	Weak	80.4(91.2)	1
g	Strong	0	1
graviton	Gravity	0	2

Quantum chromodynamics requires eight types of gluons, which in addition to acting on the color charge, also carry the color charge. This means that there is a strong interaction between gluons[5] as well as between quarks and gluons. The strength of the interaction exerted by gluons increases as separation distances increase. It is this property that is responsible for quark confinement (our inability to observe free quarks). This self-interaction and the relative strength of the strong force, make a mathematical description of the strong force difficult.

1.3 Charm Physics and Weak Decays

Since this thesis concentrates on charmed baryons, we delve a little deeper into the history of the charm quark and into the physics of weak decays, the process by which all ground state charmed baryons and mesons decay.

1.3.1 The discovery of Charm

In November 1974, two experiments [6, 7] simultaneously announced the discovery of the J/ψ, a meson with a mass of about 3.1 GeV/c^2 and a narrow width which implied a much longer lifetime than other massive mesons. This particle was interpreted by

[5]For this reason, the term "glue" is particularly relevant.

some as the bound state of charmonium, ($c\overline{c}$). This hypothesis was later confirmed with the discovery of the D^0 and D^+ mesons [8,9] in 1976, although another experiment [10, 11] had seen indications of so called "open charm" several years before the discovery of the J/ψ.

The discovery of the analogous $b\overline{b}$ resonance, Υ [12], followed shortly thereafter, indicating the existence of the third family of quarks. The discovery of the top quark [13], however, would be delayed for nearly 20 years due to its extremely large mass; so massive and short lived, in fact, that is does not combine into hadrons. Current evidence from measurements of the width of the Z^0 strongly suggest that there are only three families of quarks [14].[6]

1.3.2 Weak decays

Quarks have an interesting property in that their weak eigenstates are mixtures of the mass eigenstates. By convention the down-type (d, s, and b) quarks are chosen to be mixtures of the mass eigenstates; these new weak eigenstates are denoted by d', s', and b'. The up-type (u, c, and t) quarks are unmixed. This allows an up-type quark to decay, via the emission of a W, to any energetically allowed down-type quarks. The reverse is also true.

For the simple two family case the transitions between quark types are described by the transformation postulated by Cabibbo [15]:

$$\begin{pmatrix} d' \\ s' \end{pmatrix} = \begin{pmatrix} \cos\theta_c & \sin\theta_c \\ -\sin\theta_c & \cos\theta_c \end{pmatrix} \begin{pmatrix} d \\ s \end{pmatrix} . \tag{1.2}$$

In this description the Cabibbo angle (θ_c) has been measured to be approximately 0.23 radians. As a consequence the transitions $c \to s$ and $u \to d$ are proportional to $\cos^2\theta_c$ while the transitions $c \to d$ and $s \to u$ are proportional to $\sin^2\theta_c$. The first set of transitions are called "Cabibbo favored" while the second set of transitions are denoted "Cabibbo suppressed." (The value of $\sin^2\theta_c/\cos^2\theta_c$ is approximately $\frac{1}{20}$.)

With the discovery of a third family of quarks, the Cabibbo matrix was generalized and replaced with the CKM[7] matrix [16] which gives the transition rates as

[6] A 4$^{\text{th}}$ family with a light neutrino ($\lesssim 45$ GeV/c^2) would increase $\Gamma(Z^0)$ (the Z^0 width) which is not seen.

[7] Cabibbo-Kobayashi-Maskawa. Actually Kobayashi and Maskawa proposed this extension before the discovery of the b quark as a method which included CP violation in the Standard Model.

$$\begin{pmatrix} d' \\ s' \\ b' \end{pmatrix} = \begin{pmatrix} V_{ud} & V_{us} & V_{ub} \\ V_{cd} & V_{cs} & V_{cb} \\ V_{td} & V_{ts} & V_{tb} \end{pmatrix} \begin{pmatrix} d \\ s \\ b \end{pmatrix} . \tag{1.3}$$

In this formalism, the transition rates between families are described by the values of V. For instance, the Cabibbo suppressed $c \to d$ transition rate is proportional to $|V_{cd}|^2$. In the CKM matrix, the diagonal elements are near unity, while the off diagonal elements are small. Assuming that there are only three families, the CKM matrix is a unitary matrix, which provides additional constraints on the values of V.

These contributions modulating quark transition probabilities arise from the coupling of the relevant quarks with with the W boson. For instance, in the Cabibbo suppressed decay $D^0 \to \pi^+\pi^-$ decay shown in Figure 1.1, the transition probability is proportional to $|V_{cd}|^2 |V_{ud}|^2$, one factor for each quark-W vertex. Because of the large mass of the W, the weak force has a very short range and consequently a very small magnitude. This effect is described by the Yukawa [17] potential which describes the range of a force mediated by a massive boson.[8] Particles which decay via the weak nuclear force consequently have relatively long lifetimes.

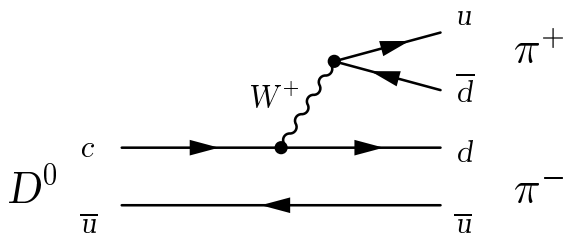

Figure 1.1: Feynman diagram for a Cabibbo suppressed decay.

1.4 Charmed Baryons

The $L = 0$ (no angular momentum between quarks) baryons are shown in Figure 1.2. The singly charmed baryons (including the Λ_c^+ and Σ_c states on which this thesis focuses) are on the second level of these multiplets, while the doubly charmed baryons, which are the subject of Chapter 9, are those on the third level of the multiplets. With the exception of the Σ_c^{*+} and $\Omega_c^{\prime 0}$ (both shown in Figure 1.2(b)), all of the $L = 0$ singly charmed baryons in Figure 1.2 have (likely) been observed. The properties of

[8] Yukawa developed this method to describe a model of the nucleus in which inter-nucleon forces are mediated by massive π mesons.

the $L = 0$ charmed baryons are listed in Table 1.4. In addition, several $L = 1$ Λ_c^+ and Ξ_c excited states have been observed: the $\Lambda_{c1}^{*+}(2593)$, the $\Lambda_{c1}^{*+}(2625)$, and most recently the $\Xi_{c1}(2720)$ [18].

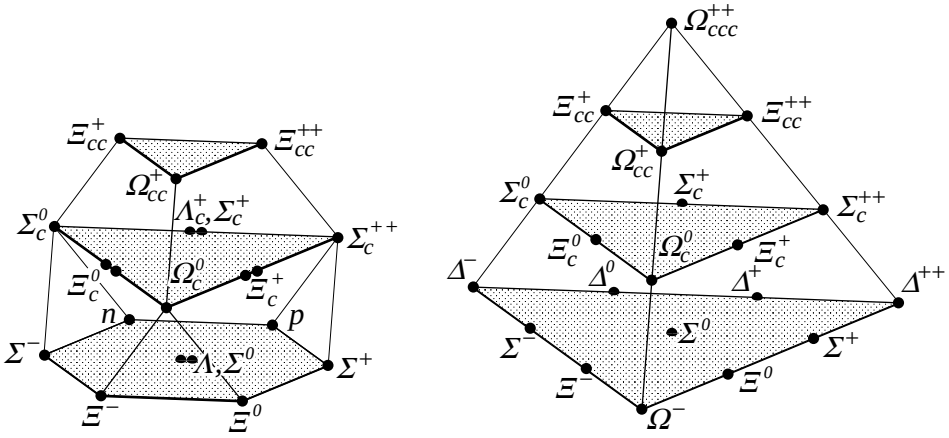

(a) $\frac{1}{2}^+$ baryons with the SU(3) octet (N states) as a base.

(b) $\frac{3}{2}^+$ baryons with the SU(3) decuplet (Δ states) as a base.

Figure 1.2: SU(4) baryon multiplets which show all the $L = 0$ baryons present in a four-quark system. Extending these diagrams to SU(5) for the baryons containing a b quark would require a 4-dimensional drawing. (Figure from Reference 4.)

1.4.1 Spectroscopy of the Λ_c^+-like baryons

Since each baryon is made of three quarks and each quark has a spin, then the same three quarks can align in several different configurations, each of which is a distinct charmed baryon. This complication is somewhat simplified by Heavy Quark Effective Theory which allows us to treat quarks as either heavy (in our case the charm quark) or light (the up, down, and strange quarks). In this theory one imagines a central heavy quark and an outlying pair of light quarks, much in the same way the hydrogen atom is a heavy proton surrounded by a light electron. Each change in the spin configuration gives rise to a change in the energy, or mass of a baryon. Unlike the hyperfine splitting in atoms, these energy level splittings are substantial.

With this simplification, and restricting ourselves to Λ_c^+-like baryons with charm, up, and down quarks, we must consider three spin configurations of the quarks. If we denote the three quarks as $[c(qq)]$ (where q is a light quark) and their spins as $[\uparrow(\uparrow\uparrow)]$, we can more easily present the configurations. The first, or ground state, system is formed when the two light quarks are anti-aligned to form a light di-quark with spin

Table 1.4: Properties of the $L = 0$ charmed baryons [4]. The $I(J^P)$ values of many of these states have not been experimentally measured; in these cases we give the predicted values. Baryons with $J = \frac{1}{2}$ belong to the SU(4) multiplet shown in Figure 1.2(a) while those with $J = \frac{3}{2}$ belong to the multiplet shown in Figure 1.2(b).

Baryon	Quark content	Mass (MeV/c^2)	$I(J^P)$
Λ_c^+	$c(ud)_a$	2284.9 ± 0.6	$0(\frac{1}{2}^+)$
Σ_c^0	cdd	2452.9 ± 0.6	$1(\frac{1}{2}^+)$
Σ_c^+	$c(ud)_s$	2453.6 ± 0.9	$1(\frac{1}{2}^+)$
Σ_c^{++}	cuu	2452.8 ± 0.6	$1(\frac{1}{2}^+)$
Σ_c^{*0}	cdd	2517.5 ± 1.4	$1(\frac{3}{2}^+)$
Σ_c^{*+}	cud	unobserved	$1(\frac{3}{2}^+)$
Σ_c^{*++}	cuu	2519.4 ± 1.5	$1(\frac{3}{2}^+)$
Ξ_c^0	$c(sd)_a$	2471.8 ± 1.4	$\frac{1}{2}(\frac{1}{2}^+)$
Ξ_c^+	$c(su)_a$	2466.3 ± 1.4	$\frac{1}{2}(\frac{1}{2}^+)$
$\Xi_c^{\prime 0}$	$c(sd)_s$	2578.8 ± 3.2	$\frac{1}{2}(\frac{1}{2}^+)$
$\Xi_c^{\prime +}$	$c(su)_s$	2574.1 ± 3.3	$\frac{1}{2}(\frac{1}{2}^+)$
Ξ_c^{*0}	csd	2644.5 ± 1.8	$\frac{1}{2}(\frac{3}{2}^+)$
Ξ_c^{*+}	csu	2647.4 ± 2.0	$\frac{1}{2}(\frac{3}{2}^+)$
Ω_c^0	css	2704.0 ± 4.0	$0(\frac{1}{2}^+)$
$\Omega_c^{\prime 0}$	css	unobserved	$0(\frac{3}{2}^+)$

0. In our notation, this is denoted as $[\uparrow(\uparrow\downarrow)]$. This is the configuration of the Λ_c^+, whose quark configuration is $[c(ud)]$ and has total $J = \frac{1}{2}$. The next lowest energy configuration, also with $J = \frac{1}{2}$, is $[\downarrow(\uparrow\uparrow)]$ where the light di-quark has spin 1. These states are the Σ_c baryons: Σ_c^0 (cdd), Σ_c^+ (cud), and Σ_c^{++} (cuu). Finally, we can have the arrangement $[\uparrow(\uparrow\uparrow)]$ with $J = \frac{3}{2}$. These states are the Σ_c^* baryons Σ_c^{*0}, Σ_c^{*+}, and Σ_c^{*++} (with the same quark content as the $J = \frac{1}{2}$ Σ_c states). The Λ_c^+ and Σ_c states are members of the octet shown in Figure 1.2(a) and the Σ_c^* states are members of the decuplet in Figure 1.2(b).

In addition to these states, states with angular momentum and radial excitations are also possible, again with various spin configurations. The $\Lambda_{c1}^{*+}(2593)$ and $\Lambda_{c1}^{*+}(2625)$ baryons are the only observed Λ_c^+-like baryons with $L = 1$, but many more must exist. The spectrum of the Λ_c^+, Σ_c, Σ_c^*, and Λ_{c1}^{*+} baryons and their dominant decay modes is shown in Figure 1.3. The Ξ_c (csq) and Ω_c^0 (css) ground states are expected to have similar spectra. Similarly to the de-excitations observed in atomic physics, each of these states decays to its corresponding ground state. However, in hadrons, these decays are often strong decays which can emit pions rather than photons.[9]

[9]If pion emission is energetically forbidden, as is the case for the lowest mass Ξ_c exited state, a high energy photon is emitted. (Of course, charge must also be conserved.)

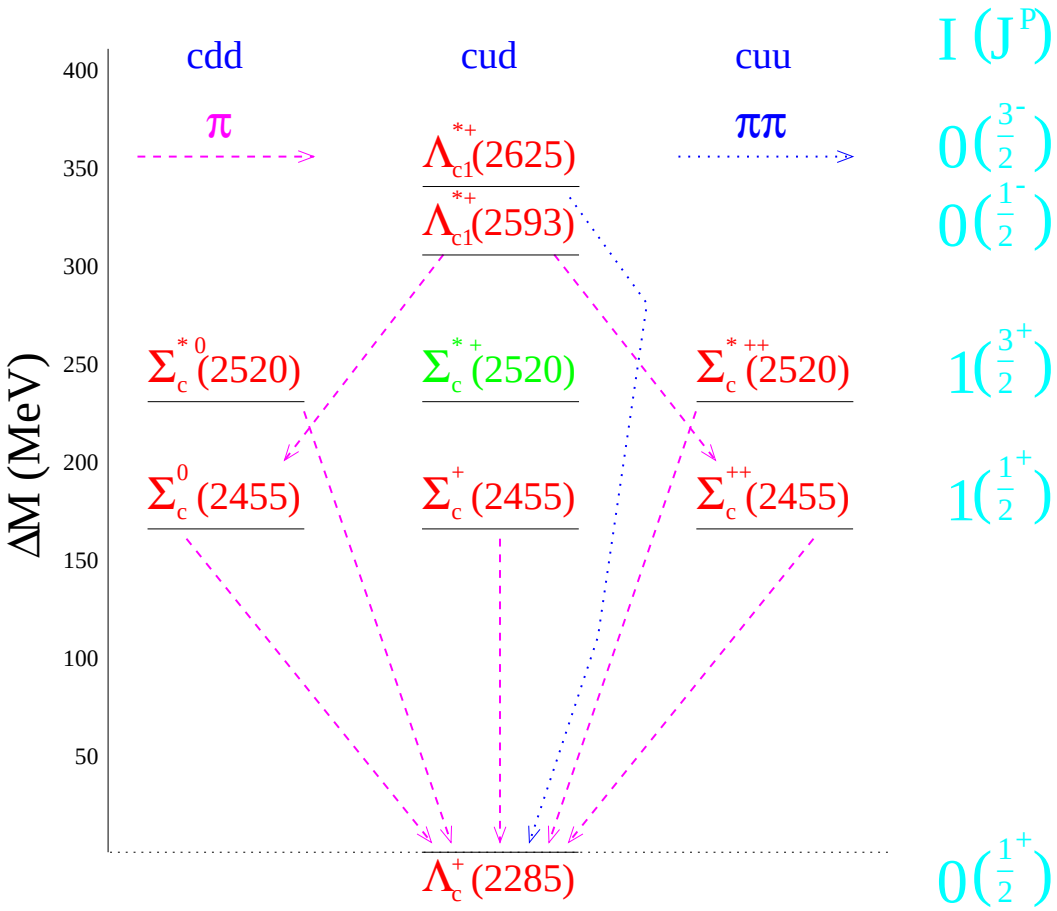

Figure 1.3: The spectrum of excited charm baryons with two light quarks and the dominant decay modes. The $\Sigma_c^{*+}(2520)$ is unobserved.

1.4.2 Charmed hadron lifetimes

The lifetime of any particle is related to its mass by the Heisenberg uncertainty relation which states that

$$\Delta E \Delta t \geq \hbar \,. \tag{1.4}$$

This means that as the lifetime, τ, of a particle becomes shorter, its energy (or mass) is less well determined. As particle physicists, we measure this uncertainty in mass as Γ, or the "natural width," of a state which is proportional to $1/\tau$. For weakly decaying particles (which have relatively long lifetimes), Γ is experimentally unmeasurable. However, for short-lived, strongly or electromagnetically decaying particles, the natural width is a physically observable effect. This is the case with the J/ψ and also for the Σ_c states as shown in Chapter 7. For each available decay mode or mechanism, the lifetime of a particle is decreased.

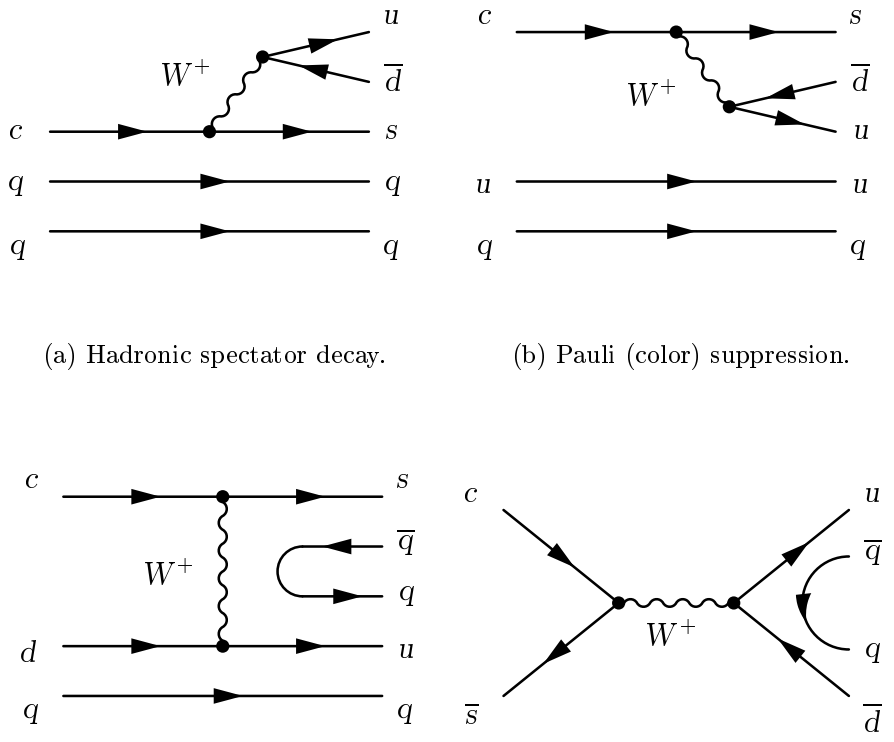

(a) Hadronic spectator decay.

(b) Pauli (color) suppression.

(c) W exchange.

(d) Annihilation.

Figure 1.4: Feynman diagrams for charm lifetime contributions. Each diagram represents a possible decay mode, depending on the initial quark content.

In the spectator quark model of weak decays, it is assumed that the non-decaying, or spectator, quarks do not interact with products of the virtual W decay. If this were the case, the lifetimes of all the charmed hadrons would be identical. However, large differences between the charm lifetimes are seen. In order to explain these differences, additional effects which depend on the quark content must be considered. For Cabibbo favored charmed baryon decays there are three major decay diagrams which may contribute to lifetimes. These three contributions and a process that can only occur for charmed mesons are shown in Figure 1.4.

The spectator process in which there is no interaction between the spectator quarks and the produced quarks in the decay is shown schematically in Figure 1.4(a). This is commonly called an "external" decay diagram. It is also this mechanism at work in semi-leptonic decays where the virtual W decays to a lepton-neutrino pair. This type of decay is available to all charmed particles. We denote its contribution to the lifetime as Γ_{ext}.

In Figure 1.4(b) we show the diagram for an internal decay. In this case if there are two quarks of the same type in the final state, this can give rise to constructive or destructive interference due to Pauli suppression and the color charge (the produced quarks must have compatible colors with the spectator quarks). When the decay products of the virtual W match the spectator quarks, the interference is destructive (denoted by $\Gamma^-_{\rm int}$) and serves to increase the lifetime of the decaying particle. When there are spectator s quarks, the s quark arising from a c quark decay interferes constructively with the spectator quarks, which is denoted by $\Gamma^+_{\rm int}$ [19].

Exchange of a W is possible in charmed baryons containing a d quark and in charmed mesons containing a $\overline{u}$ quark. This decay diagram is shown in Figure 1.4(c). We denote its contribution to the lifetime as $\Gamma_{\rm exc}$. The presence of the exchange mechanism is believed to be the primary reason the charmed baryon lifetimes are typically shorter than the charmed meson lifetimes.

Finally, in the case of the D^+_s, there is a Cabibbo favored mechanism by which the c quark and $\overline{s}$ quark can annihilate into a W^+. This process in shown in Figure 1.4(d) and is denoted by $\Gamma_{\rm ann}$. (For the D^+, this process is Cabibbo suppressed.)

Summarizing the most important contributions for the charmed hadrons, we obtain

$$\begin{aligned}
\Gamma(D^+) &= \Gamma_{\rm ext} + \Gamma^-_{\rm int} \\
\Gamma(D^0) &= \Gamma_{\rm ext} + \Gamma_{\rm exc} \\
\Gamma(D^+_s) &= \Gamma_{\rm ext} + \Gamma_{\rm ann} \\
\Gamma(\Lambda^+_c) &= \Gamma_{\rm ext} + \Gamma^-_{\rm int} + \Gamma_{\rm exc} \\
\Gamma(\Xi^+_c) &= \Gamma_{\rm ext} + \Gamma^-_{\rm int} + \Gamma^+_{\rm int} \\
\Gamma(\Xi^0_c) &= \Gamma_{\rm ext} + \Gamma^+_{\rm int} + \Gamma_{\rm exc} \\
\Gamma(\Omega^0_c) &= \Gamma_{\rm ext} + \tfrac{10}{3}\Gamma^+_{\rm int}
\end{aligned} \tag{1.5}$$

where the $\frac{10}{3}$ factor for the Ω^0_c arises since the final state contains three s quarks which constructively interfere. A very good discussion of these contributions in the baryon case is given in Reference 19. While this exercise shows conceptually why the Λ^+_c lifetime is shorter than any of the meson lifetimes, an accurate calculation requires the inclusion of Cabibbo and doubly Cabibbo suppressed processes as well. Figure 1.5 shows a comparison of the charm lifetimes.

1.4.3 Excited charmed baryons

The masses and widths of the nucleons (baryons composed three u and d quarks) are well measured and reasonably well predicted by theory. To a lesser extent, the same is true in the hyperon (composed of u, d, and s quarks) sector. However, in the charm sector, these measurements are much less advanced. To extrapolate the

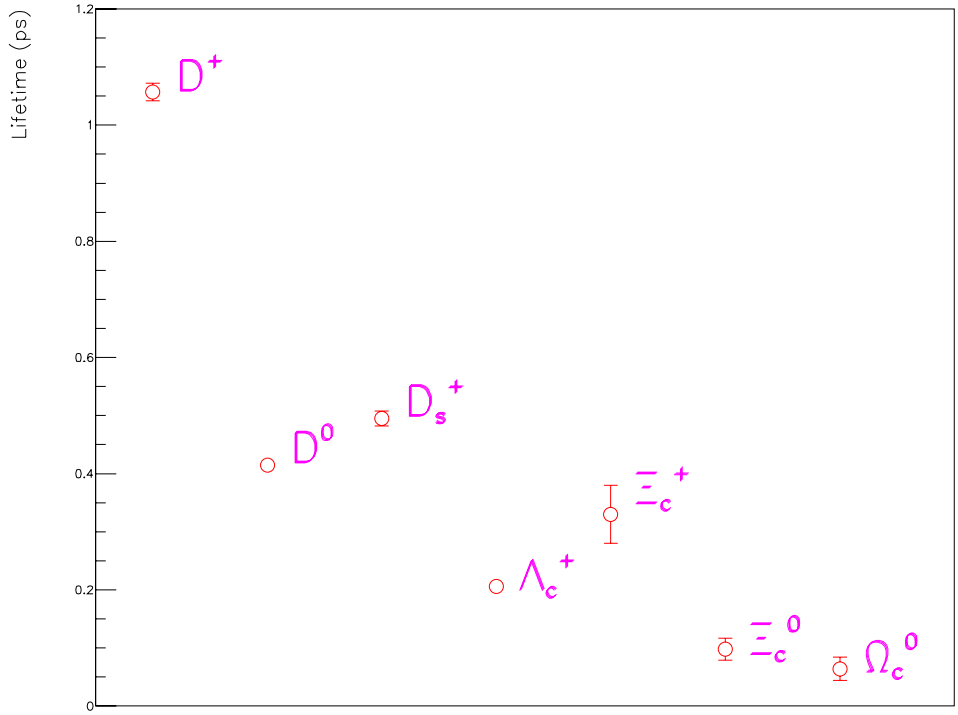

Figure 1.5: Lifetimes of the charmed hadrons [20].

properties of other charmed baryons, it is often useful to have accurate measurements of both the mass and width of a single state. Furthermore, as shown in Chapter 7, the mass and width of a strongly decaying baryon are related in the models through the available phase space for the decay. The Σ_c baryons are good candidates for such measurements since they are the most copiously produced excited charmed baryons. It is this which motivates the analyses presented in this thesis.

1.5 The FOCUS Experiment

The FOCUS experiment, also known as Fermilab Experiment 831 (E831), is a charm photoproduction experiment in the Fermilab fixed target program. Charmed particles are produced by the photon-gluon fusion process in which the virtual charm component of the photon is made real by exchanging a hard gluon with a target hadron (in our case a proton or a neutron). A diagram for this process is shown in Figure 1.6.

FOCUS is the extension of Fermilab E687, using the same beamline and many of the same spectrometer components. The primary goal of FOCUS is to reconstruct

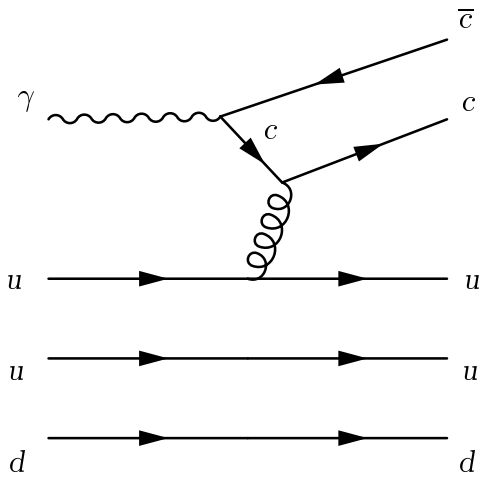

Figure 1.6: Diagram of the photon-gluon fusion process with a proton.

one million Golden Mode charm decays (the decay modes $D^0 \to K^-\pi^+$, $D^+ \to K^-\pi^+\pi^+$, and $D^0 \to K^-\pi^+\pi^+\pi^-$), a factor of 10 increase over E687 [21]. This goal was surpassed, enabling FOCUS to perform precision studies of charm decays not possible before.

The experiment took data during the 1996–1997 Fermilab fixed target run. The reconstruction of the data began early in 1998 and was completed by mid-1999.

Chapter 2

The FOCUS Beamline

In order to produce charmed particles with incident photons on a target, high energy photons must first be created. This is a multi-step process which begins with high energy protons. The first section of this chapter describes the proton acceleration process at Fermilab. The second section describes the method used by FOCUS to obtain high energy photons from protons. The final section describes the method used to measure the energy of these photons.

2.1 The 800 GeV Proton Beam

2.1.1 Proton acceleration

At Fermilab (Fermi National Accelerator Laboratory), the acceleration of protons from rest to their ultimate energy of 800 GeV is accomplished by a series of five accelerators, each of which (except for the last) transfers the beam to the next accelerator.

Cockcroft-Walton: In this accelerator ordinary hydrogen gas is ionized by the addition of electrons. The hydrogen ions (H^-) are electrostatically accelerated to an energy of 0.750 MeV through a system of voltage dividing diodes which are used to produce a single voltage gap of 750 kV.

LINAC: The LINear ACcelerator is a series of alternating high field and field free regions. The fields alternate such that the hydrogen ions always experience an accel-

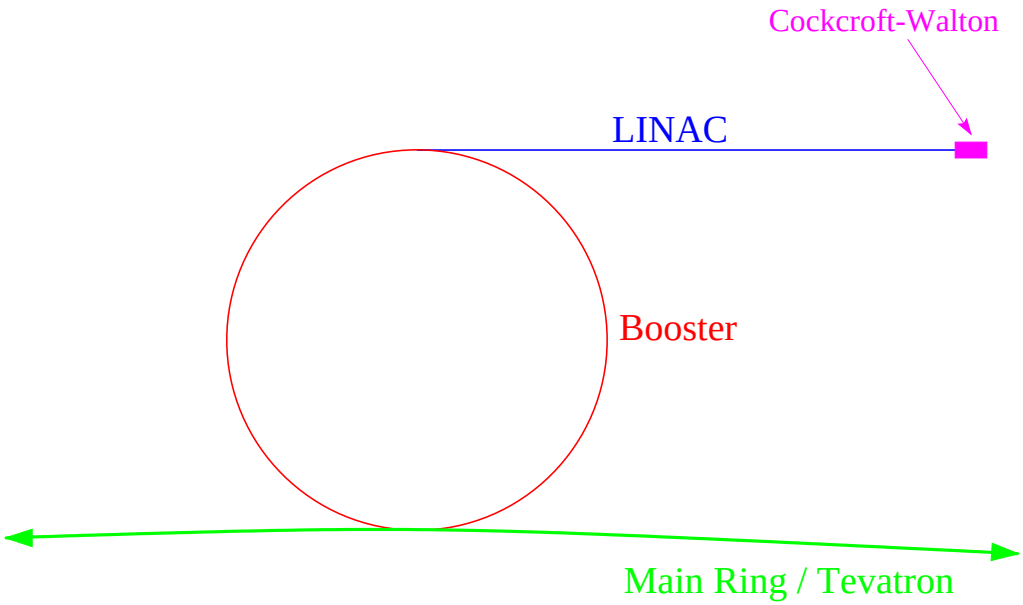

Figure 2.1: Schematic diagram of the arrangement of the Cockcroft-Walton, LINAC, and Booster.

erating electric field. The LINAC accelerates ions to an energy of 400 MeV. Upon exiting the LINAC, the ions pass through a thin carbon foil which strips off the electrons, allowing only the protons to continue.

Booster: The Booster is a rapid cycling synchrotron about 500' in diameter. The Booster accelerates a group of protons to 8 GeV and injects them into the Main Ring. It then accelerates and injects another group. Twelve such "batches" are needed to fill the Main Ring. The Booster, along with the accelerators which precede it, is shown in Figure 2.1.

Main Ring: The Main Ring is a synchrotron one kilometer in radius which uses normal steel dipole magnets. The Main Ring accelerates protons to 150 GeV before injecting them into the Tevatron.

Tevatron: The Tevatron is also a synchrotron which accelerates protons to 800 GeV and occupies the same tunnel as the Main Ring. The Tevatron uses liquid helium cooled, superconducting dipole magnets to contain the proton beam. A simplified view of the Tevatron, the Main Ring, and the Fixed Target beamlines is shown in Figure 2.2.

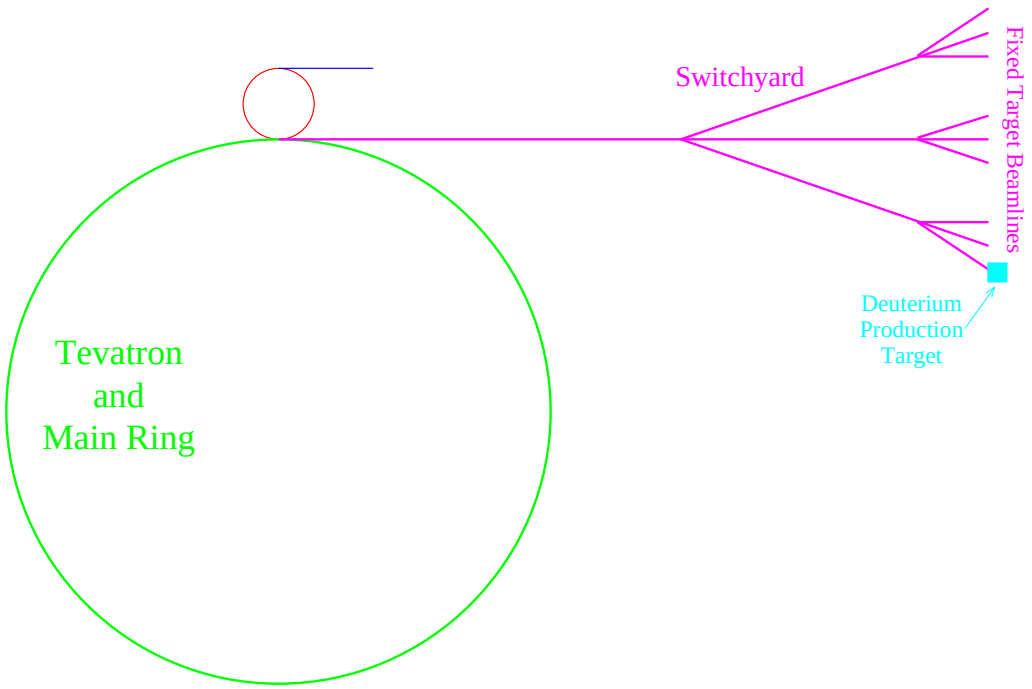

Figure 2.2: Schematic diagram of the arrangement of the Main Ring, the Tevatron, and the Switchyard.

2.1.2 Proton extraction

The acceleration process in the Tevatron takes about 40 seconds. At the end of acceleration, extraction begins and continues for roughly 20 seconds. Extraction is the process of slowly (so that protons are delivered to the experiments at low instantaneous intensity) removing the beam and sending it down the fixed target beamlines.

Through a series of electrostatic devices and specialized magnets in the "switchyard," the beam is split and directed to three major areas designated as "Proton," "Neutrino," and "Meson." The beams in each of these areas are split again into many less intense beamlines, as shown in Figure 2.2. The Wideband Photon Beam is in the Proton area of Fermilab.

The radio frequency acceleration cavities of the Tevatron operate at 53 MHz. This means that protons arrive at the experiment in regularly spaced 18 ns intervals, called "buckets." This timing is preserved by the fixed target beamlines and is present in the fixed target experiments.

2.2 The Wideband Photon Beamline

Producing the final photon beam for FOCUS is a multi-step process involving three production targets (in addition to the experimental target). Consequently, the number of photons obtained per proton is quite low. A typical spill from the Tevatron delivered about 5×10^{12} protons on the production target yielding about 1×10^{9} photons on the experimental target.

A schematic of the Wide Band photon beamline is shown in Figure 2.3.

Incident 800 GeV protons strike a cryogenically cooled liquid deuterium target 1.6 m long. Interactions in this target produce, among other particles, π^0s which decay promptly ($\tau \sim 10^{-16}$ s) into two photons. Liquid deuterium is chosen because of its large A/Z^2 ratio which maximizes the number of strong interactions while minimizing re-interactions of the the photons.

Charged particles produced in the target are swept aside using powerful dipole magnets while the neutral component of the beam strikes the photon converter, a sheet of lead 50% of a radiation length thick. Photons convert to e^+e^- pairs while other neutral particles, owing to the small number of interaction lengths, usually pass through. After the electrons and positrons are focused with quadrapole magnets, the charged portion of the beam is bent around a dump which absorbs the uninteracting neutral particles. The beam is momentum selected by being passed through collimators. For most of the FOCUS running the nominal beam energy was chosen to be 300 GeV with a "momentum bite" of $\pm 15\%$, hence the description "Wide Band."

The electrons and positrons[1] are transported by separate beamlines towards the experimental apparatus. The two beams are recombined into a single beam by the momentum recombining dipoles. The combined beam is refocused (so that it would impact the experimental target if unimpeded) and impacts the radiator which is a sheet of lead 20% of a radiation length thick where photons are produced by the bremsstrahlung process. After the beam passes through the radiator, powerful sweeping magnets remove the remaining charged portion of the beam which is directed into the RESH and POSH described in Section 2.3.2. The neutral portion of the beam (primarily photons) continues towards the experimental target. The mean photon energy produced by the 300 GeV electron beam is about 190 GeV.

Synchrotron radiation from electrons in the sweepers is emitted in a horizontal swath. This troublesome background is removed by a lead wall and a lead collimator between the electron dump and the experimental target. Electrons produced in this lead shielding are easily removed by a final sweeping magnet just upstream of the target.

[1] There is an occlusion near the neutral dump in the positron arm of the beam, which limits the positron beam to about 70% of the intensity of the electron beam.

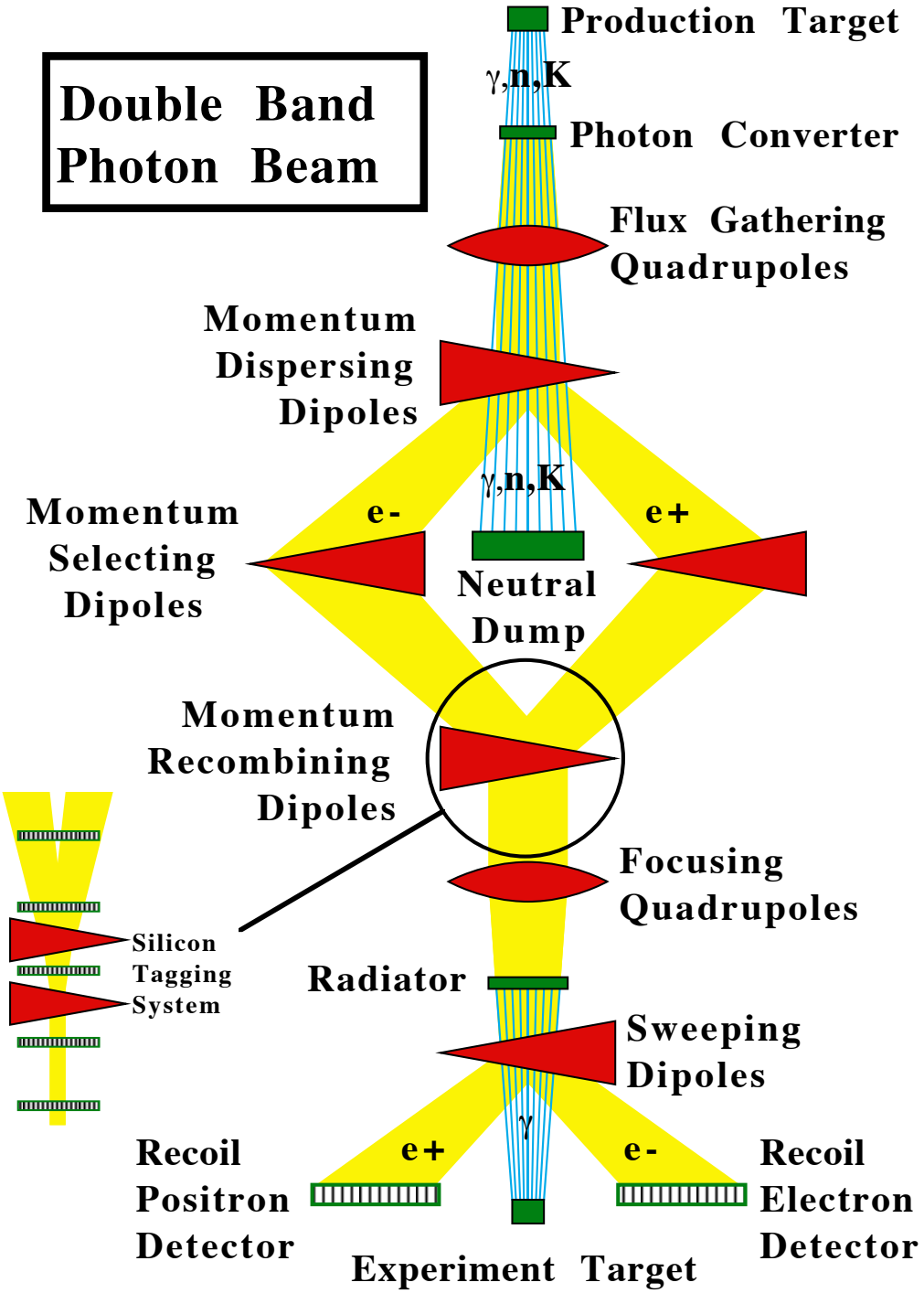

Figure 2.3: A schematic view of the major elements of the Wide Band photon beamline. The inset shows a schematic view of the electron beam tagging system.

This multi-step process has several important advantages. The primary advantage is that interactions in the experimental target caused by hadrons in the beam are greatly reduced. In order for such an interaction to occur, neutral hadrons must produce charged hadrons in the photon converter and those charged hadrons must create neutral hadrons in the radiator. At 300 GeV, the hadron contamination of the beam (defined as the number of triggered events caused by hadrons in the beam) is about 3.8%. Nearly all of this contamination is from the positron arm of the beamline. Large numbers of Λ^0's are produced in the primary target and the proton from the decay $\Lambda^0 \to p\pi^-$ often has the correct momentum to be transported down the beamline. The second advantage is that the tertiary beam allows a measurement of the energy of the final photons, as described in the next section. The primary disadvantages to a beam of this kind are that a large number of protons are required to obtain an intense photon beam and it is difficult to understand the luminosity of the photon beam.

The entire beamline between the production target and the recombining dipoles is under vacuum. From the dipoles to the experimental target, the beam is in a helium filled environment to minimize interactions with the air. The beamline is described in Reference 22. However, it should be noted that the positron arm of the beamline was also used for FOCUS.

2.3 The Photon Beam Tagging System

For some analyses, it is desirable to know the energy of the interacting photon. However it is not possible to directly measure the energy of a high energy photon in a non-destructive way. Instead, we measure the the photon energy by an indirect method.

In FOCUS, photons are produced by the bremsstrahlung process. By measuring the energy of the electron before (E_e) and after (E_r) the photon is radiated, we can infer the energy of the photon. We must also take into account bremsstrahlung radiation of multiple photons, some of which don't interact or interact electromagnetically. If these photons have a total energy $E_{\rm non}$, we find

$$E_\gamma = E_e - E_r - E_{\rm non} \tag{2.1}$$

where E_γ is the energy of the photon which produced a hadronic interaction in the target.

FOCUS has detectors which measure each of these three quantities.

2.3.1 Electron beam tagging

The beam tagging silicon (or "tagging") measures E_e, the incident electron energy. The tagging consists of five planes of silicon strip detectors, two on either side of the momentum recombining dipoles and one positioned between the two dipole magnets. This arrangement is shown in Figure 2.3. Each plane has 256 strips with a pitch of 300 μm. Since two dimensional position information is not needed for measuring momentum, the tagging only measures position in the bend (horizontal) view. The total active area of each plane is 7.7 cm wide by 5.7 cm high. The electron tagging system used in E687 is described in Reference 23; the design and operation of the system was unchanged for FOCUS. The momentum resolution of the beam tagging system is about 2%.

2.3.2 RESH and POSH calorimeters

In order to measure E_r (the energy of the electron after radiating a photon) we sweep out the electrons and positrons with dipole magnets and measure the bend angle. This is accomplished by two small calorimeters called RESH (Recoil Electron Shower) and POSH (recoil POsitron SHower). RESH and POSH each have 13 counters, labeled 0–12. RESH0 and POSH0 detect electrons and positrons which do not radiate. RESH and POSH are sampling calorimeters with alternating layers of lead and Lucite. (RESH0 and POSH0 use lead and SiO_2, chosen for its high degree of radiation hardness.) The arrangement of these counters is shown in Figure 2.4. By determining which cell or cells of the RESH or POSH the recoil electron impacts, we know the bend angle of the electron and thus its energy. The energies that these counters sample are listed in Table 2.1.

2.3.3 BGM calorimeter

In order to measure the non-interacting electromagnetic energy ($E_{\rm non}$), we use another small calorimeter, the Beam Gamma Monitor (BGM). The BGM is positioned near the point where e^+e^- pairs produced in the target are focused by the spectrometer magnets (Section 3.3). The BGM is constructed of 24 alternating layers of lead and SiO_2 and has a frontal area of 9" by 9". The BGM, like the RESH and POSH, has a depth of 24 radiation lengths and is very radiation hard.

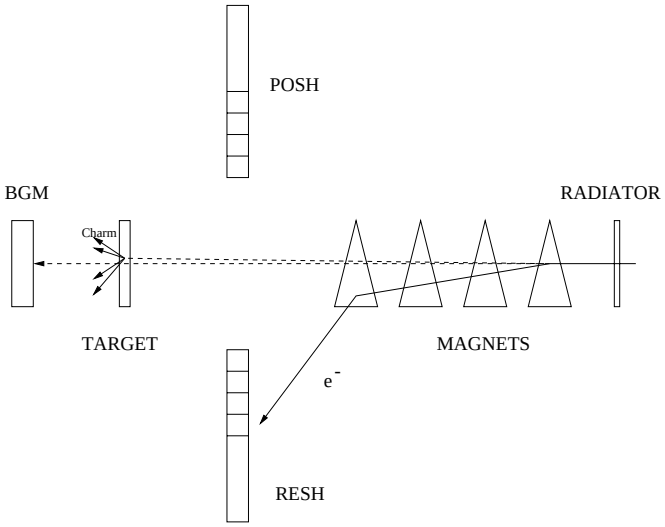

Figure 2.4: Schematic view of the RESH, POSH, and BGM calorimetry system. Electrons and positrons are deflected into the RESH and POSH. RESH0 and POSH0 are the counters closest to the beam. Noninteracting photons impact the BGM.

Table 2.1: Nominal energies for RESH & POSH counters with a 300 GeV electron beam. Listed is the central value of the recoil electron energies measured by each RESH & POSH counter. Note that RESH-10 & POSH-10 are redundant since electrons in the energy range covered by these counters impact the 11^{th} and 12^{th} counters instead. (The 11^{th} and 12^{th} counters are upstream of the others.)

Counter #	Energy (GeV)	
	RESH	POSH
0	251.7	252.3
1	153.7	152.1
2	117.2	116.2
3	94.7	94.1
4	79.5	79.0
5	68.4	68.1
6	60.1	59.8
7	53.6	53.4
8	48.3	48.2
9	41.6	39.5
10	32.3	30.0
11	41.7	41.7
12	14.9	14.9

Chapter 3

The FOCUS Spectrometer

The FOCUS spectrometer is a two magnet spectrometer with excellent particle identification. Major detector systems include silicon strip trackers for vertexing, multiwire proportional chamber trackers for momentum determination, and Čerenkov detectors for particle identification. Also present are electromagnetic and hadronic calorimeters, muon detectors, and numerous hodoscopes used in triggering.

The spectrometer is shown schematically in Figure 3.1. It is divided into two portions, termed "inner" and "outer". The inner portion subtends small angles (less than about 30 mrad) and consists of the detectors downstream of the second magnet. The outer portion subtends larger angles and is the portion of the spectrometer between the two magnets. The terms "upstream" and "downstream" are also used in describing the spectrometer; the beam enters from the upstream direction.

The FOCUS spectrometer is an upgrade of the FNAL-E687 spectrometer which is described in Reference 24. Many of the detector systems from E687 have been replaced or upgraded, but the general structure of the spectrometer is the same. Many of the upgrades are described in Reference 25.

In the following sections, the individual detectors are described with emphasis on the detectors of particular importance to the analyses presented in this thesis.

3.1 Target Configuration

Experience from E687 has shown that requiring secondary decay vertices to be outside of the target material greatly increases the cleanliness of charm signals [26]. For most of the FOCUS running we used a segmented beryllium oxide (BeO) target

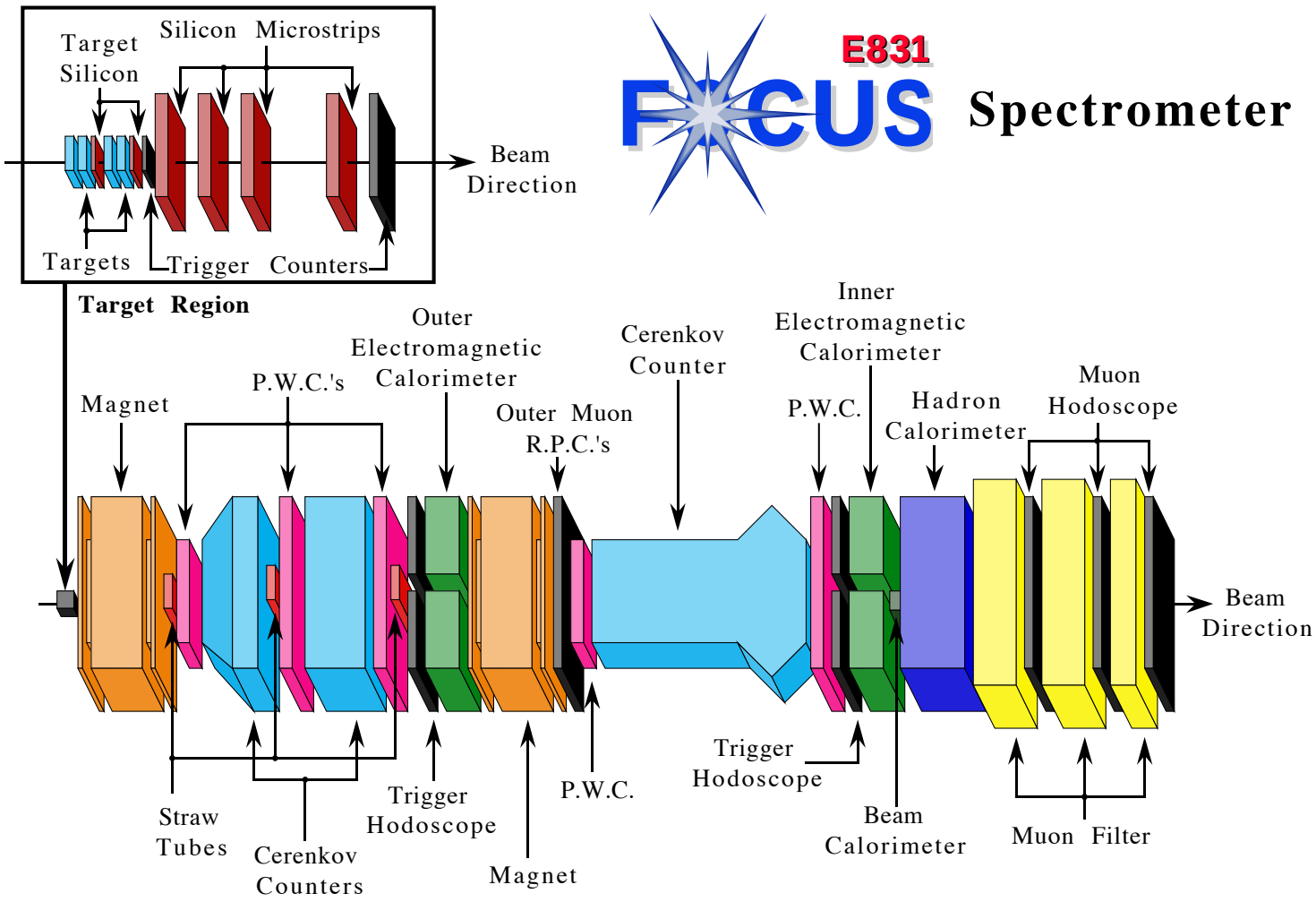

Figure 3.1: An overview of the elements of the FOCUS spectrometer. The inset shows an expanded view of the target region which is also shown in Figure 3.2.

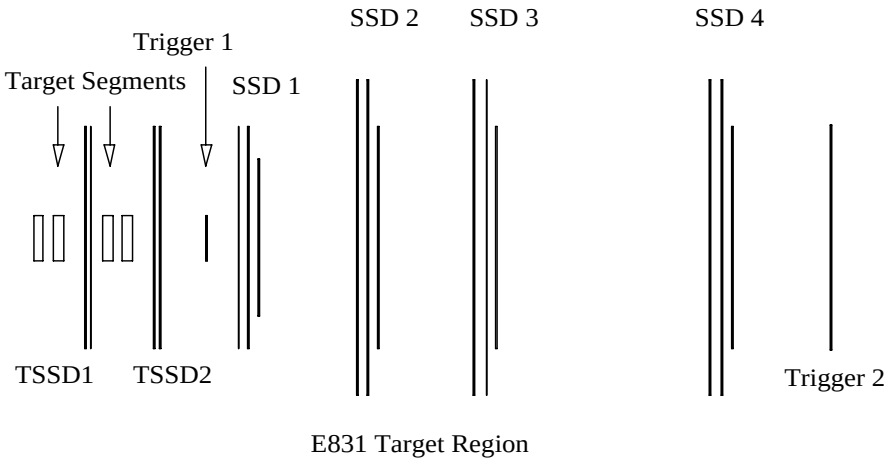

Figure 3.2: Diagram of the target region. Shown are the BeO targets, the embedded silicon microstrip (TSSD) planes, the downstream silicon microstrip (SSD) planes, and triggering hodoscopes. The beam enters from the left.

with embedded silicon strip detectors. The segmentation allows a large number of "out-of-target" decays. Studies have shown that a large portion of the out-of-target background comes from other charm decays which are easier to model than production and re-interaction processes.

BeO was chosen as the target material because of its large A and high density for a low Z material. Hadronic photoproduction is highly dependent on A while conversion pairs, a troublesome background, are proportional to Z^2. A high density target enhances the number of "out-of-target" decays by packing more target material in a smaller volume.

The final FOCUS target configuration is shown in Figure 3.2. Each of the four target segments is 6.75 mm thick in the beam direction and 25.4 mm square. Spacing between the target segments and detector elements is 10 mm. This is the target configuration with which most of our data was accumulated. Other configurations included a single beryllium (Be) target, a segmented Be target, and a segmented BeO target without embedded silicon microstrip detectors.

3.2 Silicon Microstrip Tracking

Silicon strip detectors gather charge liberated by ionizing particles. This charge (in the form of electrons and holes) is collected at the ends of the strips where it is amplified and digitized. The primary advantage of silicon strip detectors is that the

strips can be placed very close together (25 μm or less), which gives excellent spatial localization.

Tracking and vertexing in the target region is performed by two silicon microstrip systems. The first system is embedded between target segments, the second is located downstream of the targets.

3.2.1 Embedded stations

In order to increase vertex resolution, there are two stations of high resolution silicon strip detectors embedded in the target region. Each station has two views oriented at $\pm 45^\circ$ from horizontal; each view has 1024 strips with 25 μm spacing, creating an active region about 25 mm across. This dimension is well matched to the beam size and to the extent of the target segments. Each strip is about 50 mm long, giving an active area of about 50×25 mm^2 per plane. Readout is accomplished with ADCs (Analog to Digital Converters) [27].

The first station of the Target Silicon or TSSD is positioned between the second and third target segments. The second station is located just after the last target segment and upstream of the first trigger counter. Figure 3.2 and the inset of Figure 3.1 show the position of various elements in the target region. The Target Silicon system was only in place for the 1997 running of FOCUS which comprises about 2/3 of the data collected.

3.2.2 Downstream stations

Downstream of the target and upstream of the first magnet, tracking is performed by a system of silicon microstrip detectors referred to as the Silicon Strip Detector (SSD). There are four stations of detectors, as shown in Figure 3.2 and labeled as "SSD."

Each station has 3 views. With respect to the horizontal axis of the experiment, the three views are oriented at -135°, -45°, and -90° from most upstream to most downstream. The planes within a station are separated by 5 mm. The first three stations are separated by 6 cm; the last two stations are separated by 12 cm.

Each plane consists of two regions, an inner region with finer pitch strips and an outer region with more widely spaced strips. The most upstream station has 25 μm inner strips and 50 μm outer strips. The remaining three stations have 50 μm inner strips and 100 μm outer strips. Each of the 12 planes has 688 channels of ADC readout.

The properties of the SSD stations are summarized in Table 3.1 and are described in greater detail in Reference 28.

Table 3.1: The properties of the SSD planes. Station 1 is the most upstream station (closest to the target).

Station	Active Area		Strip Pitch
	Total	High Res.	
1	2.5×3.5 cm^2	1.0×3.5 cm^2	25 μm, 50 μm
2	5.0×5.0 cm^2	2.0×5.0 cm^2	50 μm, 100 μm
3	5.0×5.0 cm^2	2.0×5.0 cm^2	50 μm, 100 μm
4	5.0×5.0 cm^2	2.0×5.0 cm^2	50 μm, 100 μm

3.3 Analysis Magnets

To find the momentum of tracks, we use two high current, large aperture analysis magnets. The momentum of a particle is determined by measuring the change in the slopes of tracks before and after each magnet. The construction of the two magnets is nearly identical. The first magnet, M1, is just downstream of the silicon vertex detectors. The second magnet, M2, is in the center of the spectrometer, between the third and fourth wire chambers. Each magnet is 1.7 m long, has a 76 cm (horizontal) by 127 cm (vertical) aperture and a mass of about 245,000 kg.

The two magnets are operated with opposite polarities. Because there are a large number of e^+e^- pairs produced in the target,[1] by running with opposite polarity the pairs can be roughly focused onto the Beam Gamma Monitor (Section 2.3.3) near the downstream end of the spectrometer. The first magnet operates at a current of 1020 A yielding a kick of 0.400 GeV/c. The second magnet operates at 2000 A providing a kick of 0.836 GeV/c. The magnets deflect charged particles in the vertical direction.

3.4 Multiwire Proportional Chambers

A multiwire proportional chamber (MWPC) is constructed with alternating planes of high voltage wires and sense wires, which are at ground. All the wires are placed in a special gas environment. Gaps between planes are usually on the order of millimeters and voltage differences are typically in the kilovolt range. When a charged particle passes through the gas in the chamber, it will ionize gas molecules. The freed electrons

[1] This background is an important consideration in the design of many detectors. As will be seen, many detectors leave the "pair region" un-instrumented.

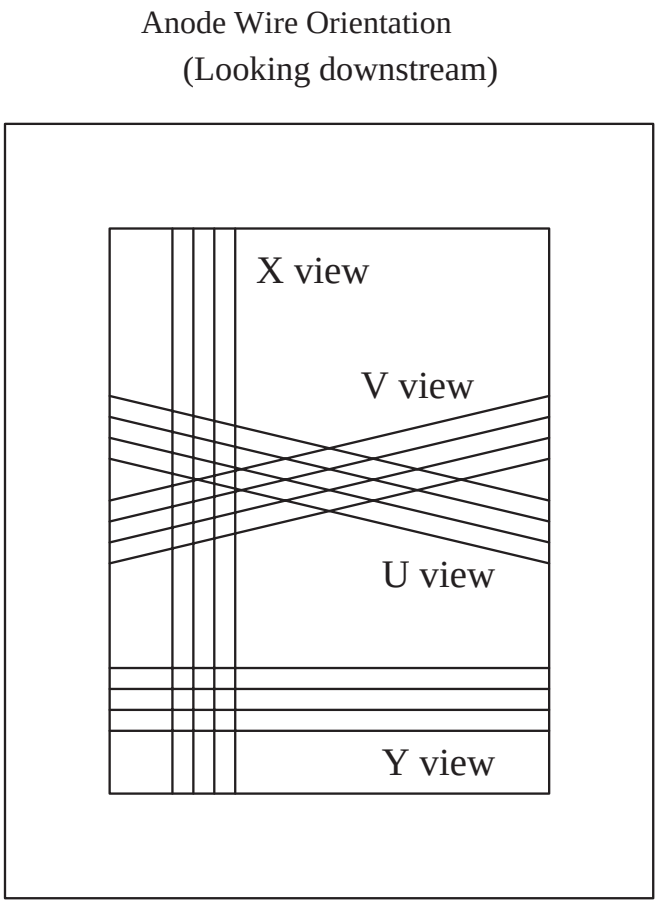

Figure 3.3: Orientation of the PWC wire planes, showing the $\pm 11.3^\circ$ angle of the U and V planes with respect to the horizontal.

are accelerated towards the sense wire by the electric field, ionizing more of the gas. In this way a cascade of charge develops and is deposited on the sense wires. The smaller the diameter of the sense wires, the higher the field gradient near the wire becomes. This in turn causes a larger cascade, increasing the efficiency of the chamber.

In FOCUS, tracking downstream of the first magnet is accomplished using five multiwire proportional chambers (called PWCs in our nomenclature). Each PWC has four planes per station. The stations are labeled (from most upstream to most downstream) P0, P1, P2, P3, and P4. We naturally divide tracks into two categories: 3-chamber tracks ("outer") which are outside the aperture of M2 and 5-chamber tracks ("inner") which traverse the entire spectrometer.

All five chambers operate with a gas mixture of 75% argon and 25% ethane bubbled through methyl alcohol. Each chamber has four planes of sense wires. The X wires run vertically and measure the position in the horizontal direction. The Y planes measure the horizontal position. The U and V planes are inclined at $\pm 11.3^\circ$ from the horizontal. This arrangement is shown in Figure 3.3.

The chambers P0 and P3 (called Type I stations) are identically constructed. P0 and P3 are just downstream of M1 and M2 respectively. These chambers have apertures of about 76 cm $\times$ 127 cm (matched to the magenet aperatures) and have 0.8 mil diameter gold plated tungsten sense wires spaced at 80 mil. The gap between high voltage planes and sense wires is 0.235".

The Type II chambers (P1, P2, and P4) have 152 cm $\times$ 229 cm apertures. The sense wire spacing is 3.3 mm with 1.0 mil diameter wires. The gap between high voltage planes and sense wires is 0.240". P1 and P2 are situated between P0 and the first magnet. P4 is situated after the last Čerenkov detector.

The positions and construction of the five chambers are summarized in Table 3.2.

Table 3.2: A summary of the properties of the five multiwire proportional chambers.

Wire Chamber	Wire spacing	Wires/plane				Size	Position
		X	Y	U	V	$(X \times Y)$	(cm from target)
P0	0.080"	376	640	640	640	76×127 cm^2	403
P1	0.130"	480	704	768	768	152×229 cm^2	644
P2	0.130"	480	704	768	768	152×229 cm^2	879
P3	0.080"	376	640	640	640	76×127 cm^2	1,444
P4	0.130"	480	704	768	768	152×229 cm^2	2,286

3.5 Straw Tube Chambers

Straw tube chambers work similarly to multiwire proportional chambers, but instead of high voltage being supplied along a plane, the high voltage is maintained on a metal coated tube (or straw) with a ground sense wire in the center. Because each sense wire has its own source of electric field, straw tube chambers can be operated reliably in higher rate environments. They also have the additional benefit of being more reliable since a single broken wire only impacts one channel.

It was originally feared that the FOCUS PWC system would not be able to handle the high rates present in the pair region and that the PWCs would have to be "deadened" in this region. To prepare for this possibility, three straw tube chambers were constructed to cover the pair region of each of the first three PWCs.

The three straw tube chambers have similar designs with the length and number of the straws being the primary difference between chambers. (P0 is smaller than P1 and P2 so the corresponding straw tube chamber is also smaller.) ST0 and ST1 are placed just in front of P0 and P1 respectively, ST2 is placed just *behind* P2.

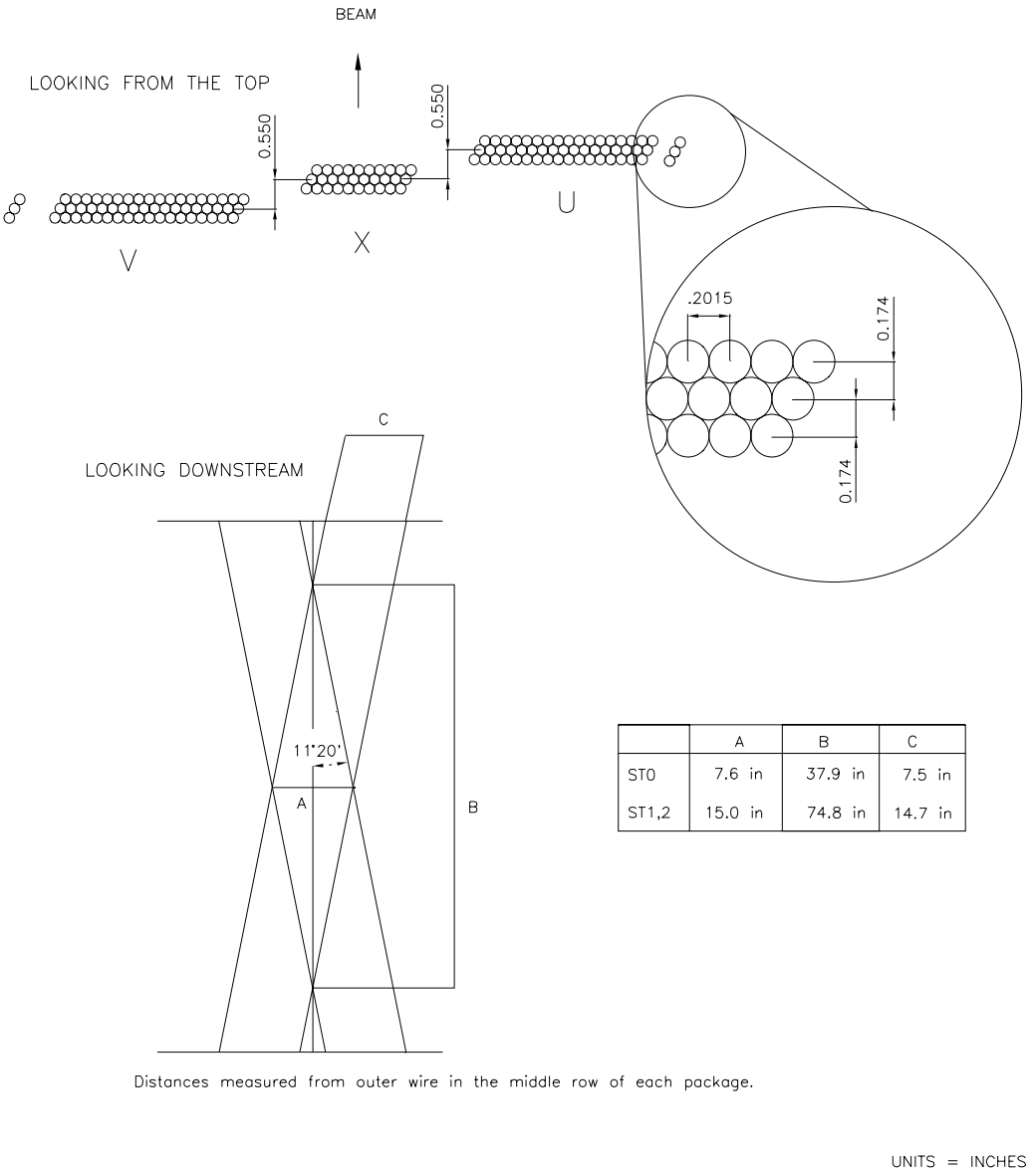

	A	B	C
ST0	7.6 in	37.9 in	7.5 in
ST1,2	15.0 in	74.8 in	14.7 in

Figure 3.4: Diagram, including measurements, showing the construction of ST0, ST1, and ST2.

There are three views per station, one vertical and two aligned at $\pm 11.3^\circ$ from vertical. Each view has three layers of straws. All the chambers use 5 mm diameter straws. The design of the straws is shown in Figure 3.4 with their properties summarized in Table 3.3.

In the end, deadening the PWC system was not necessary, so the straw tubes were not needed for tracking. However, because the straw tubes are read out with TDCs (Time to Digital Converters), they can provide useful information about the timing of events, rejecting tracks which occur in other accelerator buckets (see Section 2.1.2).

Table 3.3: A summary of the properties of the three straw tube chambers.

Straw Chamber	Straw length	Wires/view		Total Wires
		Vertical	Angled	
ST0	138 cm	3×10	3×38	258
ST1	241 cm	3×10	3×74	474
ST2	241 cm	3×10	3×74	474

3.6 Čerenkov System

Čerenkov light is emitted by particles traveling faster than the speed of light *in a medium*. In particular, light is emitted if

$$\beta = \frac{p}{E} = \frac{p}{\sqrt{p^2 + m^2}} > \frac{1}{n} \tag{3.1}$$

where n is the index of refraction of the material. (We use units where $c \equiv 1$.) Solving for the threshold p_{thresh} momentum (where $\frac{p}{E} = \frac{1}{n}$) in terms of the mass and the index of refraction of the medium we obtain

$$p_{\text{thresh}} = \frac{m}{\sqrt{n^2 - 1}} \ . \tag{3.2}$$

Additionally we know that Čerenkov light is emitted at an angle, $\cos\theta_c$, described by

$$\cos\theta_c = \frac{1}{n\beta} \ , \tag{3.3}$$

so using the direction of a track we calculate where the Čerenkov light should appear in the detector. See Figure 3.5 for an illustration of this angle.

The FOCUS spectrometer includes three threshold Čerenkov detectors. We look for the presence or absence of light to identify a particle. For a given track momentum we determine the four particle identification possibilities (e, π, K, and p). The gases in the detectors have been chosen to provide wide momentum ranges over which pions can be distinguished from kaons and protons. There is also a wide range over which kaons and protons can be distinguished from each other. The three Čerenkov detectors are called C1, C2, and C3. The properties of the Čerenkov detectors are summarized in Table 3.4. Except for slight changes in gas mixtures, these detectors are well described by Reference 24.

C1: The C1 detector is located between P0 and P1. The detector is filled with a 58% helium, 42% nitrogen mixture, which gives the detector a pion threshold of 8.5

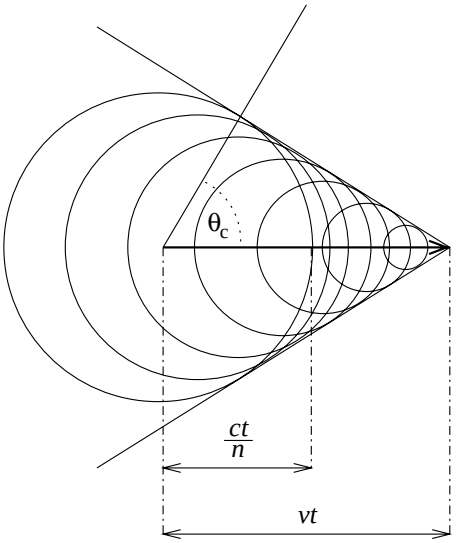

Figure 3.5: Origin of Čerenkov radiation. This figure shows the electric fields (circles) emanating from a charged particle moving along the horizontal line. When the speed of the particle exceeds c/n, a "shock wave" builds along the angled lines, resulting in the propagation of electromagnetic energy (light) at the angle θ_c. (Figure adapted from Reference 29.)

Table 3.4: Gases and threshold momenta of the three Čerenkov detectors.

Detector	Gas	Threshold (GeV/c)		
		π	K	p
C1	58% He/42% N_2	8.5	29.9	56.8
C2	N_2O	4.5	16.2	30.9
C3	He	17.0	61.0	116.2

GeV/c. The detector extends 80" in the vertical (bend) direction and 50" in the horizontal (non-bend) direction. There are 90 cells with photomultiplier tube (PMT) readout. In the outside portion of the detector, spherical mirrors are used to focus light onto each individual PMT. In the inner, high rate, portion of the detector, two planar mirrors oriented at $\pm 45^\circ$ to the beam reflect Čerenkov radiation orthogonal to the beam to where it is collected by a set of 50 PMTs. The inner PMTs are surrounded by light collecting Winston cones.[2] The cell geometry of C1 is shown Figure 3.6a.

C2: The design of C2 is similar to C1. This Čerenkov detector is located between P1 and P2 and is filled with nitrous oxide (N_2O) gas which has a pion threshold of 4.5 GeV/c. C2 has dimensions of 100" in the vertical direction and 64" in the horizontal direction. Čerenkov light is focused onto the outer 56 cells by spherical mirrors.

[2]Winston cones reflect incident light into the apex of the cone.

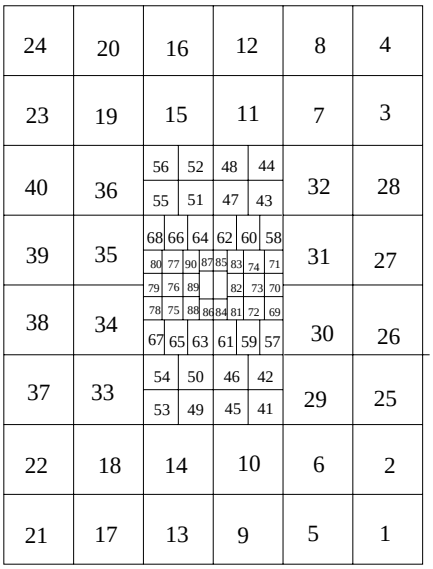

(a) C1. Cells 1–40 use spherical mirrors, 41–90 use planar mirrors.

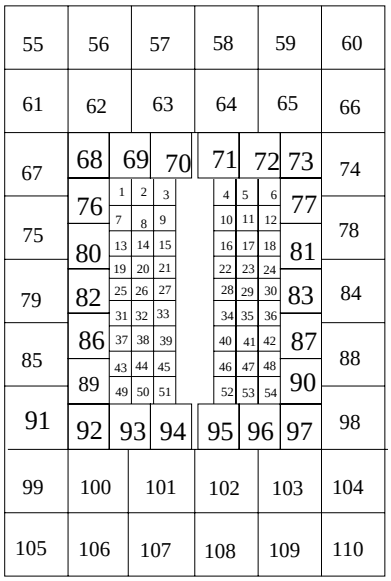

(b) C2. Cells 1–54 use planar mirrors, 55–110 use spherical mirrors.

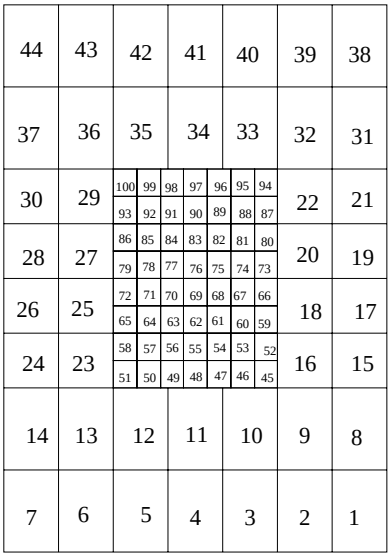

(c) C3. All cells use spherical mirrors.

Figure 3.6: The arrangement of the light gathering cells for the three Čerenkov counters, C1, C2, and C3.

Čerenkov light in the central region is reflected by a planar section, composed of 32 small planar mirrors. Light from the planar section is gathered with Winston cones. The geometry of C2 is shown Figure 3.6b.

C3: The final Čerenkov detector in the FOCUS spectrometer is C3, a helium filled device with a pion threshold of 17.0 GeV/c. C3 is located between P3 and P4 and has dimensions of 93.25" in the vertical direction and 60" in the horizontal direction. In C3, light from each cell is focused with a spherical mirror onto a PMT. The cell arrangement of C3 is shown in Figure 3.6c.

The momentum ranges over which particles can be identified are shown in Table 3.5. Note that these numbers assume a large number of emitted photons, an unrealistic assumption. Near threshold, it is often the case that only a few photons may be emitted and may avoid detection. The Čerenkov algorithm described in Section 4.2.1 takes this into account and we are able to extend these momentum ranges slightly.

Table 3.5: Particle identification ranges for the Čerenkov system. These are the positive and ambiguous identification ranges for 3- and 5-chamber tracks based on the momentum thresholds of the detectors. The performance of the Čerenkov algorithm is slightly different as there are no absolute ranges.

Definite Čerenkov ID range (GeV/c)				
	e	π	K	p
3-chamber	0.16–8.5	4.5–8.5	16.2–29.9	16.2–56.8
5-chamber	0.16–17.0	4.5–17.0	16.2–56.8	16.2–56.8 and 61.0–116.2
Ambiguous Čerenkov ID range (GeV/c)				
	e/π	$e/\pi/K$	K/p	π/K/p
3-chamber	8.5–29.9	29.9–56.8	4.5–16.2	0.16–4.5
5-chamber	17.0–61.0	61.0–116.2	4.5–16.2	0.16–4.5

3.7 Calorimetry

A calorimeter measures the energies of particles by destructive processes. In a calorimeter, particles interact with the material of the calorimeter, emitting several other particles as a result. In electromagnetic calorimeters, the relevant reactions are the bremsstrahlung process ($e^- \to e^- + \gamma$) and pair conversion ($\gamma \to e^+ e^-$). Hadronic calorimeters, rely on strong interactions of hadrons which produce other hadrons (typically pions). In both cases, the final number of charged particles is counted and the energy is inferred since $n_{\text{particles}} \propto E_{\text{incident}}$.

Sampling calorimeters contain alternating layers of interacting material and scintillating material and measure the number of charged particles passing through the scintillator. A calorimeter made of a transparent substance like lead glass detects the charged particles primarily by the Čerenkov light emitted by the fast moving particles in the medium.

Calorimetry is especially important for reconstructing neutral particles since these particle leave no ionization in any of the tracking systems. In FOCUS, these particles are the γ and the π^0 (decaying to two photons) which are detected by electromagnetic calorimeters. The hadronic calorimeter detects the K_L^0 and neutrons. The electromagnetic calorimeters are also used for electron identification.

3.7.1 Inner Electromagnetic calorimeter

The Inner Electromagnetic calorimeter (IE) is a lead glass calorimeter constructed of 802 lead glass blocks. The glass used is Schott F-2 type which has a 45% lead oxide composition. The front and rear faces of each block are 5.8 $\times$ 5.8 cm square; the length of each block is 60.2 cm. This corresponds to 18.75 radiation lengths and 2.2 proton interaction lengths. Each block is wrapped in aluminized mylar which serves to reflect and guide produced light down the length of the block to a photomultiplier tube attached to the end.

The IE is composed of two banks of lead glass elements, each of which is 37 blocks high by 11 blocks wide. The long dimension of each block lies along the beam direction. An uninstrumented gap of 5.5" (5.0" of air and 0.5" of steel support) runs along the entire height of the detector to prevent interactions with conversion e^+e^- pairs. Also, three blocks in each corner are "missing." (The original lead glass blocks were reused from another experiment, so there are not enough blocks to make perfect rectangles.) This arrangement is shown in Figure 3.7. Because the blocks are not uniform in size, the position and orientation within the array for each block was determined by an algorithm which minimized gaps between the blocks. The total dimensions of the array are 2.15 m (H) by 1.39 m (W). The IE, including the construction process, is more fully described in Reference 30.

IE Based Triggers: In addition to the signals from each block, "summing modules" are used to extract a small part of the signal and form several different energy sums for large parts of the IE. All the channels in the IE were arranged into groups of 9, roughly based on transverse energy (shown in Figure 3.7), for the purpose of providing inputs to the trigger. A sum of the entire IE energy ($E_{\rm IE}$) and a sum of the transverse energy $E_{T({\rm IE})}$ are formed.

A trigger component designed to select the decay $J/\psi \to e^+e^-$ is also formed. Using

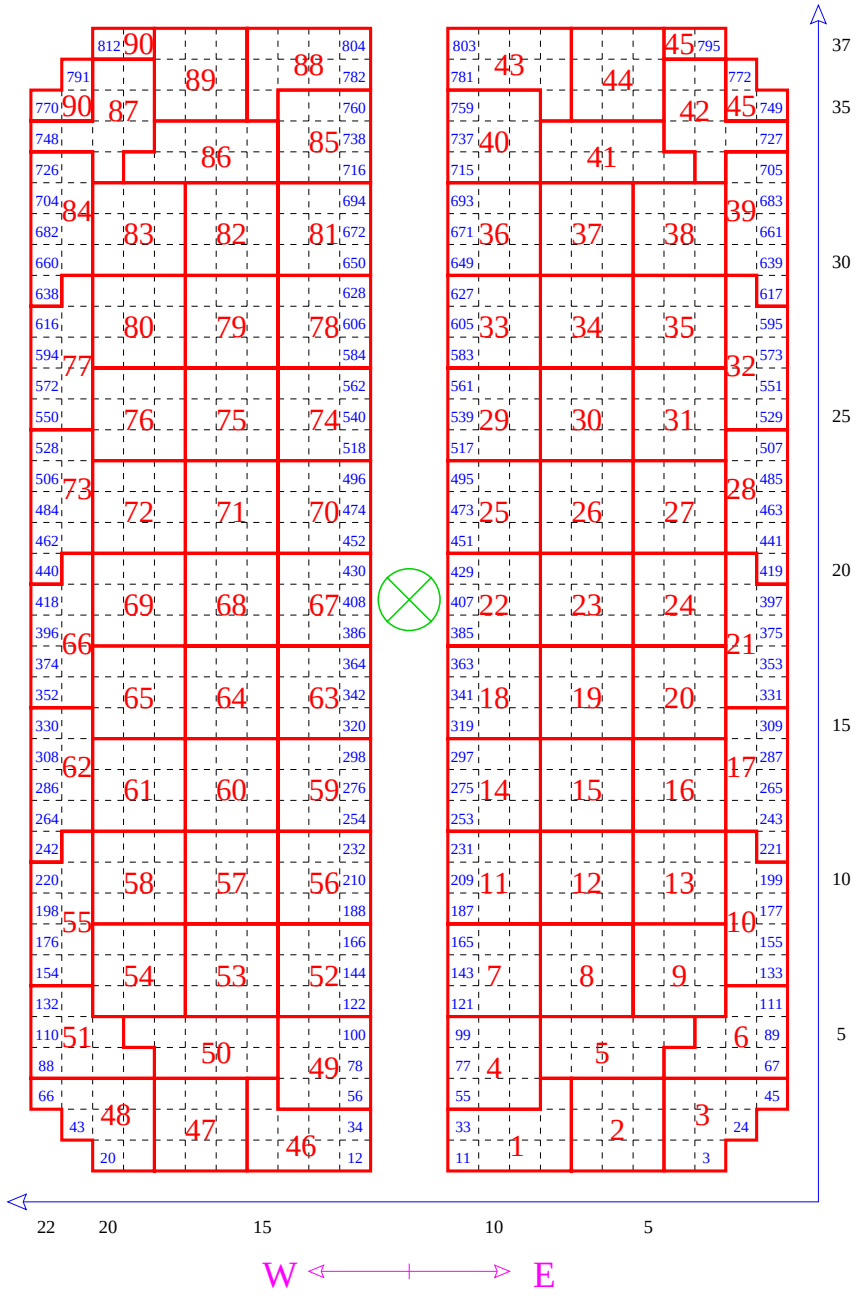

Figure 3.7: Schematic view of the Inner Electromagnetic calorimeter as seen by the beam. The thin dashed lines show each lead glass block; the thick solid lines show the blocks which make up each sum. All numbers are part of the internal numbering schemes. Sums 1–15 compose the first sextant of the dielectron trigger, sums 16–30 compose the second sextant, etc.

summed outputs, sums are made of six regions (sextants) of the IE (three roughly square regions on each side of the detector). The trigger required substantial energy (about 20 GeV) deposited in two non-adjacent sextants. (Sextants separated by the pair gap are considered non-adjacent.) Allowed and disallowed combinations are shown in Figure 3.8. See Section 3.10 for more information one how this information was used. This trigger element is described in Reference 31.

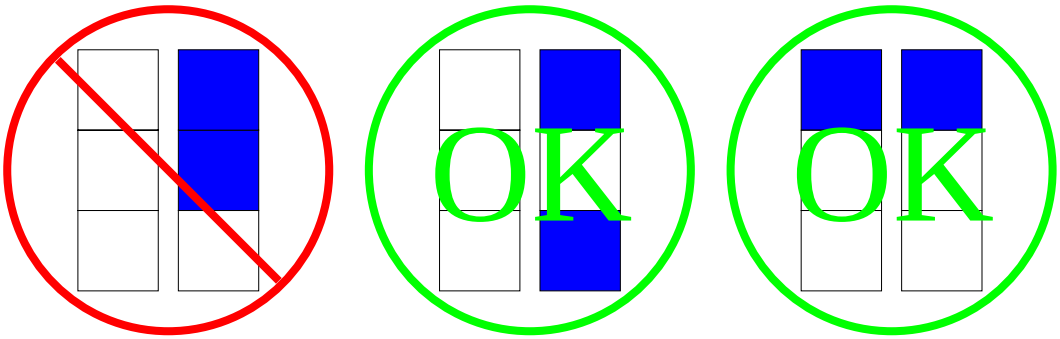

Figure 3.8: Examples of the dielectron trigger logic. The solid blocks show sextants with large energy deposited. The first case fails to cause a trigger, the second and third cases are valid dielectron triggers.

3.7.2 Outer Electromagnetic calorimeter

The Outer Electromagnetic Calorimeter, or OE, is positioned just before M2 and detects photons and electrons produced at wider angles. The total extent of the detector is 255 cm in the horizontal and 205 cm in the vertical. There is an internal aperture of 51 cm by 88 cm which matches the aperture of M2 and a small gap in the horizontal direction to prevent conversion pairs from interacting with the calorimeter. These dimensions correspond to an angular acceptance (from the target) of $28 \leq |\theta_x| \leq 142$ mrad and $49 \leq |\theta_y| \leq 114$ mrad.

The OE is a sampling calorimeter with alternating layers of lead and plastic scintillator. There are 23 layers of 3.3 cm wide rectangular scintillator paddles. Each paddle is instrumented at the end with a PMT. The detector consists of x, y, u, and v planes. (The u and v planes are oriented at $\pm 45^\circ$ from horizontal.) A side view showing the layers of the OE is shown in Figure 3.9

Additionally, there is a single plane of 100 scintillator tiles with fiber optic readout. This plane is used to aid in pattern recognition and is called the "tie-breaker" plane. (The x and y hits from two photons striking the detector at two distinct points give four possible reconstructed positions. The tie-breaker plane and u and v planes break this ambiguity.) The organization of the tie-breaker plane is shown in Figure 3.10, which also illustrates the coverage of the detector. Note that only the central, highest

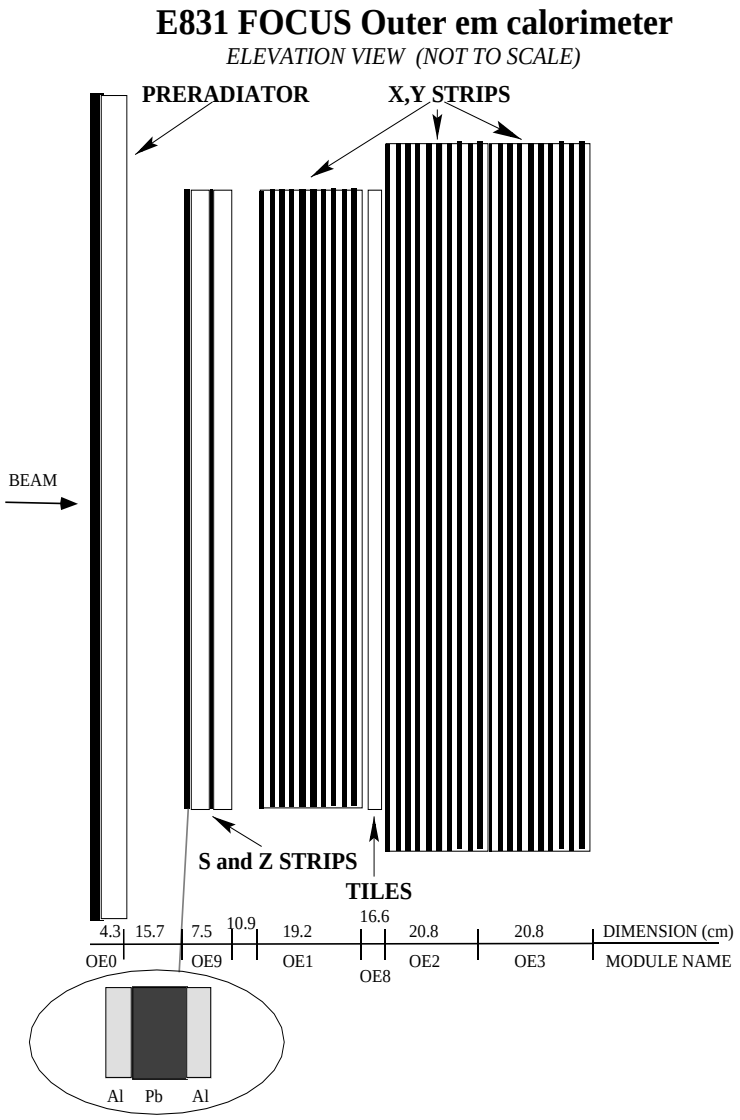

Figure 3.9: Side view of the OE showing the layout of the various layers of scintillator.

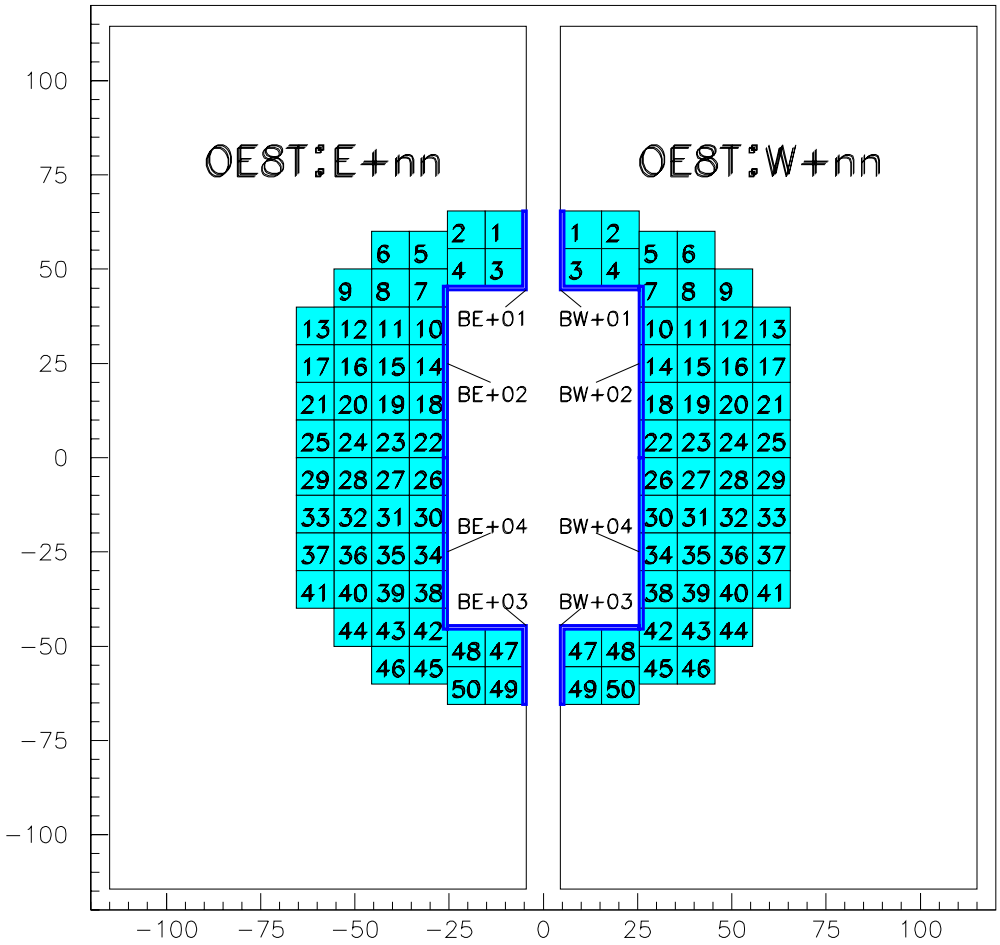

Figure 3.10: The OE tiebreaker tiles are visible around the aperture. The outer boundary shows the extent of the parts of the OE instrumented with scintillator paddles.

rate, area is instrumented with tiles. Including the tiles, there are a total of 1030 channels in the OE. The OE is more fully described in Reference 32.

3.7.3 Hadron Calorimeter

The Hadron Calorimeter (HC) is positioned behind the IE. The calorimeters detects energy released by hadrons, including neutral hadrons. The HC is constructed of alternating layers of steel and plastic scintillator tiles. The scintillators are arranged in pads within each layer; multiple layers are optically combined to form towers. The entire calorimeter is 300 cm (H) by 200 cm (W). The depth is 209 cm or 7.8 hadronic interaction lengths.

The tiles are arranged with small (20 cm square) tiles in the center and larger (40 cm and 50 cm square) tiles at the outer edges for a total of 66 tiles per layer. There are 28 layers of 4.4 cm thick[3] steel which alternate with 28 layers of scintillator. The first nine layers are combined to form the towers in the first section, the next 15 layers form the second section, and the last 4 layers form the towers in the final section. This arrangement is illustrated in Figure 3.11. This scheme allows for a small number (192) of channels of readout, but still allows a measurement of energy deposition as a function of depth by using the super-layers. Also, the last super-layer can be used to provide rudimentary muon identification which is helpful for very low energy muons. The HC is more fully described in References 33 and 34.

HC Energy Trigger: The signals from the PMT dynodes in the HC are summed, integrated and discriminated to form a hadronic energy trigger. The efficiency of this energy trigger as a function of the energy is shown in Figure 3.12. The HC energy forms an important component of the FOCUS trigger, as described in Section 3.10.

3.8 Muon Detectors

Muon identification is possible because muons are the only charged particles which can penetrate large amounts of material. As described in Section 3.7, electrons and hadrons interact destructively in material. Muons, due to their large mass relative to the electron, do not suffer from such catastrophic interactions. The method for detecting muons, then, is to place charged particle detectors behind a large amount of shielding material (typically steel).

The FOCUS experiment has two muon detection systems. The Inner Muon detectors use common scintillator detector elements. The Outer Muon system uses resistive plate chambers to detect passing muons.

3.8.1 Inner Muon detector

Muon detection in the inner region is performed by three stations of scintillating hodoscopes termed MH1, MH2, and MH3 [35]. Each station has two views; MH1 and MH2 have x and y views while MH3 has u and v views oriented at $\pm 45^{\circ}$. In front of MH1, MH2, and MH3 are 61 cm, 129 cm, and 68 cm of steel respectively. (This is in addition to the 126 cm of steel in the HC.) Because of multiple Coulomb scattering in this steel, good position resolution becomes less important for the downstream stations, so these stations have scintillating strips with a larger pitch.

[3]The first two layers are 6.4 and 5.1 cm thick, respectively

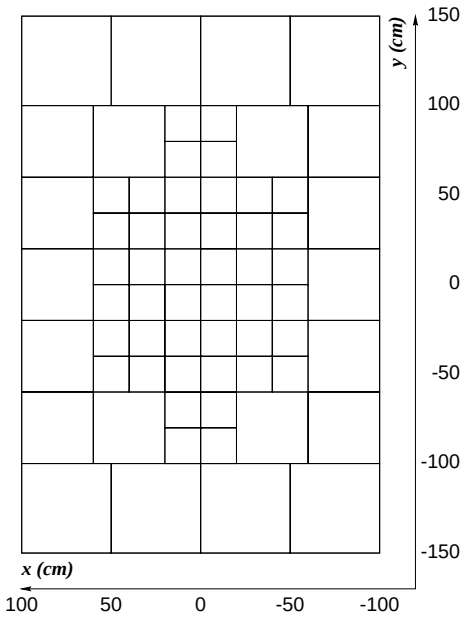

(a) Front view

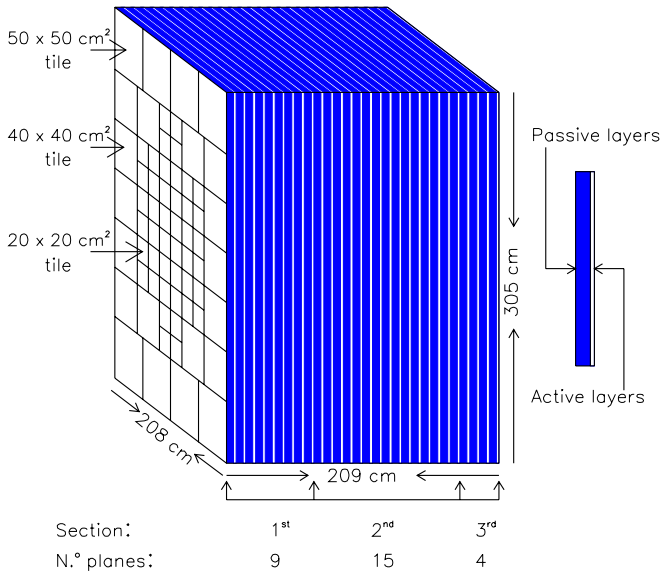

(b) Side view

Figure 3.11: Schematic views of the Hadron Calorimeter as seen by the beam and from the side.

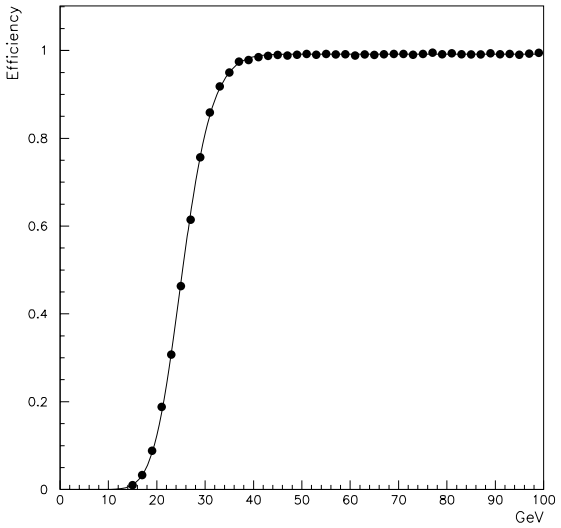

Figure 3.12: Efficiency of the HC energy trigger as a function of energy deposited in the HC.

The construction of the MH arrays is shown in Figure 3.13. Only one view in each station is shown. The numbers and sizes of counters are summarized in Table 3.6.

Table 3.6: Summary of the MH array properties. X and Y apply to MH1 and MH2; U and V apply to MH3.

		Number of counters		
Station	Pitch	X/U	Y/V	Total
MH1	5 cm	84	126	210
MH2	8 cm	52	78	130
MH3	10 cm	54	54	108

3.8.2 Outer Muon detector

The FOCUS Outer Muon (OMU) system uses Resistive Plate Chambers (RPCs) to detect high angle muons [36]. The OE and the steel of M2 provides the filter, removing most of the hadronic contamination.

RPCs are able to operate in sizable magnetic fields, an important requirement since there are substantial fringe fields in the region from M2. The RPCs used in FOCUS are a double-gap type which provides redundancy in case one gap fails. The detectors operate in streamer mode with high voltage on either side of the ground plane and a gas mixture of 5% freon, 8% isobutane, 16% CO_2, and 71% argon.

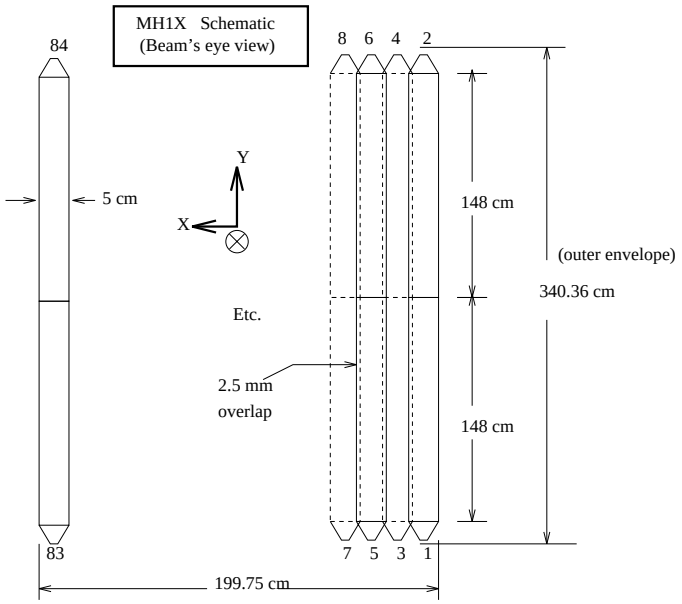

(a) MH1X. The arrangement of MH2X is similar.

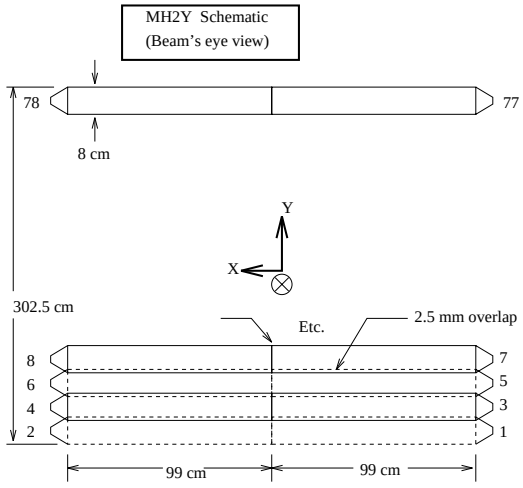

(b) MH2Y. The arrangement of MH1Y is similar.

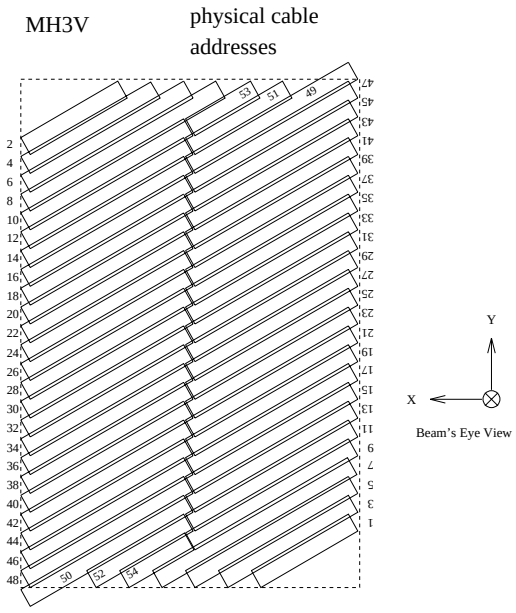

(c) MH3V. MH3U is identical except the counters are rotated by 90°.

Figure 3.13: Views showing the counter arrangements of the Inner Muon Hodoscope arrays.

The readout strips are in the center of the two gaps. A cross section of the RPC design used by FOCUS is shown in Figure 3.14.

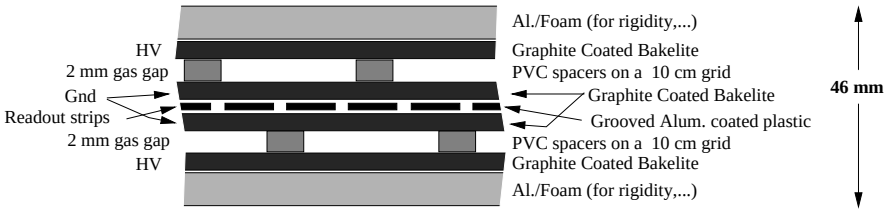

Figure 3.14: Cross sectional view of an RPC module.

For FOCUS, 24 RPC modules were constructed. Each module is 1.0 m by either 1.6 m or 1.8 m (depending on placement). Modules were constructed with readout strips running in three directions: along the long axis of the module, along the short axis, and at a 45° angle. The width of each strip is 3.1 cm. Strips along the long axis are cut in half, such that each strip only covers half the height of the module. The total number of strips per module varies from 52 (along the short axis of the 1.6 m modules) to 64 (along the long axis). However, because of multiple Coulomb scattering in M2, resolution of 12 cm is adequate. To reduce the amount of electronics and cabling required, the front end discriminators **OR** each four adjacent strips together, giving 13–16 output channels per module.

These modules are then arranged in views, as shown in Figure 3.15. Views of x, y, and u are formed, each with 8 modules, leaving an aperture (roughly matching the apertures of M2 and P3). The modules overlap slightly at the edges, which is visible in Figure 3.15.

The OMU Trigger: The OMU is also used in triggering. An on/off signal is derived for each of the 8 "towers" (the three views in each region) by requiring a hit in two of the three views. The OM_1 signal requires one tower to be on. The OM_2 signal requires two non-adjacent towers to be on. (Because of the overlap, a single muon could trigger two adjacent towers.)

3.9 Scintillating Hodoscopes

In addition to the complex detectors described above, we utilize a number of scintillation counters to trigger the experiment. These counters, combined with very fast logic circuits, help us find the events which are physically interesting.

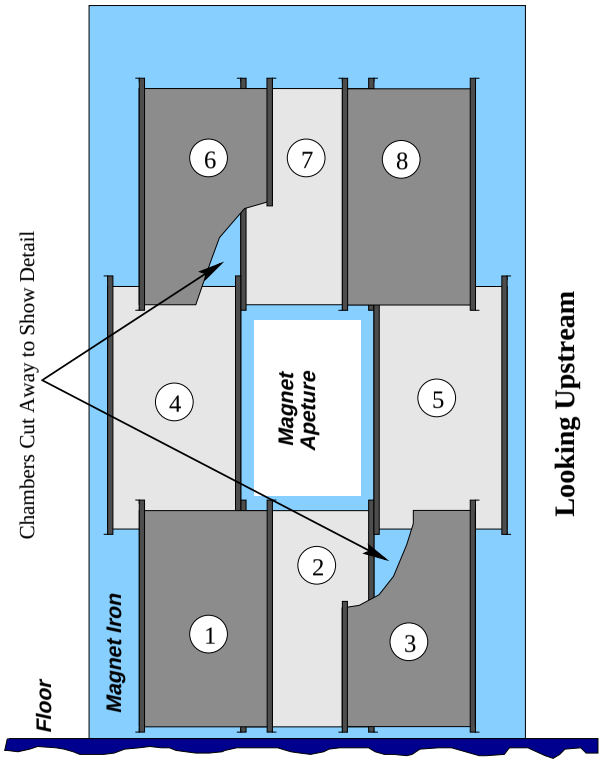

Figure 3.15: Schematic view OMU RPCs, showing one layer of 8 modules. There are three such layers.

TR1: This counter is situated between the last Target Silicon and the first SSD planes. This counter consists of a thin scintillator with a PMT readout. The purpose of TR1 is to positively identify that an interaction has occurred in the target. This counter is shown in Figure 3.2 as the counter labeled "Trigger 1."

TR2: This "counter" consists of four individual counters arranged in quadrants, just downstream of the last SSD plane. The four signals are discriminated and combined with a logical **OR**. A pulse in this counter indicates that a charged particle entered the aperture of M1. This counter is shown in Figure 3.2 as the counter labeled "Trigger 2."

H×V: This array of 36 counters is positioned between C3 and the IE. The H × V array is shown in Figure 3.16a. The H × V has a central gap to avoid counting conversion pairs. The counters from this detector are input into a fast trigger logic module which supplies two output signals: $(\mathrm{H} \times \mathrm{V})_1$ and $(\mathrm{H} \times \mathrm{V})_2$ which signal that at least one or two charged particles, respectively, have passed through the array.

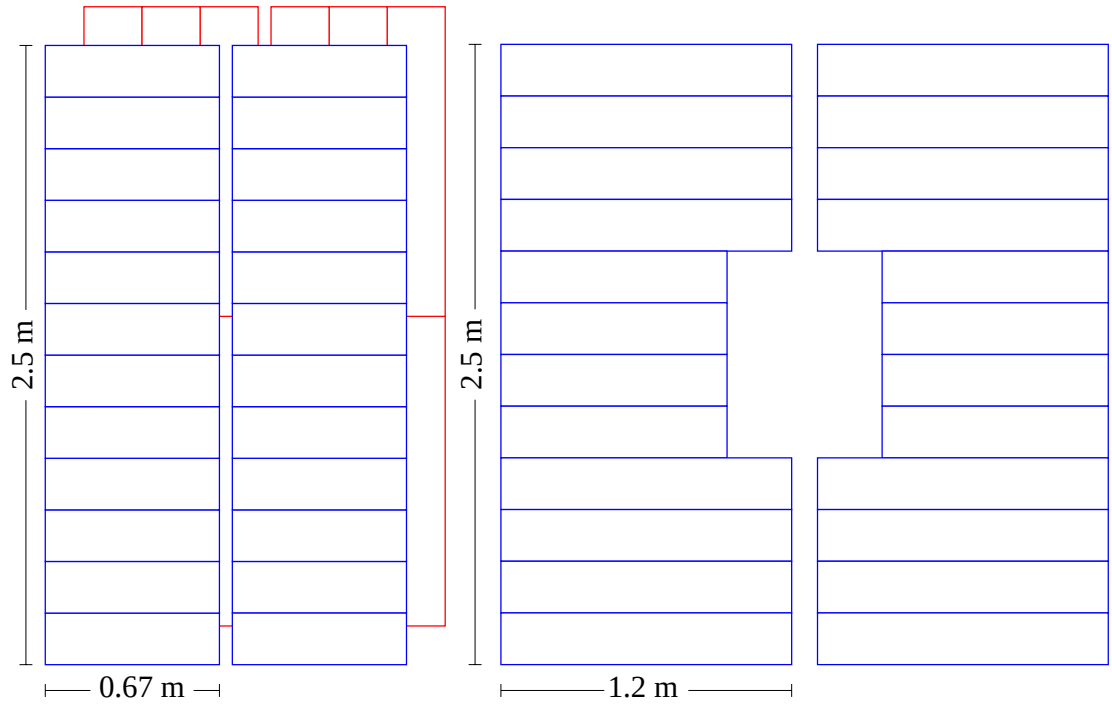

(a) H × V (b) OH

Figure 3.16: The H × V and OH hodoscope arrays.

OH: This array of 24 counters is positioned at the front of the OE. They are shown in Figure 3.16b. The OH array has an aperture sized to match the aperture of M2 and a gap in the center of the array to avoid detecting electron pairs. We derive the signal OH_1 from the array, which signifies that at least one particle passed through the OH array.

IM1 & IM2: These hodoscopes are positioned in approximately the same locations as the MH2 and MH3 arrays. IM1H and IM1V are positioned just downstream of MH2; IM2H is positioned just upstream of MH3. The arrangements of the three arrays are shown in Figure 3.17. The individual counters are much larger than those in the MH systems and are used only for triggering purposes. All the signals from these counters are input into the same logic used to form the $(H \times V)_1$ and $(H \times V)_2$ signals. The corresponding signals from the IM arrays are called IM_1 and IM_2 and signify that at least one or two muons were observed in the inner region.

AM & AMD: In order to reduce the number of triggered events due to muons from the primary production target, it is necessary to have a reliable way of detecting muons entering the experiment. The AM and AMD hodoscope arrays are two

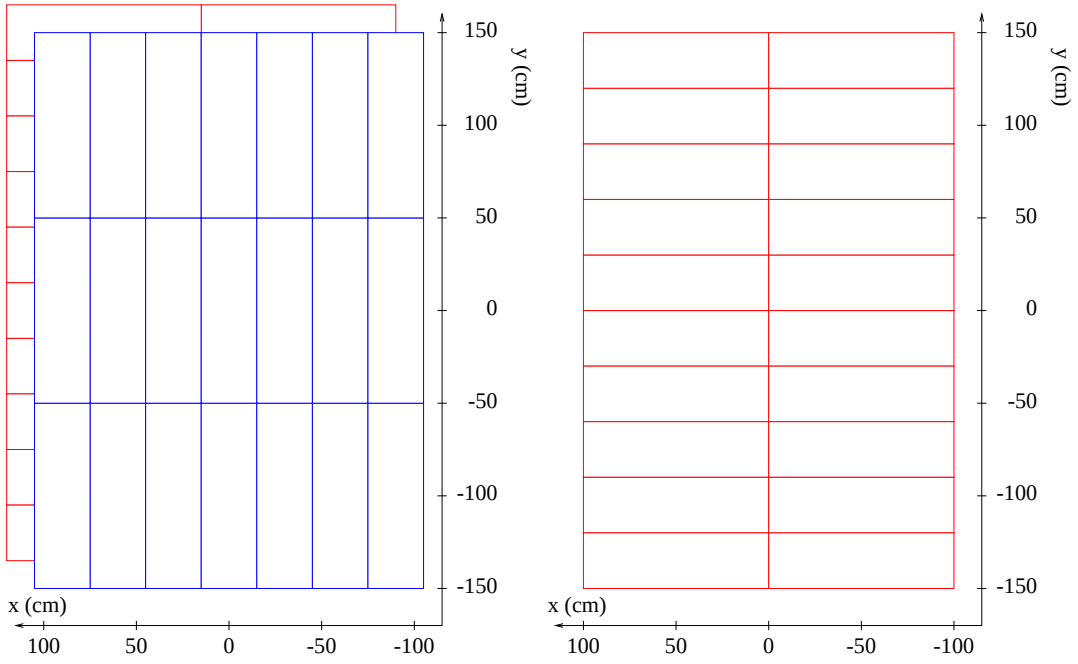

(a) IM1V and IM1H

(b) IM2H

Figure 3.17: The IM trigger counter arrays. a) shows the IM1V and IM1H arrays, b) shows the IM2H array. IM1H and IM2H are identically designed.

"walls" of scintillator upstream of the target surrounding the beam. A coincidence between the two arrays is an excellent indication that a "halo" muon[4] is present in the spectrometer. This signal is used as a veto on certain muon triggers.

3.10 The Trigger

A trigger separates interesting events from the uninteresting background. FOCUS typically had $\sim 100 \times 10^6$ (mostly electromagnetic) interactions per spill and only triggered on $\sim 30 \times 10^3$ (mostly hadronic) interactions per spill. The decision to keep an event is made in two stages. The first stage is called the "Master Gate" (MG). The MG decision is made within 200 ns of the beginning of the interaction. The transit time from the spectrometer is about 160 ns, leaving about 40 ns in which to make this decision.

If the event passes the MG selection criteria, the readout process begins. The second level of selection is the second level trigger. This decision is made 1.2 μs after the MG

[4]A muon produced far upstream in the primary target. When these reach the experiment they usually have very low angles.

decision is made. If an event passes the second level trigger, the readout is continued. If it fails, the readout electronics are cleared and reset. Resetting takes 1 μs.

In FOCUS, the following signals are used to form Master Gates. Unless otherwise noted, descriptions of these signals can be found in Section 3.9.

TR1	Triggers on interactions in the target.	
TR2	Triggers on particles downstream of SSD.	
OH_1	At least one particle in the outer region.	
$(\mathrm{H} \times \mathrm{V})_1$	At least one particle in the inner region.	
$(\mathrm{H} \times \mathrm{V})_2$	At least two particles in the inner region.	
E_{HI}	Hadronic energy over a high threshold.	(Section 3.7.3)
E_{LO}	Hadronic energy over a lower threshold.	(Section 3.7.3)
E_{IE}	Electromagnetic energy over the threshold.	(Section 3.7.1)
IE_2	At least two hits in the IE.	(Section 3.7.1)
IM_1	At least one hit in the IM counters.	
IM_2	At least two hits in the IM counters.	
OM_1	At least one hit in the OM array.	(Section 3.8.2)
OM_2	At least two hits in the OM array.	(Section 3.8.2)

Most physics triggers have a 2-body requirement which we define as

$$2\mathrm{B} \equiv (\mathrm{H} \times \mathrm{V})_2 + [(\mathrm{H} \times \mathrm{V})_1 \cdot \mathrm{OH}_1] \tag{3.4}$$

where we use the standard logical algebra that '+' is a logical **OR**, '$\cdot$' is a logical **AND**, and '!' is a logical **NOT**. In words, this requirement is "two particles in the inner region or one in the inner region and one in the outer region." In the latter case, the two particles must also be on opposite sides of the spectrometer to avoid triggering on a halo muon. With this piece of shorthand, we can compactly write all seven of the FOCUS triggers in Table 3.7.

Table 3.7: The FOCUS Master Gates. Master Gates denoted (PS) are prescaled and are used for calibration.

Trigger	Definition	Physics signal
MG1	$\mathrm{TR1}\cdot\mathrm{TR2}\cdot 2\mathrm{B}\cdot E_{\mathrm{HI}}$	Hadronic trigger
MG2	$\mathrm{TR1}\cdot\mathrm{TR2}\cdot 2\mathrm{B}\cdot \mathrm{IE}_2$	$J/\psi \to e^+e^-$
MG3	$\mathrm{TR1}\cdot\mathrm{TR2}\cdot[\mathrm{IM}_1 + \mathrm{OM}_1] \cdot E_{\mathrm{LO}}$	Semi-muonic decays
MG4	$\mathrm{TR1}\cdot\mathrm{TR2}\cdot 2\mathrm{B}\cdot[\mathrm{IM}_2 + \mathrm{OM}_2 + \mathrm{IM}_1 \cdot \mathrm{OM}_1]$	$J/\psi \to \mu^+\mu^-$
MG5	$\mathrm{TR1}\cdot\mathrm{TR2}$	e^+e^- pairs (PS)
MG6	$\mathrm{TR1}\cdot\mathrm{TR2}\cdot 2\mathrm{B}$	Two-body events (PS)
MG7	$\mathrm{TR1}\cdot\mathrm{TR2}\cdot[\mathrm{IM}_1 + \mathrm{OM}_1]$	One-muon events (PS)

When the second level decision is made we have additional information. These new pieces of information take too long to form to be included in the Master Gate, but

are ready by the second level decision time. The pieces commonly used in second level triggering are:

MULTn	Enough hits for at least n track(s) in PWC system.
AM·AMD	No halo muons.
IM(E+W)	Excludes hits in both halves of IM triggers.
$E_{\text{IE-2}}$	Better electromagnetic energy sum.

Using this new information as well as the Master Gate information, we form the second level triggers listed in Table 3.8. Note that not all of the Master Gates generated (i.e., MG3 and MG7) were used for final triggering.

Table 3.8: A typical second level trigger set for FOCUS. The actual triggers changed occasionally, especially the di-muon triggers.

Trigger	Definition	Physics signal
TRIG1	MG1·$E_{\text{IE-2}}$·MULT4	Hadronic trigger
TRIG2	MG2·$(\text{H} \times \text{V})_2$ ·E_{IE}	$J/\psi \to e^+e^-$
TRIG4	MG4·$\text{IM}_2 \cdot (\text{H} \times \text{V})_2$·!(AM·AMD)	J/ψ, inner only
TRIG5	MG5	Prescaled MG5
TRIG6	MG6	Prescaled MG6
TRIG8	MG1	Prescaled MG1
TRIG9	MG4·OH·OM_2·MULT2·!(AM·AMD)	J/ψ, outer only
TRIG11	MG4·IM_1·OM_1·MULT1·$(\text{H} \times \text{V})_1$ · IM(E+W)	J/ψ, inner/outer

3.11 Data Acquisition System

In order to analyze the interactions in the spectrometer, the analog signals from each of the detectors must be digitized and recorded. This is the task of the Data AcQuisition system (DAQ). The FOCUS DAQ has to deal with input data in a number of different data formats, merge all this data into one stream, and put the output on 8 mm magnetic tape. Figure 3.18 shows an overview of this process.

Information from the Čerenkov detectors, the three calorimeters, and the beam calorimetry is read out with FASTBUS ADCs. These data are put on the DAQ bus, an RS-485 bus, by several FSCCs.[5]

Information from the wire chambers is in PCOS[6] format while information from the straw chambers is in FERA[7] format. The SSD, Target Silicon, and hodoscope readout

[5]FASTBUS Smart Crate Controller
[6]Proportional Chamber Operating System
[7]Fast Encoding and Readout ADC

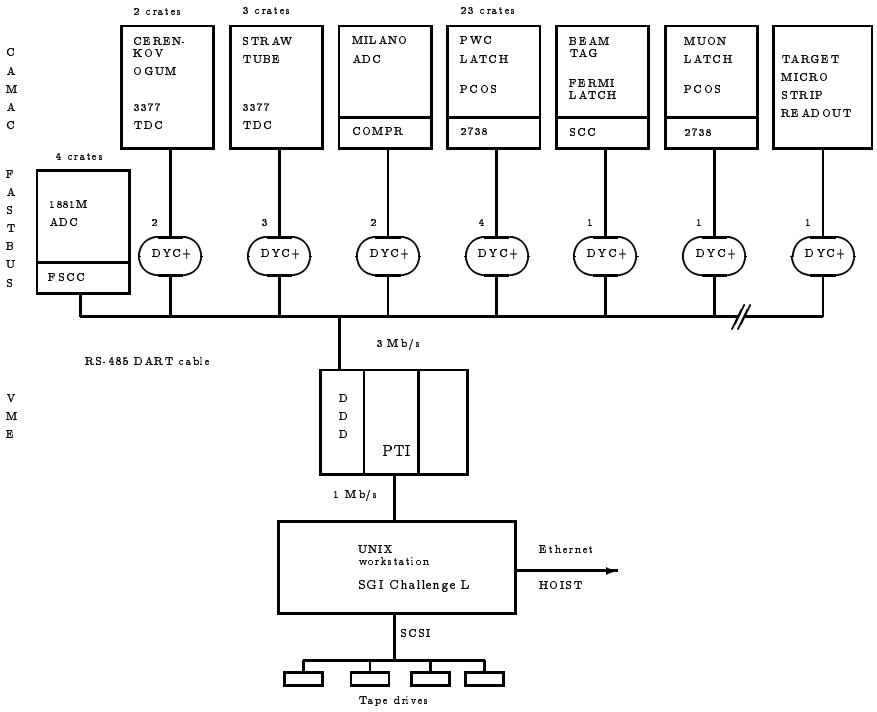

Figure 3.18: Structural overview of the DAQ, showing how the multiple sources are merged into one data stream and written to tape.

systems all have their own unique data formats. Data from all of these sources are put onto the bus by a number of DYC3[8] modules.

Data for each event is taken off the RS-485 DAQ bus and placed into a Dual Ported Memory (DPM); data can be written to and read from this memory simultaneously. The data are transferred via a VME[9] bus from the DPM into our data logging computer, a dual processor SGI Challenge L. From there the data are buffered on disk and written to tape.

During the run, the FOCUS DAQ performed extremely well, typically logging 30–40,000 events per 20 second spill with a typical event size of ∼4kB. The livetime (the fraction of the time the DAQ spent waiting for the next event) was typically 85–90% with a readout time of about 35 μs. See Reference 37 for a complete description of the individual DAQ elements and a description of the whole system.

[8]Damn Yankee Controller

[9]VersaModule Eurocard. Developed by Motorola.

Chapter 4

Data Reconstruction

In this chapter we describe the reconstruction algorithms and data processing for FOCUS. In Section 4.1, we describe the algorithms which reconstruct particles in the spectrometer. In Section 4.2, we describe the process of identifying the types of particles found. Finally, in Section 4.3, we describe the production of reconstructed information, a process which begins with the raw data written by the DAQ and ends with small datasets usable by an individual experimenter.

Throughout this chapter, many signals of reconstructed particles are shown. These all come from the same dataset (about 0.3% of the raw data) and can be compared to each other. In some cases the fits don't model the backgrounds very well, but the fitted values of the signals are still useful for comparisons.

4.1 Reconstruction Algorithms

In the past, high energy experimenters used devices such as bubble and cloud chambers to photograph the tracks of particles under study. The interaction rates of most modern particle physics experiments are much too high for any of these photographic observation methods. With the exception of a few experiments using photographic emulsions as a detector, today's experiments rely on electronic devices to capture the fleeting signatures of particles traversing the experimental apparatus.

The challenge this imposes is that experimenters must determine, based on the electronic signals of hits on wire chamber wires or energy deposited in a calorimeter, what occurred in an interaction. The detectors, trigger, and DAQ described in the previous chapter are all designed to collect all possible information from a single photon interaction and to store that information as compactly as possible. This information

is called an "event." In this section we describe how the raw information in that event is used reconstruct the complex interactions.

4.1.1 SSD tracking

Finding tracks with the SSD (see Section 3.2.2) detector is performed in three stages. First, hit strips are grouped into clusters of hits. Second, projections of clusters are found in each of the three measurement directions. Finally, these projections are combined into tracks.

Clusters of up to three hit channels are grouped into hit clusters. Using the ADC information, it is possible to determine if one or two[1] traversing particles created a single cluster by comparing the total ADC counts present to the number expected for a single Minimum Ionizing Particle (MIP). For multi-strip, single-MIP hits, enhanced position resolution is achieved by fitting the ADC values in the cluster with a pulse height sharing algorithm.

Projections are found in each of the three SSD measurement directions by taking all combinations of hits in the four SSD planes of a given direction and fitting those hits to a straight line. Projections are rejected if χ^2 per degree of freedom (χ^2/DOF) > 3.0. Projections must contain hits from at least three of the four planes; hits are allowed to be shared among 3-plane projections and in the first plane of 4-plane projections.

Tracks are formed by intersecting all combinations of three projections (one from each view) and requiring that $\chi^2/\mathrm{DOF} < 8.0$ for these combinations. Shared projections among tracks are arbitrated based on the lowest χ^2/DOF and groups of tracks with nearly identical parameters are reduced to a single equivalent track.

In E687, the spatial resolution of a track in the high resolution region of the SSD was

$$\sigma_x = 11.0\ \mu\mathrm{m}\sqrt{1+\left(\frac{17.5\ \mathrm{GeV}/c}{p}\right)^2} \tag{4.1}$$

$$\sigma_y = 7.7\ \mu\mathrm{m}\sqrt{1+\left(\frac{25.0\ \mathrm{GeV}/c}{p}\right)^2}, \tag{4.2}$$

while the resolution of a track entirely in the low resolution region of the SSD was about twice as large. In FOCUS, this resolution is slightly better because the pulse height sharing algorithm is being used. The constant term results from the resolution of the detector while the momentum dependent term is dominated by multiple

[1] Recall that there are a large number of $\gamma \to e^+e^-$, or "pair" events where the opening angle between the electrons is essentially zero in the target region.

Coulomb scattering in the silicon planes. The resolution in y is better than that in x because all three silicon planes provide y information, while only two provide information in x.

The Target Silicon, or TSSD, is not used in finding the initial tracks in the target region.

4.1.2 PWC track reconstruction

The PWC (see Section 3.4) tracks are also found using a projection method. Initially, the x (non-bend) components of SSD tracks are extrapolated through the spectrometer. PWC hits close to the extrapolation are used to form x projections. Projections in the y, u, and v PWC planes are formed independently and combined with the x projections to form tracks. Unused hits in x are then used to form additional projections which are combined with the other unused projections to form additional tracks.

The x projections found by extrapolating the SSD tracks must have hits in P0. Each track must have hits in at least three chambers and be missing no more than four hits, only two of which may be in a single chamber. A least squares fit is performed on all tracks to determine the track parameters (slopes and intercepts) and χ^2/DOF. For tracks passing through M2, the bend in the y direction is also included as a fit parameter, allowing a rough determination of the momentum. Tracks which leave hits in all five PWCs are called "tracks" while those which leave hits in only the first three chambers are called "stubs."

Additional algorithms are employed to recover tracks which do not satisfy the above criteria. For example, microstrip tracks are used to seed low-momentum, two chamber tracks which exit the spectrometer after P1. Halo muon tracks, useful for certain studies, are reconstructed over a large area by reconstructing tracks with hits in P1, P2, and P4. (Recall that P0 and P3 are much smaller chambers.) These muons are assumed to pass through the magnet steel with little deflection.

Occasionally the wire chambers have a very large number of hits which would produce a large number of tracks. These events are too cluttered to extract reasonable physics, so in the interest of reducing the reconstruction time the number of tracks is limited to a maximum of 30. This limit is reached in roughly 3.5% of the events.

4.1.3 Linking

In order to obtain useful information for reconstructing charm decays, SSD and PWC tracks must be "linked," or associated with each other. This serves two purposes. First, it associates a momentum with an SSD track if the corresponding PWC track's momentum is measured in M2. Second, it allows a determination of the momentum of stubs, using the bend angle in M1.

Linking is performed by extrapolating both SSD and PWC tracks to the center of M1. The slopes and intercepts of the two types of tracks are required to be consistent at this point. A loose cut is made to discard obviously incorrect choices. A global least squares fit using both PWC and SSD hits is performed to test the hypothesis that the tracks come from the same particle. The links are arbitrated based on χ^2/DOF as returned by this fit. Because of e^+e^- pair production (with almost no opening angle), a maximum of two PWC tracks are allowed to be associated with each SSD track.

4.1.4 Momentum determination

The momenta of particles are measured by determining their deflection angles in a magnetic field. FOCUS uses two magnets to measure the momenta of particles; M1 is used to measure the momenta of 3-chamber tracks, and M2 is used to measure the momenta of 5-chamber tracks.

For 5-chamber tracks, particles are traced through the magnetic field using the known magnetic field in M2 and the track parameters on both sides of the magnet as inputs to the calculation. This fit is performed iteratively until both an accurate momentum and improved track parameters are obtained.

Linked stubs and 4-chamber tracks are subjected to a similar procedure using the SSD track parameters, the track parameters between M1 and M2, and the known field of M1.

Unlinked stubs pose a special problem since there is no information for them before they enter the magnetic field of M1. To obtain an approximate momentum measurement of these particles, the x projection of the track is extrapolated into the target region and the closest vertex is chosen as the point of origin. If no vertices are reconstructed, the unlinked stub is assumed to originate from the center of the target material.

The momentum resolution for stubs measured in M1 is approximately[2]

$$\frac{\sigma_p}{p} = 0.034 \times \frac{p}{100\ \text{GeV}/c}\sqrt{1+\left(\frac{17\ \text{GeV}/c}{p}\right)^2} \tag{4.3}$$

and the resolution for tracks measured in M2 is

$$\frac{\sigma_p}{p} = 0.014 \times \frac{p}{100\ \text{GeV}/c}\sqrt{1+\left(\frac{23\ \text{GeV}/c}{p}\right)^2}. \tag{4.4}$$

At high momentum, the resolution is limited by the position resolution of the PWC system; at low momenta it is dominated by multiple Coulomb scattering.

4.1.5 Vertexing

In order to perform certain kinds of reconstruction (for instance, finding the momentum of unlinked stubs described in Section 4.1.4), approximate vertex locations are required for each event. However, the approach described in this section has certain inefficiencies, so it is *not* typically used to find the vertices used in physics analyses. The vertexing method used in analyses is described in Section 5.1.

To find these vertices, $\chi^2(x,y,z)$ in the equation

$$\chi^2 = \sum_{i=1}^{n}\left(\frac{x-(x_i+x_i'z)}{\sigma_{x,i}}\right)^2 + \left(\frac{y-(y_i+y_i'z)}{\sigma_{y,i}}\right)^2, \tag{4.5}$$

is minimized where (x,y,z) are the coordinates of the vertex; x_i, y_i, x_i', and y_i' are the SSD track parameters; and $\sigma_{x,i}$ and $\sigma_{y,i}$ are the errors on the SSD tracks. The index i sums over the tracks in the vertex.

To find the initial set of vertices all the SSD tracks in an event are forced into a single vertex. If $\chi^2/\text{DOF} > 3.0$, the track which contributes the most to the χ^2 is removed from the vertex and the vertex is re-fit. This process is repeated until $\chi^2/\text{DOF} < 3.0$. At this point, all the tracks which no longer belong to a vertex are again forced into a single vertex and the process continues until all possible vertices have been formed.

[2]These are the momentum resolutions for E687. The wire spacing and location of the wire chambers was changed slightly for FOCUS.

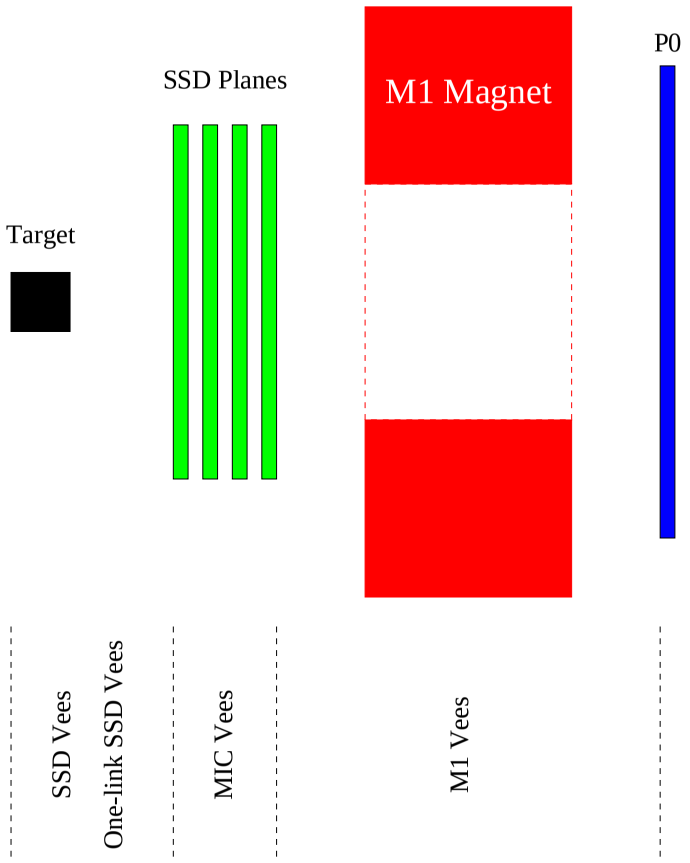

Figure 4.1: Spectrometer regions and Vee reconstruction algorithms. This diagram of the upstream portion of the spectrometer is simplified and not to scale.

4.1.6 Vee (Λ^0 and K_s^0) reconstruction

The decays $\Lambda^0 \to p\pi^-$ and $K_s^0 \to \pi^+\pi^-$ candidates are called "vees" because they consist of two charged tracks, or "prongs," that come from a neutral parent as shown in Figure 4.2. In order to reconstruct these decays it is necessary to intersect two tracks over a large region in z, including inside of M1. There are a number of algorithms to do this, depending on where the decay occurs and if the prongs are tracks or stubs. The most useful of these algorithms are described below. Figure 4.1 shows which region of the spectrometer where each of these reconstruction algorithms is used.

All vee reconstruction algorithms have certain requirements in common. To test the K_s^0 hypothesis, the $\pi^\pm$ mass is assigned to each of the prongs and the resulting mass is required to be consistent with the known K_s^0 mass. To test the Λ^0 hypothesis, the proton mass is assigned to the highest momentum prong and the mass is required to be consistent with the Λ^0 mass.

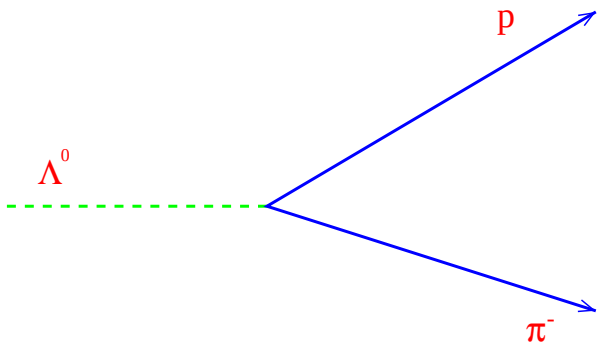

Figure 4.2: Illustration of the vee topology for the decay $\Lambda^0 \to p\pi^-$. The dotted line denotes the neutral, unseen particle, solid lines represent the two charged prongs. The decay $K_s^0 \to \pi^+\pi^-$ is identical except the prongs are both pions.

SSD and MIC vees

The simplest type of vee to reconstruct is one in which the K_s^0 or Λ^0 decays upstream of the SSD detector and produces two linked tracks. In this case,the two SSD tracks are required to form a good vertex and that the vertex must be well separated from, and point back to, the most upstream vertex. These vees have the best resolution because full microstrip information is available.

The second type of vee for which microstrip information exists is the MIC vee category. These are vees which decay within the SSD region, rather than upstream of it. In these vees, unlinked PWC tracks are extrapolated upstream to the third and fourth SSD planes where confirming hits are found. The track is then refit with these additional hits and a vertex is calculated for the pair of tracks.

Signals of the SSD and MIC vee types are shown in Figure 4.3.

M1 vees

The most prevalent vee category is termed the "M1 vees." These particles decay inside the magnetic field of M1, between the last SSD plane and the first PWC plane. The M1 vees are divided into three categories, Track-Track, Track-Stub, and Stub-Stub vees based on the prong track type. In all cases, the x projections of the tracks are intersected to find a rough intersection point within the magnet.

In the Track-Track and Track-Stub cases where at least one of the momenta is known, an iterative magnet tracing procedure is used to determine the vertex position and, in the Track-Stub case, the momentum of the stub.

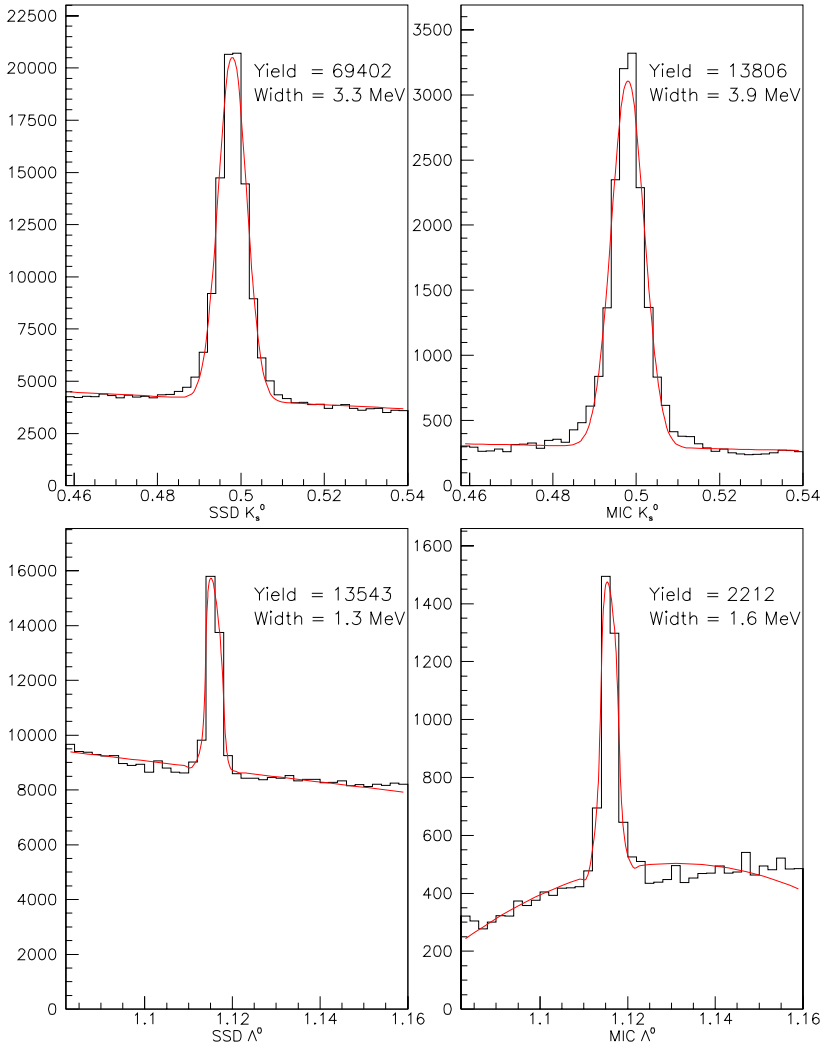

Figure 4.3: Signals for SSD and MIC Vees. The K_s^0 signals are shown at the top, the Λ^0 signals at the bottom. Plots on the left are for SSD vees, those on the right are for MIC vees.

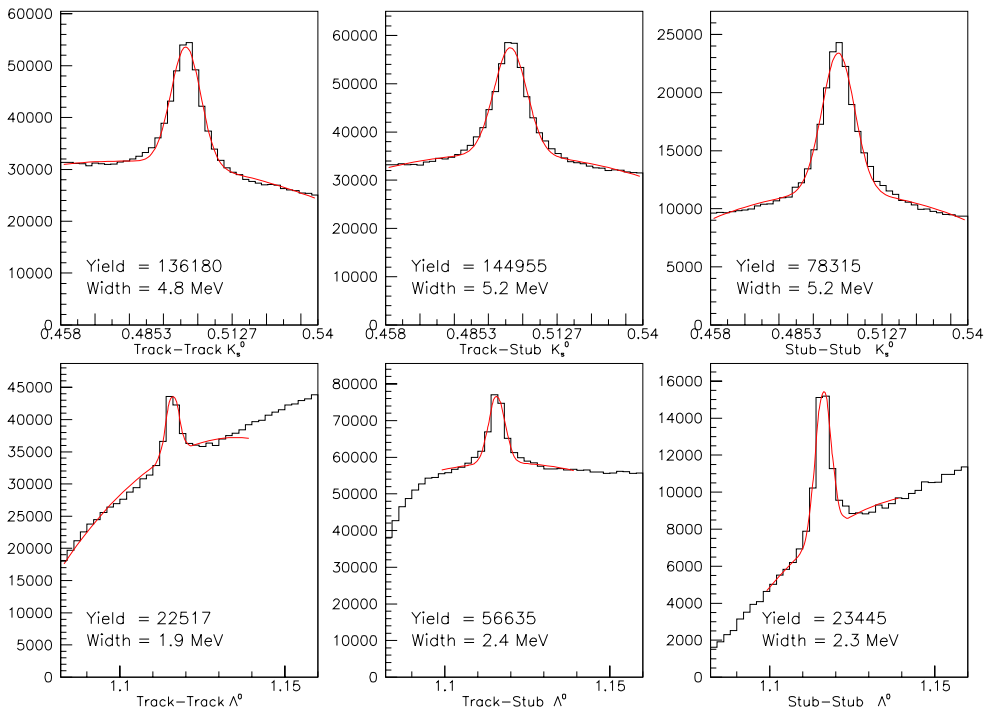

Figure 4.4: Signals of M1 Vees for the three topologies. The K^0_s signals are shown at the top, the Λ^0 signals at the bottom.

In the Stub-Stub case, the process is similar except that a constraint is added by forcing the resultant vee to point back to the primary vertex. In this way the prongs are momentum balanced and the vee and daughter momenta can all be calculated.

Signals of all three types of M1 vees are shown in Figure 4.4.

One-link SSD vees

The final vee category which we discuss is the "One-link SSD" category. These vees consist of one prong which is a linked track or stub and one SSD track which is unlinked. While there is complete information for the linked track, there is no momentum information for the unlinked track. To determine the missing momentum information, the momentum of the unlinked track is chosen so that the vee is forced to originate from the most upstream vertex. Signals for these types of vees are shown in Figure 4.5.

There are other vee topologies that are reconstructed as well, but these typically have either very poor or very small signals and are excluded from many analyses.

Typically in skims, analyses, and other reconstruction algorithms which use vees, par-

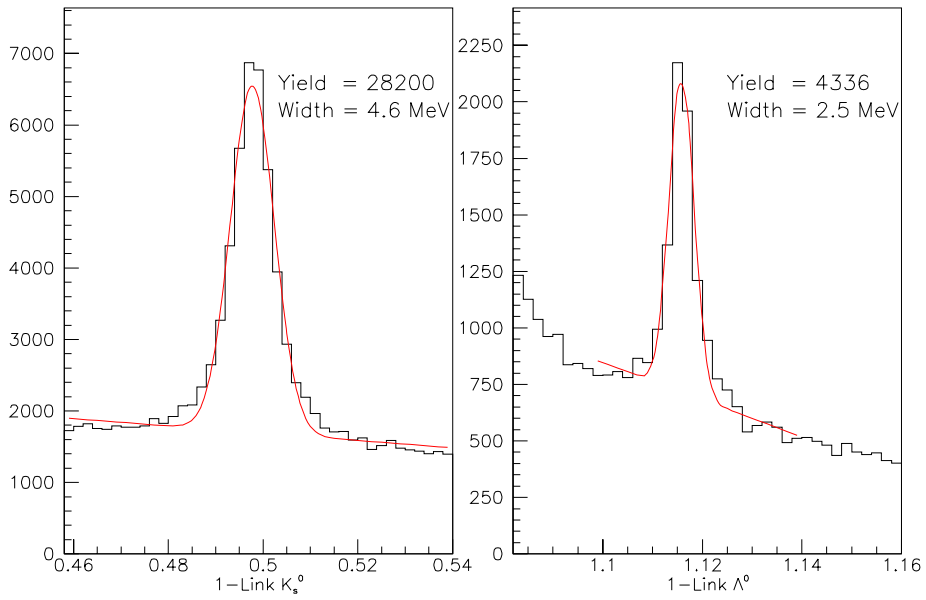

Figure 4.5: One-link SSD Vee signals for K_s^0 and Λ^0.

ticle identification requirements are placed on the vee prongs to reduce backgrounds. This is especially useful on the proton in Λ^0 decays.

4.1.7 Kink (Σ^- and Σ^+) reconstruction

The "kink" algorithm is used to reconstruct the decays $\Sigma^+ \to p\pi^0$, $\Sigma^+ \to n\pi^+$, and $\Sigma^- \to n\pi^-$. The branching ratios for these decays are 51.6%, 48.3%, and 99.8% respectively [4]. This means we have the opportunity to reconstruct nearly all the Σ^- and Σ^+ decays.

These decays are called kinks because, observing only the charged particles, we see a track enter from upstream and an intersecting track leave at a different angle. This topology is illustrated in Figure 4.6

In order to reconstruct kinks, unlinked SSD tracks (presumably the Σ) which point into the M1 aperture are matched with unlinked PWC tracks that also point into the aperture. PWC tracks which were previously used to form vees are not considered. The matching is performed with the x projections of the two tracks.

For 5-chamber PWC tracks which intersect upstream of M1, the momentum of the Σ candidate is obtained by assuming the Σ mass and solving the kinematic equations. However, this gives two momentum solutions for each Σ, both of which must be considered to be valid. For 5-chamber PWC intersections within M1, both the proton

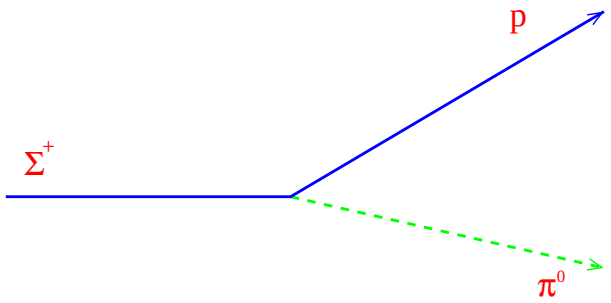

Figure 4.6: Illustration of kink topology for the decay $\Sigma^+ \to p\pi^0$. The dotted line denotes the neutral, unseen particle.

and the Σ are traced through the magnetic field. The momentum of the Σ is varied until the intersection distance is minimized, giving an approximate value for the Σ momentum. As before, the kinematic equations are solved, but in this case the Σ momentum value closest to the value found during the iteration is chosen.

For 3-chamber PWC tracks, the Σ decay must occur upstream of M1. The (x, y, z) of the Σ decay vertex is obtained by taking the x and z intersection points of the two tracks. The y value is determined from the SSD track parameters at the z of intersection. Again, the Σ mass is assumed to calculate the Σ momentum.

In order to reject topologically similar backgrounds, particle ID from the Čerenkov system is placed on the proton candidates and an E/p cut is made on neutrons, as described in Section 4.1.10. Requiring a confirming π^0 also reduces background, but this is not done at the reconstruction stage because such a requirement is very inefficient.

4.1.8 Cascade (Ξ^- and Ω^-) reconstruction

Using the "cascade" reconstruction algorithms, we are able to reconstruct the decays $\Xi^- \to \Lambda^0\pi^-$ and $\Omega^- \to \Lambda^0 K^-$, which have branching ratios of 99.9% and 67.8% respectively. Because we are often able to reconstruct the Λ^0 in these decays, we are able to fully reconstruct many of these hyperon decays. This decay topology is illustrated in Figure 4.7.

The cascade reconstruction considers two cases. In the first case, the Ξ^- or Ω^- decays in the target region, upstream of the SSD detectors. In this case, we require that the charged track (the π^- or the K^-) forms a good vertex with a Λ^0 momentum vector and that the combination points back to another vertex.

In the second case, the Ξ^- or Ω^- decays downstream of the SSD detector. This is similar to the kink topology, but the neutral particle (Λ^0) is fully reconstructed. The

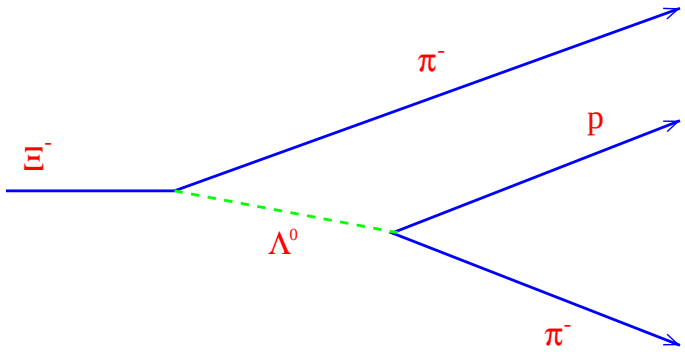

Figure 4.7: Illustration of the cascade topology for the decay $\Xi^- \to \Lambda^0\pi^-$. The decay of $\Omega^- \to \Lambda^0 K^-$ is identical, except the K^- replaces the first π^-.

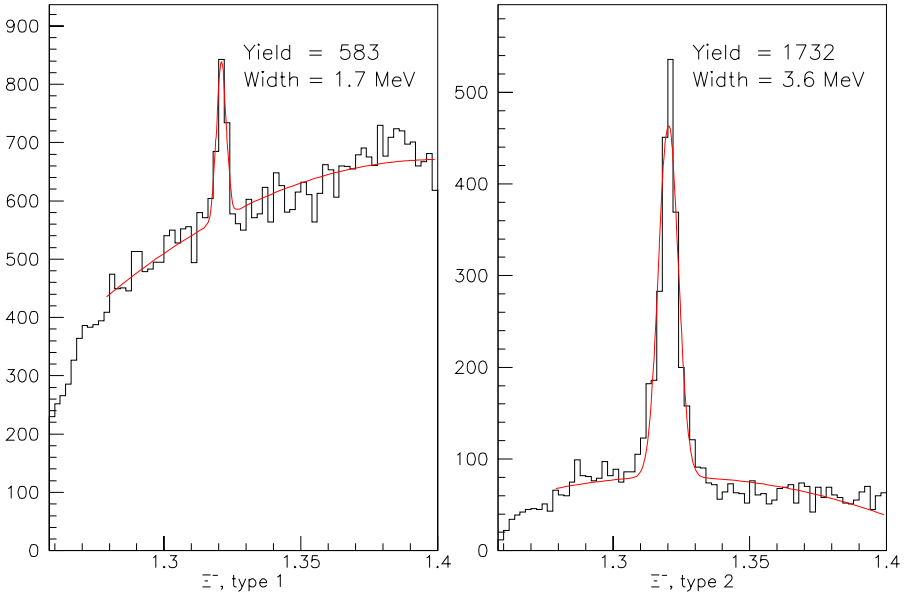

Figure 4.8: Signals of $\Xi^- \to \Lambda^0\pi^-$ and $\Omega^- \to \Lambda^0 K^-$.

algorithm begins by finding a vertex between a Λ^0 and an unlinked PWC track, both of which must be traced into the magnetic field of M1. When the best fit for this vertex is found, the unlinked SSD track (the Ξ^- or Ω^-) is also traced into M1. If the two traced objects intersect, the entire decay is refit with the new Ξ^- decay vertex position.

Both cascade topologies place additional requirements on the Λ^0 in order to reject backgrounds.

4.1.9 Electromagnetic (γ and π^0) reconstruction

Inner Electromagnetic calorimeter

The first step in the reconstruction process for the IE calorimeter (see Section 3.7.1) is to convert ADC values into energy values for each lead glass block. This is done with a look-up table in which each ADC count (after a pedestal subtraction) is equivalent to about 10 MeV of deposited energy. Each block has its own set of conversion values which vary over time.

In the IE, interacting particles usually deposit energy in a shower that extends over as many as 20 blocks. However, almost all the energy is deposited in the central 9 (3×3) blocks or less. The reconstruction algorithm begins by finding the highest energy block in the entire array. It then groups the 8 surrounding blocks into a "cluster." The energies of the 9 blocks are summed to give the cluster energy. This process repeats until all possible clusters have been formed.

The energy weighted average position of the cluster is found by

$$x_g = \frac{\sum_i E_i x_i}{\sum_i E_i} \tag{4.6}$$

where x_g is the x-position of the cluster and i denotes each of the 9 blocks; E_i and x_i denote the individual block energies and positions respectively. An identical calculation is performed to find y_g.

From this weighted average, following the method described in Reference 38, an improved cluster position, x_c is calculated via

$$x_c = 0.76 \sinh^{-1}\left[\frac{(x_g - x_b)}{S/2} \sinh\left(\frac{S/2}{0.76}\right)\right] + x_b \tag{4.7}$$

and a similar calculation is made for y_c. Here, (x_b, y_b) are the coordinates of the center of the central block in the cluster and S is the dimension of the blocks.

An additional position correction, parameterized by a sixth order polynomial, is then applied. This correction is derived by comparing the impact positions of well measured electron tracks with the average reconstructed positions of electromagnetic showers in the FOCUS IE.

After all the clusters are reconstructed, the clusters are matched to PWC tracks. Any track within 6.0 cm of a cluster center is associated with that cluster. Clusters can be matched to more than one track and, in principle, tracks can be matched to more

than one cluster, although this rarely happens due to the extent of the clusters and the 6.0 cm cut.

The energy resolution for the IE is approximately 5% (constant term only).[3] The position resolution (average distance between reconstructed cluster centers and track impact points) for all charged tracks is about 9 mm.

Outer Electromagnetic calorimeter

The reconstruction of showers in the OE (see Section 3.7.2) is seeded by the stubs. Clusters in the different strips are formed around stubs which intersect the OE. Unused clusters are then combined into neutral clusters. The diagonal counters and the "tie-breaker" plane are used to resolve ambiguities as to which track a hit strip is associated with.

The x and y cluster positions are found with a method similar to that used in the IE reconstruction: first finding the weighted center-of-energy position and then correcting for systematic effects. The position resolution of the OE varies from 0.9 cm at 3 GeV to 0.3 cm at 10 GeV.

Energies for clusters are determined by summing the energies of the counters associated with that cluster. The energy resolution of the OE is approximately $3\% + 15\%/\sqrt{E\ (\mathrm{GeV})}$.

π^0 reconstruction

In order to reconstruct the decay $\pi^0 \to \gamma\gamma$, we combine clusters from both calorimeters which are inconsistent with charged tracks. For convenience, we assume that the π^0 decays at the center of the target. Knowing the energy of the clusters, we can infer the momentum vector of each γ and reconstruct an invariant π^0 mass. There are three classes of π^0's based on which calorimeters are used in the reconstruction. In IE-IE and OE-OE π^0's both photons are in the same detector. In IE-OE π^0's one photon is in each detector. Invariant mass plots for all three π^0 types are shown in Figure 4.9.

When combining π^0's with other daughter particles, we find a significant advantage in using the energy constraint method of Nakano and Miyake [39]. This method assumes that the uncertainty in the reconstructed π^0 mass is due entirely to uncertainties in the energies of the two photons. New photon energies are calculated which fix the

[3] Typically calorimeter resolutions are quoted with a constant term and a $1/\sqrt{E}$ term. In FOCUS, the electrons are so energetic that the $1/\sqrt{E}$ term is difficult to measure.

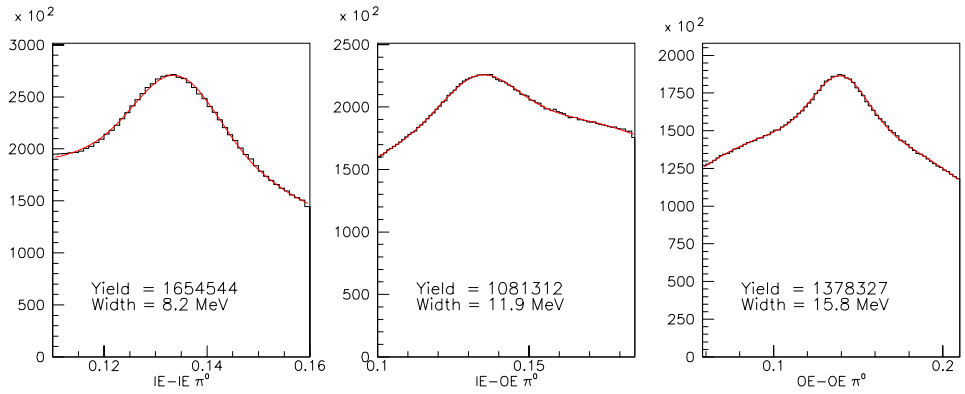

Figure 4.9: π^0 signals. The left plot is for IE-IE π^0's, the center is for IE-OE π^0's, and the right plot is of OE-OE π^0's. From left to right the resolution worsens.

π^0 mass to the known π^0 mass. These new energies are used to form an improved π^0 momentum vector.

4.1.10 Neutral hadron reconstruction

Reconstruction of neutral hadrons in the HC (see Section 3.7.3) begins by associating neutral clusters in the IE with clusters in the HC. About 80% of the hadrons in the inner portion of the spectrometer undergo a nuclear interaction in the IE and begin showering. The IE gives good position information ($\sigma \sim 0.9$ cm) for these hadronic showers. The energy assigned to neutral hadrons is the sum of the energy deposited in the IE and the energy deposited in the HC. The energy resolution of the HC is found to be $0.86\% + 85\%/\sqrt{E\ (\mathrm{GeV})}$ [33].

The primary use of the neutral hadron reconstruction is to find confirming neutral showers for the kink reconstruction described in Section 4.1.7.

4.2 Particle Identification

Once the reconstruction algorithms have "found" a particle, the question of the particle's identity often remains. For instance, long lived charged particles can be electrons, muons, pions, kaons, or protons. The task of the particle identification algorithms is to distinguish these possibilities using information from the detectors described in Chapter 3.

In Section 4.2.1 we describe the Čerenkov algorithm which distinguishes between electrons and the different flavors of hadrons. In Section 4.2.2 we describe the muon

identification algorithm. Finally, in Section 4.2.3 we describe the methods used to separate electrons from other charged particles.

4.2.1 Čerenkov identification

Čerenkov identification is used to identify the particle type of each track. This is particularly important for the hadrons ($\pi^{\pm}$, $K^{\pm}$, and $p/\overline{p}$) because they interact similarly in matter. These particles are identified by examining the Čerenkov light and its distribution.

The Čerenkov identification algorithm (called **CITADL**[4]) used in FOCUS is based on likelihood ratios between the various particle hypotheses. The particle possibilities considered for each track are $e^{\pm}$, $\pi^{\pm}$, $K^{\pm}$, and $p/\overline{p}$.[5] For each of these four hypotheses the likelihood, $\mathcal{L}$, is calculated by observing the status of the cells within the Čerenkov cone of the particle. The probability that a particle associated with a track of known momentum[6] will fire a particular Čerenkov cell is computed using Poisson statistics. This calculation is based on the predicted number of Čerenkov photons striking the cell under each particle hypothesis. An accidental firing rate is also included in this calculation to model spurious hits; this cell-by-cell correction factor depends on the beam intensity on an event-by-event basis. The accidental firing rates are typically less than 1% except for cells close to the uninteracting beam.

The product of the firing probabilities for all relevant cells in the three detectors is computed to form $\mathcal{L}$. The value $W_{\rm obs}(i) \equiv -2\ln\mathcal{L}$ is calculated for each particle hypothesis i. Čerenkov identification is performed by cutting on the difference between two likely hypothesis. For example, a typical cut separating a kaon from a pion is

$$W_{\rm obs}(\pi) - W_{\rm obs}(K) > 3 \ . \tag{4.8}$$

(The fact that we are using a *negative* log likelihood means we expect $W_{\rm obs}(\pi)$ to be *larger* than $W_{\rm obs}(K)$ for a kaon.)

This identification method has distinct advantages over the standard method of particle identification using threshold Čerenkov detectors, which simply determines the on/off status of the cells and return a simple yes or no for consistency with a given particle hypothesis. First, discrimination between two hypotheses can be extended beyond the threshold momentum ranges. Second, using this likelihood approach, the Čerenkov cuts can be more carefully selected and tuned for a particular physics anal-

[4]Čerenkov Identification Through A Digital Likelihood

[5]The $\mu^{\pm}$ hypothesis is not considered separately from the $\pi^{\pm}$ since the momentum range over which the two hypotheses can be separated is limited. Also, as explained in the next section, we have excellent muon identification.

[6]See Section 3.6 for the geometries and firing thresholds of the three Čerenkov detectors.

ysis since there is a continuous value to cut on rather than simple on/off values for each particle hypothesis. The **CITADL** algorithm is fully described in Reference 40.

4.2.2 Muon identification

Inner Muon detectors

Muons are identified in the MH system (described in Section 3.8.1) by applying two requirements. First, candidate tracks are required to have hits in at least four of the six MH planes. If this requirement is satisfied, a χ^2 is calculated which gives the probability that the track under consideration is compatible with the MH hits assigned to it. This calculation takes into account both the multiple Coulomb scattering of the muon within the steel filters and the granularity of the scintillator paddles. Also, the largest confidence level of a second track causing the observed hits is reported which serves as an isolation cut. The muon identification algorithm is well described elsewhere [41–43].

Because low momentum muons may be stopped in the steel filters of the MH detector, the requirement on the number of planes is relaxed from four to two planes for muons with momentum less than 10 GeV. This serves to increase the efficiency at low momentum.

Above 10 GeV, the typical efficiency of the muon identification algorithm is above 98% with a proton misidentification rate of less than 0.1%. The pion misidentification rate is larger (about 1%), but this is due to in flight $\pi^+ \rightarrow \mu^+\nu_\mu$ decays in the spectrometer where the μ^+ flight direction closely matches the pion's. This contamination is reduced by requiring light in the Čerenkov system in the narrow ranges where muons are expected to produce light but pions are not. A comparison of the calculated momenta with M1 and M2 also rejects some of these in flight decays.

Outer Muon detectors

Muons are identified in the Outer Muon system (see Section 3.8.2) with a method similar to that used in the Inner Muon system. However, there is an added complication since the iron shield (M2) has an internal magnetic field which deflects muons. The OM identification routine accounts for this by tracing muons through the magnetic field in the M2 steel and applying the multiple Coulomb scattering smearing (in both the OE and M2) to the traced position. This process is described in detail in Reference 44.

The OM reconstruction algorithm is efficient for muons down to $E \approx 4$ GeV, the range of muons in the OE and M2.

4.2.3 Electron identification

Although the Čerenkov system can provide some electron identification, the ability to separate electrons from pions is not available above 8.5 GeV for stubs and 17 GeV for tracks (see Table 3.4). Above these energies, calorimetry information is needed to separate electrons from hadrons and muons.

In both the IE and the OE, the identification method relies primarily on requiring that $E/p \approx 1.0$ for the track in question. In the IE, a cut of $0.8 < E/p < 1.2$ is typically used. For the OE, the window is a somewhat wider. Almost all the electromagnetic energy is contained in the calorimeters while most of the hadronic energy, even if an interaction occurs, passes through. (Muons leave almost no energy in these calorimeters.)

In the OE, electrons are further separated from hadrons by studying the shower evolution as a function of z (electromagnetic showers peak well within the detector). A discriminant analysis of the evolution is incorporated into the electron identification code.

The IE electron identification is improved by requiring that the Čerenkov identification algorithm confirms the assumption that the track is an electron. This effect is shown in Figure 4.10.

4.3 Data Processing

The FOCUS raw data set consists of about 6.5 billion photon interaction events on 6000 8 mm tapes. The total data set size is roughly 25 TB (terabytes). Because this is much more data than an individual experimenter can handle, the reconstruction and event selection process was performed in three steps, reducing the amount of data at each step.

In the first step, "Pass1," each event was reconstructed and written to tape. In the second step, "Skim1," some events were discarded and the events were split into several sets of output based on broad physics topics. In "Skim2," the final step, each of these sets of data were split further, based on more narrow physics topics. An overview of the entire FOCUS data reconstruction process is shown in Figure 4.11.

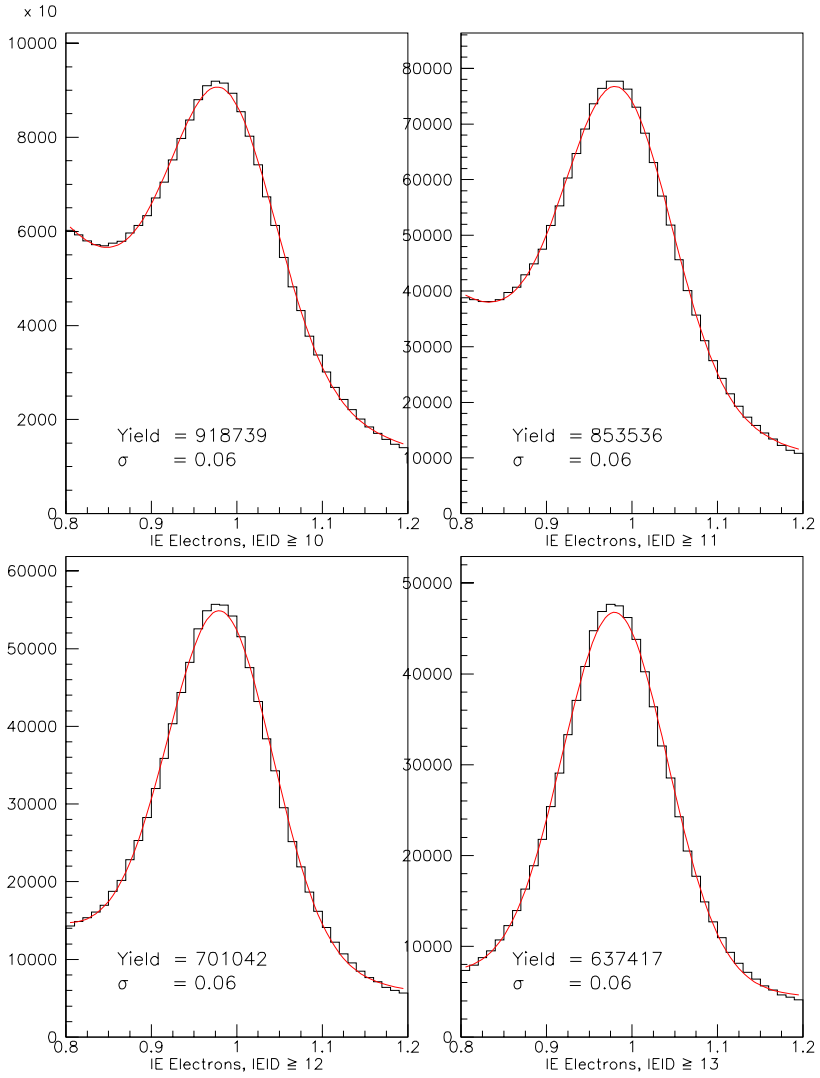

Figure 4.10: IE electron signals. A large value of **IEID** denotes better confirmation of the electron hypothesis by the Čerenkov system. Misidentification decreases with increasing **IEID**.

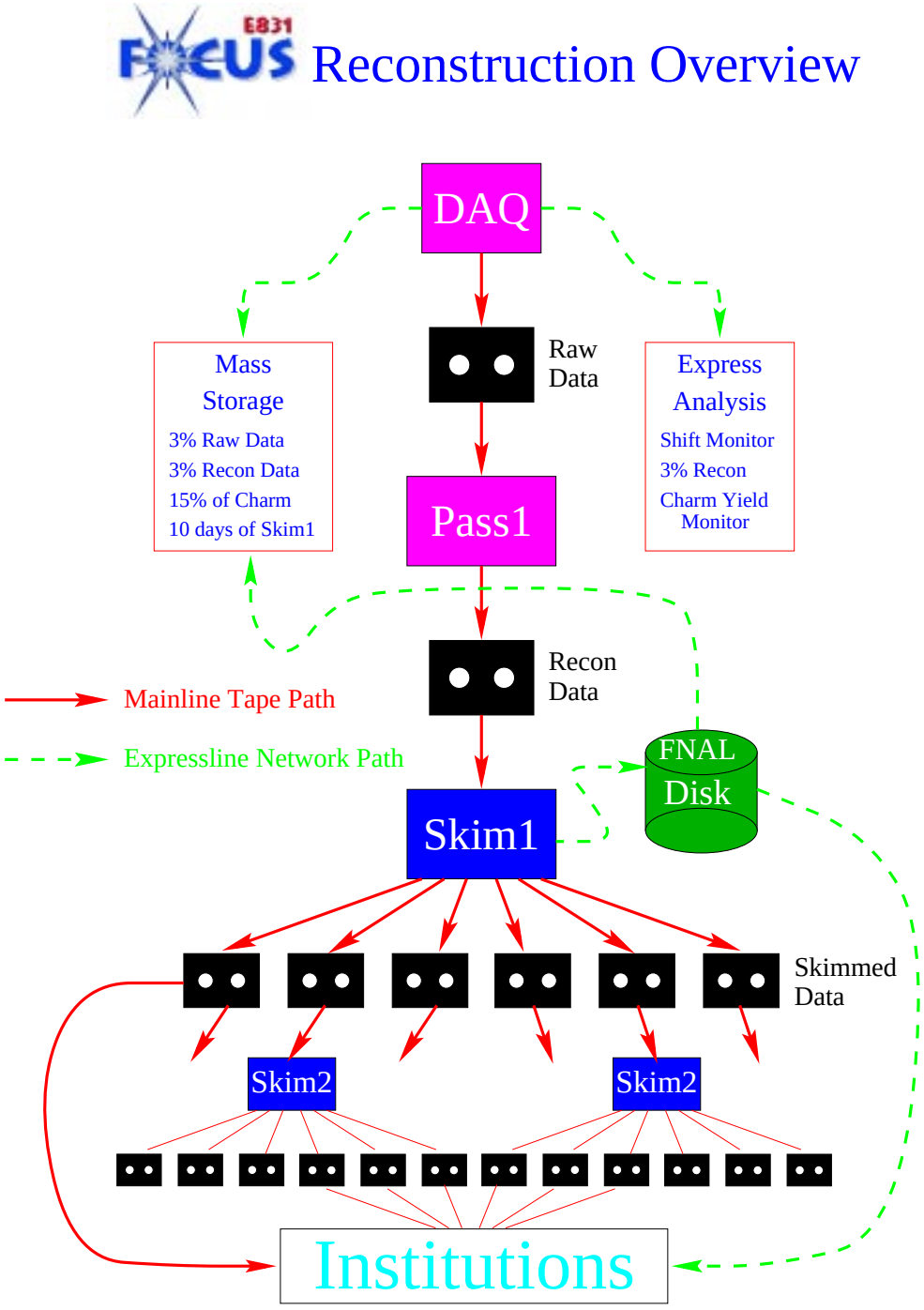

Figure 4.11: Overview of the FOCUS reconstruction process. The solid lines show the path of the data written to 8 mm tapes (the source for all final analyses). The dotted lines illustrate the distribution of large amounts of data via the Internet, which was used to help collaborators get data quickly for studies and preliminary analyses.

4.3.1 Event reconstruction (Pass1)

The first phase of the data reconstruction, called Pass1, began in January, 1998 and finished in October, 1998. In Pass1, the raw data on tapes written by the DAQ were reconstructed and analyzed and the resulting reconstructed data were written to another set of 6000 8 mm data tapes.

Because events in a high energy physics experiment are self-contained and independent, the individual events can be reconstructed by different computers. So while the total amount of computing power required to process the entire FOCUS data set was very large, the actual processing was done on many work-station class computers. This was accomplished for Pass1 by using the Fermilab software product CPS (Cooperative Process Software) [45]. This software groups together a "server" node and about 10 "worker" nodes. Together these computers are called a "farm." CPS allows transmission of data and control information among many processes running on multiple computers. In essence, it merges many computers into a single logical, faster computer.

The server node is responsible for reading and writing the data, but sends the events via a high-speed network to the worker nodes for the computationally intense processing. In the normal mode of operation, the server node read about 80 events from disk and send them to one worker node. When the worker node completed the reconstruction of the events, it sent the reconstructed event data back to the server node and requested another group of events. The server node would write the reconstructed events to disk. Separate programs were responsible for moving the data between the tapes and disks. A schematic of this process is shown in Figure 4.12.

FOCUS used up to eight of these computing farms at Fermilab consisting of up to 90 worker nodes. There were roughly equal numbers of SGI[7] workstations based on the MIPS R5000 CPU[8] and IBM[9] workstations based on the IBM/Motorola PowerPC CPU. Over the course of the ten month reconstruction effort, the amount of available computing fluctuated considerably. In the system's most robust configuration, the total computing power available was in excess of 12,000 MIPS.[10] An average CPU efficiency of about 85–90% was maintained over the entire period.

At the Pass1 level, the reconstruction algorithms for all of the detectors were executed. The most computationally intensive portions of the reconstruction code are the tracking algorithms, but shower reconstruction and particle identification combine to make another large fraction of the total computing required to process an event. Monitoring packages which analyze the events were also run. In order to maintain

[7] Silicon Graphics, Inc.
[8] Central Processing Unit
[9] International Business Machines
[10] Millions of Instructions Per Second

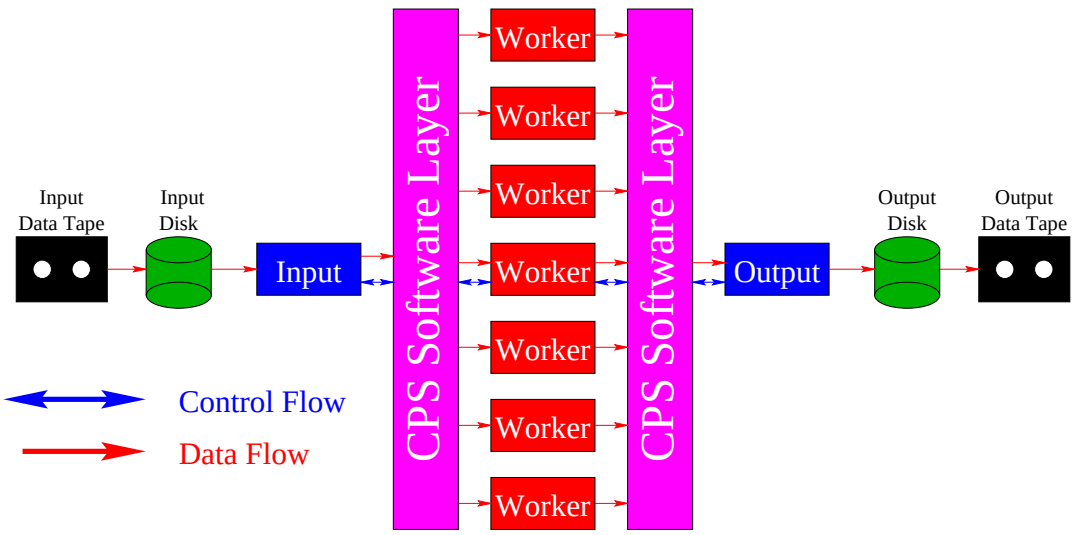

Figure 4.12: Diagram of the Pass1 process.

a 1:1 relationship between input and output tapes, reconstructed calorimetry information was not output. However, the raw information was saved. Events which had reconstruction errors (such as too many hits) were discarded, also saving space on the output tape. The fraction of events discarded at this stage was typically about 10%. The output from Pass1 was designed so that, if problems were found, the entire reconstruction (or parts of it) could be redone without reverting to the original data tapes.

4.3.2 Event selection (Skim1)

In order to make data set sizes more manageable, the Skim1 process split the reconstructed data into six "Super-streams" containing summarized information rather than the full information output by Pass1. Each Super-stream contains data satisfying requirements for physics in one or two broad categories (see Table 4.1). About half of the events surviving the Pass1 process were written out by Skim1, with many of those events being written into multiple Super-streams.

As with Pass1, Skim1 used clusters of computers to take advantage of the parallelism inherent in high energy physics data. However, in Skim1, data were analyzed as disk files, each containing about 40,000 events, rather than Pass1's much smaller chunks of data. Because Pass1 did not save the reconstructed calorimetry information, Skim1

Table 4.1: Descriptions of Super-streams. There are about 30 different skims, grouped into six Super-streams based on physics topics and the types of information present.

Super Stream	Physics Topics	Skim2 Institution
1	Semi-leptonic	Puerto Rico
2	Topological vertexing and K_s^0	Illinois
3	Calibration and rare decays	CBPF, Brazil
4	Baryons	Fermilab
5	Diffractive (light quark states)	California, Davis
6	Hadronic meson decays	California, Davis

executed the calorimetry algorithms again. Skim1 also re-ran the Vee and Čerenkov reconstruction since those algorithms were improved during Pass1 production.

Six output files, one for each Super-stream, were generated from each input file. These files were concatenated and output to six sets of 200–500 8 mm tapes. The data were also transferred over the Internet to Fermilab for easy access by experimenters.

Skim1 was run on two computer clusters of about 4000 MIPS each, located at the University of Colorado and Vanderbilt University. The University of Colorado cluster consisted entirely of Digital[11] workstations using the Alpha CPU. The Vanderbilt University system was a mixed system of Alpha workstations and workstations based on the Intel Pentium II processor running Linux. Skim1 began in October, 1998 and finished in February, 1999. An overview of the Skim1 process at Colorado is shown in Figure 4.13. The process used at Vanderbilt was similar.

4.3.3 Final event splitting (Skim2)

Because the size of the Skim1 output data sets (200–500 tapes) is still too large to be easily used by an individual, the six Skim1 Super-streams were split again into many sub-streams. Some events that did not pass more stringent cuts were discarded at this point, but not all skims applied additional cuts.

Skim2 processing was accomplished at five institutions, as shown in Table 4.1. From each Super-stream, 5–12 sub-streams were written, covering a variety of physics topics and calibration data samples. The sub-streams relevant to the analyses presented in this thesis are presented in Table 4.2. The Skim2 computing models varied by institution, but were generally similar to that used for Skim1. The first Skim2 process

[11]Now Compaq

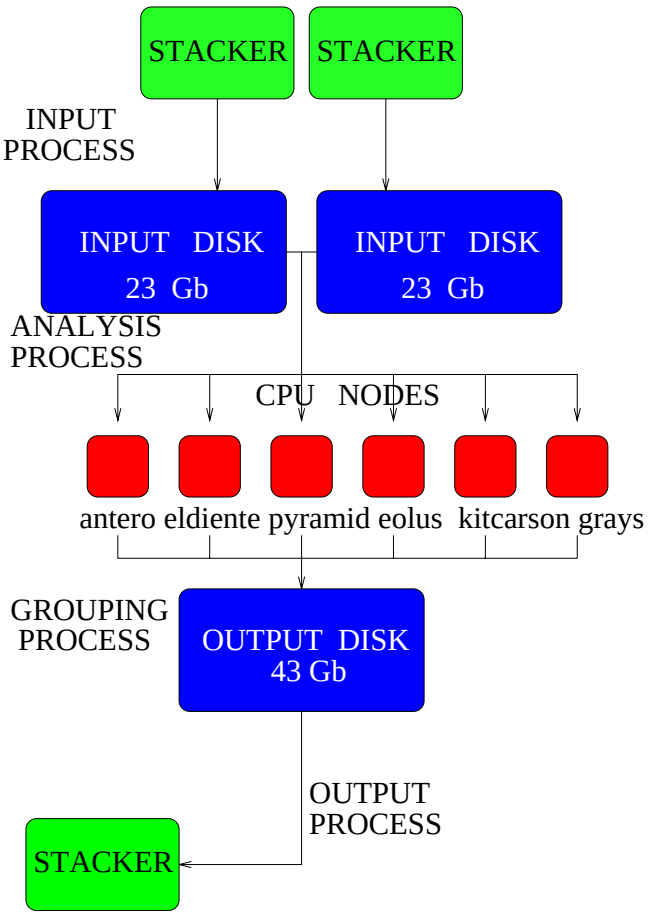

Figure 4.13: Diagram of the Skim1 process. Data is read from the tape stackers (jukeboxes), processed, and written again using another stacker.

began production in January, 1999 and all Skim2 processes were completed by June, 1999.

Table 4.2: Descriptions of several sub-streams. These are only the streams used in this thesis. Many others exist for other types of physics.

Super Stream	Sub Stream	Physics Topics	Number of tapes
4	FSDD	$\Lambda_c^+ \to pK^-\pi^+$	15
4	FSDL	Ξ^- and Ω^-	17
3	FSCG	Golden Modes	44

Chapter 5

Selection of Λ_c^+ candidates

In this chapter we detail the methods used for selecting Λ_c^+ candidates and explain many of the reconstruction methods used in FOCUS. While portions of this discussion are only applicable to Λ_c^+ reconstruction, other portions are applicable to the reconstruction of the Σ_c, Λ_{c1}^{*+}, and Ξ_{cc} candidates in later chapters.

In this thesis, only the $\Lambda_c^+ \to pK^-\pi^+$ decay mode of the Λ_c^+ is considered. This decay mode has an absolute branching ratio of $5.0 \pm 1.3\%$. This decay mode is chosen for its large branching fraction and ease of reconstruction (all of the decay products are charged and long lived).

Section 5.1 explains the vertexing algorithm used in FOCUS and the cuts it makes possible. Section 5.2 describes some of the Čerenkov cuts available from the **CITADL** algorithm. In Section 5.3 two kinematic cuts are investigated. Section 5.4 explains two ways of improving the momentum vectors for charm daughters. Finally, in Section 5.5 the effects and interactions of some of these cuts with each other are shown and the process of selecting a useful set of cuts for an analysis is explained.

5.1 Vertexing

Using the microstrip detectors described in Section 3.2, we take advantage of the fact that charmed particles travel a short distance in the spectrometer before they decay. This means we can reconstruct two distinct vertices in the event: the *primary* or production vertex and the *secondary* or decay vertex. A diagram of a $\Lambda_c^+ \to pK^-\pi^+$ decay and its vertices is shown in Figure 5.1. By reconstructing the two vertices, we obtain several quantities on which we can cut to reduce non-charm backgrounds.

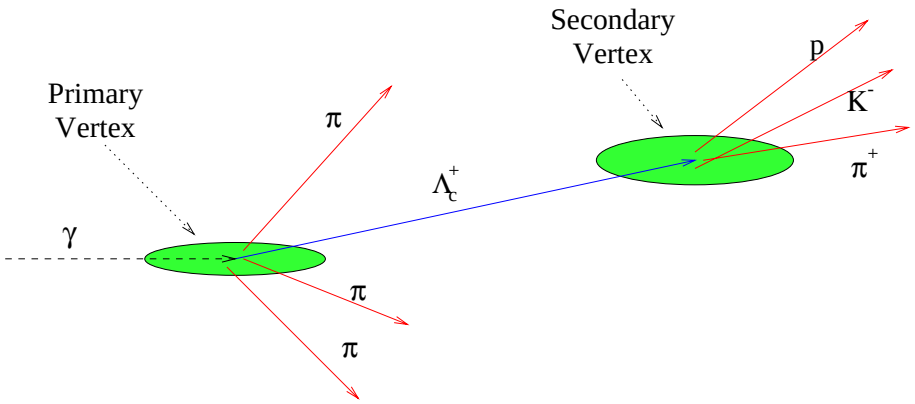

Figure 5.1: Schematic of a $\Lambda_c^+ \to pK^-\pi^+$ decay. The ellipses illustrate the centers and errors of the vertices. L, described in the text, is the distance between the centers of the two ellipses.

For the analyses presented in this thesis, we use a candidate driven vertexing algorithm called **DVERT** [46]. To reconstruct a $\Lambda_c^+ \to pK^-\pi^+$ decay candidate, we find three separate tracks that match our requirements for being a proton, kaon, and pion respectively. We then use the vertexing algorithm to form a vertex from these three tracks. Assuming a valid vertex can be found, we point the momentum vector of the Λ_c^+ candidate back towards its origin and select additional tracks that form a good vertex with the Λ_c^+ candidate. These tracks and the Λ_c^+ momentum vector form the primary vertex.

This method has been shown to be more efficient [47] at extracting fully reconstructed charm decays than methods which form well separated vertices without any knowledge of the decay topology being searched for. There are several reasons that this candidate driven algorithm is superior. First, there is no default separation required between vertices. Second, primary tracks may pass through the secondary, but can be excluded from it. Finally, including additional tracks in the secondary will affect the point-back of the charm candidate, causing it to miss the primary.

5.1.1 Vertex confidence levels

Each vertex formed by **DVERT** has an associated confidence level. We call these values **CLP** for the primary vertex and **CLS** for the secondary. In Figure 5.1, it is evident that tracks will not intersect exactly. Instead, we calculate the probability that within their errors, all candidate tracks are consistent with intersecting. Minimal cuts on these values require that the confidence levels are greater than 1%. However, a slightly larger cut is sometimes useful in rejecting random combinatoric backgrounds.

5.1.2 Detachment (L/σ_L)

The detachment cut is the most powerful cut in most charm analyses. By requiring a significance of separation between the primary and secondary vertices, short lived hadronic background is effectively removed. The detachment cut requires that L/σ_L be greater than some value where L is the measured distance between the two vertices and σ_L is the error on that measurement. This requirement is illustrated in Figure 5.1 where the errors on vertex positions are shown using ellipses. (The error in the longitudinal direction is typically several hundred μm per vertex while the errors in the transverse directions are only a few μm.)

5.1.3 Primary isolation (ISO1)

ISO1 is one of three isolation tests we can perform on vertices. **ISO1** determines the largest confidence level that one of the tracks in the secondary actually comes from the primary. The lower this value, the less likely it is that any of the charm candidate tracks are really associated with the primary vertex.

5.1.4 Secondary isolation I (ISO2)

ISO2 determines the largest confidence level that a track not in the primary or secondary belongs to the secondary. The lower the value, the more likely it is that the secondary is a "pure" vertex. This type of cut is useful for rejecting background from higher multiplicity decays than the one of interest.

5.1.5 Secondary isolation II (ISO3)

ISO3 is similar to **ISO2**. **ISO3** determines the largest confidence level that any other track, including those in the primary, belongs to the secondary. This type of cut is rarely used since it is quite likely that one of the primary tracks passes through the secondary.

5.2 Čerenkov Identification

As described in Section 4.2.1, the **CITADL** algorithm calculates negative log likelihoods for the electron, pion, kaon, and proton hypothesis for each PWC track. By

cutting on *differences* between the different particle hypotheses, we enforce particle identification.

Kaon identification: Kaon identification is straightforward. Since most of the particles produced in target interactions are electrons or pions, we cut on the difference between the kaon and pion hypothesis. (This implies an effective cut on kaon vs. electron since for real kaons, the kaon hypothesis should be closer to the π hypothesis than the electron hypothesis.) The cut variable is $\Delta W(\pi K)$ which is defined as $W_{\rm obs}(\pi) - W_{\rm obs}(K)$. We usually require positive values for $\Delta W(\pi K)$, meaning that the kaon hypothesis is favored over the pion hypothesis.

Proton identification: Proton identification is a little more complex. For $\Lambda_c^+ \to pK^-\pi^+$ we place a strong cut on the variable $\Delta W(\pi p)$, defined similarly to $\Delta W(\pi K)$. We also place a weaker cut on $\Delta W(Kp)$ to remove background from the decays $D^+ \to K^-K^+\pi^+$ and $D_s^+ \to K^-K^+\pi^+$ where the proton is misidentified as a kaon. Typical cut values are $\Delta W(\pi p) > 5$ and $\Delta W(Kp) > 1$.

Pion identification: To identify pions, we use a cut called $\pi_{\rm con}$ (pion consistency). This cut determines how likely the pion hypothesis is compared to the other hypotheses. The definition of $\pi_{\rm con}$ is

$$\pi_{\rm con} \equiv \min(W_{\rm obs}(e), W_{\rm obs}(K), W_{\rm obs}(p)) - W_{\rm obs}(\pi) \tag{5.1}$$

which allows for values in the range $(-\infty, \infty)$. This type of cut typically incurs small losses in signal at a value of -6, which means that some other hypothesis is favored over the pion hypothesis, but not by a large amount. Because of the limited momentum range of positive pion identification, requiring $\pi_{\rm con} > 0$ is inefficient, although the purity of signals with such a cut is very high.

5.3 Other Cuts

5.3.1 Momentum

In a fixed target experiment, charmed particles are usually produced carrying a significant fraction of the beam momentum. In addition, acceptance and identification of high momentum parent particles is more efficient. For these reasons, a cut on the Λ_c^+ momentum of 40 GeV/c removes a small amount of background with almost no loss in signal.

5.3.2 Lifetime

Because a large part of the background in $\Lambda_c^+ \to pK^-\pi^+$ comes from $D^+ \to K^-K^+\pi^+$ and $D_s^+ \to K^-K^+\pi^+$ decays, requiring short lived Λ_c^+ candidates can be very effective in eliminating charm backgrounds. The D_s^+ lifetime is slightly more than two times that of the Λ_c^+ and the D^+ lifetime is about five times as large. Requiring that the Λ_c^+ candidate lives less than five or even ten times the nominal Λ_c^+ lifetime reduces backgrounds considerably with negligible loss in yield.

5.4 Improving Momentum Vectors

While the momentum resolution quoted in Section 4.1.4 is quite good, we can make two small improvements. The first is obtained by improving the measurement of the magnitude of the momentum and the second is obtained by improving the direction measurement at the point of production.

5.4.1 Refitting track momenta

As explained in Section 4.1.4, the momentum of tracks is determined only from the bend angle in M2, while the momentum of stubs is determined from the bend angle in M1. While there is no way to improve the momentum determination of stubs, the measurement can be improved for tracks by including information about the bends in both magnets.

We use an algorithm called **TRKFIT** which performs a fit using the bend angles in both M1 and M2 as well as the track parameters and errors in the three different tracking regions (the target region and the inner and outer spectrometer regions). This algorithm improves the overall mass resolution on the decay $\Lambda_c^+ \to pK^-\pi^+$ by about 8%, making it somewhat easier to separate signal events from random combinatorics. This effect is shown in Figure 5.2.

While we always use this method in the analyses presented, we check the effect of reverting to the standard method of momentum determination as a systematic effect.

5.4.2 Improving track directions

A more subtle improvement in mass resolution is obtained by using the direction vectors obtained from the candidate vertexing algorithm (**DVERT**) described above.

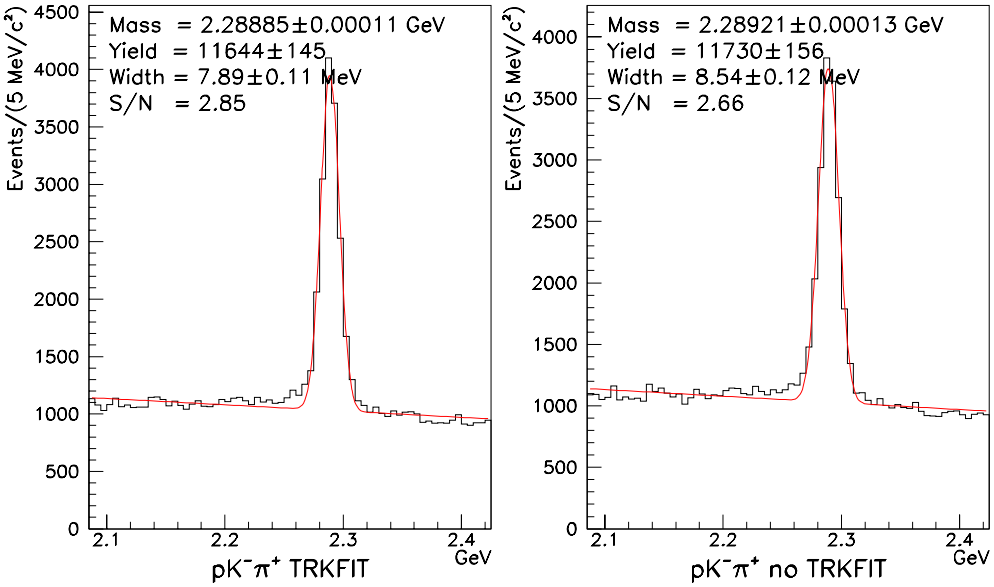

Figure 5.2: Effect of using **TRKFIT** momentum vectors. The plot on the left uses the **TRKFIT** algorithm, the plot on the right uses the standard momentum finding algorithms. Applying **TRKFIT** improves the resolution ("width" in the plot) and increases signal-to-noise.

The standard (or **TRACCE**) direction vectors for linked tracks are determined solely from the downstream microstrip stations. Using the **DVERT** direction vectors allows us to incorporate Target Silicon information into the direction vectors. This improves the mass resolution by about 1%. A comparison between Λ_c^+'s reconstructed with the **TRACCE** vectors and the **DVERT** vectors is shown in Figure 5.3.

5.5 Optimizing Cuts

With a large variety of cuts to choose from, it is important to understand the effect of these cuts and their interactions with each other. In this section, several "cut tree" plots are presented which show the Λ_c^+ yield vs. signal-to-noise for many different combinations of cuts. The cuts chosen for each plot are often related to each other so that any interactions can be seen.

Each plot is a log-log plot, which is useful in determining cut interactions. In the log-log plot, if the branch representing the evolution of a cut is independent of the previous cut, its shape remains the same regardless of the starting point. All the plots are on the same scale and have the same starting point. Each plot includes an evolution in L/σ_L, denoted by inverted triangles. From each point representing

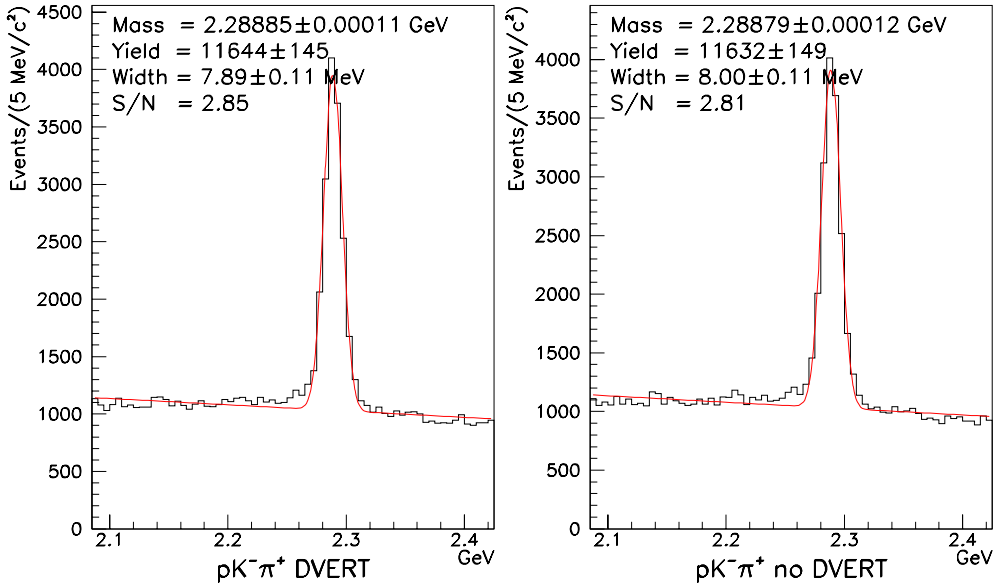

Figure 5.3: Effect of using **DVERT** direction vectors. The plot on the left uses the **DVERT** direction vectors, the plot on the right uses the standard direction vectors. Using the **DVERT** vectors improves the resolution slightly.

a particular L/σ_L cut, the second cut is evolved, and from each of these points, the third cut is evolved. (Showing the evolution of a fourth cut would, in most cases, be too confusing.)

The initial cuts in each plot are:

- $L/\sigma_L > 3$
- $\Delta W(\pi K) > 2$
- $\Delta W(\pi p) > 4$
- $\Delta W(Kp) > 0$
- CLS > 0.01
- CLP > 0.01

These cuts correspond to our skim of the FSDD sub-skim (see Section 4.3.3). The Skim2 cuts on the FSDD sub-skim are $\Delta W(\pi K) > 0.5$, $\Delta W(\pi p) > 0.5$, $\Delta W(Kp) > 0$, and $L/\sigma_L > 1.5$.

Kaon and pion Čerenkov cuts: Figure 5.4 shows how $\Delta W(\pi K)$ and $\pi_{\rm con}$ cuts affect the Λ_c^+ signal. We see several interesting features. First, the effect of the $\Delta W(\pi K)$ cut changes with L/σ_L.[1] (Comparing the shapes of the $\Delta W(\pi K)$ evolution at $L/\sigma_L > 3$ and $L/\sigma_L > 12$, we see that this cut becomes more effective with increasing L/σ_L.) Second, we see that $\pi_{\rm con}$ cuts of about -4 or less can improve signal to noise with very little loss in signal. Third, we notice that requiring $\pi_{\rm con} > 0$ incurs a large loss in signal. Finally, as we expect, the two Čerenkov cuts are independent of each other.

Proton Čerenkov cuts: In Figure 5.5, the effects of $\Delta W(\pi p)$ and $\Delta W(Kp)$ cuts are illustrated. The effectiveness of these cuts is fairly constant with increasing L/σ_L. However, the two Čerenkov cuts are strongly correlated. As the $\Delta W(Kp)$ cut increases, the $\Delta W(\pi p)$ cut is less and less effective. (Compare the $\Delta W(\pi p)$ evolutions at the beginning and end of any $\Delta W(Kp)$ evolution.) This is not surprising since a cut in $\Delta W(Kp)$ often has an inherent cut in $\Delta W(\pi p)$. (For a real proton, we expect the relationship $-W_{\rm obs}(p) \geq -W_{\rm obs}(K) \geq -W_{\rm obs}(\pi)$ to hold.)

Isolation cuts: In Figure 5.6, cut trees for the isolation cuts **ISO1** and **ISO2** are shown. This plot is somewhat confusing, but it shows several things. First, there is a weak correlation between the two isolation cuts. Second, the two isolation cuts are strongly correlated with the L/σ_L cut. Finally, neither isolation cut is very effective at extracting Λ_c^+ candidates until the L/σ_L cut becomes fairly large ($L/\sigma_L > 6$ or so).

Kinematic cuts: In all of these cut trees, the main branch is initially quite surprising. Typically we expect (based on our experiences with charmed mesons) that as L/σ_L increases, the signal-to-noise should increase dramatically. That the Λ_c^+ signal-to-noise *decreases* at high L/σ_L is very counter intuitive. In Figure 5.7 we find a clue to why this occurs. While a cut in Λ_c^+ momentum is unremarkable, requiring that the observed Λ_c^+ lifetime is less than four times the known Λ_c^+ lifetime has a dramatic effect on signal-to-noise, especially at high L/σ_L. As mentioned earlier, it appears that a large number of the background Λ_c^+ candidates, especially at high L/σ_L, are in fact long-lived charm mesons. By requiring a candidate lifetime more in line with the short-lived Λ_c^+, we remove large amounts of this background with a minimal effect on the Λ_c^+ yield. (For a cut of $t_{\rm life} < 4\tau_{\Lambda_c^+}$ we expect to lose about $1/e^4$ of the real Λ_c^+ candidates.)

These cut trees help us, for a particular analysis, find an appropriate set of cuts to apply. In an analysis where a large Λ_c^+ sample is important, we can choose cuts which preserve a large portion of the Λ_c^+ yield. Where purity of the Λ_c^+ signal is more

[1] This is likely due to contamination from charm backgrounds.

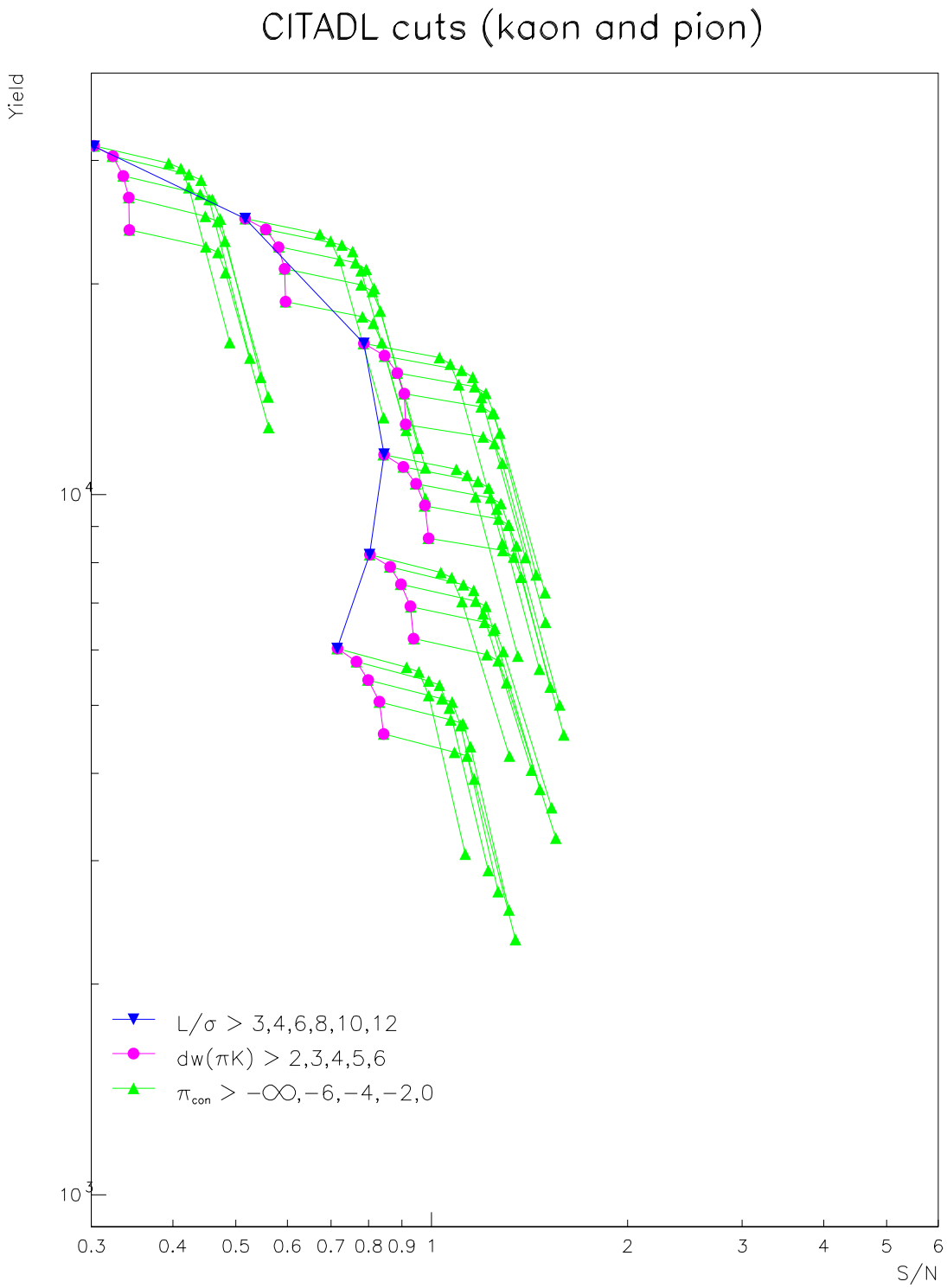

Figure 5.4: Effect of CITADL cuts on the kaon and pion. The circles represent an evolution in π-K separation and the triangles represent an evolution in pion consistency with the values shown in the key.

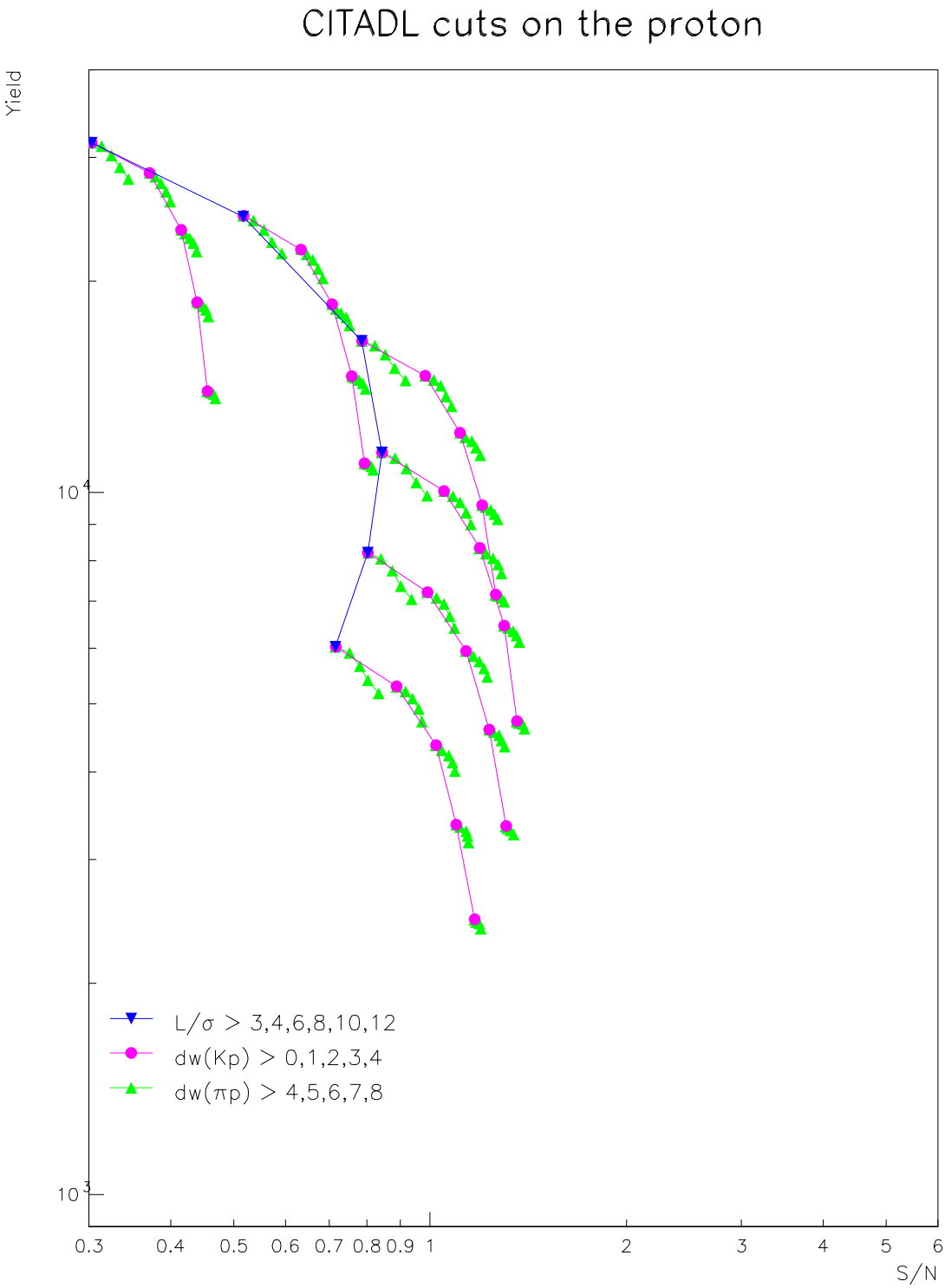

Figure 5.5: Effect of CITADL cuts on the proton. The circles represent an evolution in K-proton separation and the triangles represent an evolution in π-proton separation.

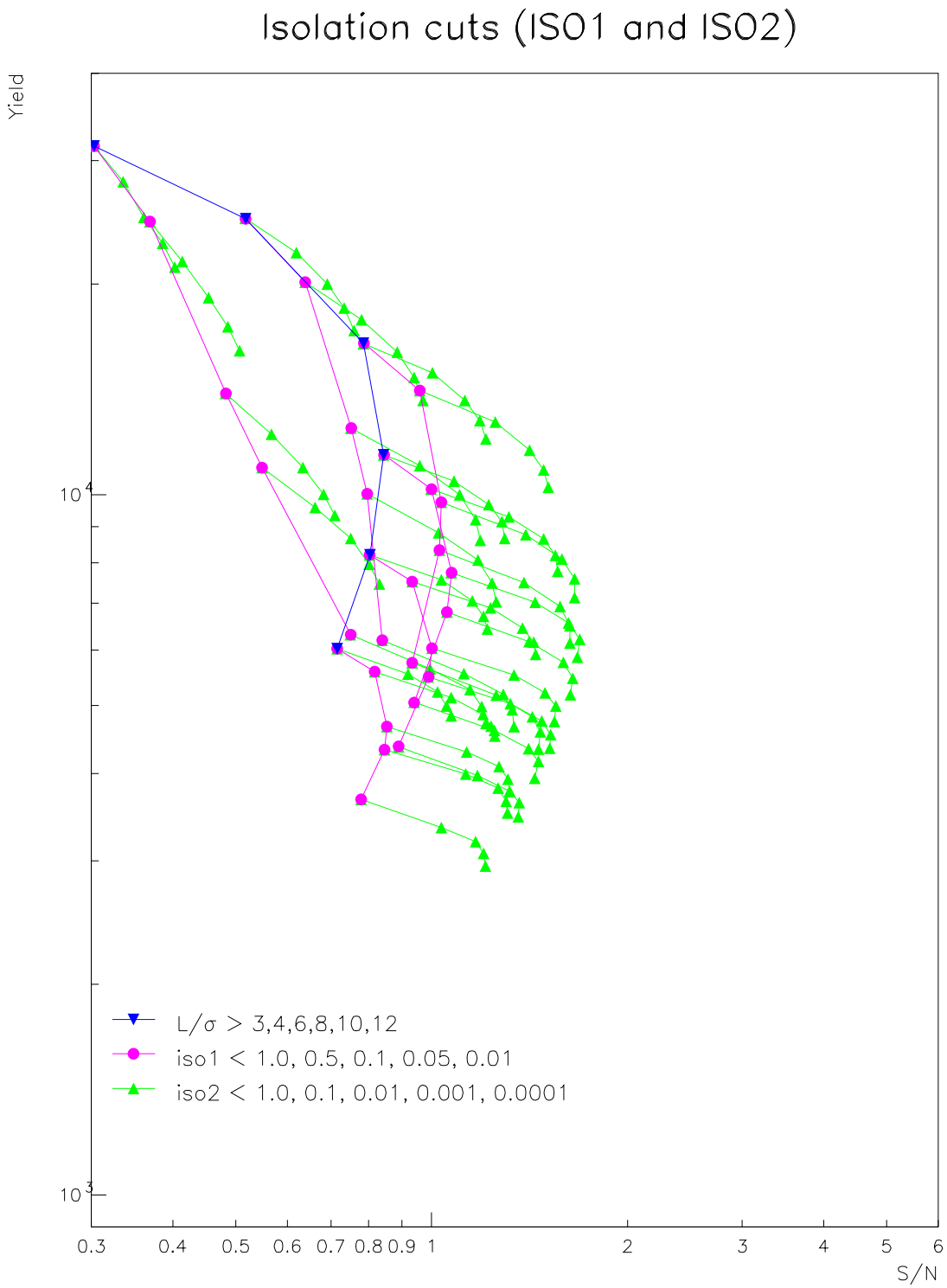

Figure 5.6: Effect of isolation cuts. Circles and triangles show evolutions in **ISO1** and **ISO2** respectively.

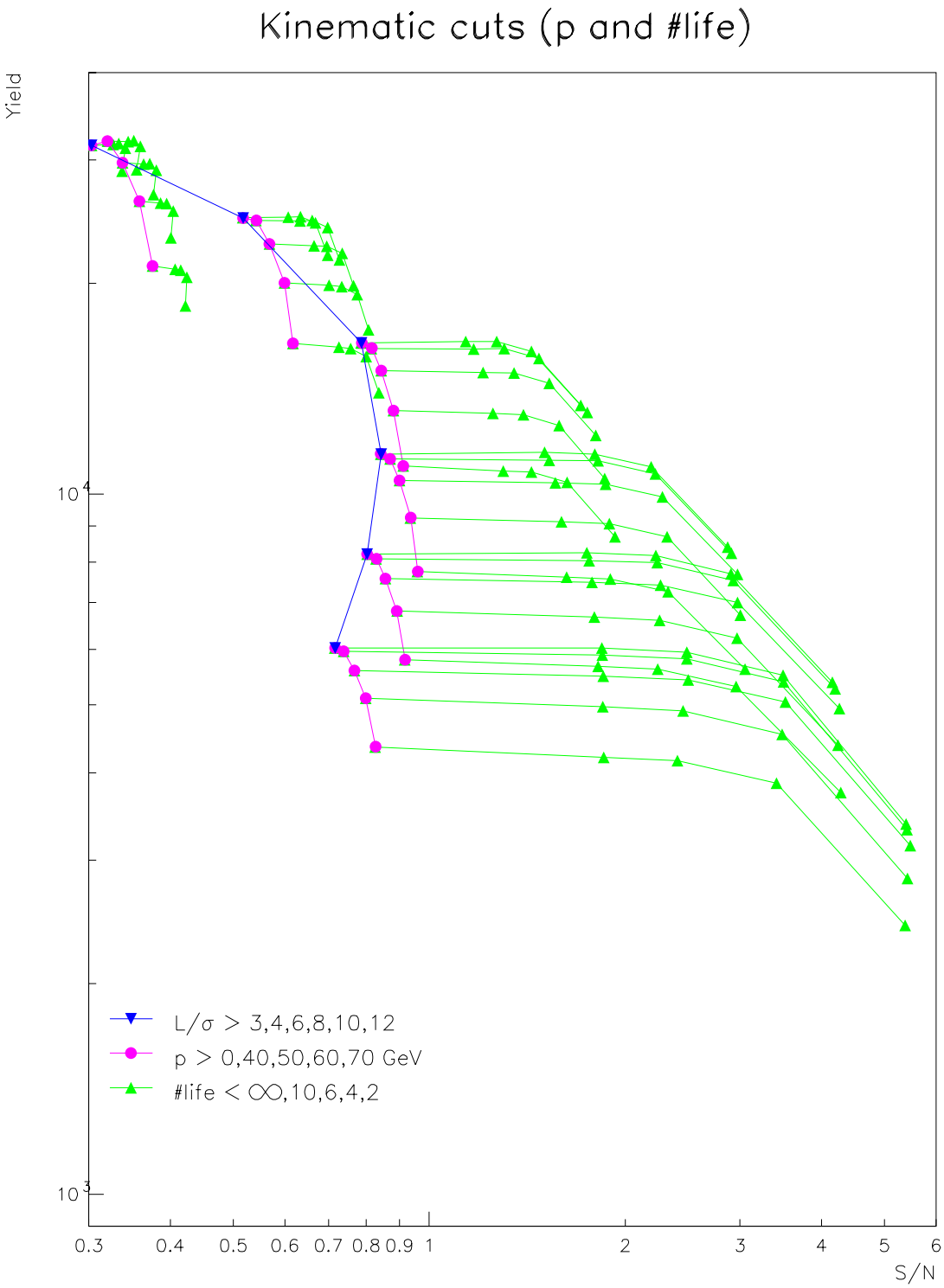

Figure 5.7: Effects of kinematic cuts. The circles represent an evolution in Λ_c^+ momentum and the triangles represent an evolution in Λ_c^+ lifetime.

important, we can pick a set of cuts which gives much improved signal-to-noise while still keeping the sample as large as possible.

Chapter 6

Measurements of the Σ_c Baryon Mass Splittings

In this chapter we present measurements of the $\Sigma_c - \Lambda_c^+$, $\Sigma_c^0 - \Sigma_c^+$, and $\Sigma_c^0 - \Sigma_c^{++}$ mass differences. The measurements of the Σ_c^0 and Σ_c^{++} masses represent an improvement over the current measurements, while the measurement of the Σ_c^+ mass is included to present the spectroscopy of the entire Σ_c system. (Only one other experiment has measured the masses of all three Σ_c's.)

In an analysis of the decays $\Sigma_c \to \Lambda_c^+ \pi^\pm$, we find $m_{\Sigma_c^0} - m_{\Lambda_c^+} = 167.54 \pm 0.19 \pm 0.34$ MeV/c^2, $m_{\Sigma_c^{++}} - m_{\Lambda_c^+} = 167.59 \pm 0.20 \pm 0.27$ MeV/c^2, and $m_{\Sigma_c^{++}} - m_{\Sigma_c^0} = 0.05 \pm 0.28 \pm 0.09$ MeV/c^2. In an analysis of the decay $\Sigma_c^+ \to \Lambda_c^+ \pi^0$ we find $m_{\Sigma_c^+} - m_{\Lambda_c^+} = 168.03 \pm 1.01 \pm 0.30$ MeV/c^2 and $m_{\Sigma_c^+} - m_{\Sigma_c^0} = 0.49 \pm 1.03 \pm 0.45$ MeV/c^2. These results are obtained with a sample of 362 ± 36 $\Sigma_c^0 \to \Lambda_c^+ \pi^-$ decays, 118 ± 40 $\Sigma_c^+ \to \Lambda_c^+ \pi^0$ decays, and 487 ± 41 $\Sigma_c^{++} \to \Lambda_c^+ \pi^+$ decays.

In Section 6.1 we review the theoretical calculations of Σ_c mass splittings. In Section 6.2 we briefly review measurements from other experiments. In Section 6.3 we detail the Λ_c^+ and Σ_c reconstruction methods and cuts used. In Section 6.4 we examine systematic errors from a variety of sources including fitting and reconstruction methods, overall knowledge of the momentum scale, and "split sample" techniques. In Section 6.5 we present the final values and compare them with other experiments and the world averages.

6.1 Theory of Baryon Masses

Before any experimental measurements of the Σ_c masses were available, most initial predictions of the splittings between the Σ_c^0 and the Σ_c^{++} were large (on order of several MeV/c^2). One might naively expect to find the mass hierarchy $m_{\Sigma_c^0} > m_{\Sigma_c^+} > m_{\Sigma_c^{++}}$, since in every other case, baryons with d quarks are heavier than the corresponding baryons with u quarks. (See Table 6.1.) Measurements now show $m_{\Sigma_c^{++}} - m_{\Sigma_c^0}$ to be quite small (less than 1 MeV/c^2) and more recent theoretical models predict mass splittings of $\mathcal{O}(1\ \mathrm{MeV}/c^2)$.

Table 6.1: Mass splittings of the well measured baryons. States on the right are identical to states on the left with the quark substitution(s) d $\rightarrow$ u. Values are the PDG [4] averages.

Particles	Mass Splitting (MeV/c^2)
$n - p$	1.293318±0.000009
$\Delta^0 - \Delta^{++}$	2.6±0.4
$\Sigma^- - \Sigma^+$	8.08±0.08
$\Sigma^- - \Sigma^0$	4.86±0.08
$\Sigma^{*0} - \Sigma^{*+}$	0.9±1.1
$\Sigma^{*-} - \Sigma^{*+}$	4.4±0.6
$\Xi^- - \Xi^0$	6.4±0.6
$\Xi^{*-} - \Xi^{*0}$	2.9±0.9
$\Sigma_c^0 - \Sigma_c^{++}$	−0.66±0.28
$\Sigma_c^0 - \Sigma_c^+$	−1.4±0.6
$\Sigma_c^{*0} - \Sigma_c^{*++}$	−1.9±1.9
$\Xi_c^0 - \Xi_c^+$	4.7±2.1

Accurate calculation of these masses is complicated by the need to include several canceling contributions. The Σ_c case is particularly problematic since small contributions which are safely ignored in calculating hyperon mass splittings to a few percent now become important. In order to make order of magnitude calculations of Σ_c mass splittings, these minor effects need to be included.

Recently, there has been a lack of theoretical interest in Σ_c spectroscopy, at least in the literature. The last group of papers are from the mid-1980s around the time of the first preliminary measurements from ARGUS. There were a number of papers published in the late 1970s as well. The recent paper by Genovese, *et al.* [48] reviews a number of these earlier calculations and recalculates the mass splittings based on a consistent set of assumptions.

6.1.1 Contributions to isospin mass splittings

This section is intended as a brief overview of some of the contributions which are included in baryon mass calculations. A more detailed treatment is given in Reference 49.

Quark mass differences: The u and d quarks differ both in their intrinsic masses and in their constituent masses.[1] Typical values for $m_d - m_u$ are on order of a few MeV/c^2. The larger mass of the d quark manifests itself in the mass difference between baryons, and leads one to naively expect that all "d quark" baryons should be heavier than the corresponding "u quark" baryons.

Rosner [49] also points out that the contribution to mass from the kinetic energy may increase or decrease with increasing quark mass depending on the r dependence of the effective potential. For potentials of the form $V = \lambda r^\nu$, $\nu < 0$ gives increasing kinetic energy with increasing mass while for $\nu > 0$, kinetic energy decreases with increasing mass.

Potential Model: Models of the strong potential between quarks vary from model to model, but a fairly typical quark-quark potential model [48, 50] is of the form

$$V(r) = -\frac{\kappa}{r} + \lambda r^p - \Lambda + \frac{2\pi\kappa'}{3m_1 m_2}\,\tilde{\delta}(r, r_0)\,\vec{\sigma}_1 \cdot \vec{\sigma}_2. \tag{6.1}$$

In this notation, $\tilde{\delta}(r, r_0)$ is a smeared delta function (representing Pauli exclusion) and r_0 is a constant related to the quark-quark separation. Different models choose different forms of $\tilde{\delta}(r, r_0)$, different values for the many parameters, and additional or modified contributions from other sources. κ, κ', λ, and Λ are all constants which vary from model to model.

Coulomb interactions: In addition to the strong interaction between quarks, each quark interacts with its neighbors via the Coulomb force. The interaction between two quarks is of the familiar form

$$\Delta E_{ij} = \alpha q_i q_j \left\langle \frac{1}{r_{ij}} \right\rangle. \tag{6.2}$$

Typically, calculations assume that $\langle 1/r_{ij} \rangle$ is the same for all quark pairs in a multiplet, but this is not a completely accurate assumption [49]. With this assumption, Equation (6.2) simplifies to $\Delta E_{ij} = c_1 q_i q_j$ where c_1 is a constant.

[1] The constituent mass is the effective mass of the quark in the hadron potential.

Strong hyperfine interactions: The spins of confined quarks in S-wave states interact via single gluon exchange given by terms of the form

$$\Delta E_{ij} = c_2 \frac{|\Psi_{ij}(0)|^2 \langle \sigma_i \cdot \sigma_j \rangle}{m_i m_j}, \tag{6.3}$$

where c_2 is a constant and $\Psi_{ij}(0)$ is the wave function for two quarks with no separation. Quark masses play a role here too, as illustrated by the $m_i m_j$ term in the denominator.

Electromagnetic hyperfine interactions: Similarly, the electromagnetic hyperfine interaction contributes to the potential and is of the form

$$\Delta E_{ij} = -\frac{2\pi\alpha q_1 q_2 |\Psi_{ij}(0)|^2 \langle \sigma_i \cdot \sigma_j \rangle}{3 m_i m_j}. \tag{6.4}$$

Typically one assumes that $|\Psi_{ij}(0)|^2$ is a constant for all quark pairs, so that both hyperfine interactions can be more easily parameterized. However, the validity of this approximation is somewhat questionable.

To form an estimate of the baryon mass splittings, differences between the quark masses and the quark potential are combined with the sums of the ΔE_{ij} values above and a difference is calculated.

For a more thorough discussion of these contributions, other possible contributions, and the limitations of the simplifying assumptions made, see References 48 and 49.

6.1.2 Theoretical predictions

In Table 6.2 we summarize the predictions of $m_{\Sigma_c^{++}} - m_{\Sigma_c^0}$ from various theoretical works. We only include calculations after about 1985. Note that the values from Reference 48 are recalculations of several earlier models, many from before 1985. There is a wide range of predicted values, many of which are inconsistent with the recent measurements.

6.2 Measurements from Other Experiments

There are only two measurements of the Σ_c^0 and Σ_c^{++} mass differences with similar precision to the measurement presented in this thesis. The first is a 1993 measurement from CLEO II [55], the second is from FNAL-E791 [56] and was published in 1996.

Table 6.2: Theoretical predictions of $m_{\Sigma_c^{++}} - m_{\Sigma_c^0}$ and $m_{\Sigma_c^+} - m_{\Sigma_c^0}$.

Author	$m_{\Sigma_c^{++}} - m_{\Sigma_c^0}$ (MeV/c^2)	$m_{\Sigma_c^+} - m_{\Sigma_c^0}$ (MeV/c^2)
Capstick [51]	1.4	-0.2
Chan [52]	0.3	1.05
Genovese [48]	-2 to 3	-2 to 1
Hwang [53]	3.0	-0.5
Isgur [54]	-2.0	-1.8

Both measurements result from samples of 120–130 events. These measurements are presented in Table 6.3.

Table 6.3: Experimental measurements of Σ_c^{++} and Σ_c^0 mass differences.

	Mass difference (MeV/c^2)		
Experiment	$\Sigma_c^{++} - \Lambda_c^+$	$\Sigma_c^0 - \Lambda_c^+$	$\Sigma_c^{++} - \Sigma_c^0$
CLEO II	$168.20 \pm 0.30 \pm 0.20$	$167.10 \pm 0.30 \pm 0.20$	$1.10 \pm 0.40 \pm 0.10$
FNAL-E791	$167.76 \pm 0.29 \pm 0.15$	$167.38 \pm 0.29 \pm 0.15$	$0.38 \pm 0.40 \pm 0.15$
PDG Fit	167.87 ± 19	167.30 ± 0.20	0.57 ± 0.23

The only significant measurement of $m_{\Sigma_c^+}$ is presented in the same CLEO II paper [55] which finds that $m_{\Sigma_c^+} - m_{\Lambda_c^+} = 168.5 \pm 0.4 \pm 0.2$ MeV/c^2 and $m_{\Sigma_c^+} - m_{\Sigma_c^0} = 1.4 \pm 0.5 \pm 0.3$ MeV/c^2 from 111 events.

Several other experiments [57–62] have measured the $\Sigma_c^0 - \Lambda_c^+$ and $\Sigma_c^{++} - \Lambda_c^+$ mass splittings, but these measurements have total errors greater than 0.5 MeV/c^2.

6.3 Event Selection and Reconstruction

6.3.1 Λ_c^+ selection

Λ_c^+ candidates are reconstructed in the $\Lambda_c^+ \to pK^-\pi^+$ decay mode only. Candidates are reconstructed using **TRKFIT** to improve the momentum resolution on all tracks. **DVERT** direction vectors are used for all tracks for the same reason.

In reconstructing Σ_c^0 and Σ_c^{++} candidates, we use the following cuts on Λ_c^+ candidates:

- $L/\sigma_L > 6$
- $t_{\rm life} < 10\tau_{\Lambda_c^+}$

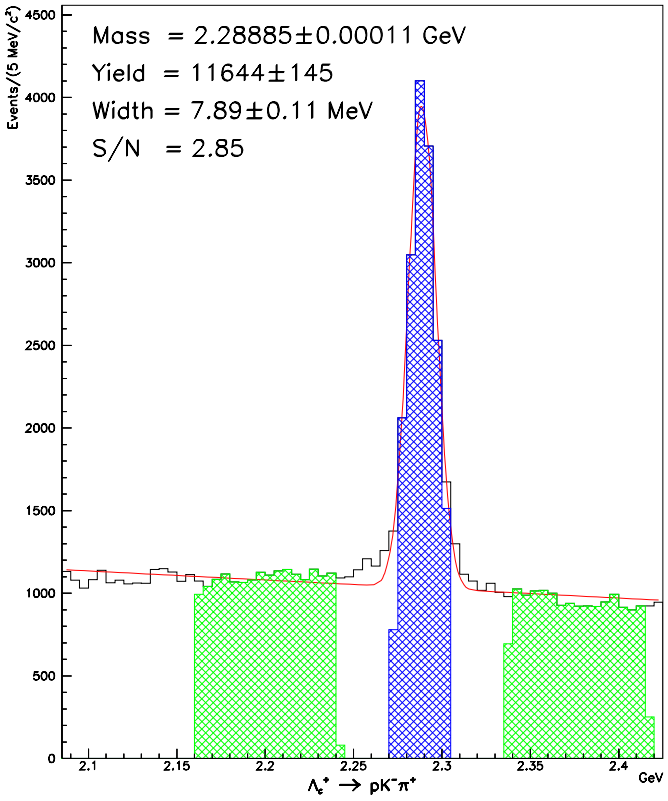

Figure 6.1: $\Lambda_c^+ \to pK^-\pi^+$ candidates used in the reconstruction of Σ_c^0 and Σ_c^{++} candidates. The central hatched region shows the 2σ cut around the nominal Λ_c^+ mass. The outer hatched regions are $6-16\sigma$ sidebands which are used in background studies. (The cut and bin boundaries do not coincide.)

- $p(\Lambda_c^+) > 40$ GeV/c
- CLP and CLS > 0.01
- $\Delta W(\pi p) > 4.0$
- $\Delta W(Kp) > 1.0$
- $\Delta W(\pi K) > 3.0$
- $\pi_{\rm con} > -6.0$

Finally, Λ_c^+ candidates are required to have a mass within $\pm 2\sigma$ of the measured Λ_c^+ mass. The resulting Λ_c^+ signal and 2σ mass cut are shown in Figure 6.1.

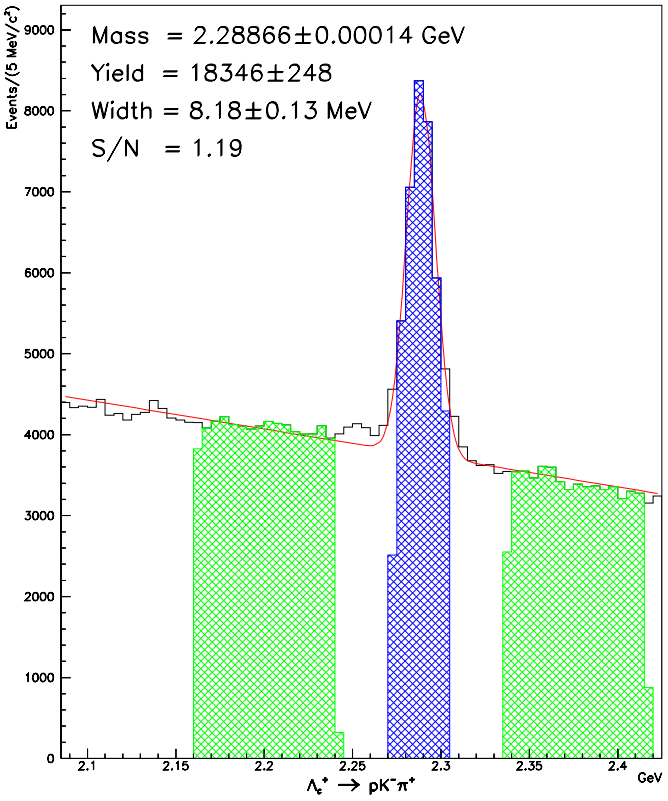

Figure 6.2: $\Lambda_c^+ \rightarrow pK^-\pi^+$ candidates used in the reconstruction of Σ_c^+ candidates. The central hatched region shows the 2σ cut around the nominal Λ_c^+ mass. The outer hatched regions are $6-16\sigma$ sidebands which are used in background studies.

To reconstruct Σ_c^+ candidates we use the same cuts as above, except

- $L/\sigma_L > 4$
- $\Delta W(\pi p) > 3.0$

The Λ_c^+ candidates used to reconstruct Σ_c^+ candidates are shown in Figure 6.2. Primarily due to the looser L/σ_L cut, this sample is significantly larger than that used to analyze the $\Lambda_c^+\pi^\pm$ channels. This is done to increase the Σ_c^+ sample size to the point where a reasonable measurement of the mass can be made.

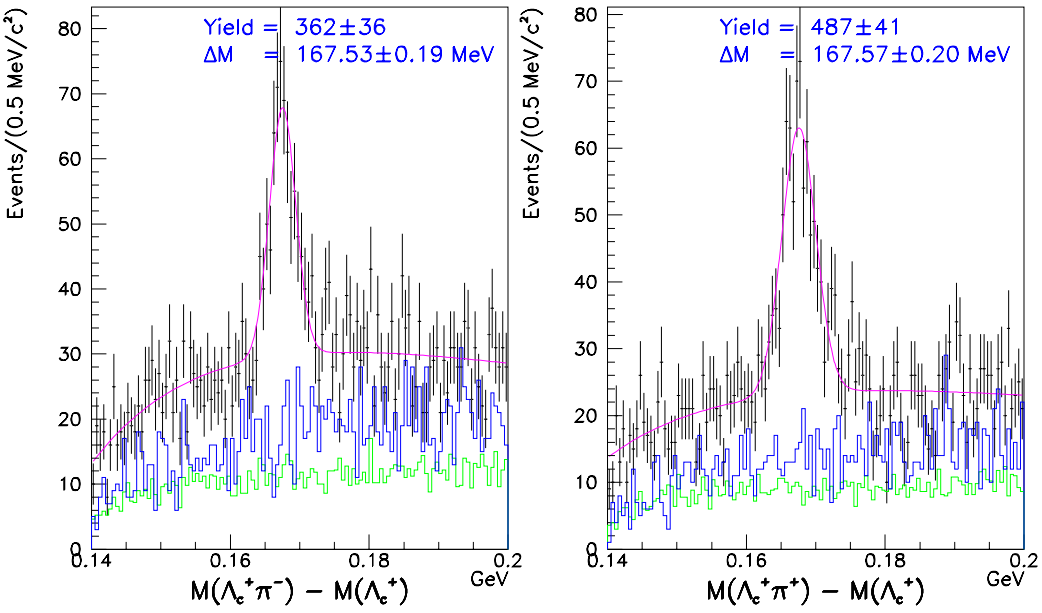

Figure 6.3: Mass difference distributions for $m_{\Sigma_c^0} - m_{\Lambda_c^+}$ and $m_{\Sigma_c^{++}} - m_{\Lambda_c^+}$. The lowest histograms are from the sidebands in Figure 6.1 scaled appropriately. The middle histograms are those formed by combining Λ_c^+ candidates with pions from the previous event.

6.3.2 Σ_c^0 and Σ_c^{++} reconstruction

The reconstruction of the Σ_c^0 and Σ_c^{++} is straightforward. Again **TRKFIT** and **DVERT** direction vectors are used and we require a good $\Lambda_c^+\pi^\pm$ vertex with a confidence level greater than 1%. We also require $\pi_{\rm con} > -4$ for the soft pion. We do not explicitly require the soft pion to be in the primary vertex found during the Λ_c^+ reconstruction.

In order to improve our resolution on the value of $m_{\Sigma_c} - m_{\Lambda_c^+}$, we employ the standard method of calculating mass differences. We use the reconstructed masses and momenta of the Λ_c^+ and the soft pion to calculate a mass for the Σ_c. We then subtract the reconstructed mass of the Λ_c^+ and report the mass difference. In addition to improving the mass resolution, this also removes the bulk of the systematic contributions related to calculating the mass of the Λ_c^+ and leaves only systematic contributions on the measurement of the soft pion momentum.

The resulting $\Sigma_c - \Lambda_c^+$ mass difference distributions and backgrounds are shown in Figure 6.3.

6.3.3 Σ_c^+ reconstruction

Reconstructing the Σ_c^+ requires that we find a soft π^0, which is combined with the Λ_c^+ candidate. Guided by the studies of the decays $D^{*0} \to D^0\pi^0$ and $D^{*+} \to D^+\pi^0$ in Appendix A, we reconstruct π^0's using the **PI0FIT** constraining method [63] which performs a fit that incorporates uncertainties in the positions as well as the energies of each photon shower in the electromagnetic calorimeters.[2] Again, guided by our earlier studies we choose the following π^0 cuts:

- IE-IE π^0's only
- π^0's are assumed to come from the primary vertex
- Minimum number of blocks per IE cluster: 2
- π^0's with both clusters of size 2 are rejected
- Mass of π^0 within 25 MeV/c^2 of the nominal mass
- $\chi^2(\pi^0) < 2.0$
- $E_{\rm cluster} > 1.0$ GeV
- Energy in the center block, $E_{\rm center} > 0.5$ GeV
- Fraction of energy in the center block, $f_{\rm center} > 0.35$

Some of these requirements warrant additional explanation. First, although IE-OE π^0's give a visible signal in $D^* \to D\pi^0$, the mass resolution and signal-to-noise are considerably degraded in comparison to IE-IE π^0's. Including these π^0's would dramatically increase $\Lambda_c^+\pi^0$ background without adding much Σ_c^+ signal. This precludes their use in reconstructing the Σ_c^+. Second, we use a loose (± 25 MeV/c^2) mass cut since soft π^0's have much worse resolution than π^0's with higher momentum. (A cut of 15 MeV/c^2 is typical for hard π^0's.) Finally, the "standard" π^0 reconstruction requires IE clusters with 4 or more blocks. However, many soft π^0's don't satisfy this requirement. These departures from the standard π^0 reconstruction algorithm are explored more fully in Appendix A.

We also arbitrate π^0's based on the χ^2 returned from the constraint routine. If two (or more) π^0's have a shared photon, we select the π^0 with the lowest χ^2. The performance of this arbitration on $D^* \to D\pi^0$ is shown in Appendix A.

Combining the π^0 candidates with Λ_c^+ candidates, we obtain the $\Lambda_c^+\pi^0$ mass difference distributions shown in Figure 6.4.

[2] In the low energy (soft π^0) regime this method is nearly indistinguishable from the energy constraint method of Nakano and Miyake [39].

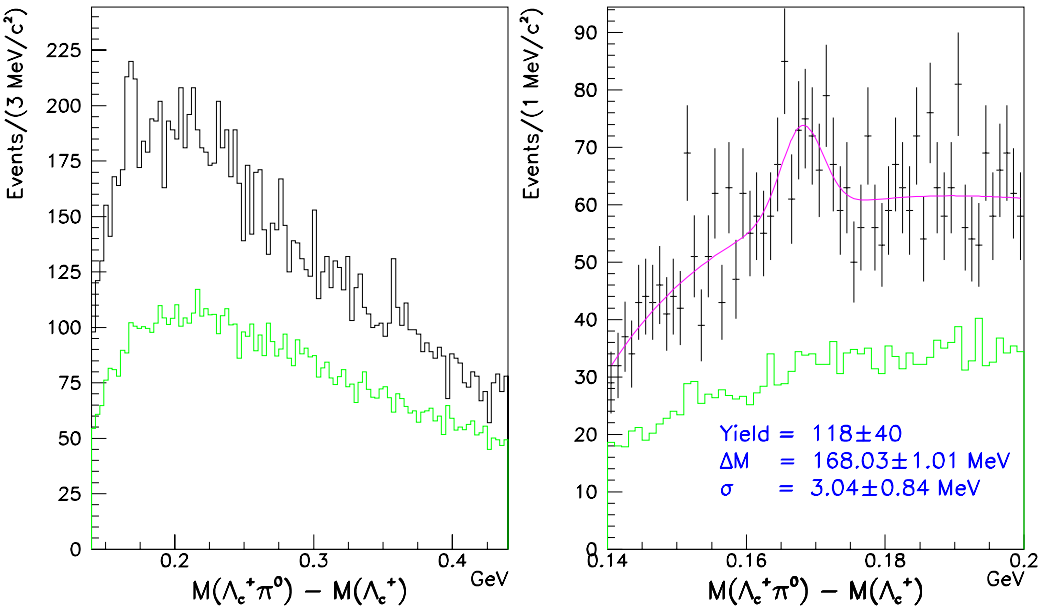

Figure 6.4: Mass difference distributions for $m_{\Sigma_c^+} - m_{\Lambda_c^+}$. The left histogram is included for illustrative purposes only; wider binning makes the Σ_c^+ more visible. The lower histograms in each plot are from the sidebands in Figure 6.2 scaled appropriately.

6.4 Determining Systematic Errors

6.4.1 Background contributions and fitting methods

There are two sources of combinatoric backgrounds. The first source is fake Λ_c^+ candidates combined with additional pions in the event. The second background is from real Λ_c^+ candidates combined with other pions from the production vertex. (Since the Σ_c has no measurable lifetime, pions from a real Σ_c decay are indistinguishable from other pions in the primary vertex.) A third background contribution comes from the $\Lambda_{c1}^{*+}(2625)$ which decays via $\Lambda_{c1}^{*+} \to \Lambda_c^+ \pi^+ \pi^-$ in what is measured to be a nearly pure 3-body decay [64, 65]. These pions combined with Λ_c^+ candidates result in a background in the region $\Delta M < 0.205$ GeV/c^2. The shapes of these three backgrounds are shown in Figure 6.5.

Fitting the overall $\Lambda_c^+ \pi$ distributions can therefore be quite difficult. We have explored two methods:

1. Fitting to fixed background shapes with floating normalizations.

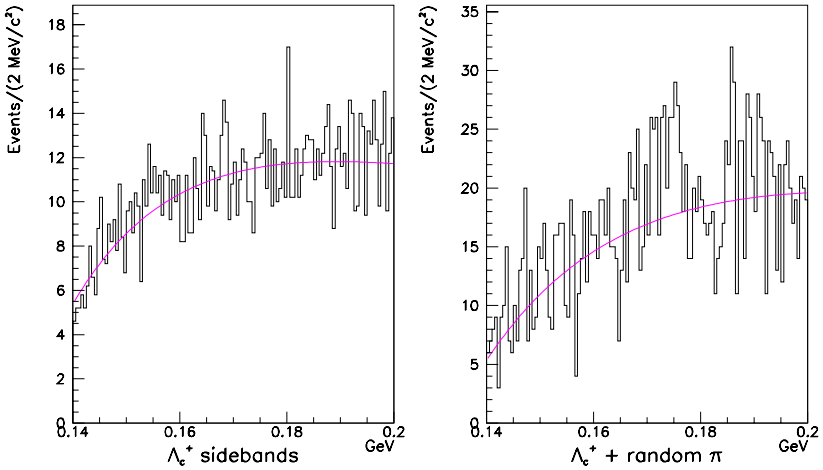

(a) Sidebands

(b) Random π

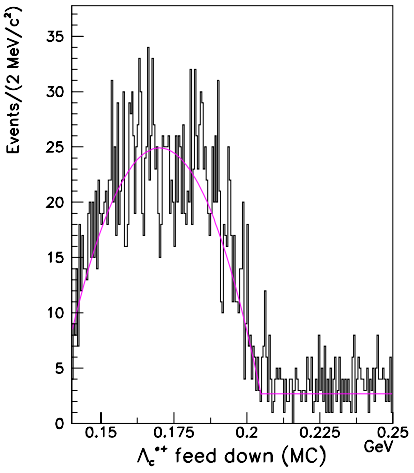

(c) $\Lambda_{c1}^{*+}(2625)$ feed down

Figure 6.5: $\Lambda_c^+\pi^+$ backgrounds. a) the background shape from the Λ_c^+ sidebands. b) the background shape from Λ_c^+ and $\pi^\pm$ from different events. c) the Monte Carlo generated shape for $\Lambda_{c1}^{*+}(2625)$ feed down into the Σ_c^{++} signal region plus a constant background.

2. Fitting to a free background shape.

In addition, for the Σ_c^0 and Σ_c^{++}, we can choose to include or ignore the contribution from $\Lambda_{c1}^{*+}(2625)$ feed down. This gives us four (two[3] in the case of Σ_c^+) different choices of fitting method, which help determine possible fit related systematics.

In fitting the Σ_c mass peaks, we use a simple Gaussian function. This is not technically correct since we have shown that these states have a measurable width as detailed in Chapter 7. However, for determining the mass of a state, a Gaussian fit is adequate.

To fit with fixed background shapes, we fit both the distribution from the Λ_c^+ sidebands, shown in Figure 6.5(a), and the distribution formed by combining a Λ_c^+ from one event and a pion from the previous event, shown in Figure 6.5(b), to a phase space function of the form $N(1+\alpha(\Delta M - m_\pi)\Delta M^\beta)$. ($\Delta M$ is $M(\Lambda_c^+\pi) - M(\Lambda_c^+)$, the mass difference.) N, α, and β are allowed to vary freely in fitting each background component. We then fit the signal distribution to

$$N_1(1+\alpha_1(\Delta M - m_\pi)\Delta M^{\beta_1}) + N_2(1+\alpha_2(\Delta M - m_\pi)\Delta M^{\beta_2}) + \text{Gaussian} \qquad (6.5)$$

where N_1 and N_2 are allowed to vary freely while α and β are fixed to the values previously found from the background distributions.

To fit with a "free" background, we fit the signal distribution to

$$N(1+\alpha(\Delta M - m_\pi)\Delta M^\beta) + \text{Gaussian} \qquad (6.6)$$

and allow N, α, β, and all parameters associated with the Gaussian to vary freely.

In order to determine the contribution from $\Lambda_{c1}^{*+}(2625)$ feed down, we make an estimate of the contamination using Monte Carlo. We generate a sample of $\Lambda_{c1}^{*+}(2625) \to \Lambda_c^+\pi^+\pi^-$ decays and apply both the Λ_{c1}^{*+} and the Σ_c^0 and Σ_c^{++} reconstructions. The result of the Σ_c reconstruction, shown in Figure 6.5(c), is the contamination from $\Lambda_{c1}^{*+}(2625)$ feed down plus random combinatorics. We fit this distribution to the function

$$A_{\rm MC}(1 - a(\Delta M - b)^2) + C_{\rm BG} \qquad (6.7)$$

where the quadratic term (the contamination) is restricted to the range $\Delta M < 0.205$ GeV/c^2. $C_{\rm BG}$ is a constant representing the random combinatoric background. The value of $A_{\rm MC}$ represents the amplitude, or height, of the feed down contribution in Monte Carlo. In order to estimate this contribution in the data, we normalize to Monte Carlo. We assume that the relative reconstruction efficiencies for $\Lambda_c^+\pi^\pm$ and

[3] To model the random π component of the background for Σ_c^+ events, we use charged, not neutral, random pions. The momentum spectra of charged and neutral pions will most likely differ. But, this is a good check on the fit, regardless.

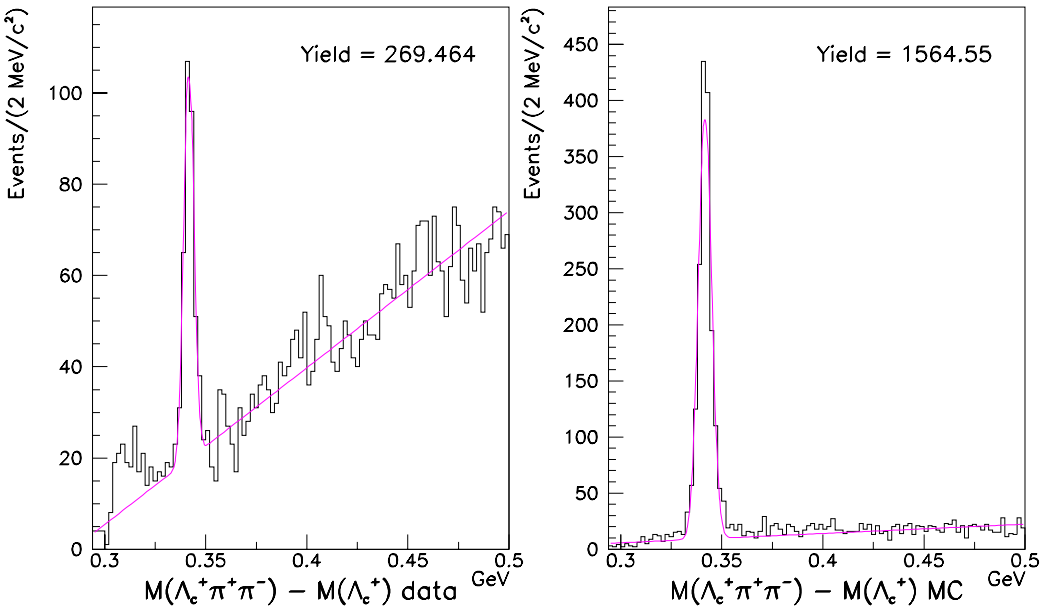

Figure 6.6: $\Lambda_{c1}^{*+}(2625)$ signals from data and Monte Carlo used to calculate the $\Lambda_{c1}^{*+}(2625)$ feed down contribution. The $\Lambda_{c1}^{*+}(2593)$ (which is not fitted) is evident in the data shown on the left. Monte Carlo is shown on the right.

$\Lambda_c^+\pi^+\pi^-$ are the same in data and Monte Carlo so that

$$\frac{A_{\rm data}}{A_{\rm MC}} = \frac{Y(\Lambda_{c1}^{*+})_{\rm data}}{Y(\Lambda_{c1}^{*+})_{\rm MC}} \tag{6.8}$$

where Y is the fitted $\Lambda_{c1}^{*+}(2625)$ yield. We then solve for the amplitude of the Λ_{c1}^{*+} feed down in the data:

$$A_{\rm data} = A_{\rm MC} \times \frac{Y(\Lambda_{c1}^{*+})_{\rm data}}{Y(\Lambda_{c1}^{*+})_{\rm MC}}\,. \tag{6.9}$$

We use identical cuts on the Λ_c^+ and soft pion(s) in all four reconstructions (Σ_c and Λ_{c1}^{*+} for Monte Carlo and data). To include the $\Lambda_{c1}^{*+}(2625)$ contribution into the signal distribution, we fix a and b in Equation (6.7) to their fit values, fix $A_{\rm data}$ to the calculated value, and add this contribution to Equation 6.5 or 6.6. The data and Monte Carlo $\Lambda_{c1}^{*+}(2625)$ signals used to calculate this contribution, or shape, are shown in Figure 6.6.

For the Σ_c^0 and Σ_c^{++}, we find that all four of these fitting methods give very close agreement for the values of ΔM as shown by the first four points of Figure 6.7.

For the Σ_c^+ the two fit values (fixed and free backgrounds) also agree very closely, giving a systematic of only 0.01 MeV/c^2.

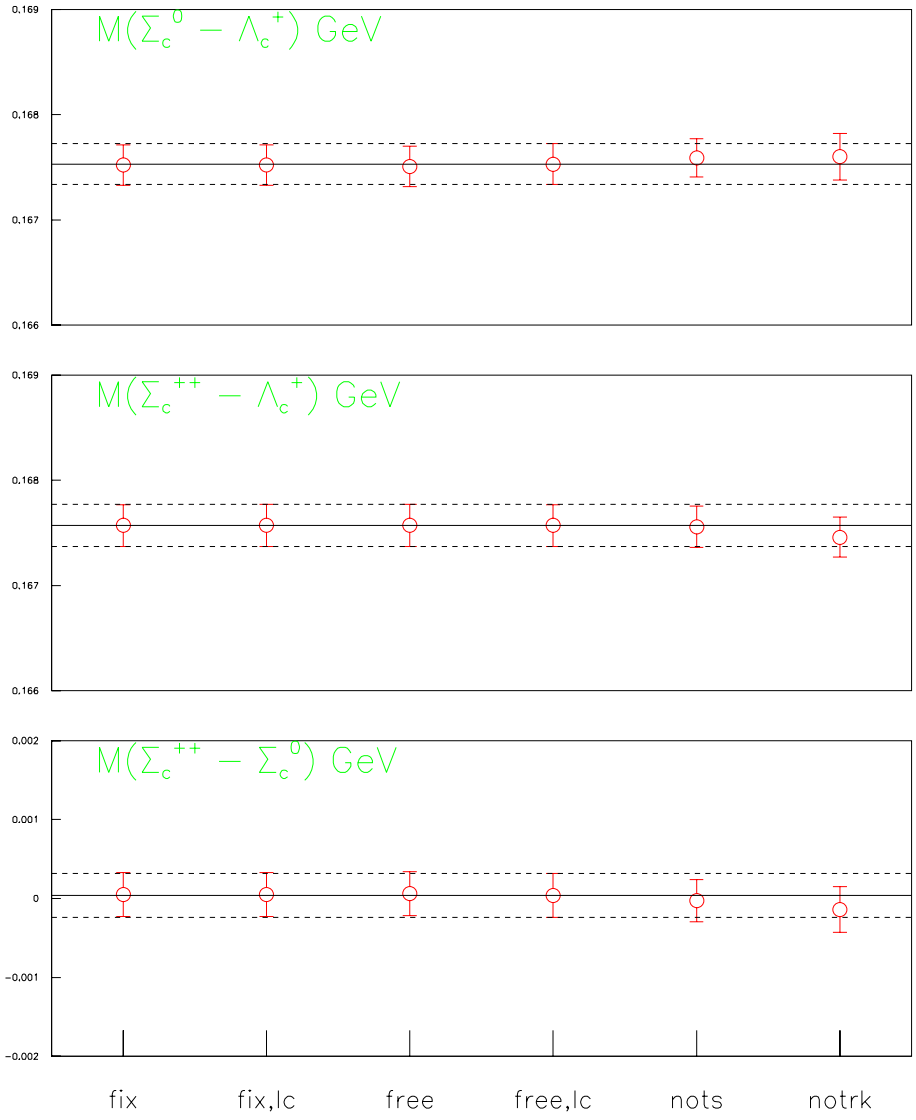

Figure 6.7: Σ_c^0 and Σ_c^{++} systematic errors from fitting and reconstruction methods. The three plots are respectively, the values of $m_{\Sigma_c^0} - m_{\Lambda_c^+}$, $m_{\Sigma_c^{++}} - m_{\Lambda_c^+}$, and $m_{\Sigma_c^{++}} - m_{\Sigma_c^0}$. The first four points are values obtained using fixed background shapes with floating normalizations ('fix'), a free parameter phase space background fit ('free'), and including ('lc') or ignoring the $\Lambda_{c1}^{*+}(2625)$ feed down. The fifth and sixth points are obtained by using **TRACCE** vectors and not using **TRKFIT** respectively. The solid and dashed lines are our measurement and statistical errors.

6.4.2 Reconstruction methods

We check the stability of our Σ_c^0 and Σ_c^{++} measurements under different reconstruction methods in two ways. First, we use the standard direction vectors instead of the improved **DVERT** vectors. We see no appreciable systematic due to the choice of direction vectors, as illustrated by the 'nots' (no target silicon) point in Figure 6.7.

As a second check, we use the standard momentum values instead of the **TRKFIT** values. This does give a systematic error. In fact it is the dominant error in this study of reconstruction and fitting methods, as evidenced by the 'notrk' point in Figure 6.7.

Neither of these checks apply to the Σ_c^+ case since there is no tracking information for the π^0.

6.4.3 Systematic reconstruction biases

As a check on the $\Lambda_c^+\pi^\pm$ reconstruction code, we use Monte Carlo to look for a systematic difference between generated and reconstructed quantities. This study suggests that there is a discrepancy of about 0.1 MeV/c^2 between the generated and reconstructed $\Sigma_c - \Lambda_c^+$ mass differences. There is no evidence for a systematic shift in the $\Sigma_c^{++} - \Sigma_c^0$ mass difference. Figure 6.8 shows the reconstructed Σ_c mass difference distributions for Monte Carlo generated $\Sigma_c \to \Lambda_c^+\pi$ decays. The input and recovered values are summarized in Table 6.4.

Table 6.4: Differences between generated and reconstructed parameters in $\Lambda_c^+\pi^\pm$ Monte Carlo and those reconstructed by the analysis and fitting programs. Mass differences have units of MeV/c^2.

Quantity	Generated	Reconstructed	Difference
$m_{\Sigma_c^0} - m_{\Lambda_c^+}$	167.54	167.44 ± 0.02	0.10 ± 0.02
$m_{\Sigma_c^{++}} - m_{\Lambda_c^+}$	167.59	167.51 ± 0.02	0.08 ± 0.02
$m_{\Sigma_c^{++}} - m_{\Sigma_c^0}$	0.05	0.07 ± 0.03	-0.02 ± 0.03

At this time, an accurate Monte Carlo simulation of π^0's does not exist, so we are unable to make a similar check on the Σ_c^+.

6.4.4 Effect of the overall mass scale uncertainties

If the momentum scale is systematically incorrect, the mass scale will also be systematically wrong. For charged particles, this effect can be caused by an incorrect

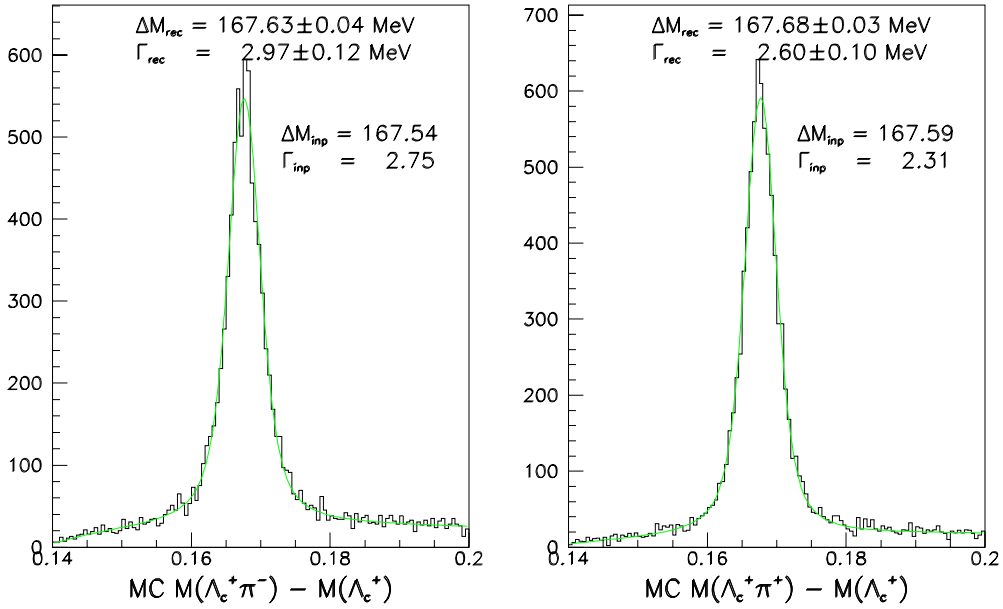

Figure 6.8: Reconstructed Monte Carlo distributions for generated Σ_c^{++} and Σ_c^0. Input and reconstructed parameters are listed.

knowledge of the magnetic field, systematic problems in understanding tracking systems, or an overall scaling of the geometry of the experiment. In reconstructing π^0's, a scaling of the geometry is the most likely cause of a systematic error. By measuring the $\Sigma_c - \Lambda_c^+$ mass differences, we remove these effects on the measurement of the Λ_c^+ mass. However, a small systematic can survive due to problems in the π momentum calculation.

Soft pion momentum (Σ_c^0 and Σ_c^{++})

Currently there is a small problem with momentum determination in the spectrometer. This causes the masses of states to be measured on $\mathcal{O}(0.1\%)$ too high; the exact value depends on the kinematics of the decay. This will be corrected in the future, but for now we include this as a systematic effect. In order to assess the magnitude of this effect, we measure this shift for several prominent decay modes. (We expect that the Σ_c will be most similar to the kinematically similar D^*.) These measurements are presented in Table 6.5. The D and D^* results are from 25% of the data sample while the $\Lambda_c^+ \to pK^-\pi^+$ signal is from the whole data sample.

As a reasonable estimate, we choose a relative error ($\Delta M/M$) for the Σ_c measurements of 0.15% which gives an error on the mass difference of 0.25 MeV. This error is likely correlated with the **TRKFIT** error reported in Section 6.4.2 so that the true systematic is probably being inflated by considering the same problem twice. Also, this effect

Table 6.5: Mass errors for high statistics decays. FOCUS values and PDG [4] values are compared for several high statistics modes. Masses are in MeV/c^2.

Mode	PDG Value	FOCUS Value	ΔM	$\Delta M/M$
$D^{*+} \to D^0\pi^+$ [a]	145.40 ± 0.03	145.50 ± 0.01	0.10 ± 0.03	6.9×10^{-4}
$D^0 \to K^-\pi^+$	1864.6 ± 0.50	1867.55 ± 0.08	3.0 ± 0.50	1.6×10^{-3}
$D^+ \to K^-\pi^+\pi^+$	1869.3 ± 0.50	1871.69 ± 0.06	2.4 ± 0.50	1.3×10^{-3}
$D^0 \to K^-\pi^+\pi^+\pi^-$	1864.6 ± 0.50	1866.87 ± 0.03	2.3 ± 0.50	1.2×10^{-3}
$\Lambda_c^+ \to pK^-\pi^+$	2284.9 ± 0.60	2288.85 ± 0.11	4.0 ± 0.60	1.8×10^{-3}

[a] The value quoted is the $D^{*+} - D^0$ mass difference.

is negligible in the measurement of $m_{\Sigma_c^{++}} - m_{\Sigma_c^0}$ since both masses are shifted by essentially the same amount.

π^0 momentum (Σ_c^+)

The π^0 constraining method should remove any systematic effect due to the energy calibration of the electromagnetic calorimeter. However, a systematic effect can survive if the geometry of the calorimeter is incorrect.

To explore any possible remaining systematic, we reconstruct the decays $D^{*0} \to D^0\pi^0$ and $D^{*+} \to D^+\pi^0$ where the D mesons decay via the golden modes $D^0 \to K^-\pi^+$, $D^+ \to K^-\pi^+\pi^+$, and $D^0 \to K^-\pi^+\pi^+\pi^-$. We then compare the measured mass differences with the PDG [4] values. The results of this study are shown in Figure 6.9. We see that our measurements of the D^* masses are accurate to within 0.1 MeV/c^2. Taking into account the larger phase space available in $\Sigma_c^+ \to \Lambda_c^+\pi^0$, we estimate our systematic error on $m_{\Sigma_c^+}$ to be 0.3 MeV/c^2 or less.

6.4.5 Mass differences as a function of L/σ_L

We have seen a sizeable systematic problem in the Σ_c^0 distributions reconstructed with low L/σ_L Λ_c^+ candidates. This effect is illustrated in Figure 6.10; the measurement of the Σ_c^0 mass difference doesn't become stable until $L/\sigma_L > 6$. For this reason we choose events with $L/\sigma_L > 6$, a rather tight detachment cut.

Applying cuts of $\pi_{\rm con} > 0$ for the soft pion and $L/\sigma_L > 3$ gives a similar signal-to-background ratio for the Σ_c^0 as when we require $L/\sigma_L > 6$. With this cut the systematic effect at low L/σ_L is not present. This leads us to conclude that the

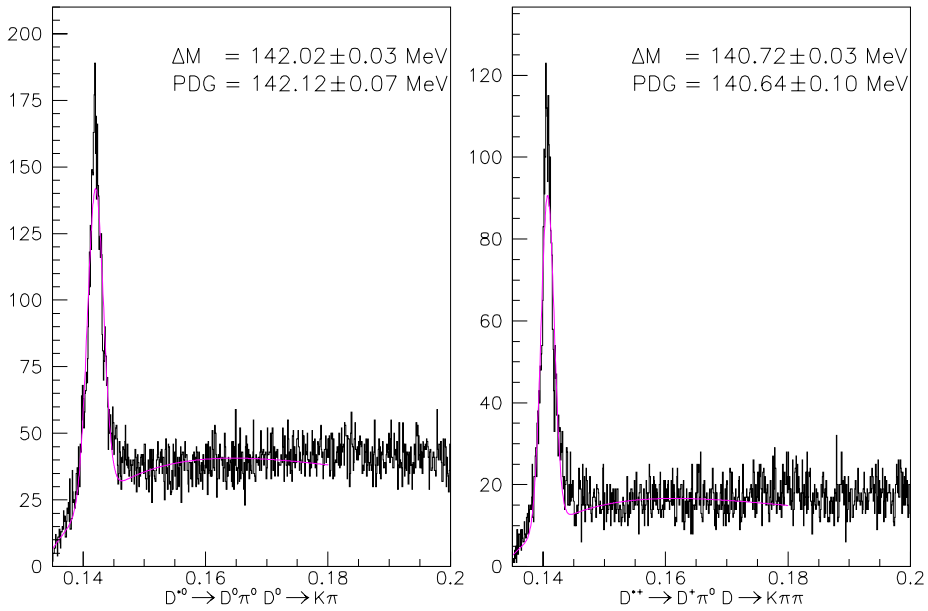

Figure 6.9: $D^{*0} \to D^0\pi^0$ and $D^{*+} \to D^+\pi^0$ mass differences.

apparent systematic effect at low L/σ_L is not due to any physics, but instead may be caused by fitting Σ_c distributions with large amounts of background.

6.4.6 Systematic errors from "split samples"

In order to assess the other systematic errors present, we use a "split sample" technique of estimating systematic errors. In these studies, we divide the data into two roughly equal portions based on kinematic variables or running conditions and perform our measurement on each statistically independent sub-sample. We choose variables where one might expect, either through reconstruction methods or changes in running conditions, to introduce a bias in the measured quantity.

Σ_c^0 and Σ_c^{++} split samples

We perform studies of the Σ_c^0 and Σ_c^{++} masses by splitting the sample based on several criteria:

- Particle/anti-particle

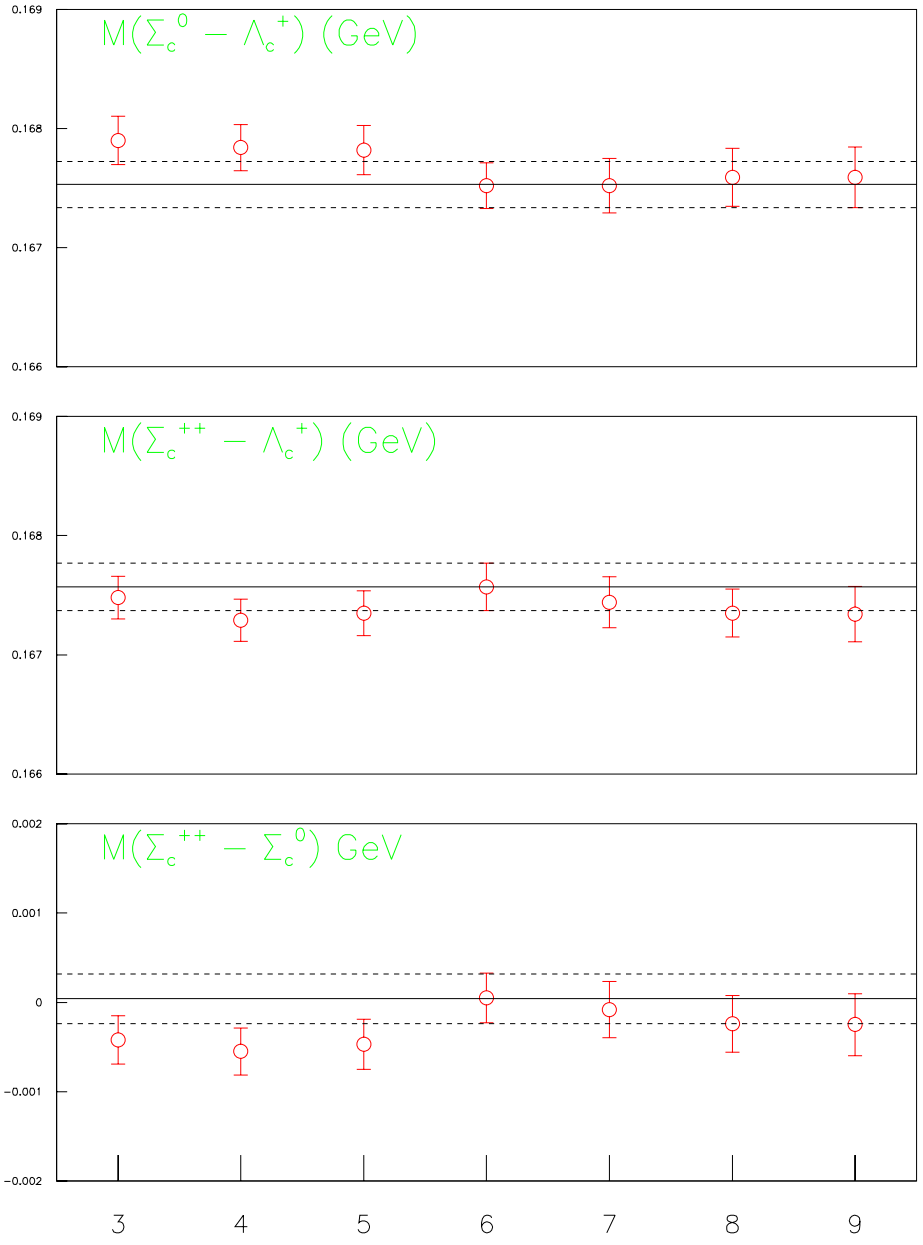

Figure 6.10: Σ_c^0 and Σ_c^{++} mass differences as a function of the L/σ_L cut. Stable results are not reached until $L/\sigma_L > 6$. The solid and dashed lines are the measurement and statistical errors.

- Pre/post Target Silicon runs[4]
- L/σ_L
- Λ_c^+ momentum $p(\Lambda_c^+)$
- Soft pion momentum $p(\pi_s)$

The only systematic effect originates from splitting the data according to the momentum of the soft pion, $p(\pi_s)$, and only in the case of the Σ_c^0. This effect is illustrated by the last two points in the top plot in Figure 6.11. In this case, a systematic error of 0.21 MeV/c^2 survives.

Σ_c^+ split samples

For the Σ_c^+, we are able to check split samples of the following quantities:

- Particle/anti-particle
- Pre/post Target Silicon runs
- L/σ_L
- Λ_c^+ momentum $p(\Lambda_c^+)$
- π^0 mass[5]

The split sample fitted values for the Σ_c^+ are shown in Figure 6.12. Although the fitted values do vary substantially, none of the effects studied pass the requirement of being statistically significant variations since the statistical error on the mass difference is quite large.

6.4.7 Total systematic error calculations

We calculate all our systematic errors using the methods outlined in Appendix B. For the Σ_c^0 and Σ_c^{++} mass differences the systematic errors are tabulated in Table 6.6.

[4]Run 9750 is the first run in which the Target Silicon information is used by the reconstruction. This run is picked as the dividing line. This dividing line roughly corresponds to the dividing line between 1996 & 1997 data. All three terms are used interchangeably.

[5]We split the sample on a run-by-run basis according to the average π^0 mass reconstructed for that run during the initial data reconstruction. This separates the data into two samples, one where the calorimeter energy calibration was, on average, high and another where the energy calibration was low.

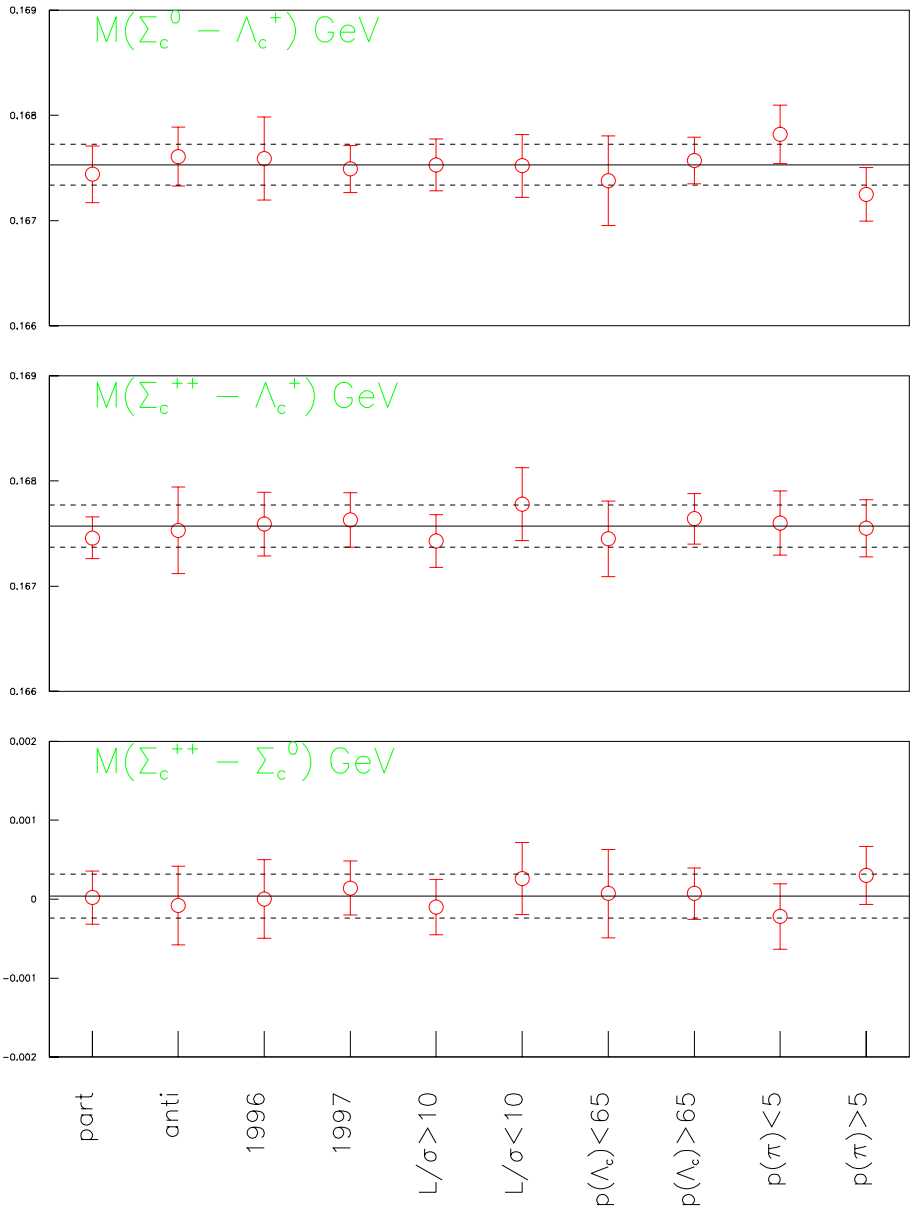

Figure 6.11: Σ_c^0 and Σ_c^{++} systematic errors from split samples. The solid and dashed lines are the measurement and statistical errors. Points 1 & 2 are for particle and antiparticle separately. Points 3 & 4 are for runs less than and greater than 9750. Points 5 & 6 split the sample at $L/\sigma_L = 7$. Points 7 & 8 split the sample in Λ_c^+ momentum at 70 GeV/c. Points 9 & 10 split the sample in soft pion momentum at 5 GeV/c.

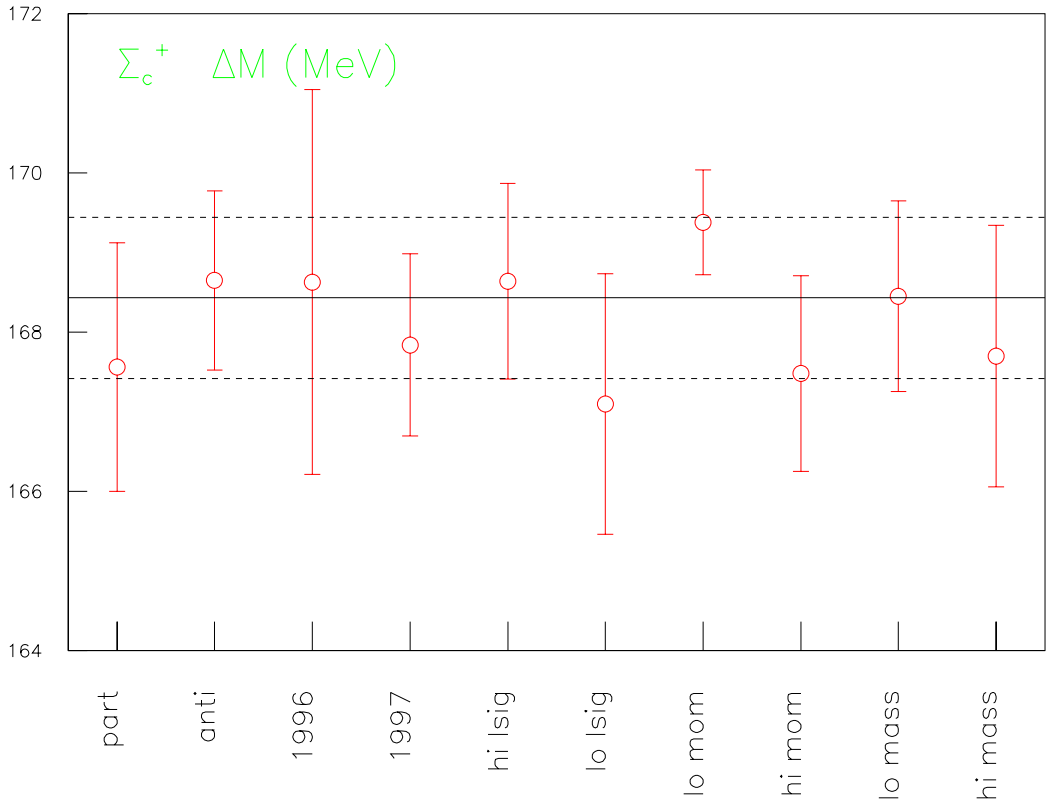

Figure 6.12: Summary of Σ_c^+ split sample systematic errors. The solid and dashed lines are the measurement and statistical errors. Points 1 & 2 are for particle and antiparticle separately. Points 3 & 4 are for runs less than and greater than 9750. Points 5 & 6 split the sample at $L/\sigma_L = 6$. Points 7 & 8 split the sample in Λ_c^+ momentum at 55 GeV/c. Points 9 & 10 split the sample in π^0 mass for each run.

For the Σ_c^+, the systematic errors are tabulated in Table 6.7. The totals quoted are the quadratic sums of the individual errors.

6.5 Final Values and Comparisons

Σ_c^0 and Σ_c^{++}: Considering all the statistical and systematic errors, we measure $m_{\Sigma_c^0} - m_{\Lambda_c^+} = 167.54 \pm 0.19 \pm 0.34\,\mathrm{MeV}/c^2$, $m_{\Sigma_c^{++}} - m_{\Lambda_c^+} = 167.59 \pm 0.20 \pm 0.27\,\mathrm{MeV}/c^2$, and $m_{\Sigma_c^{++}} - m_{\Sigma_c^0} = 0.05 \pm 0.28 \pm 0.09$ MeV/c^2 where the first error is statistical and the second is systematic. These measurement are presented and compared with other measurements [55–58, 60] and the PDG [4] average in Figure 6.13. These values are completely consistent with the E791 [56] values. The FOCUS and CLEO II [55] values for $m_{\Sigma_c^{++}} - m_{\Lambda_c^+}$ differ by 1.2σ and the corresponding values for $m_{\Sigma_c^{++}} - m_{\Sigma_c^0}$ differ

Table 6.6: Summary of systematic errors for $m_{\Sigma_c^0} - m_{\Lambda_c^+}$, $m_{\Sigma_c^{++}} - m_{\Lambda_c^+}$, and $m_{\Sigma_c^{++}} - m_{\Sigma_c^0}$.

Source	Mass difference (MeV/c^2)		
	$\Sigma_c^0 - \Lambda_c^+$	$\Sigma_c^{++} - \Lambda_c^+$	$\Sigma_c^{++} - \Sigma_c^0$
Fitting	0.04	0.05	0.09
Momentum scale	0.25	0.25	0.00
Monte Carlo bias	0.10	0.10	0.00
Λ_c/Λ_c	0.00	0.00	0.00
L/σ_L	0.00	0.00	0.00
1996/1997	0.00	0.00	0.00
$p(\Lambda_c)$	0.00	0.00	0.00
$p(\pi_s)$	0.21	0.00	0.00
Total	0.34	0.27	0.09

Table 6.7: Summary of systematic errors for $m_{\Sigma_c^+} - m_{\Lambda_c^+}$.

Source	Mass difference
	$\Sigma_c^+ - \Lambda_c^+$
Fitting	0.01 MeV/c^2
Momentum scale	0.30 MeV/c^2
Λ_c/Λ_c	0.00 MeV/c^2
L/σ_L	0.00 MeV/c^2
1996/1997	0.00 MeV/c^2
$p(\Lambda_c)$	0.00 MeV/c^2
π^0 mass	0.00 MeV/c^2
Total	0.30 MeV/c^2

by 2.1σ. These measurements are compared with the CLEO II and E791 values in Table 6.8.

Table 6.8: Comparison of measurements of Σ_c^{++} and Σ_c^0 mass differences.

Experiment	Mass difference (MeV/c^2)		
	$\Sigma_c^{++} - \Lambda_c^+$	$\Sigma_c^0 - \Lambda_c^+$	$\Sigma_c^{++} - \Sigma_c^0$
CLEO II	$168.20 \pm 0.30 \pm 0.20$	$167.10 \pm 0.30 \pm 0.20$	$1.10 \pm 0.40 \pm 0.10$
FNAL-E791	$167.76 \pm 0.29 \pm 0.15$	$167.38 \pm 0.29 \pm 0.15$	$0.38 \pm 0.40 \pm 0.15$
FOCUS	$167.59 \pm 0.20 \pm 0.27$	$167.54 \pm 0.19 \pm 0.34$	$0.05 \pm 0.28 \pm 0.09$

Σ_c^+: In the Σ_c^+ analysis, we find $m_{\Sigma_c^+} - m_{\Lambda_c^+} = 168.03 \pm 1.01 \pm 0.30$ MeV/c^2 and $m_{\Sigma_c^+} - m_{\Sigma_c^0} = 0.49 \pm 1.03 \pm 0.45$ MeV/c^2. We add the systematic errors for the Σ_c^+ and Σ_c^0 in quadrature since these should be completely uncorrelated. These values are completely compatible with the CLEO II measurement, as shown in Table 6.9.

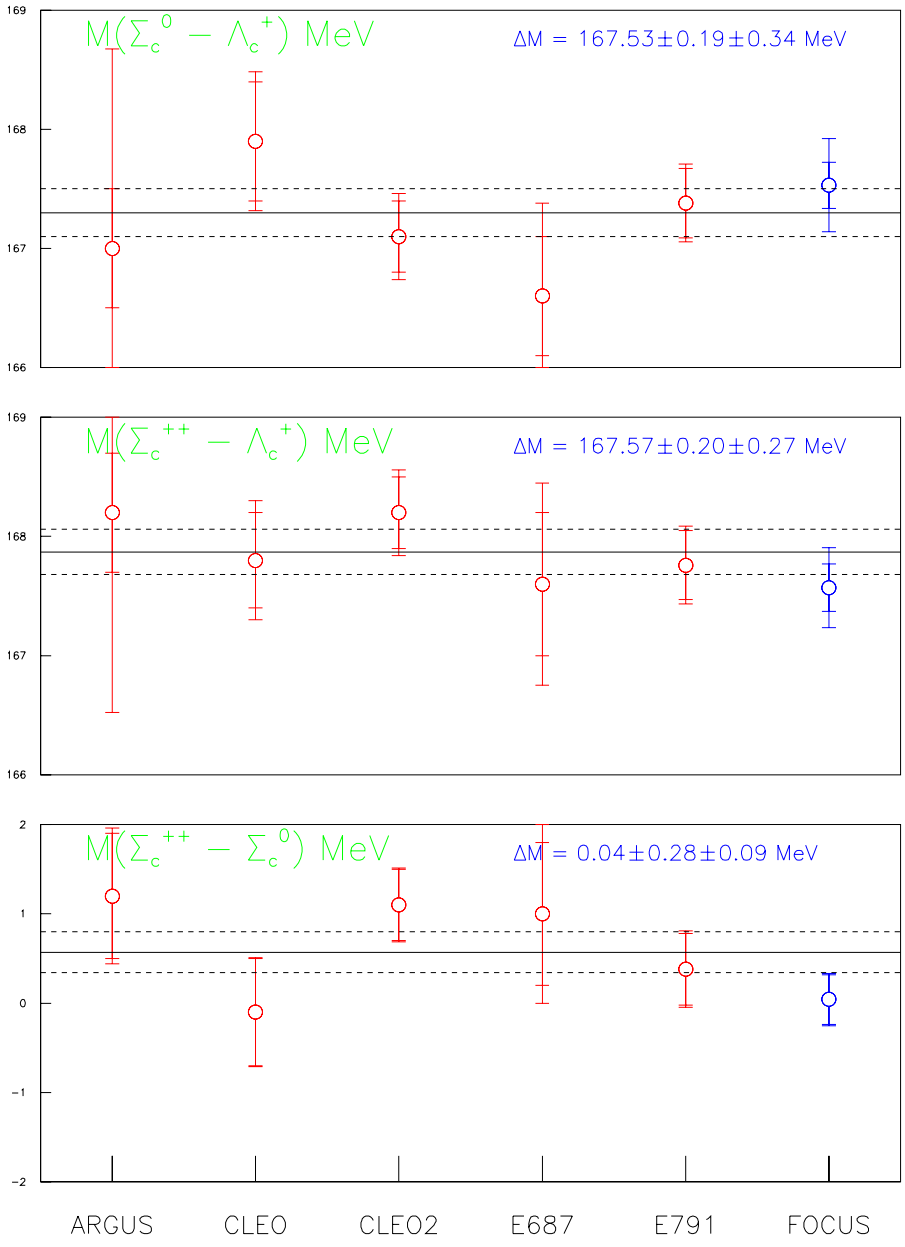

Figure 6.13: Final measurements of $m_{\Sigma_c^0} - m_{\Lambda_c^+}$, $m_{\Sigma_c^{++}} - m_{\Lambda_c^+}$, and $m_{\Sigma_c^{++}} - m_{\Sigma_c^0}$ and comparisons with other experiments. The FOCUS measurements are the last set of points; the solid and dashed lines are the PDG fit values.

Table 6.9: Comparison of measurements of Σ_c^+ mass differences.

	Mass difference (MeV/c^2)	
Experiment	$\Sigma_c^+ - \Lambda_c^+$	$\Sigma_c^+ - \Sigma_c^0$
CLEO II	$168.5 \pm 0.4 \pm 0.2$	$1.4 \pm 0.5 \pm 0.3$
FOCUS	$168.03 \pm 1.01 \pm 0.30$	$0.49 \pm 1.03 \pm 0.45$

6.6 Conclusions

The Σ_c^0 and Σ_c^{++} mass difference measurements presented here are competitive with the world's best measurements and will improve further when systematics due to the momentum scale are reduced. While the errors on the Σ_c^+ mass are larger than those from CLEO, a later analysis may be able to include other Λ_c^+ decay modes, thereby decreasing the statistical error. In order to reduce systematic uncertainties, it is instructive to have measurements of all three Σ_c mass differences from a single experiment.

Chapter 7

Σ_c^0 and Σ_c^{++} Width Measurements

In this chapter, we present preliminary measurements of $\Gamma(\Sigma_c^0)$ and $\Gamma(\Sigma_c^{++})$ which are compared with the existing theoretical predictions and a recent CLEO report [66]. We find $\Gamma(\Sigma_c^0) = 2.58 \pm 0.79^{+0.51}_{-0.55}$ MeV/c^2 and $\Gamma(\Sigma_c^{++}) = 2.53 \pm 0.77^{+0.51}_{-0.56}$ MeV/c^2. Low statistics and a width similar to the experimental resolution[1] combine to make this a challenging measurement. These results are obtained with a sample of 425 ± 55 $\Sigma_c^0 \to \Lambda_c^+ \pi^-$ decays and 540 ± 59 $\Sigma_c^{++} \to \Lambda_c^+ \pi^+$ decays.

Most theoretical predictions of $\Gamma(\Sigma_c)$ are in the 1–3 MeV/c^2 range, as shown in Section 7.1, which is in the measurement range of FOCUS. In Section 7.2 we show that a comparison of the FOCUS Monte Carlo and data suggests $\Gamma(\Sigma_c^0) \approx \Gamma(\Sigma_c^{++}) \approx \mathcal{O}(1 \text{ MeV}/c^2)$. This observation motivates further analysis. In Section 7.3 we discuss the reconstruction and simulation methods used in the analysis. In Section 7.4 we explain the measurement and fitting methods and present preliminary values with statistical errors. Section 7.5 is concerned with various sources of possible systematic errors. In Section 7.6 we present two mini–Monte Carlo studies which shed light on particular problems which may occur with the measurement.

7.1 Theoretical Predictions of Σ_c Widths

There have been several recent theoretical predictions for the widths of the Σ_c states; all of them predict $\Gamma(\Sigma_c)$ in the range 1–3 MeV/c^2. Several different theoretical models have been used, including the Relativistic Three Quark Model (RTQM), Heavy

[1] Throughout this chapter we strictly adhere to the terminology that "width" refers to Γ, the natural width of a state and "resolution" refers to the standard deviation, σ, in a Gaussian resolution function.

Hadron Chiral Perturbation Theory (HHCPT), and the Light Front Quark Model (LFQM).

In both the Relativistic Three Quark Model [67, 68] and the Light Front Quark Model [69], the partial decay width for $\Sigma_c \to \Lambda_c^+ \pi$ is given by

$$\Gamma(\Sigma_c \to \Lambda_c^+ \pi) = g^2 I_1^2 \frac{|\vec{q}|^3}{6\pi} \frac{M_{\Lambda_c^+}}{M_{\Sigma_c}} \tag{7.1}$$

where g is a coupling constant, $I_1 \equiv I(6 \to 3^* + \pi) = 1$ for $\Sigma_c \to \Lambda_c^+ \pi$, is a group flavor factor for the transition. $|\vec{q}|$ is the pion momentum in the Σ_c rest frame. In the LFQM, $g = 6.81$ GeV^{-1}; RTQM uses $g = 8.88$ GeV^{-1}.

The decay rate is parameterized a little differently in Heavy Hadron Chiral Perturbation Theory [70, 71]:

$$\Gamma(\Sigma_c \to \Lambda_c^+ \pi) = \frac{h_1^2}{f^2} \frac{|\vec{q}|^3}{6\pi} \frac{M_{\Lambda_c^+}}{M_{\Sigma_c}} \tag{7.2}$$

where $h_1 = 1.0$ is an independent coupling constant and $f \simeq 132$ MeV is the pion decay constant.

Rosner [72] performs his calculation by assuming that the decay rate

$$\Gamma(B \to B'\pi) = C\,|(\pi B'|B)|^2\,|\vec{q}|^3 \tag{7.3}$$

where $(\pi B'|B)$ are isoscalar factors for the decay. Rosner assumes that C is constant for all baryon decays and uses the value of $\Gamma(\Sigma^* \to \Lambda\pi)$ to find, using ratios, the values of $\Gamma(\Sigma_c \to \Lambda_c^+ \pi)$.

These models predict partial widths, but $\Sigma_c \to \Lambda_c^+ \pi$ is the only allowed strong decay mode. (Although it doesn't affect the present measurement, the partial width of $\Sigma_c^+ \to \Lambda_c^+ \gamma$ is predicted to be very small.) As a result, we safely take the partial width as the total width for each state. The resulting predictions from the models are shown in Table 7.1.

Table 7.1: Predicted Σ_c widths from various theoretical models. All units are MeV/c^2.

Author	$\Gamma(\Sigma_c^0)$	$\Gamma(\Sigma_c^{++})$	Method
Ivanov [67, 68]	2.65 ± 0.19	2.85 ± 0.19	RTQM
Tawfig [69]	1.57	1.64	LFQM
Huang [70]	2.4	2.5	HHCPT
Pirjol [71]	1.0–3.0	1.1–3.1	HHCPT
Rosner [72]	1.32 ± 0.04	1.32 ± 0.04	Ratios

Direct measurements of the Σ_c widths are important since most of the current the-

oretical models predict the widths of charmed baryons by extrapolating from the hyperon widths. Accurate measurements of the Σ_c or Σ_c^* widths will enable more accurate predictions of the widths of other excited charm states.

7.2 First Evidence for a Non-zero Σ_c Width

At present the FOCUS collaboration is in the process of changing its scattering and absorption model to a method which combines Moliere [73–75] scattering with a charm absorption cross section which is half that of the neutron [76, 77]. This model is used in the analyses in this thesis, but minor changes are possible in the near future. We find that this model gives much better agreement between the experimental resolution and the Monte Carlo prediction that what was obtained using the previous Rossi [78] scattering model.

In this case the agreement between the experimental resolution and the resolution in the Monte Carlo is very good. Of special interest is the decay $D^{*+} \to D^0\pi^+$, which is kinematically similar to the decays under study in this chapter ($\Sigma_c^{++} \to \Lambda_c^+\pi^\pm$). Comparisons of the mass resolution for the Golden Mode decays are shown in Figure 7.1. The comparison for $D^{*+} \to D^0\pi^+$ is shown in Figure 7.2. (Since $\Gamma(D^{*+}) < 0.131$ MeV/c^2 at the 90% confidence level, the natural width will have little effect on the apparent experimental resolution measured in FOCUS.) For each of these well measured decay modes, the data and Monte Carlo agree on the resolution to within 3%.

In comparison, fits of the Σ_c states to Gaussian functions (as was done in the previous chapter) yield $\sigma \approx 2.3 \pm 0.2$ MeV/c^2 while the Monte Carlo prediction is $\sigma \approx 1.5$ MeV/c^2, as seen in Figure 7.4. This is strong evidence that the Σ_c widths are $\mathcal{O}(1$ MeV/$c^2)$, which should be measurable using the FOCUS data.

7.3 Event Selection and Reconstruction

In this analysis, we use several different data and Monte Carlo data sets in our measurements and studies:

- The Σ_c and Λ_c^+ data sample is the complete FOCUS data sample, as described in the previous chapters.
- The D and D^{*+} data sample is the same 25% sample used in Chapter 6 and Appendix A.

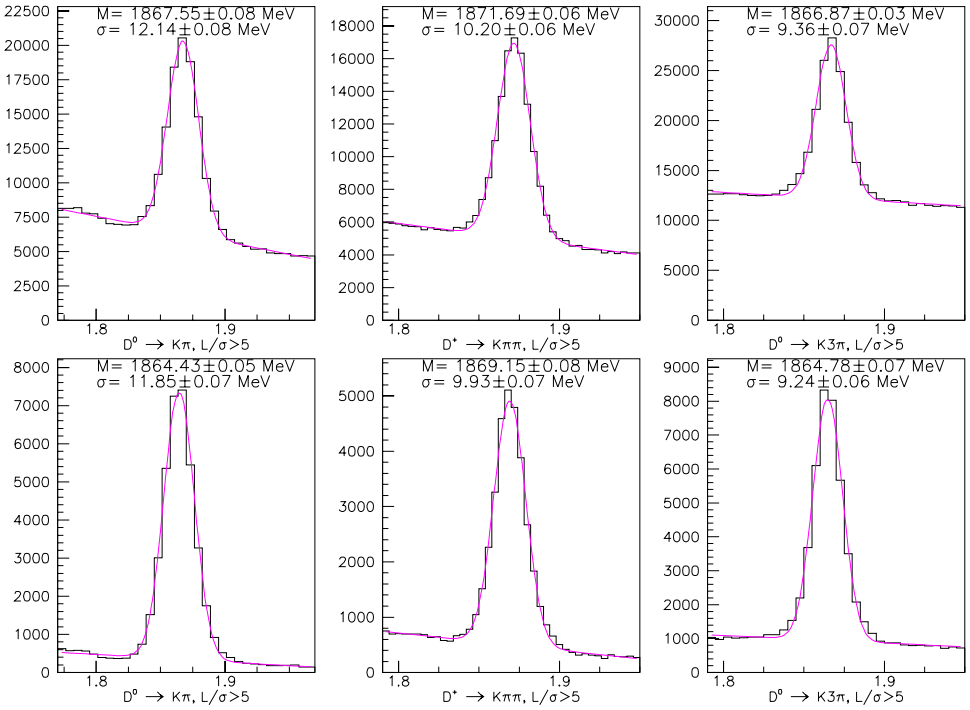

Figure 7.1: Comparison of Monte Carlo and data σ's for D^+ and D^0 Golden Mode decays. Data plots are on the top, Monte Carlo plots are on the bottom.

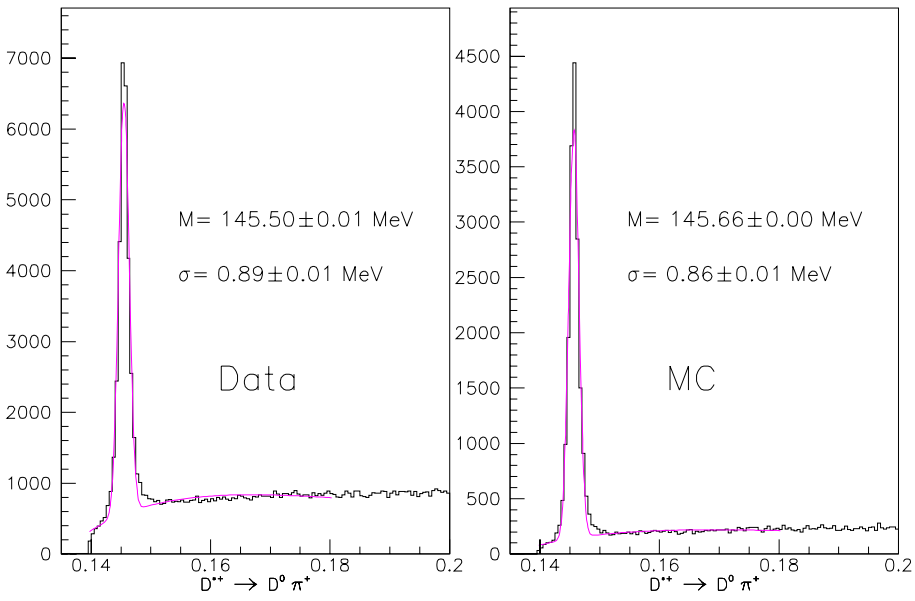

Figure 7.2: D^{*+} mass differences for data and Monte Carlo.

- The Σ_c Monte Carlo signals are "mode specific." Only generated events with a Σ_c are accepted and all final states are specified.

- The D and D^{*+} Monte Carlo signals are generated using $c\overline{c}$ Monte Carlo. Any event containing a charmed particle is accepted and all particles are allowed to decay according to the accepted branching ratios.

In reconstructing Λ_c^+ and Σ_c candidates, we use the same general reconstruction methods presented in previous chapters, but with minor changes in the cuts.

7.3.1 Λ_c^+ selection

We apply slightly less stringent cuts on $\Lambda_c^+ \to pK^-\pi^+$ candidates than those used in the Σ_c mass analysis. The cuts applied are:

- $\Lambda_c^+(L/\sigma_L) > 4.0$
- $t_{\rm life} < 10\tau_{\Lambda_c^+}$
- $p(\Lambda_c^+) > 40$ GeV/c
- CLP and CLS > 0.01
- $\Delta W(\pi p) > 4.0$
- $\Delta W(Kp) > 0.0$
- $\Delta W(\pi K) > 2.0$
- $\pi_{\rm con} > -6.0$
- The primary vertex is in the two most downstream targets

This target requirement is applied for two reasons. First, due to absorption and acceptance effects, only a small fraction of the reconstructed Σ_c events have a primary in the two upstream targets.[2] Second, the mass resolution for these events is severely degraded, so we lose nothing in the precision of the final measurement by discarding them. After applying all these cuts, the Λ_c^+ candidates which are used to reconstruct the Σ_c states is shown in Figure 7.3.

[2]While the loss in Λ_c^+ yield is significant, the corresponding loss in Σ_c yield is minimal. This is likely due to acceptance effects for the soft pion.

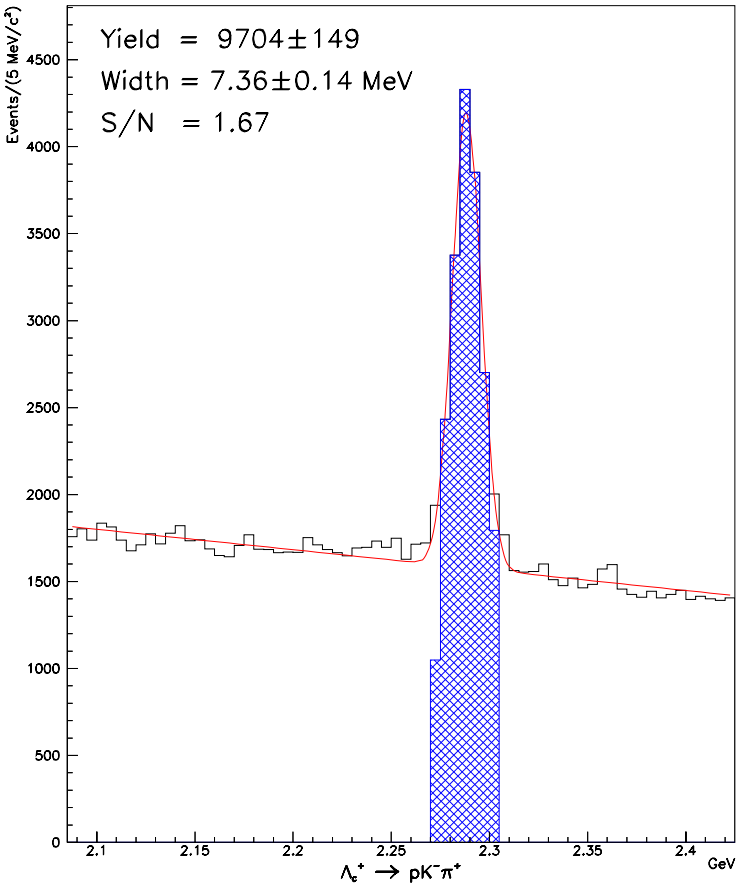

Figure 7.3: $\Lambda_c^+ \to pK^-\pi^+$ candidates used in the reconstruction of Σ_c^0 and Σ_c^{++}. The central hatched region shows the 2σ cut around the nominal Λ_c^+ mass.

7.3.2 Σ_c^0 and Σ_c^{++} reconstruction

The Σ_c reconstruction is nearly identical to the mass analysis case. We use the mass difference method and require a good $\Lambda_c^+\pi^\pm$ vertex. We use a slightly looser cut on the soft pion of $\pi_{\rm con} > -6.0$. (We used $\pi_{\rm con} > -4.0$ in the mass difference analysis.)

7.4 Measurement Method

The usual method for determining the width of a resonance is to fit to a Breit–Wigner function convoluted with a fixed-σ Gaussian function which represents the experimental resolution. Because the width of the Σ_c states is comparable to our experimental resolution and the statistics are limited, this method has certain instabilities as shown in Section 7.6.

In order to measure the natural widths of narrow states, we must accurately know the experimental resolution, $\sigma_{\rm res}$. To find the central value of Γ we assume $\sigma_{\rm MC}$, the estimate of the experimental resolution from the Monte Carlo is the true experimental resolution. Deviations from $\sigma_{\rm MC}$ are discussed in the next section.

Once we have determined the experimental resolution, we fit the Σ_c invariant mass distributions to the function

$$N(1 + \alpha(\Delta M - m_\pi)\Delta M^\beta) + \text{convoluted Breit–Wigner} \tag{7.4}$$

where N, α, and β are allowed to vary freely. The signal shape is a Breit–Wigner convoluted with a Gaussian function with $\sigma = \sigma_{\rm MC}$. The Breit–Wigner parameters are also allowed to vary. The resulting fits to the data are shown in Figure 7.4, as are the fits to the Monte Carlo used to extract the experimental resolution.

7.5 Systematic Errors

In this section, we explore various sources of systematic error on our measurement. Unless otherwise noted Monte Carlo distributions have been generated with $\Gamma(\Sigma_c) = 0$.

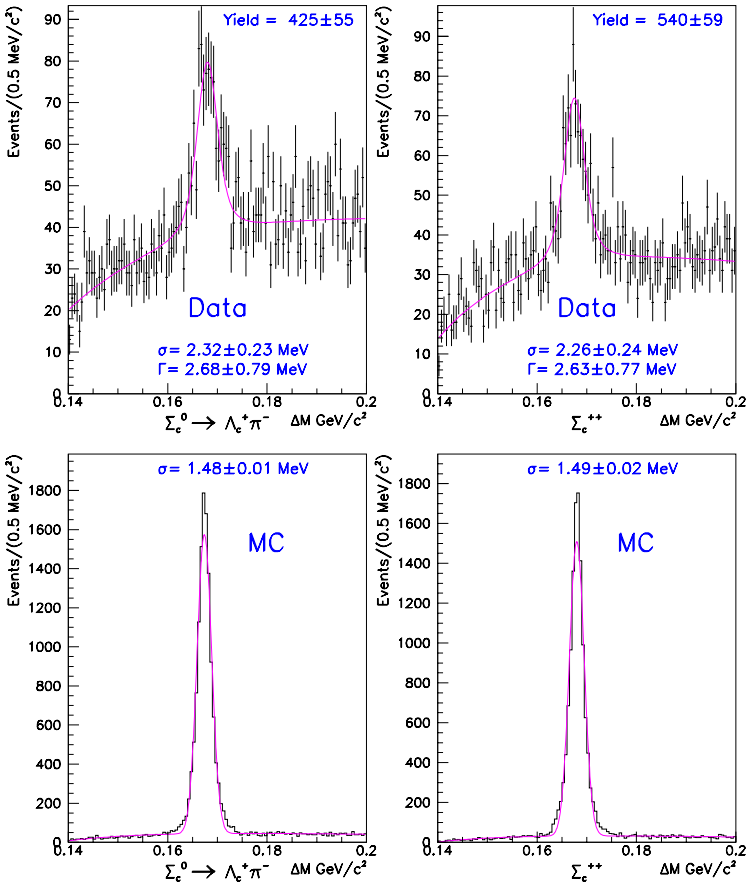

Figure 7.4: Σ_c mass differences for data and Monte Carlo. The top plots are for the data, the bottom Monte Carlo. The left plots show the Σ_c^0 and the right plots show the Σ_c^{++}. The Monte Carlo events are Σ_c^0 and Σ_c^{++} generated with $\Gamma(\Sigma_c) = 0$.

7.5.1 Agreement between Monte Carlo and data

While the Monte Carlo dependence of this analysis is primarily limited to assuming that the Monte Carlo accurately predicts the experimental resolution, it is necessary to make several tests to verify the correctness of the Monte Carlo and our fitting method.

Modeling experimental resolution: Any problem in the ability of the Monte Carlo to accurately predict the experimental resolution is a potential significant systematic effect. In Table 7.2, we present the measured and Monte Carlo predicted resolutions for several well measured decays (taken from Figures 7.1 & 7.2). From this study, we conclude that the Monte Carlo estimates of the experimental resolution are valid to 3%. We determine the effect such an error would have on our measurement by finding $\Gamma(\Sigma_c)$ for $\sigma_{\rm res} = (1.00 \pm 0.03) \cdot \sigma_{\rm MC}$. These values are shown in Table 7.3.

Table 7.2: Resolution from Monte Carlo and data for high statistics modes.

Mode	$\sigma_{\rm MC}$ (MeV/c^2)	$\sigma_{\rm data}$ (MeV/c^2)	$\sigma_{\rm MC}/\sigma_{\rm data}$
$D^{*+} \to D^0\pi^+$	0.86 ± 0.01	0.89 ± 0.01	0.97 ± 0.02
$D^0 \to K^-\pi^+$	11.85 ± 0.06	12.14 ± 0.08	0.98 ± 0.01
$D^+ \to K^-\pi^+\pi^+$	9.93 ± 0.06	10.20 ± 0.06	0.97 ± 0.01
$D^0 \to K^-\pi^+\pi^+\pi^-$	9.24 ± 0.06	9.36 ± 0.07	0.99 ± 0.01

Table 7.3: Effect on $\Gamma(\Sigma_c)$ of varying $\sigma_{\rm res}$. Values have units of MeV/c^2.

	Γ (MeV/c^2)			
State	$\sigma_{\rm res} = \sigma_{\rm MC}$	$\sigma_{\rm res} = 0.97 \cdot \sigma_{\rm MC}$	$\sigma_{\rm res} = 1.03 \cdot \sigma_{\rm MC}$	Systematic
Σ_c^0	2.58	2.68	2.47	$^{+0.10}_{-0.11}$
Σ_c^{++}	2.53	2.63	2.39	$^{+0.10}_{-0.14}$

Fit bias: By generating Monte Carlo events with our measured Σ_c widths and fitting the resulting Monte Carlo distributions using the convolution method, we can check for biases introduced by the reconstruction and fitting methods. The Monte Carlo reconstructed distributions are shown in Figure 7.5. It is apparent that we reconstruct a width about 0.2 MeV/c^2 larger than the input width, so we assign a systematic error of -0.2 MeV/c^2. Looking carefully at the Monte Carlo distributions in Figure 7.4, we see non-Gaussian tails which are not well matched by the fit. It would appear that our inability to recover the input Γ arises because the true resolution is larger than our estimate. (If $\sigma_{\rm res}$ is systematically too small, the resulting Γ will be systematically too large.) However, since the true resolution is non-Gaussian, it is difficult to determine the correct value of $\sigma_{\rm res}$.

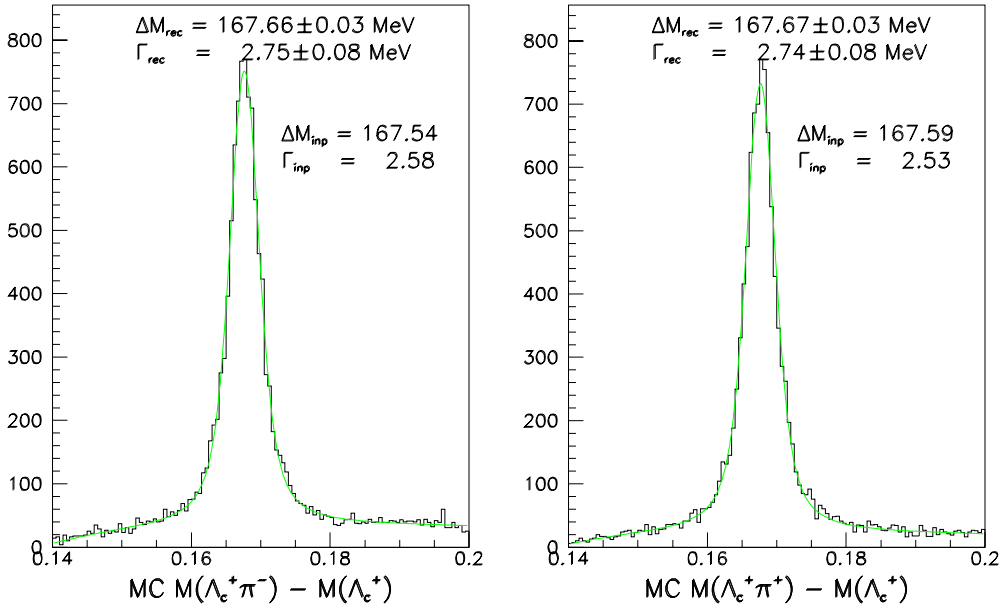

Figure 7.5: Reconstructed Monte Carlo distributions for generated Σ_c^{++} and Σ_c^0. Input and reconstructed parameters are listed.

Check of the fitting method: To ensure that the fit bias found above is not a product solely of the fitting method, we use a mini–Monte Carlo which generates distributions similar to those seen in the data. In this case we control the width, the resolution (which is a true Gaussian), and the background level. We generate 5000 such distributions and fit each one using the same fitting method used for the data and the Monte Carlo. We then plot the normalized errors, defined as

$$\frac{\Gamma_{\rm fit} - \Gamma_{\rm input}}{\sigma(\Gamma_{\rm fit})} \tag{7.5}$$

and fit this resulting distribution to a Gaussian. This distribution and fit are shown in Figure 7.6. The Gaussian fit should be centered at $\langle x \rangle = 0.0$ with $\sigma = 1.0$. There is a very small bias introduced of $0.14 \times \sigma(\Gamma_{\rm fit})$, but $\sigma(\Gamma_{\rm fit})$ is about 0.05 MeV/c^2 for these mini–Monte Carlo distributions, much too small to account for the shift we see with the real Monte Carlo. This procedure confirms that the fitting algorithm for a convoluted Breit–Wigner is working correctly.

Σ_c momentum in data and Monte Carlo: In Figure 7.7, we show the momentum of the Σ_c in data and in Monte Carlo. We perform a subtraction of the momentum distribution using Σ_c sidebands for both the data and Monte Carlo distributions. We then normalize the Monte Carlo to data. A significant difference in the momentum distributions would mean that the Monte Carlo is a poor representation of the data and would call into question our ability to use the Monte Carlo to

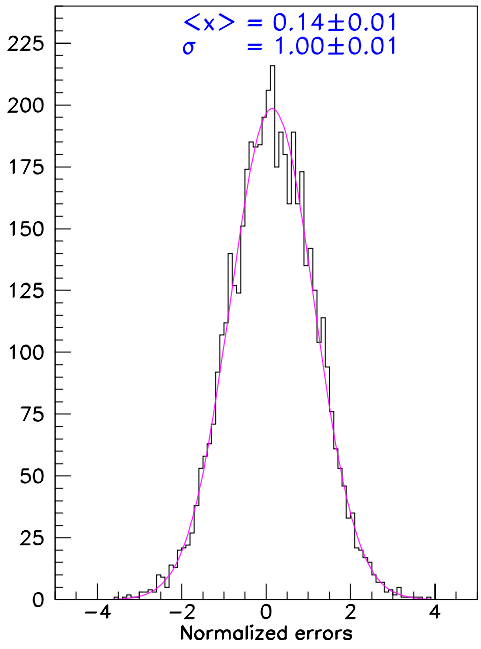

Figure 7.6: Normalized errors for mini–Monte Carlo distributions.

predict the resolution. Fortunately, there does not appear to be any large mismatch between the data and Monte Carlo momentum spectra.

7.5.2 Test of the method with $\Xi^0(1530)$

As another test of our fitting method, we apply the same methods to the decay $\Xi^0(1530) \to \Xi^-\pi^+$. The width of the $\Xi^0(1530)$ has been determined to be 9.1 ± 0.5 MeV/c^2 [4].

The results of this study are shown in Figure 7.8. In the upper left figure, we use Monte Carlo events generated with the nominal $\Xi^0(1530)$ mass but $\Gamma = 0$ to determine that the experimental resolution is about 3.0 MeV/c^2. However, the non-Gaussian nature of the Monte Carlo resolution function is even more apparent here.

In the upper-right plot, we show that if we use 3.0 MeV/c^2 as the experimental resolution, we obtain $\Gamma(\Xi^{0*}) = 10.7 \pm 0.2$ MeV/c^2, significantly larger than the measured value. (We fit the distribution with the usual background function and a convoluted P-wave Breit–Wigner.)

The lower left plot shows the results of applying the fitting method to Monte Carlo events generated with $\Gamma(\Xi^{0*}) = 9.1$ MeV/c^2. In this case we must fit with an S-wave

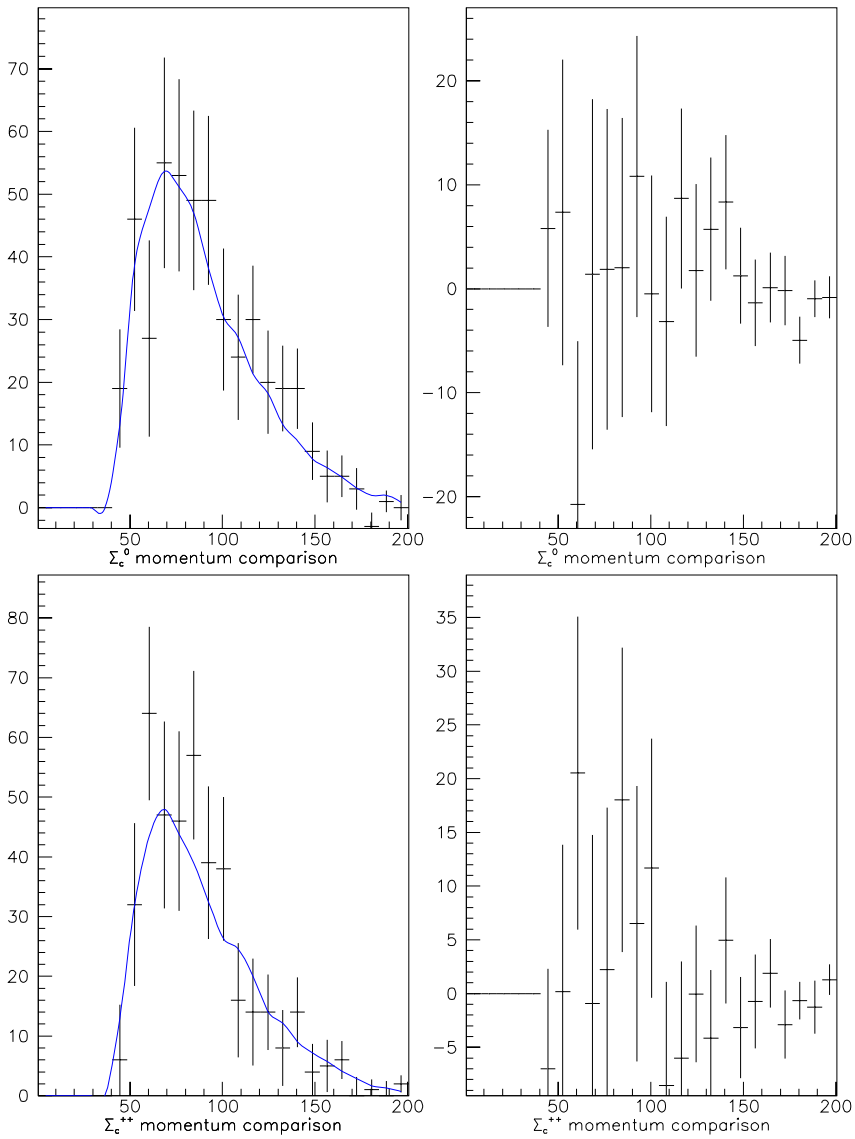

Figure 7.7: A comparison of Monte Carlo (line) and data (points) Σ_c momentum. The plots on the right show the subtraction of the normalized Monte Carlo from the data. Both data and Monte Carlo distributions are background subtracted.

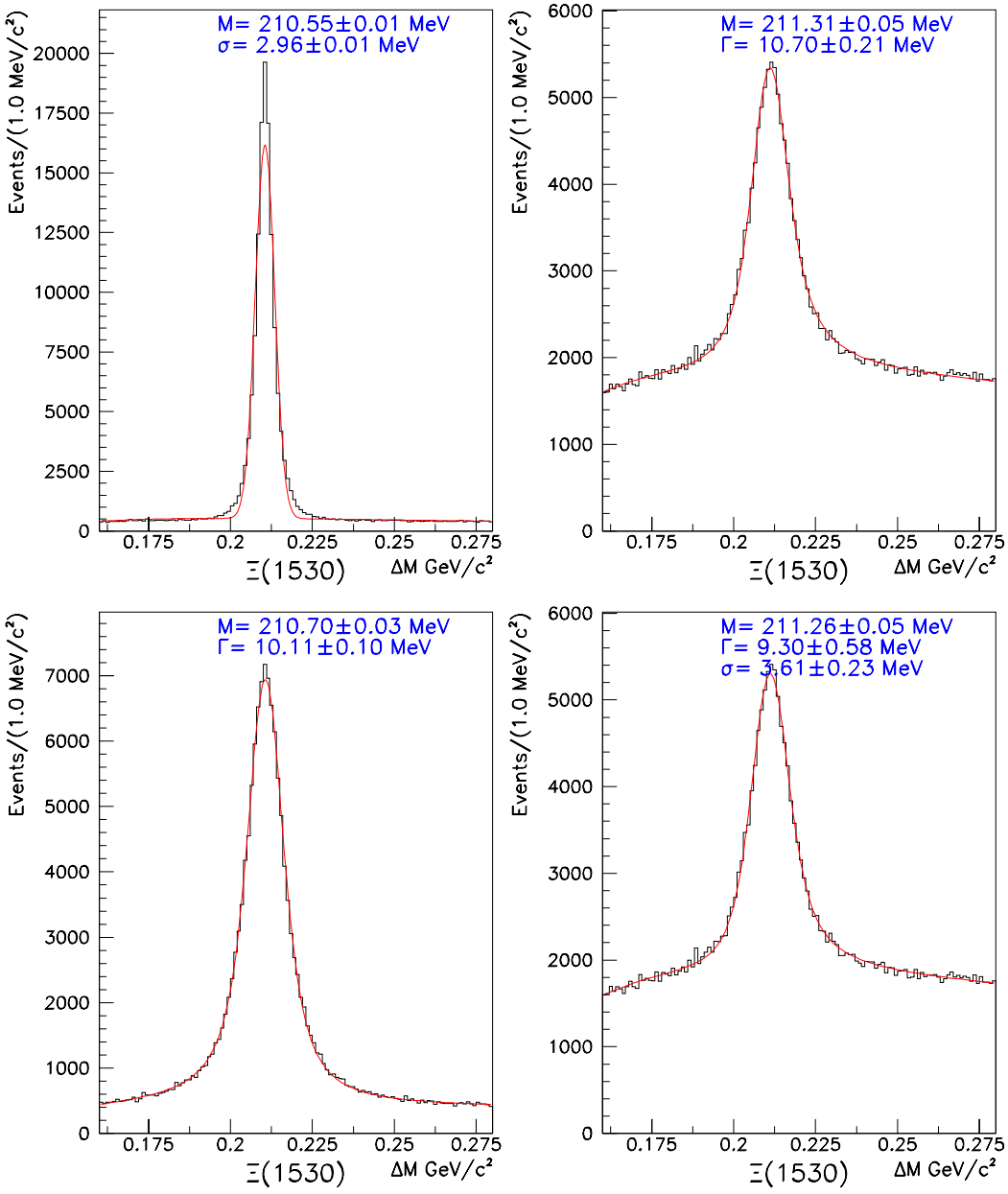

Figure 7.8: A study of $\Xi^0(1530) \to \Xi^-\pi^+$. The upper left plot shows Monte Carlo events with $\Gamma = 0$ fit to a Gaussian function. The upper right plot shows data events fit to a convoluted P-wave Breit–Wigner. The lower left plot shows Monte Carlo events with $\Gamma = 9.1$ MeV/c^2 fit to a convoluted S-wave Breit–Wigner. The final plot shows data events fit to a convoluted P-wave Breit–Wigner where both Γ and the experimental resolution are allowed to vary.

Breit–Wigner, since the Monte Carlo generates the mass according to the S rather than P-wave Breit–Wigner. We see that we recover a width that is 1.0 MeV/c^2 too large. If we simply subtract this 1.0 MeV/c^2 from the value obtained with the data, we get $\Gamma(\Xi^{0*}) = 9.7 \pm 0.2$ MeV/c^2, which is compatible with the measured value. (Obviously, if we were actually making such a measurement, systematic effects on $\Gamma(\Xi^{0*})$ would also have to be considered.)

Finally, in the lower right plot, we show the effect of fitting the data as before, but allowing both the experimental resolution *and* the width to vary. With such large numbers of events available, this fit is actually possible and we obtain results consistent with both our earlier estimate (9.7 ± 0.2 MeV/c^2) and the accepted value (9.1 ± 0.5 MeV/c^2).

From this study we conclude that aside from the non-Gaussian nature of the experimental resolution, which we have already included as a systematic error in our measurements of $\Gamma(\Sigma_c)$, there are no major outstanding problems with our measurement method.

7.5.3 Split sample tests

In split sample tests, the two samples often have different experimental resolutions. In order to compensate for this effect, we use the experimental resolution found in the Monte Carlo for each split sample to determine the value of Γ for that split sample. This implies that we trust the *relative* dependence of σ on the value we use to split the sample. We then apply the methods outlined in Appendix B to calculate any contribution to the systematic error.

Because of the instabilities of the fitting method outlined in Section 7.6, we investigate the stability of systematic effects in two ways. First, we compare the σ values obtained when we fit the two split distributions to

$$N(1 + \alpha(\Delta M - m_\pi)\Delta M^\beta) + \text{Gaussian} \tag{7.6}$$

which helps determine whether there really is a difference in the distributions. Truly different distributions should have statistically distinct values of σ when fit with a Gaussian. Second, we determine Γ using an $L/\sigma_L > 5.0$ cut (the standard cut is $L/\sigma_L > 4.0$). If the suspected systematic is real, the Γ values should not change with this minor change in technique.

Particle/antiparticle: In Figure 7.9, we show the results of splitting the data sample into the particle and anti-particle sub-samples. We determine $\Delta\Gamma(\Sigma_c^{++}) =$

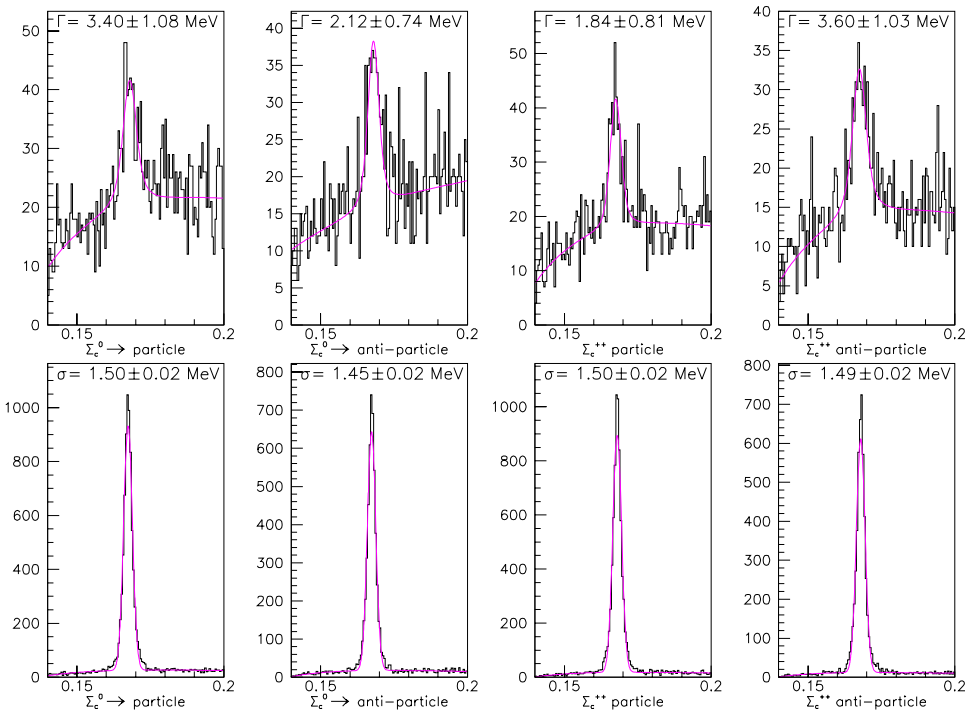

Figure 7.9: Data and Monte Carlo split samples for particle and antiparticle.

0.39 MeV/c^2; there is no systematic for the Σ_c^0. The difference between values of $\Gamma(\Sigma_c^{++})$ is stable under both tests.

***L*/σ_L:** In Figure 7.10 we show the Σ_c distributions for data and Monte Carlo when we split the sample at $L/\sigma_L(\Lambda_c^+) = 7.0$. We see a possible systematic effect in $\Delta\Gamma(\Sigma_c^0) = 0.48$ MeV/c^2, but when we require $L/\sigma_L > 5.0$ for the whole data sample we see no evidence for a systematic problem.

Run period: In Figure 7.11 we show the Σ_c distributions for data and Monte Carlo when we divide the sample into pre-Target Silicon and post-Target Silicon run periods. There are no systematic effects for either the Σ_c^0 or the Σ_c^{++}. (We use run 9750 as in the mass difference analysis.)

Λ_c^+ momentum: In Figure 7.12, we show the Σ_c distributions and fits when we split the sample at $p(\Lambda_c^+) = 70$ GeV/c. In this case as well, there are no systematic effects for either the Σ_c^0 or the Σ_c^{++}.

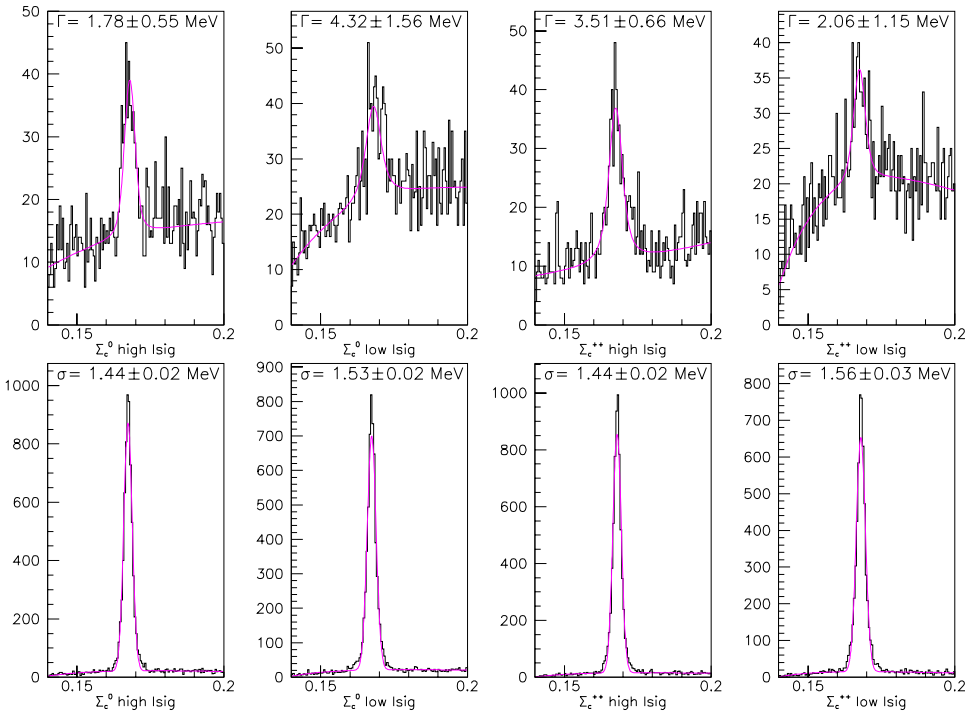

Figure 7.10: Data and Monte Carlo split samples for L/σ_L. We split at $L/\sigma_L = 7.0$.

Soft pion momentum: In Figure 7.13, we see that the fitted values of Γ vary significantly in the Σ_c^{++} case when we split the sample at $p(\pi_s) = 5$ GeV/c. This gives a systematic error of 0.56 MeV/c^2. However, when we fit the signal to a Gaussian function, the two split samples are completely consistent. (The variations in $\Gamma(\Sigma_c^0)$ are nearly as large, but don't pass the threshold of being larger than the statistical errors, as outlined in Appendix B.)

Target segment: The results of splitting the sample into samples where the primary is in Target 3 and Target 4 are shown in Figure 7.14.[3] In this case, the fit to Γ for Target 3 in the Σ_c^0 sample "collapses", a tendency discussed in Section 7.6. However, because of the large statistical errors, this doesn't result in a statistically significant systematic difference.

In Table 7.4 we tabulate the split sample systematic errors and whether they are stable under the two tests. Because of the fitting difficulties and varying stability of the possible systematics, we choose to apply an overall split sample systematic of ± 0.5 MeV/c^2 for both modes rather than applying each individually reported error.

[3]The targets are numbered from upstream to downstream, so for the majority of the data, Target 4 is the most downstream. In this analysis, there isn't enough data to perform a fit when the primary

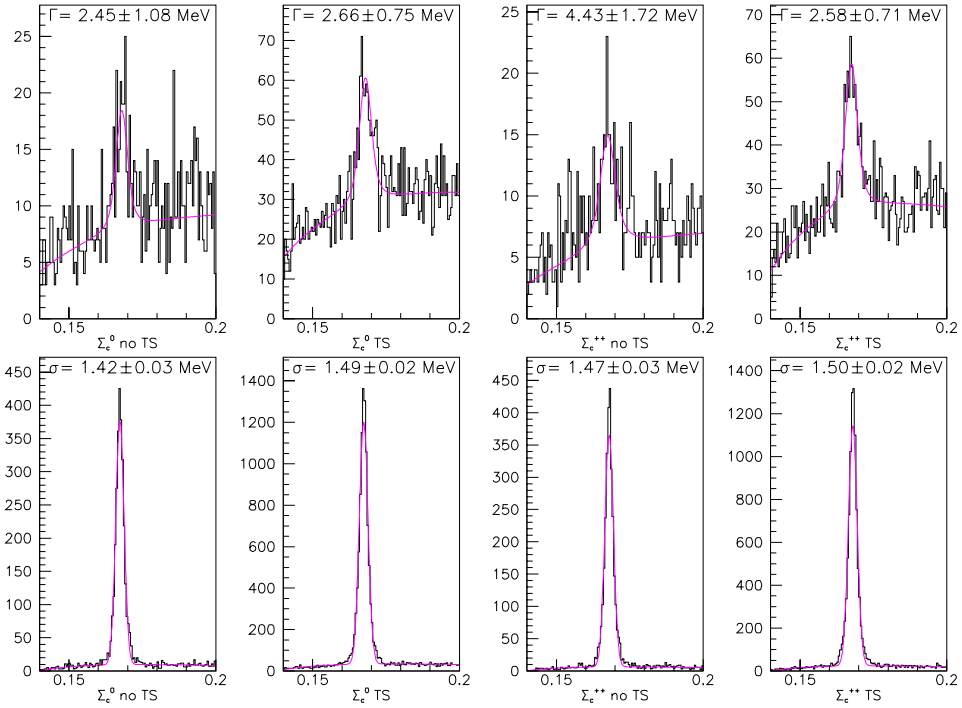

Figure 7.11: Data and Monte Carlo split samples in run period for both Σ_c states. We split the data at run 9750 (the point at which the Target Silicon became fully operational).

Table 7.4: Split sample systematic errors on $\Gamma(\Sigma_c)$. The total is the sum of the components added in quadrature. Units are MeV/c^2. ✓denotes that the difference is stable under the two tests, × denotes that the difference is not stable.

Source	$\Gamma(\Sigma_c^0)$	$\Gamma(\Sigma_c^{++})$	Stable	
			Σ_c^0	Σ_c^{++}
$\Sigma_c/\overline{\Sigma_c}$	0.00	±0.39	—	✓
$L/\sigma_L(\Lambda_c^+)$	±0.48	0.00	×	—
Run #	0.00	0.00	—	—
Λ_c^+ momentum	0.00	0.00	—	—
Soft π momentum	0.00	±0.58	—	×
Target	0.00	0.00	—	—

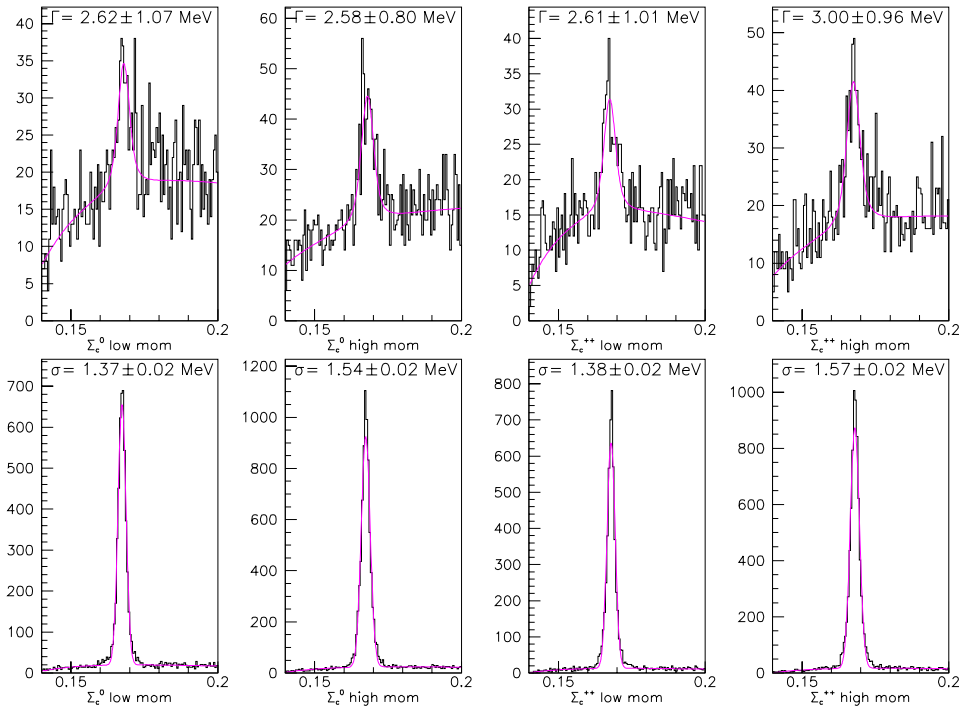

Figure 7.12: Data and Monte Carlo split samples in $p(\Lambda_c^+)$ for both Σ_c states. We split at $p = 70$ GeV/c.

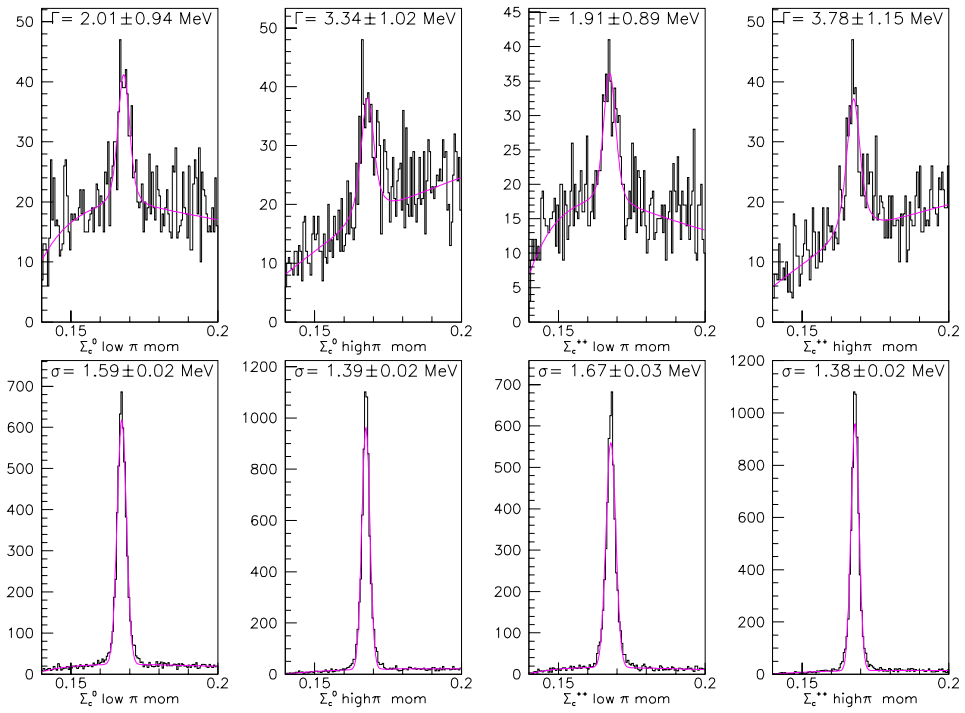

Figure 7.13: Data and Monte Carlo split samples in $p(\pi_s)$ for both Σ_c states. We split at $p(\pi_s) = 5$ GeV/c.

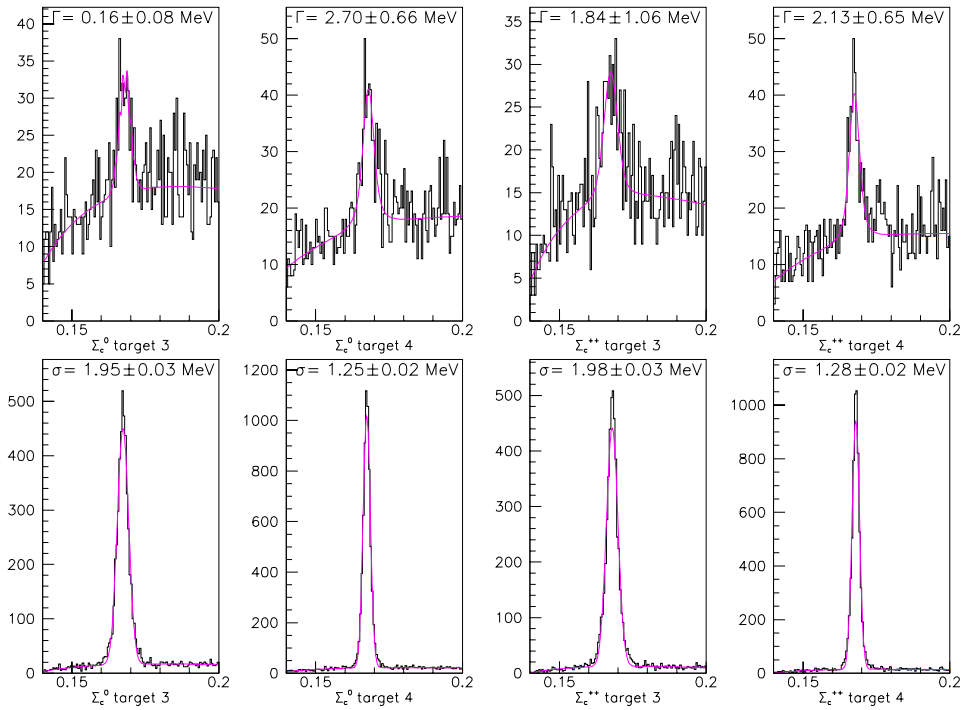

Figure 7.14: Data and Monte Carlo split samples in target number for both Σ_c states. Target 4 is the most downstream target.

7.5.4 Total Systematic Errors

The total systematic errors are presented in Table 7.5, including the split sample systematic error of 0.5 MeV/c^2 for both Σ_c states. With these systematic errors, we obtain final measurements of $\Gamma(\Sigma_c^0) = 2.58 \pm 0.79^{+0.51}_{-0.55}$ and $\Gamma(\Sigma_c^{++}) = 2.53 \pm 0.77^{+0.51}_{-0.56}$.

Table 7.5: Summary of systematic errors on $\Gamma(\Sigma_c)$. The total is the sum of the components added in quadrature. Units are MeV/c^2.

Source	$\Gamma(\Sigma_c^0)$	$\Gamma(\Sigma_c^{++})$
MC resolution	$^{+0.10}_{-0.11}$	$^{+0.10}_{-0.14}$
Fitting bias	-0.20	-0.20
Split Samples	± 0.50	± 0.50
Total	$^{+0.51}_{-0.55}$	$^{+0.51}_{-0.56}$

is in Target 1 or 2. (There was a very limited portion of the run in which we used one or three targets.)

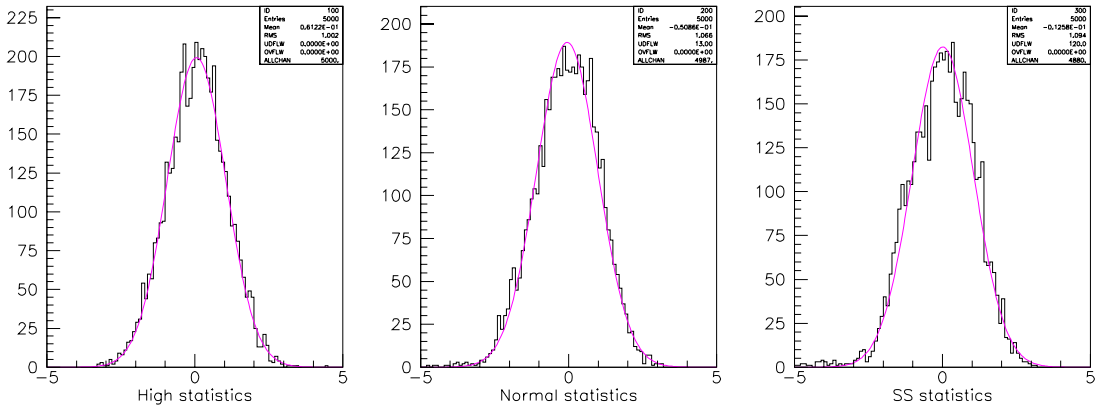

Figure 7.15: Normalized errors $((\Gamma_{\rm fit} - \Gamma_{\rm input})/\Delta\Gamma_{\rm fit})$ for 5000 fits to mini–Monte Carlo distributions. The mini–Monte Carlo distributions are a convoluted Breit–Wigner on a linear background which approximates the data. The first plot is for a high statistics signal of 10 000 events; the second plot is for 600 event samples (approximately what we see in the data). The third plot is for 300 event samples (which approximate the split sample statistics). There are 0, 13, and 120, respectively, underflows in the three plots.

7.6 Possible Pitfalls of the Fitting Method

As alluded to earlier, extracting Γ using a convoluted Breit–Wigner has certain instabilities due to the relatively small number of Σ_c events. To understand these problems, we perform two studies, one with a mini–Monte Carlo that mimics the data and another with the data itself.

The first test is to generate mini–Monte Carlo distributions similar to those in the data. We generate distributions with a nominal "mass" of 168 MeV/c^2 and Γ = 2.5 MeV/c^2 and then smear the distribution using a Gaussian with σ = 1.7 MeV/c^2. We also add a constant background to the distribution to mimic the background seen in the data. We fit these distributions with a linear background and a convoluted Breit–Wigner (σ = 1.7 MeV/c^2) and compare the returned values with the input parameters. This study is similar to the mini–Monte Carlo study presented in Section 7.5.1, except that additional background events are added to mimic the data.

A troubling effect is illustrated in Figure 7.15, which shows normalized errors on the value of Γ for numerous such mini–Monte Carlo samples. It is evident that for high statistics, the fitting method works fine. However, when the statistics and background are chosen to approximate the data, the fit has a tendency (exhibited in the low end tails and number of underflows) to "collapse," or pick a narrow width with small errors much more often than it should. This effect is amplified when we attempt to mimic the typical split sample distribution.

The mini–Monte Carlo tests are somewhat idealized in that the background shape is simple. We make another test by splitting the data into two samples many times based on random variables rather than physics variables which might contain *real* systematic effects. Normalized errors in this study for both the Σ_c^0 and Σ_c^{++} distribution are shown in Figure 7.16. The results of this test are quite similar to the idealized case for the Σ_c^0. However, in the Σ_c^{++} case we notice a troubling effect. First, we notice that there appears to be a bias in the reconstructed width. The normalized errors aren't centered around zero. Looking at the actual reconstructed width (also shown in Figure 7.16) it appears that there are two distributions superimposed. One where the measured widths are about 2.5 MeV/c^2 with a small variance and another where the widths are about 4.5 MeV/c^2 with a much larger variance.

The tendencies of the fits to collapse and the problems in fitting the Σ_c^{++} distributions suggest that the systematics found in Section 7.5 may in fact be due to statistical fluctuations and not real systematic effects.

7.7 Conclusions

We have determined preliminary values of the Σ_c widths of $\Gamma(\Sigma_c^0) = 2.58 \pm 0.79^{+0.51}_{-0.55}$ MeV/c^2 and $\Gamma(\Sigma_c^{++}) = 2.53 \pm 0.77^{+0.51}_{-0.56}$ MeV/c^2. No published limits or measurements exist for any of the $\Gamma(\Sigma_c)$ values. Very recently CLEO has reported measurements of $\Gamma(\Sigma_c^0) = 2.63^{+0.36}_{-0.33} \pm 0.50$ MeV/c^2 and $\Gamma(\Sigma_c^{++}) = 2.98^{+0.38}_{-0.35} \pm 0.50$ MeV/c^2 [66]. The measurements presented here are consistent with the CLEO measurements, although the errors are somewhat larger. Our measurements are not precise enough to rule out or favor any of the recent theoretical predictions.

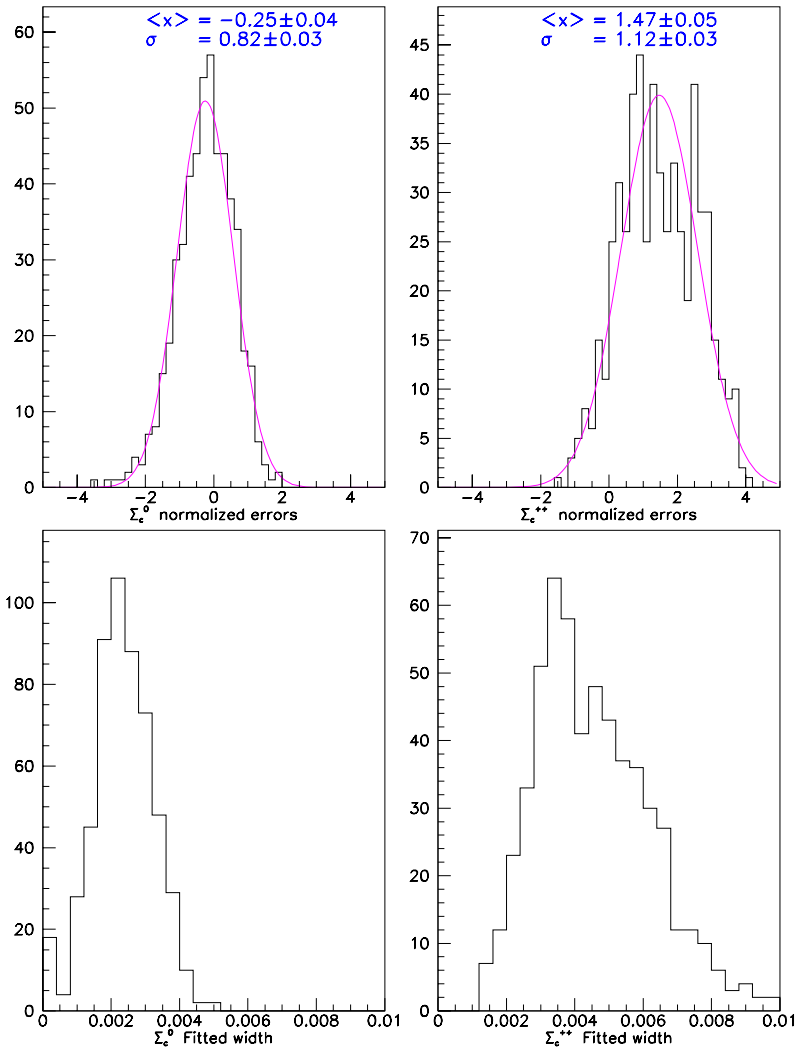

Figure 7.16: Normalized errors $((\Gamma_{\rm ss}-\Gamma_{\rm full})/\Delta\Gamma_{\rm ss})$ for 1000 fits to randomly split data distributions. The first plot is for the Σ_c^0 data, the second plot is for the Σ_c^{++} data. The presence of non-Gaussian tails on the high side of the distributions suggests that too often a large Γ is found.

Chapter 8

Observation of Σ_c^{*0} and Σ_c^{*++}

In this chapter we report the observation of two broad excited charm baryon resonances decaying to $\Lambda_c^+\pi^\pm$. This observation confirms an earlier report by CLEO II [79]. These states are interpreted as the Σ_c^{*0} and Σ_c^{*++} with $I(J^P) = 1(\frac{3}{2}^+)$; none of the quantum numbers have been measured. From samples of 593 ± 146 $\Sigma_c^{*0} \to \Lambda_c^+\pi^-$ and 593 ± 146 $\Sigma_c^{*0} \to \Lambda_c^+\pi^+$ decays, we obtain preliminary measurements of the properties of these states. We find $m_{\Sigma_c^{*0}} - m_{\Lambda_c^+} = 232.7 \pm 1.2$ MeV/c^2, $\Gamma(\Sigma_c^{*0}) = 9.4 \pm 3.7$ MeV/c^2, $m_{\Sigma_c^{*++}} - m_{\Lambda_c^+} = 234.2 \pm 1.5$ MeV/c^2, and $\Gamma(\Sigma_c^{*0}) = 23.6 \pm 4.5$ MeV/c^2. We make no attempt to determine systematic errors or to optimize cuts for a reduced statistical error.

8.1 Λ_c^+ and Σ_c^* Reconstruction

The reconstruction of these states proceeds identically to the Σ_c reconstruction in earlier chapters. The cuts on the Λ_c^+ and Σ_c^* candidates (which have not been extensively studied) are the same as those used in the Σ_c width analysis, except we don't require that the primary vertex is in the downstream targets. The Λ_c^+ candidates used in the Σ_c^* analysis are shown in Figure 8.1.

In fitting the $\Lambda_c^+\pi^\pm$ mass distributions, we use a Gaussian fitting function for the Σ_c signals and a convoluted Breit–Wigner for the Σ_c^* signals. The background function is the same as in the previous chapters. In the Σ_c^* case we use a P-wave Breit–Wigner since these states are believed to be the $\frac{3}{2}^+$ states. For both states, the Monte Carlo prediction of the experimental resolution is about 2.8 MeV/c^2.

The results of the reconstruction and the fit are shown in Figure 8.2, where the

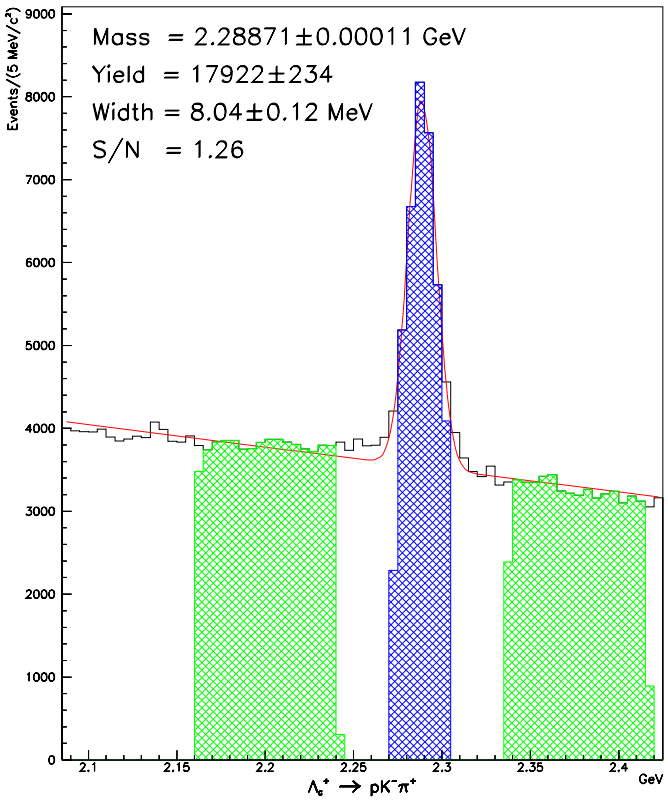

Figure 8.1: $\Lambda_c^+ \to pK^-\pi^+$ candidates used in the reconstruction of Σ_c^0 and Σ_c^{++} candidates. The central hatched region shows the 2σ cut around the nominal Λ_c^+ mass. The outer hatched regions are $6-16\sigma$ sidebands which are used in background studies. (The cut and bin boundaries do not coincide.)

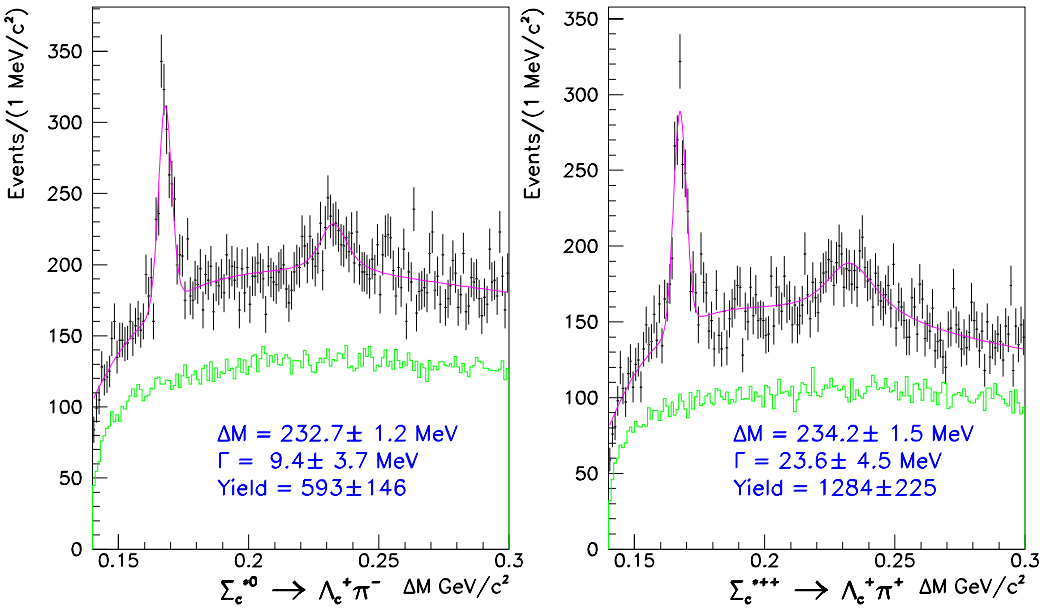

Figure 8.2: Mass difference distributions for $m_{\Sigma_c^0} - m_{\Lambda_c^+}$ and $m_{\Sigma_c^{++}} - m_{\Lambda_c^+}$. The lower histograms are from the sidebands in Figure 8.1 scaled appropriately. The yield and its error are highly correlated with the width of the Breit–Wigner.

divergences from the sideband background shapes are clearly visible near $\Delta M = 230$ MeV/c^2.

8.2 Conclusion

In Table 8.1, we compare these preliminary measurements of the Σ_c^* properties to the published values from CLEO II [79]. Within errors, the FOCUS and CLEO measurements are consistent. We measure $m_{\Sigma_c^{*0}} - m_{\Sigma_c^{*++}}$ to be -1.5 ± 1.9 MeV/c^2 (statistical errors only), which is compatible with the world average [4] of -1.9 ± 1.9 MeV/c^2.

Further analysis in this area is clearly required; perhaps by adding additional Λ_c^+ decay modes, a more accurate measurement with improved statistical and systematic errors can be obtained.

Table 8.1: Comparison of Σ_c properties with other experiments.

Expt.	Value (MeV/c^2)			
	$m_{\Sigma_c^{*0}} - m_{\Lambda_c^+}$	$m_{\Sigma_c^{*++}} - m_{\Lambda_c^+}$	$\Gamma(\Sigma_c^{*0})$	$\Gamma(\Sigma_c^{*++})$
CLEO II	$232.6 \pm 1.0 \pm 0.8$	$234.5 \pm 1.1 \pm 0.8$	$13.0^{+3.7}_{-3.0} \pm 4.0$	$17.9^{+3.8}_{-3.2} \pm 4.0$
FOCUS[a]	232.7 ± 1.2	234.2 ± 1.5	9.4 ± 3.7	23.6 ± 4.5

[a]Statistical error only

Chapter 9

A Search for Doubly Charmed Baryons

9.1 Introduction

It is possible that doubly charmed baryons exist in the FOCUS dataset. In this chapter, we report on a search for the lightest of these baryons, the Ξ_{cc}^{+} (quark content ccd) and Ξ_{cc}^{++} (ccu). Additionally, there is the Ω_{cc}^{+} (ccs) and the Holy Grail of charm baryon spectroscopy, the Ω_{ccc}^{++} (ccc). However, these two states are almost certainly produced much more rarely, so we do not search for them.

9.2 Theoretical Expectations

Masses: As a rough estimate of the mass of the Ξ_{cc} baryons, we can simply take the Λ_c^+ mass ($\sim$ 2300 MeV/c^2), add the charm quark mass ($\sim$ 1600 MeV/c^2), and subtract the light quark constituent mass ($\sim$ 300 MeV/c^2). This gives predicted masses of about 3.6 GeV/c^2. Some (more carefully calculated) theoretical predictions for the Ξ_{cc} masses are shown in Table 9.1.

Lifetimes: Estimating the Ξ_{cc} lifetimes is tricky as the Ξ_{cc}^{++} has Pauli suppression in the internal diagram as shown in Figure 9.1(a). (There are two u quarks in the final state.) For the Ξ_{cc}^{+}, W exchange is possible as shown in Figure 9.1(b). The presence of two c quarks is, of course, also very important. This is thought to decrease the lifetimes of the Ξ_{cc}^{++} and Ξ_{cc}^{+} by about a factor of one half from the D^+ and D^0 which have the same modifying diagrams. These calculations give lifetimes which are

Table 9.1: Theoretical predictions of masses and lifetimes for the Ξ_{cc} states.

	MeV/c^2		τ(ps)	
Author	$M(\Xi_{cc}^+)$	$M(\Xi_{cc}^{++})$	$\tau(\Xi_{cc}^+)$	$\tau(\Xi_{cc}^{++})$
Richard [80]	3.63	3.63	—	—
Stong [81]	3.742	3.742	—	—
Kiselev [82]	—	—	0.11 ± 0.03	0.43 ± 0.11
Gershtein [83]	3.478	3.478	—	—
Bjorken [84]	3.64	3.64	0.15	0.50

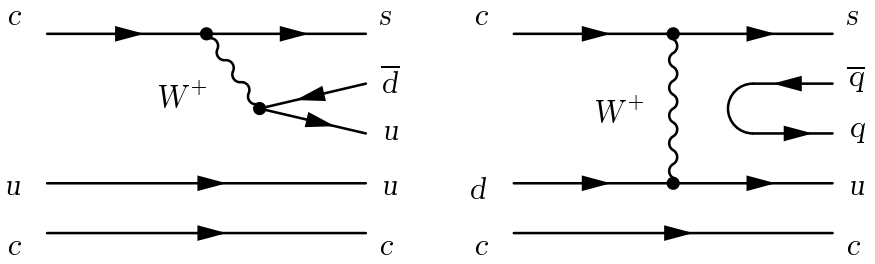

(a) Internal diagram for Ξ_{cc}^{++} showing Pauli suppression.

(b) W exchange diagram for Ξ_{cc}^+.

Figure 9.1: Feynman diagrams for Ξ_{cc} decays.

comparable to the Ξ_c^+ and Ξ_c^0. Theoretical predictions for the lifetimes of the Ξ_{cc} states are also shown in Table 9.1. However, early predictions of the singly charmed baryon masses and lifetimes proved to be quite inaccurate, so these predictions should be viewed with some skepticism.

Decay modes: Following the work of Bjorken [84] and an earlier E687 search [85], we consider Cabibbo favored decay modes that are fully reconstructible. These final states have three properties in common: 1) $C = 1$, $S = -1$, and baryon # = 1. We can divide the final states into three categories based on the identity of the final state charmed particle: decays to Ξ_c, decays to Λ_c^+, and decays to D. If we further restrict ourselves to all charged final states where we also allow Λ^0 and K_s^0 daughters, we are left with the likely "discovery" modes shown in Table 9.2.

Table 9.2: Likely Ξ_{cc} discovery modes.

Modes for Ξ_{cc}^+		
$D^+K_s^0p\pi^-$	$\Lambda_c^+K^-\pi^+$	$\Xi_c^+\pi^+\pi^-$
D^+K^-p	$\Lambda_c^+K^-\pi^+\pi^-\pi^+$	$\Xi_c^+\pi^+\pi^-\pi^+\pi^-$
$D^+\Lambda^0$	$\Lambda_c^+K_s^0$	$\Xi_c^0\pi^+$
$D^+\Lambda^0\pi^+\pi^-$	$\Lambda_c^+K_s^0\pi^+\pi^-$	$\Xi_c^0\pi^+\pi^-\pi^+$
$D^0\Lambda^0\pi^+$		$\Xi_c^0\pi^+\pi^-\pi^+\pi^-\pi^+$
$D^0K_s^0p$		
Modes for Ξ_{cc}^{++}		
$D^0\Lambda^0\pi^+\pi^-$	$\Lambda_c^+K_s^0\pi^+$	$\Xi_c^+\pi^+$
$D^+\Lambda^0\pi^+$	$\Lambda_c^+K_s^0\pi^+\pi^-\pi^+$	$\Xi_c^+\pi^+\pi^-\pi^+$
	$\Lambda_c^+K^-\pi^+\pi^-$	$\Xi_c^+\pi^+\pi^-\pi^+\pi^-\pi^+$
		$\Xi_c^0\pi^+\pi^+$
		$\Xi_c^0\pi^+\pi^+\pi^-\pi^+$

9.3 The Search

In this analysis, we only consider the $\Lambda_c^+K^-n\pi$ decay modes of the Ξ_{cc}. These are likely to be the first decay modes observed with a Λ_c^+ in the final state. Even if the $\Lambda_c^+K_s^0$ modes have comparable branching fractions, they are more difficult to observe since the $K_s^0 \to \pi^+\pi^-$ reconstruction is not as efficient as the charged track reconstruction. Also, nearly 1/3 of the K_s^0's decay via $\pi^0\pi^0$, which is unreconstructable in the FOCUS spectrometer.

We begin with a Λ_c^+ sample with the following cuts:

- Use $\Lambda_c^+ \to pK^-\pi^+$ only
- $\Lambda_c^+(L/\sigma_L) > 5.0$
- $\Lambda_c^+(\Delta W(\pi p)) > 4.0$
- $\Lambda_c^+(\Delta W(Kp)) > 1.0$
- $\Lambda_c^+(\Delta W(\pi K)) > 3.0$
- $\Lambda_c^+(\pi_{\rm con}) > -4.0$
- Λ_c^+ momentum > 40 GeV/c
- Λ_c^+ mass $< 2\sigma$ from nominal

The Λ_c^+ candidates used in this search are shown in Figure 9.2. The $L/\sigma_L(\Lambda_c^+)$ cut can be tightened during the search, as can the particle ID on the Ξ_{cc} candidate. Also

recall that we expect that we *may* see both Ξ_{cc} and Λ_c^+ vertices, so we can also cut on $L/\sigma_L(\Xi_{cc})$.

9.3.1 Monte Carlo expectations

To guide our search, we generate a Monte Carlo sample of Ξ_{cc}^+ and Ξ_{cc}^{++}, both with mass = 3.6 GeV/c^2. We allow these particles to decay to the three Λ_c^+ states without a K_s^0 in the final state. Since the Monte Carlo is incapable of generating doubly charmed baryons, we "alias" to produced Λ_c^+'s. In other words, anytime a Λ_c^+ is generated, it is replaced by a Ξ_{cc}. This undoubtably fails to faithfully reproduce the Ξ_{cc} momentum as well as the correct track multiplicity. Such a Monte Carlo must be used cautiously.

In order to determine whether or not there is any advantage to using a mass difference technique at the probable mass scale of the Ξ_{cc} baryons, we calculate the generated Ξ_{cc} candidate masses two ways. First, by using the masses and momenta of the stable daughter particles (including the daughters of the Λ_c^+). Second, with the mass difference technique used in previous chapters, but adding the nominal Λ_c^+ mass to the mass difference. This simply places the results of both techniques on the same scale. Both sets of signals with our basic Λ_c^+ and Ξ_{cc} cuts are shown in Figure 9.3. From these plots we see that we still have an advantage in using the $\Xi_{cc} - \Lambda_c^+$ mass difference rather than the Ξ_{cc} mass.

9.3.2 Ξ_{cc} reconstruction

The **DVERT** vertexing algorithm described in Chapter 5 is still useful with the more complicated Ξ_{cc} decay topology, but it works somewhat differently. Previously, when we forced the Λ_c^+ to verticize with other tracks, we presumed we were finding the primary vertex. Now, such a requirement should find the Ξ_{cc} decay vertex, or a combination of the Ξ_{cc} and primary vertices. To reconstruct a Ξ_{cc} candidate, we combine Λ_c^+ candidates with the appropriate combination of K^- and $\pi^\pm$ tracks and demand that these tracks form a good Ξ_{cc} candidate. We then attempt to form the "true" primary vertex using the Ξ_{cc} momentum vector as a point back. We do not, however, require that such a vertex is found. If a primary vertex is found, we calculate L/σ_L for the Ξ_{cc} candidate.

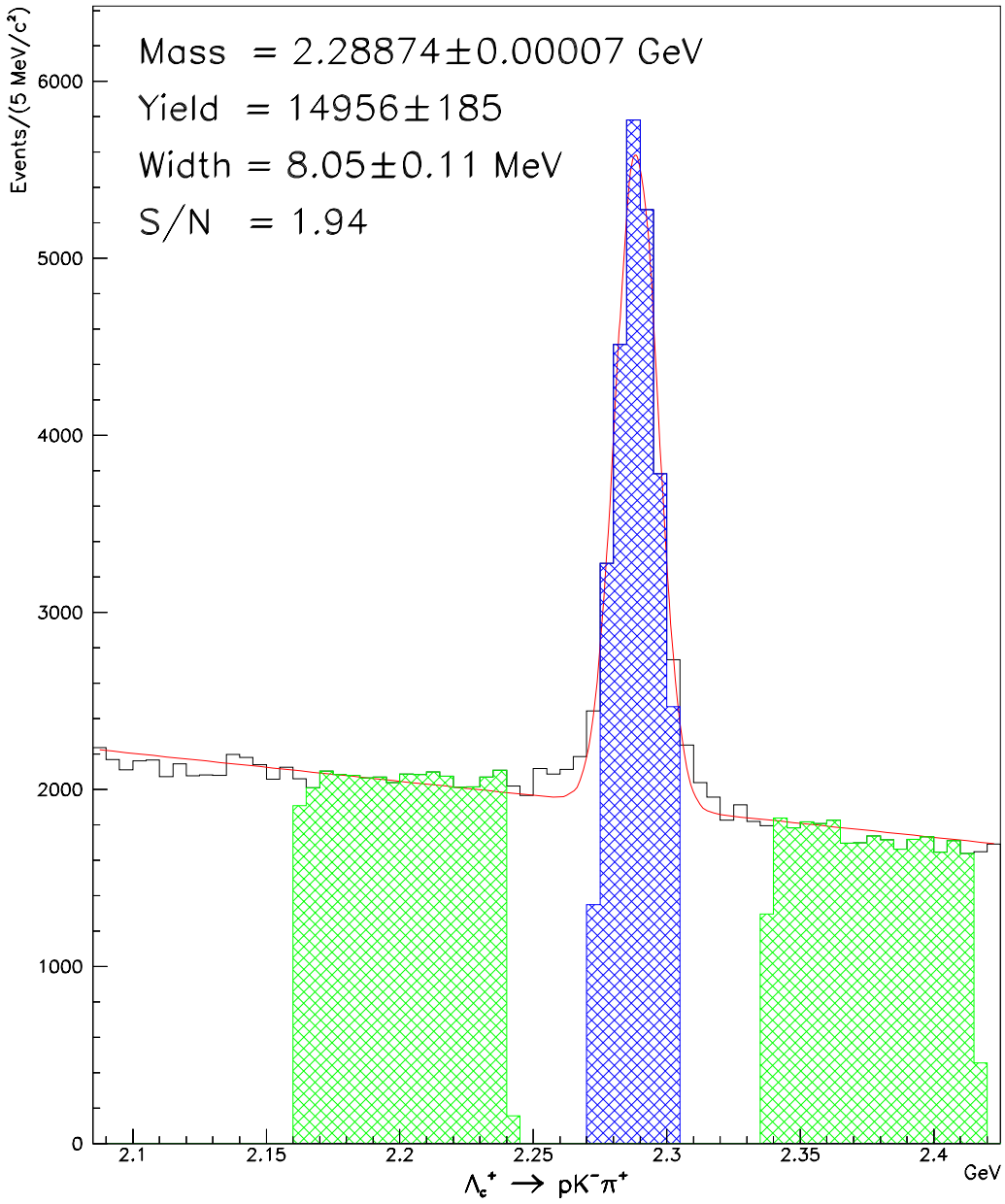

Figure 9.2: Λ_c^+ candidates used in the search for Ξ_{cc} states. The central hatched portion is the 2σ signal region, the outer hatched portions are 6–16σ sidebands used to obtain Ξ_{cc} background shapes.

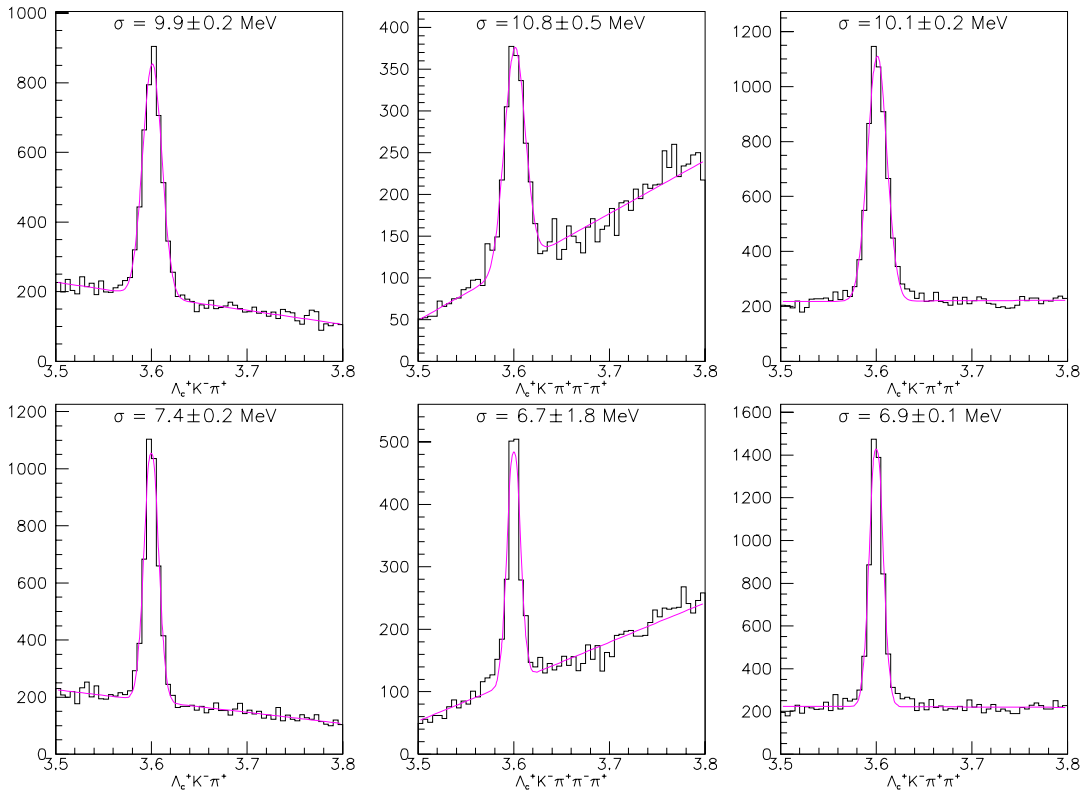

Figure 9.3: Monte Carlo signals for three decay modes of Ξ_{cc}^{+} and Ξ_{cc}^{++}. The top plots are masses, the bottom plots are $\Xi_{cc} - \Lambda_c^+$ mass differences where we have added the PDG Λ_c^+ mass [4].

9.3.3 Possible cuts

With a decay chain that includes two weakly decaying particles and at least five daughter particles in the final state, we have a large selection of cuts to explore. We reduce some of these choices as explained below.

L/σ_L cuts: A loose cut on L/σ_L for the Λ_c^+ is essential; without such a cut, we can't see the Λ_c^+ signal. A very tight cut may be problematic since the Ξ_{cc} daughters may combine with daughters from the two opposite side charm particles and/or tracks from the primary vertex to cause a poorly defined "primary" (actually the Ξ_{cc} decay vertex). Because the lifetime of the Ξ_{cc} states is unknown, we place little initial confidence in L/σ_L cuts for the Ξ_{cc}.

ISO cuts: Because of the complexity of a likely Ξ_{cc} decay (recall that there will also be *two* opposite side charm particles), we place no confidence in isolation cuts and do not apply or investigate them.

Particle identification: Čerenkov identification on Ξ_{cc} and Λ_c^+ daughters should behave normally. The only complication is that the average multiplicity of $cc\overline{cc}$ events is certain to be higher than for $c\overline{c}$ events. To reduce the number of cuts to explore, we freeze the Λ_c^+ particle identification cuts at the values given above which have been shown to give clean Λ_c^+ signals with small losses.

As a result, the fake Λ_c^+ contamination is reduced by the standard particle ID cuts and a modest L/σ_L cut. Fake Ξ_{cc} candidates will be rejected primarily by the application of particle ID and, possibly, requiring $L/\sigma_L(\Xi_{cc})$.

9.3.4 Signals from the data

We have looked at numerous combinations of possible cuts on the Ξ_{cc}, including:

- Tighter $\pi_{\rm con}$ cuts on one or all of the π daughters of the Ξ_{cc}
- Tighter $\Delta W(\pi K)$ cuts on the K daughter of the Ξ_{cc}
- L/σ_L cuts on the Ξ_{cc}

Representative samples of the invariant mass distributions and background from Λ_c^+ sidebands with these cuts are shown below. In each decay mode we present four plots where the $\Delta W(\pi K)$ cut is slightly tighter than our initial cut and four different cuts have been placed on $L/\sigma_L(\Xi_{cc})$. Figure 9.4 shows Ξ_{cc}^{++} candidates in the decay mode $\Xi_{cc}^+ \to \Lambda_c^+ K^-\pi^+$, Figure 9.5 shows Ξ_{cc}^{++} candidates in the decay mode $\Xi_{cc}^{++} \to \Lambda_c^+ K^-\pi^+\pi^+$, and Figure 9.6 shows Ξ_{cc}^+ candidates in the decay mode $\Xi_{cc}^{++} \to \Lambda_c^+ K^-\pi^+\pi^+\pi^-$.

In this preliminary search, we see what might be a signal in the $\Lambda_c^+ K^-\pi^+\pi^+\pi^-$ near 3.58 GeV/c^2. However, there are two problems with this "signal." First, it is too narrow. All the counts above background are in one or two bins, which means that $\sigma \approx 2$ MeV/c^2, while the Monte Carlo prediction is $\sigma \approx 7$ MeV/c^2. Second, under different binning and/or with different cuts, the excess over the background is not nearly so obvious. We conclude that this excess is not likely to be a real Ξ_{cc} signature. The other two channels show no evidence for a signal.

9.4 Conclusion

While we see no evidence for Ξ_{cc} production in this preliminary study, later analyses may have more success. For the decay modes studied in this analysis, a more

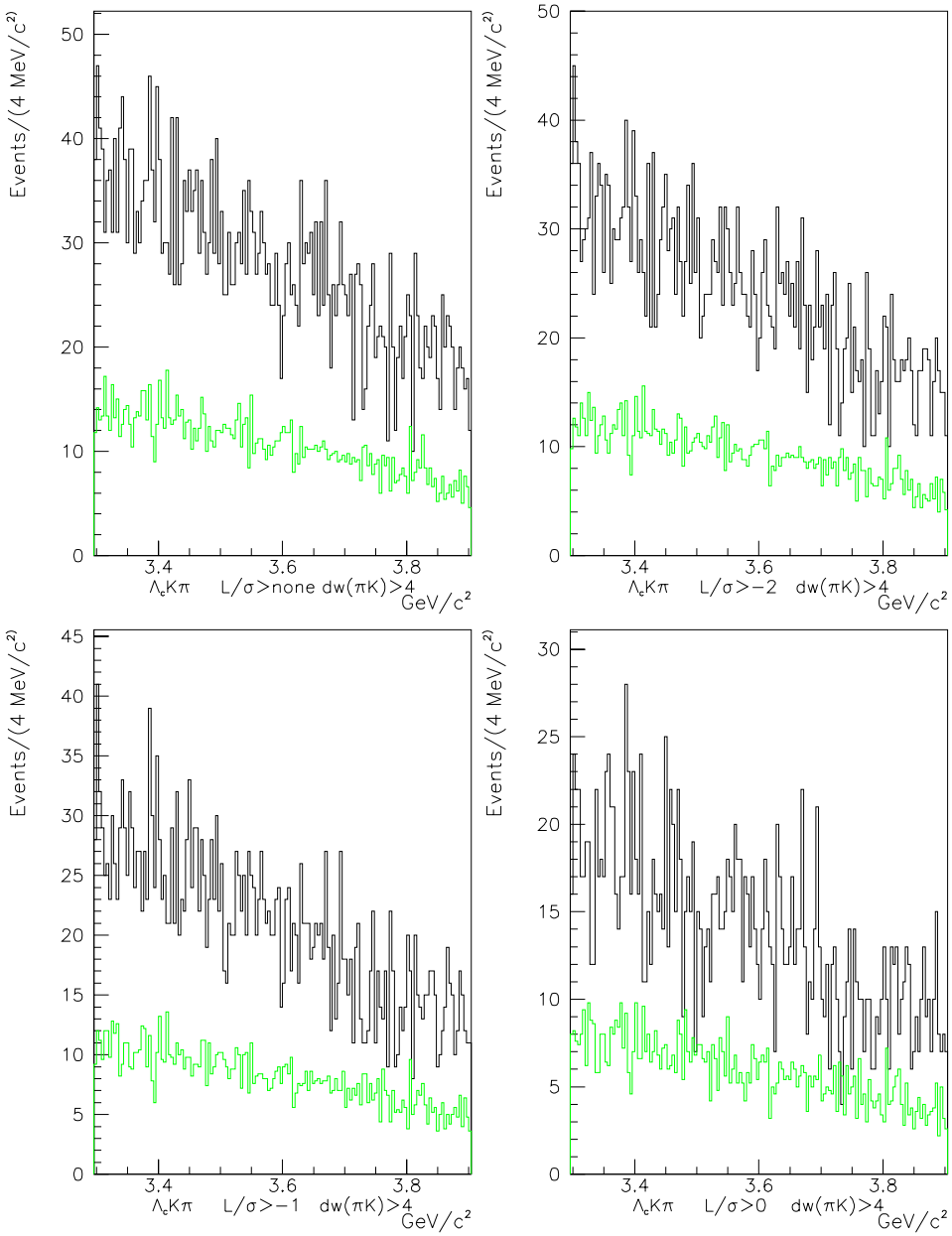

Figure 9.4: Mass plots for the $\Lambda_c^+ K^- \pi^+$ channel. From upper left to lower right, the $L/\sigma_L(\Xi_{cc})$ cut is increased. The lower histogram is obtained using the sidebands in Figure 9.2.

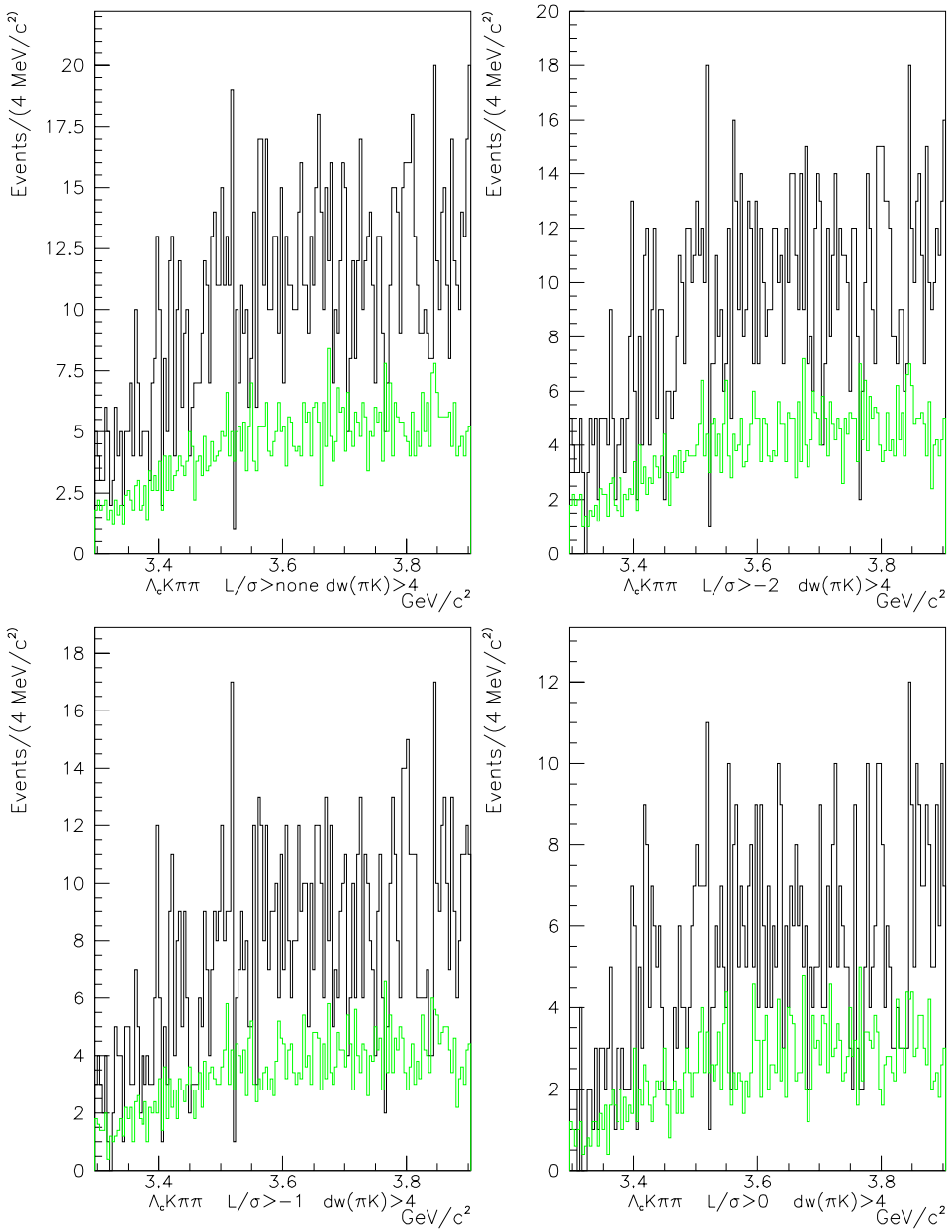

Figure 9.5: Mass plots for the $\Lambda_c^+ K^- \pi^+ \pi^+$ channel. From upper left to lower right, the $L/\sigma_L(\Xi_{cc})$ cut is increased. The lower histogram is obtained using the sidebands in Figure 9.2.

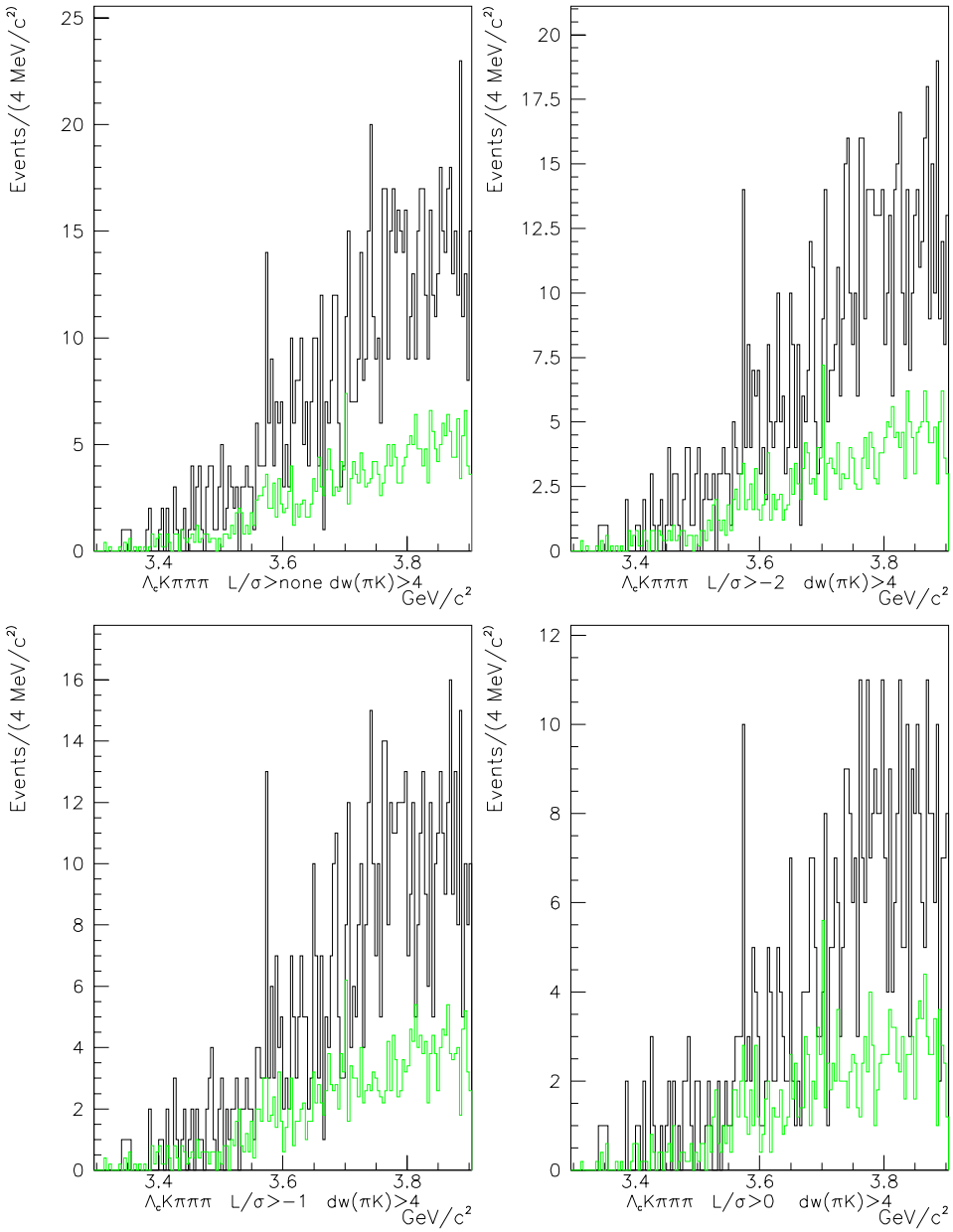

Figure 9.6: Mass plots for the $\Lambda_c^+ K^- \pi^+ \pi^+ \pi^-$ channel. From upper left to lower right, the $L/\sigma_L(\Xi_{cc})$ cut is increased. The lower histogram is obtained using the sidebands in Figure 9.2.

exhaustive look using additional Λ_c^+ decay modes may prove fruitful. An investigation of additional likely Ξ_{cc} decay modes involving D mesons and Ξ_c baryons may be successful.

Chapter 10

Conclusion

10.1 Results and Comparisons

In this thesis, several complementary sets of measurements have been shown. Here we summarize these measurements and compare our measurements with those from other experiments with similar precision and with the world averages (where available).

10.1.1 Σ_c measurements

Our measurements of the Σ_c^0 and Σ_c^{++} mass differences (Table 10.1) are competitive with the world's best measurements and our measurement of the $\Sigma_c^{++} - \Sigma_c^0$ mass difference is comparable in precision to the current world average.

Table 10.1: Comparison of measurements of Σ_c^{++} and Σ_c^0 mass differences.

Experiment	Mass difference (MeV/c^2)		
	$\Sigma_c^{++} - \Lambda_c^+$	$\Sigma_c^0 - \Lambda_c^+$	$\Sigma_c^{++} - \Sigma_c^0$
CLEO II [55]	$168.20 \pm 0.30 \pm 0.20$	$167.10 \pm 0.30 \pm 0.20$	$1.10 \pm 0.40 \pm 0.10$
E791 [56]	$167.76 \pm 0.29 \pm 0.15$	$167.38 \pm 0.29 \pm 0.15$	$0.38 \pm 0.40 \pm 0.15$
PDG avg. [4]	167.87 ± 0.20	167.31 ± 0.21	0.66 ± 0.28
FOCUS	$167.59 \pm 0.20 \pm 0.27$	$167.54 \pm 0.19 \pm 0.34$	$0.05 \pm 0.28 \pm 0.09$

The measurements of Σ_c^+ mass differences (Table 10.2) complete the set of Σ_c mass difference measurements and represent only the second measurement of the Σ_c^+ mass.

No theoretical model accurately predicts all of the well measured baryon mass splittings. With experiments steadily improving these values, the disagreement with theoretical predictions is, in some cases, becoming more pronounced.

Table 10.2: Comparison of measurements of Σ_c^+ mass differences.

Experiment	Mass difference (MeV/c^2)	
	$\Sigma_c^+ - \Lambda_c^+$	$\Sigma_c^+ - \Sigma_c^0$
CLEO II [55]	$168.5 \pm 0.4 \pm 0.2$	$1.4 \pm 0.5 \pm 0.3$
World avg. [4]	168.7 ± 0.6	1.4 ± 0.6
FOCUS	$168.03 \pm 1.01 \pm 0.30$	$0.49 \pm 1.03 \pm 0.45$

Our measurements of the Σ_c^0 and Σ_c^{++} natural widths may be the first published measurements of these quantities. A preliminary measurement from another experiment is also available. These measurements are summarized in Table 10.3. Unfortunately, these measurements are not of sufficient precision to discriminate between the various theoretical models.

Table 10.3: Comparison of measurements of Σ_c widths.

Experiment	Width (MeV/c^2)	
	$\Gamma(\Sigma_c^{++})$	$\Gamma(\Sigma_c^0)$
CLEO II[a] [66]	$2.98^{+0.38}_{-0.35} \pm 0.50$	$2.63^{+0.36}_{-0.33} \pm 0.50$
World avg.	—	—
FOCUS	$2.53 \pm 0.77^{+0.51}_{-0.56}$	$2.58 \pm 0.79^{+0.51}_{-0.55}$

[a]Preliminary result

10.1.2 Σ_c^* measurements

Finally, our observation of the excited charm baryon states, presumed to be the Σ_c^{*0} and Σ_c^{*++}, confirm an earlier observation by another experiment. Our preliminary measurements are consistent with these earlier measurements, as shown in Tables 10.4 and 10.5. The corresponding Σ_c^{*+} has not yet been observed.

Table 10.4: Comparison of Σ_c^* mass measurements.

Experiment	Mass Difference (MeV/c^2)	
	$m_{\Sigma_c^{*0}} - m_{\Lambda_c^+}$	$m_{\Sigma_c^{*++}} - m_{\Lambda_c^+}$
CLEO II [79]	$232.6 \pm 1.0 \pm 0.8$	$234.5 \pm 1.1 \pm 0.8$
World avg. [4]	232.6 ± 1.3	234.5 ± 1.4
FOCUS[a]	232.7 ± 1.2	234.2 ± 1.5

[a]Statistical error only

Table 10.5: Comparison of Σ_c^* width measurements.

Experiment	Width (MeV/c^2)	
	$\Gamma(\Sigma_c^{*0})$	$\Gamma(\Sigma_c^{*++})$
CLEO II [79]	$13.0^{+3.7}_{-3.0} \pm 4.0$	$17.9^{+3.8}_{-3.2} \pm 4.0$
World avg. [4]	—	—
FOCUS[a]	9.4 ± 3.7	23.6 ± 4.5

[a]Statistical error only

10.2 Concluding Remarks

Because these measurements all come from a single experiment with identical reconstruction methods and similar analysis requirements, the suite of measurements is more valuable than the sum of the measurements individually.

However, each of these measurements offers an opportunity for improvement. The systematic errors on the Σ_c^0 and Σ_c^{++} mass difference measurements will be reduced by incorporating the forthcoming correction to the FOCUS momentum scale. The other measurements can be improved by including additional Λ_c^+ decay modes which should reduce the statistical errors on the measurements. Due to time and other constraints, it was not possible to include other decay modes in this thesis.

Efforts to perform mass (and possibly width) measurements for the Ξ_c excited states are under way, and searches for the Σ_c^{*+} and Ω_c' (which would complete the spectrum of $L = 0$ charmed baryons) are planned. The knowledge gained from these measurements, combined with the values presented in this thesis, may provide renewed impetus for refined theoretical models of heavy baryons.

Bibliography

[1] M. Gell-Mann, Phys. Lett. **8**, 214 (1964).

[2] G. Zweig, An SU_3 model for strong interaction symmetry and its breaking II, 1964, CERN-TH-412 (unpublished, later published in [3]).

[3] D. B. Lichtenberg and S. P. Rosen, editors, *Developments in the Quark Theory of Hadrons, Vol. 1. 1964–1978*, Hadronic Press, Inc., Nonantum, MA, 1980.

[4] C. Caso et al., Eur. Phys. J. **C3**, 1 (1998).

[5] Y. Fukuda et al., Phys. Rev. Lett. **81**, 1562 (1998).

[6] J. J. Aubert et al., Phys. Rev. Lett. **33**, 1404 (1974).

[7] J. E. Augustin et al., Phys. Rev. Lett. **33**, 1406 (1974).

[8] G. Goldhaber et al., Phys. Rev. Lett. **37**, 255 (1976).

[9] I. Peruzzi et al., Phys. Rev. Lett. **37**, 569 (1976).

[10] K. Niu, E. Mikumo, and Y. Maeda, Prog. Theor. Phys. **46**, 1644 (1971).

[11] K. Hoshino et al., Prog. Theor. Phys. **53**, 1859 (1975).

[12] S. W. Herb et al., Phys. Rev. Lett. **39**, 252 (1977).

[13] F. Abe et al., Phys. Rev. **D50**, 2966 (1994).

[14] The LEP Collaborations: Aleph, Delphi, L3, and OPAL, Phys. Lett. **B276**, 247 (1992).

[15] N. Cabibbo, Phys. Rev. Lett. **10**, 531 (1963).

[16] M. Kobayashi and T. Maskawa, Prog. Theor. Phys. **49**, 652 (1973).

[17] H. Yukawa, Proc. Phys. Math. Soc. Jap. **17**, 48 (1935).

[18] J. P. Alexander et al., Phys. Rev. Lett. **83**, 3390 (1999).

[19] B. Guberina, R. Ruckl, and J. Trampetic, Z. Phys. **C33**, 297 (1986).

[20] C. Caso et al., Eur. Phys. J. **C3**, 1 (1998), and 1999 off-year partial update for the 2000 edition available on the PDG WWW pages (URL: `http://pdg.lbl.gov/`).

[21] Wideband Beam Photon Collaboration, Fermilab proposed experiment 831, 1990, Fermilab document FNAL–Proposal–831.

[22] P. L. Frabetti et al., Nucl. Instrum. Meth. **A329**, 62 (1993).

[23] G. Alimonti et al., Nucl. Instrum. Meth. **A314**, 411 (1992).

[24] P. L. Frabetti et al., Nucl. Instrum. Meth. **A320**, 519 (1992).

[25] FOCUS Collaboration, Description and performance of the fermilab focus spectrometer, 1999, `http://www-focus.fnal.gov/nim/focus-nim/nim.ps`, In preparation for publication in *Nucl. Instrum. Meth.*

[26] P. L. Frabetti et al., Phys. Lett. **B407**, 79 (1997).

[27] J. Wilson and M. Purohit, E831 at South Carolina (DOE review), `http://scuch8.psc.sc.edu/hep/doe_rev.ps`.

[28] G. Bellini et al., Nucl. Instrum. Meth. **A252**, 366 (1986).

[29] J. D. Jackson, *Classical Electrodynamics*, John Wiley & Sons, Inc., New York, second edition, 1975.

[30] L. Cinquini, J. Cumalat, E. Erdos, B. O'Reilly, and E. Vaandering, A description of the Inner Electromagnetic Calorimeter for FOCUS, FOCUS memo, `http://www-hep.colorado.edu/~e687/focus_doc/iecal.ps`.

[31] E. W. Vaandering, Thoughts on a dielectron trigger, 1996, FOCUS memo: E831-mem-1996/8, `http://www-focus.fnal.gov/ewv/ie_dielectron.ps`.

[32] S. Bianco et al., The upgraded outer EM calorimeter of FOCUS at Fermilab, 1999, hep-ex/9912066, to appear in the proceedings of *VIII International Conference on Calorimetry in HEP.*

[33] G. Bonomi, An iron/scintillator tile calorimeter for the FOCUS experiment at Fermilab, in *Calorimetry in high energy physics. Proceedings, 7th International Conference, Tucson, USA, November 9-14, 1997*, edited by E. Cheu, T. Embry, J. Rutherfoord, and R. Wigmans, pages 276–280, Singapore, Singapore: World Scientific, 1998.

[34] G. Boca et al., Nucl. Instrum. Meth. **A409**, 561 (1998).

[35] J. Wiss, FOCUS MH homepage, `http://www.hep.uiuc.edu/e687/muon/muon.html`.

[36] P. Liguori, P. Sheldon, P. Vitulo, M. Webster, and J. Wilson, OM design and considerations, 1994, FOCUS memo, http://www-focus.fnal.gov/papers/outermu_1.ps.

[37] A. Kreymer and F. Prelz, DAQ architecture for E831, 1997, FOCUS memo, http://www-focus.fnal.gov/papers/daq_main/daq_main/daq_main.html.

[38] G. A. Akopdzhanov et al., Nucl. Instr. Meth. **140**, 441 (1977).

[39] I. Nakano and K. Miyake, Jap. J. Appl. Phys. **24**, 506 (1985).

[40] J. Wiss, CITADL: A proposal for a new Čerenkov algorithm for FOCUS, 1997, FOCUS memo, http://web.hep.uiuc.edu/e831/citadl/citadl.ps.

[41] J. Wiss, Thoughts on muon identification algorithms for E831, 1994, FOCUS memo, http://web.hep.uiuc.edu/e687/muon/mu_id_thoughts.ps.

[42] C. Cawlfield, M. Ruesnink, and J. Wiss, Muon identification χ^2 confidence levels, 1994, FOCUS memo, http://web.hep.uiuc.edu/e687/muon/chisq.ps.

[43] J. E. Ramírez-Vargas, Algoritmo de identificacion de muones, Master's thesis, Universidad de Puerto Rico, Recinto Universitario de Mayagüez, 1997.

[44] M. G. Hosack, Confidence level for outer muons (2nd ed.), 1998, FOCUS memo, http://www-focus.fnal.gov/papers/omu_conf2.ps.

[45] M. Fausey et al., Cooperative Process Software, CPS Homepage, http://www-hppc.fnal.gov/farms/cps/cpspage.html.

[46] R. L. Culbertson, *Four-Body Semileptonic Decays of D Mesons*, PhD thesis, University of Illinois at Urbana-Champaign, 1993.

[47] P. L. Frabetti et al., Phys. Lett. **B351**, 591 (1995).

[48] M. Genovese, J.-M. Richard, B. Silvestre-Brac, and K. Varga, Phys. Rev. **D59**, 014012 (1999).

[49] J. L. Rosner, Phys. Rev. **D57**, 4310 (1998).

[50] R. K. Bhaduri, L. E. Cohler, and Y. Nogami, Nuovo Cim. **65A**, 376 (1981).

[51] S. Capstick, Phys. Rev. **D36**, 2800 (1987).

[52] L.-H. Chan, Phys. Rev. **D31**, 204 (1985).

[53] W. Y. P. Hwang and D. B. Lichtenberg, Phys. Rev. **D35**, 3526 (1987).

[54] N. Isgur, Phys. Rev. **D21**, 779 (1980), Erratum: ibid, D23, 817 (1981).

[55] G. Crawford et al., Phys. Rev. Lett. **71**, 3259 (1993).

[56] E. M. Aitala et al., Phys. Lett. **B379**, 292 (1996).

[57] T. Bowcock et al., Phys. Rev. Lett. **62**, 1240 (1989).

[58] H. Albrecht et al., Phys. Lett. **211B**, 489 (1988).

[59] M. Diesburg et al., Phys. Rev. Lett. **59**, 2711 (1987).

[60] P. L. Frabetti et al., Phys. Lett. **B365**, 461 (1995).

[61] A. N. Aleev et al., Dubna JINR - 3(77)-96 (96/05,rec.Nov.) 31-46.

[62] J. C. Anjos et al., Phys. Rev. Lett. **62**, 1721 (1989).

[63] G. Gianini, A new routine for the π^0 identification and energy estimate, 1998, FOCUS memo.

[64] P. L. Frabetti et al., Phys. Rev. Lett. **72**, 961 (1994).

[65] K. W. Edwards et al., Phys. Rev. Lett. **74**, 3331 (1995).

[66] D. Besson, Heavy quarks: Spectroscopy, transitions, decays, 1999, Talk at *Physics in Collision Conference*, `http://umwnt1.physics.lsa.umich.edu/PIC99/_Talks/besson/besson.htm`.

[67] M. A. Ivanov, J. G. Korner, V. E. Lyubovitsky, and A. G. Rusetsky, Phys. Lett. **B442**, 435 (1998).

[68] M. A. Ivanov, J. G. Korner, V. E. Lyubovitsky, and A. G. Rusetsky, Phys. Rev. **D60**, 094002 (1999).

[69] S. Tawfiq, P. J. O'Donnell, and J. G. Korner, Phys. Rev. **D58**, 054010 (1998).

[70] M.-Q. Huang, Y.-B. Dai, and C.-S. Huang, Phys. Rev. **D52**, 3986 (1995).

[71] D. Pirjol and T.-M. Yan, Phys. Rev. **D56**, 5483 (1997).

[72] J. L. Rosner, Phys. Rev. **D52**, 6461 (1995).

[73] G. Molière, Z. Naturforsch **3a**, 78 (1948).

[74] H. A. Bethe, Phys. Rev. **89**, 1256 (1953).

[75] G. Molière, Z. Naturforsch **10a**, 177 (1955).

[76] J. E. Wiss, 1999, Private communication.

[77] M. G. Hosack, Molière MCS for Rogue, 1999, FOCUS memo: E831-mem-1999/15, `http://www.hep.vanderbilt.edu/~mgh/analysis/mcs/moliere.ps`.

[78] B. Rossi, *High-Energy Particles*, Prentice-Hall, Inc., 1952.

[79] G. Brandenburg et al., Phys. Rev. Lett. **78**, 2304 (1997).

[80] J.-M. Richard, Hadrons with two heavy quarks, 1994, hep-ph/9407224.

[81] M. L. Stong, Spectra of baryons containing two heavy quarks, 1995, hep-ph/9505217.

[82] V. V. Kiselev, A. K. Likhoded, and A. I. Onishchenko, Phys. Rev. **D60**, 014007 (1999).

[83] S. S. Gershtein, V. V. Kiselev, A. K. Likhoded, and A. I. Onishchenko, Mod. Phys. Lett. **A14**, 135 (1999).

[84] J. D. Bjorken, Estimates of decay branching fractions for hadrons containing charm and bottom quarks, 1986, Unpublished.

[85] H. W. K. Cheung, A search for doubly charm baryons, 1993, E687 memo.

[86] J. M. Link, 1999, Private communication.

[87] J. Wiss and R. Gardner, Estimating systematic errors, 1994, E687 memo: E687-94-030, `http://web.hep.uiuc.edu/e687/memos/DALITZ_SYS.PS`.

Appendix A

Soft π^0 Studies Using D^* Decays

In this appendix, we present a study of π^0 reconstruction methods (vertexing and energy constraints) and various cuts on soft π^0's from $D^* \to D\pi^0$ decays. The initial determination of good π^0 requirements concentrated on all π^0's which are heavily biased towards high momentum π^0's. The kinematics of soft π^0's are quite different and demand a different set of requirements. The findings of this study help us make intelligent choices in the kinematically similar $\Sigma_c^+ \to \Lambda_c^+\pi^0$ analysis. The high statistics available in $D^* \to D\pi^0$ decays provide an understanding of soft π^0's in a way that studying $\Sigma_c^+ \to \Lambda_c^+\pi^0$ decays simply cannot.

A.1 The D Sample

***D* reconstruction:** The data come from a 25% sample of Golden Mode ($D^0 \to K^-\pi^+$, $D^+ \to K^-\pi^+\pi^+$, and $D^0 \to K^-\pi^+\pi^+\pi^-$) decays from Super-stream 3. (See Section 4.3.2.) This Super-stream is chosen because it contains a Golden Mode skim with all the raw calorimetry information.[1] In addition to the standard **SuperEZD**[2] requirements, we make tighter cuts to provide a small, clean sample of D decays. These requirements are:

- $L/\sigma_L > 5$
- $\pi_{\rm con} > -6$
- $\Delta W(\pi K) > 1.0$

[1] We need the raw calorimetry information since the reconstructed π^0's have had cuts applied that are too restrictive.

[2] **SuperEZD** is a skimming package designed to select fully reconstructed charm decays in known decay modes.

The D's are reconstructed (as are all decays in this thesis) with **DVERT** direction vectors and **TRKFIT** momenta. The resulting D signals can be seen in Figure A.1.

***D** reconstruction:** A 2σ mass cut is made around the mean D mass. The π^0 requirements vary throughout this study and are explained below. The D momentum vector and reconstructed D mass are combined with the reconstructed π^0 momentum vector and the PDG π^0 mass to form the D^* mass. The initial D mass is subtracted and the resulting mass difference is plotted. (In the same way we compute all mass differences in this thesis.)

Figure A.2 shows D^* signals with the "standard" cuts (on the left) and signals with a new set of cuts optimized for soft π^0's (on the right). We are able to make a factor of 2–3 improvement in yield without significant sacrifices in signal purity. The sections that follow detail this improvement and describe additional cuts which can enhance the signal-to-noise of excited states.

A.2 The π^0 Reconstruction Method

The choice of a π^0 reconstruction method is not initially obvious as there are two possible choices for the vertex location and three methods for constraining the π^0 mass. This gives six possible reconstruction methods, each of which we investigate before finally choosing a method. In this discussion we consider only IE-IE π^0's since they are the only π^0's we can use in the Σ_c^+ analysis.

Vertex position: We can either choose to reconstruct all π^0's at the center of the target once per event, or reconstruct new π^0's for each charm candidate using the primary vertex as the π^0 vertex.

Constraining the Mass: Here, three methods have been used with the FOCUS data. First, we can simply use the π^0 momentum vector as the sum of the photon momenta (no constraint). Second, we can use the constraining method of Nakano and Miyake [39] which adjusts the individual photon energies in order to constrain the mass. Finally, we can use the **PI0FIT** method [63] which takes into account the position resolution of the calorimeters as well when adjusting photon energies. In the low energy limit (soft π^0), this method is very similar to the simple energy constrained method.

We expect a broadening of the mass difference peak if any of these methods is less than optimal. A summary of the fit results is shown in Figure A.3. We can see that

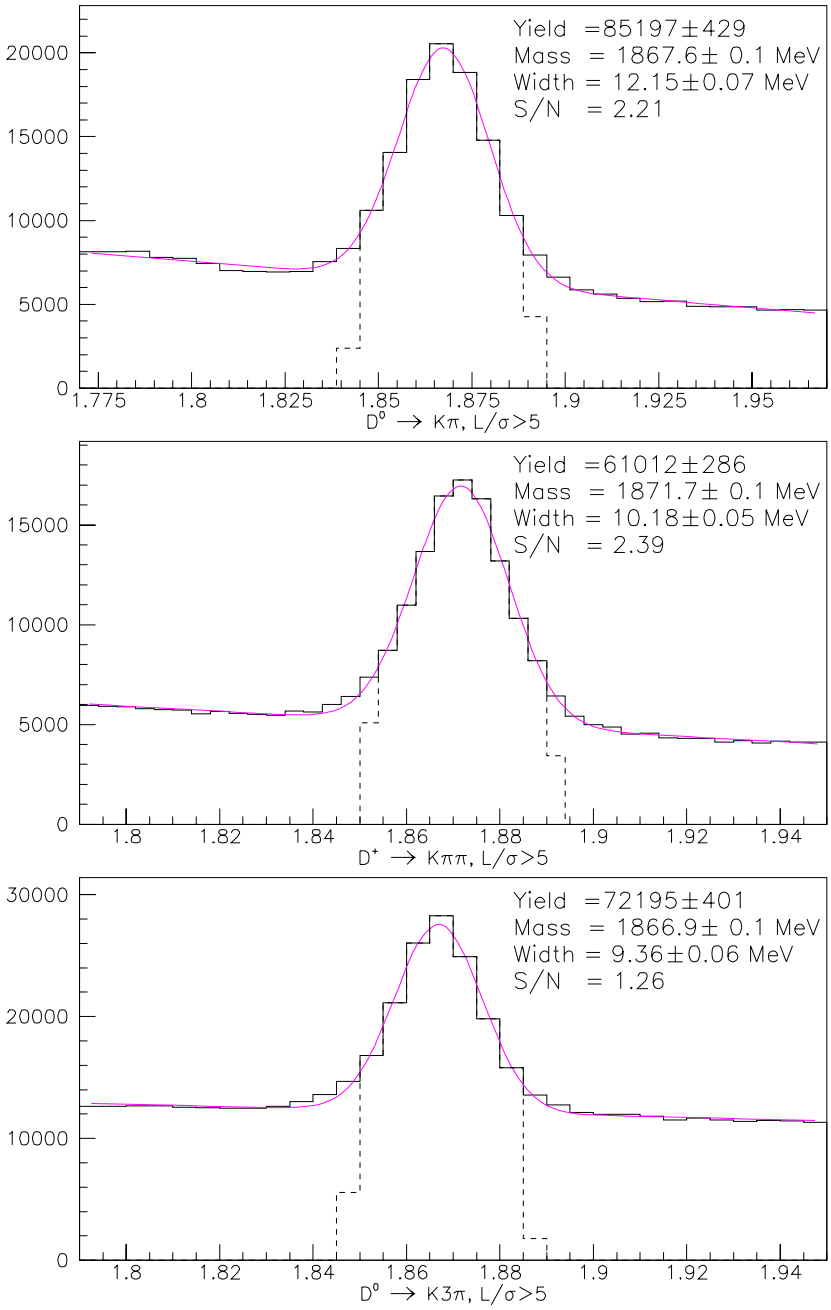

Figure A.1: Golden Mode D signals used in this study. The dashed lines denote the 2σ mass cut used in the D^* search.

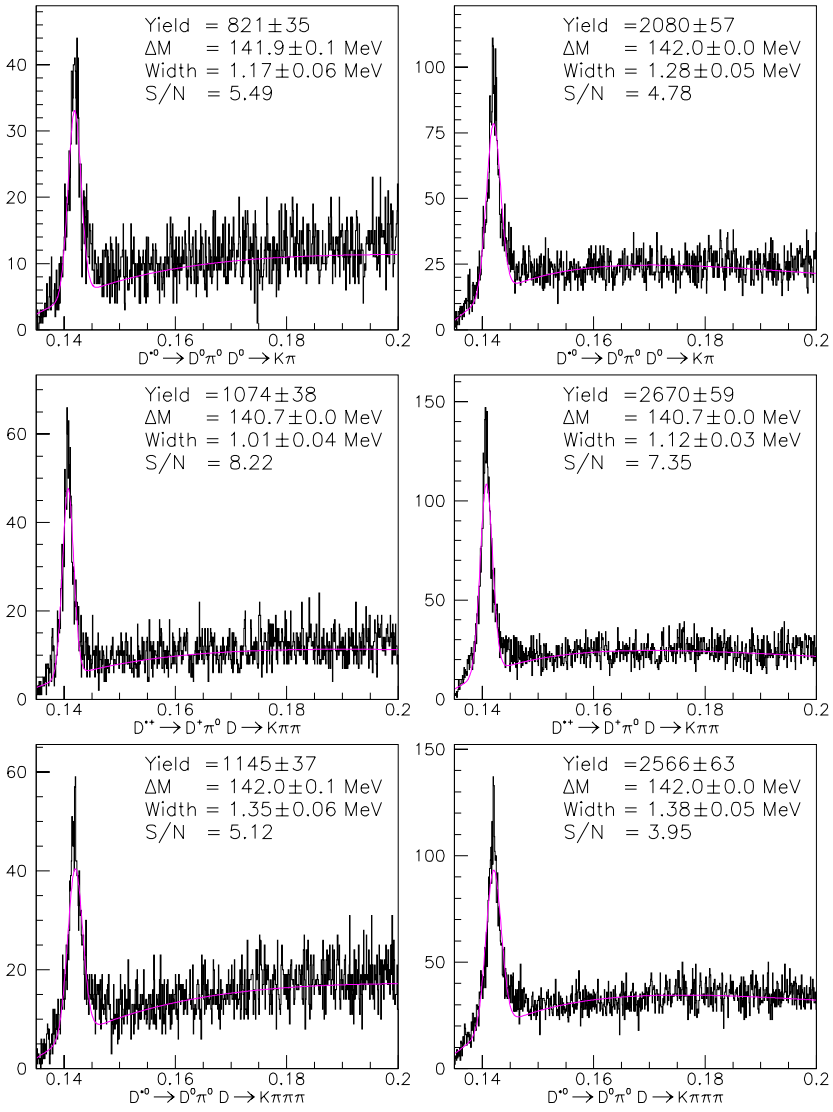

Figure A.2: The D^* signals for the three D decay modes. On the left are the signals with the initial method and cuts (constrained mass and no cluster combinations smaller than **(5,5)**). On the right are the signals with final method and cuts (**PI0FIT** constraint and no cluster combinations smaller than **(2,3)**).

the width and signal-to-noise are both somewhat worse for the unconstrained method. Neither the choice of vertex or constraining method makes a significant difference. Because it is believed that the **PI0FIT** method combined with constraining the π^0's to come from the primary vertex is the most correct method from a technical standpoint, this combination is used as the starting point in the later studies.

It should be noted that in Figure A.3 and the figures that follow that the systematic differences between the "Widths" (really the σ of the Gaussian fitting function) of D^{*+} and D^{*0} are due to kinematics. All our results are consistent with $\Gamma(D^*) = 0$.

A.3 Studies of topological π^0 cuts

The initial cuts on the π^0's used in the method study above are those imposed by the standard reconstruction algorithm, namely:

1. At least 4 blocks in each IE cluster
2. No π^0's with two 4-block clusters or one 4-block and one 5-block cluster
3. At least 1 GeV in the center block of each cluster
4. At least 35% of the cluster energy in the center block
5. Clusters are not associated with tracks

We attempted to relax all these cuts (except #5). Very little change was seen, except in relaxing the requirements on the number of blocks. In Figure A.4 we see that as we require fewer and fewer blocks in the clusters, the D^* yield increases without significant degradation of signal quality. The D^* yield is more than doubled when we allow π^0's with 2 or 3 blocks in each cluster.

In hindsight, this result is not terribly surprising since the initial cuts were obtained by looking at all π^0's. Soft π^0's have lower photon energies and hence smaller cluster sizes, but the results are very encouraging.

For our final set of cuts, we allow clusters of two or more blocks and only exclude π^0's with two blocks in both clusters. (The 5^{th} point in Figure A.4.)

We have also investigated completely removing the two cuts on center energy in a cluster (cuts 3 and 4 above), both for the initial set of cuts and for the case where we allow all cluster topologies except two blocks in each cluster. This has almost no effect, so we leave these cuts in place.

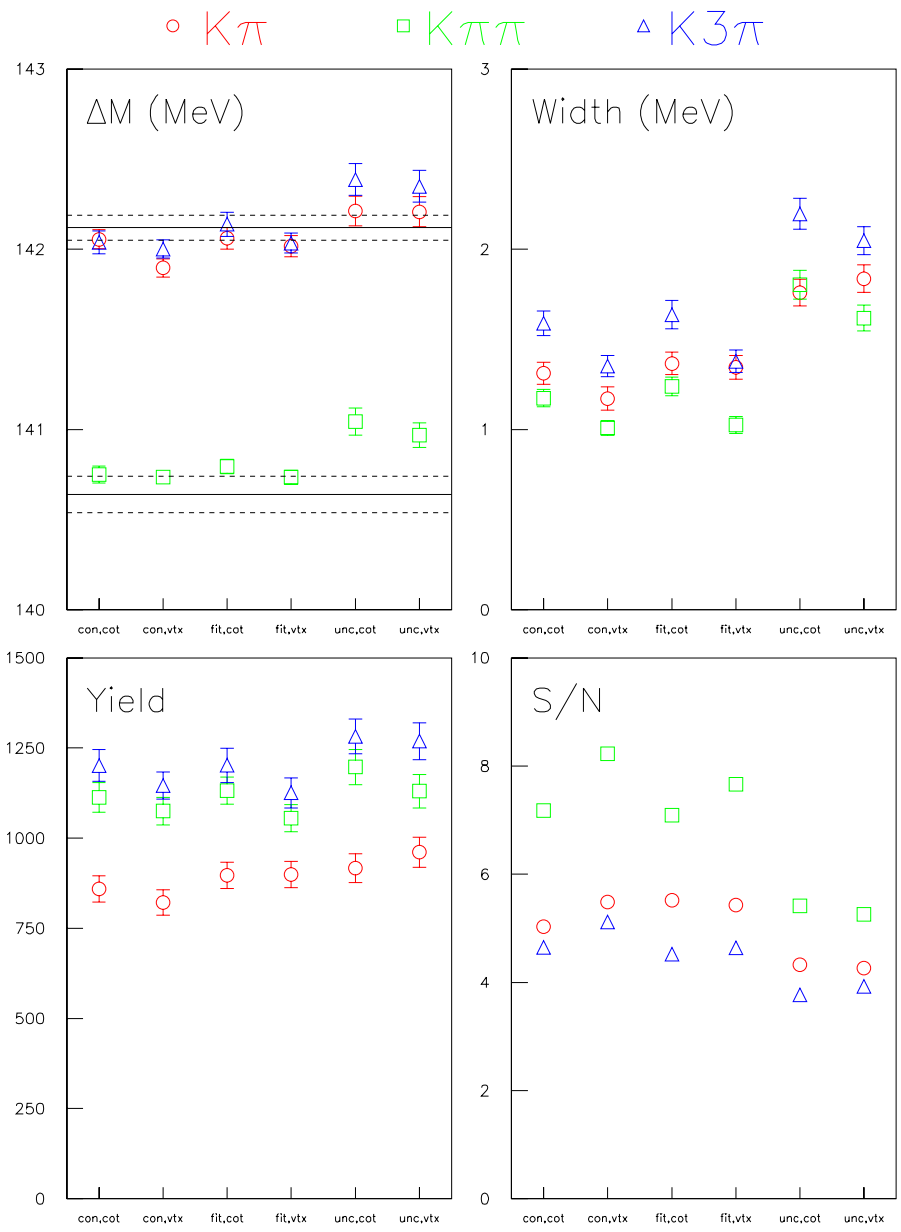

Figure A.3: Summary of π^0 reconstruction methods. Shown are mass difference, width, yield and signal-to-noise for the D^* signals in each Golden Mode final state. We denote **con**: simple mass constraint, **fit**: **PI0FIT** constraint, **unc**: no mass constraint, **cot**: center of target used as vertex, and **vtx**: true primary used as vertex. The six points are labeled on the x axis. The horizontal lines represent the PDG [4] averages and errors for the D^{*0} (upper) and D^{*+} (lower) masses.

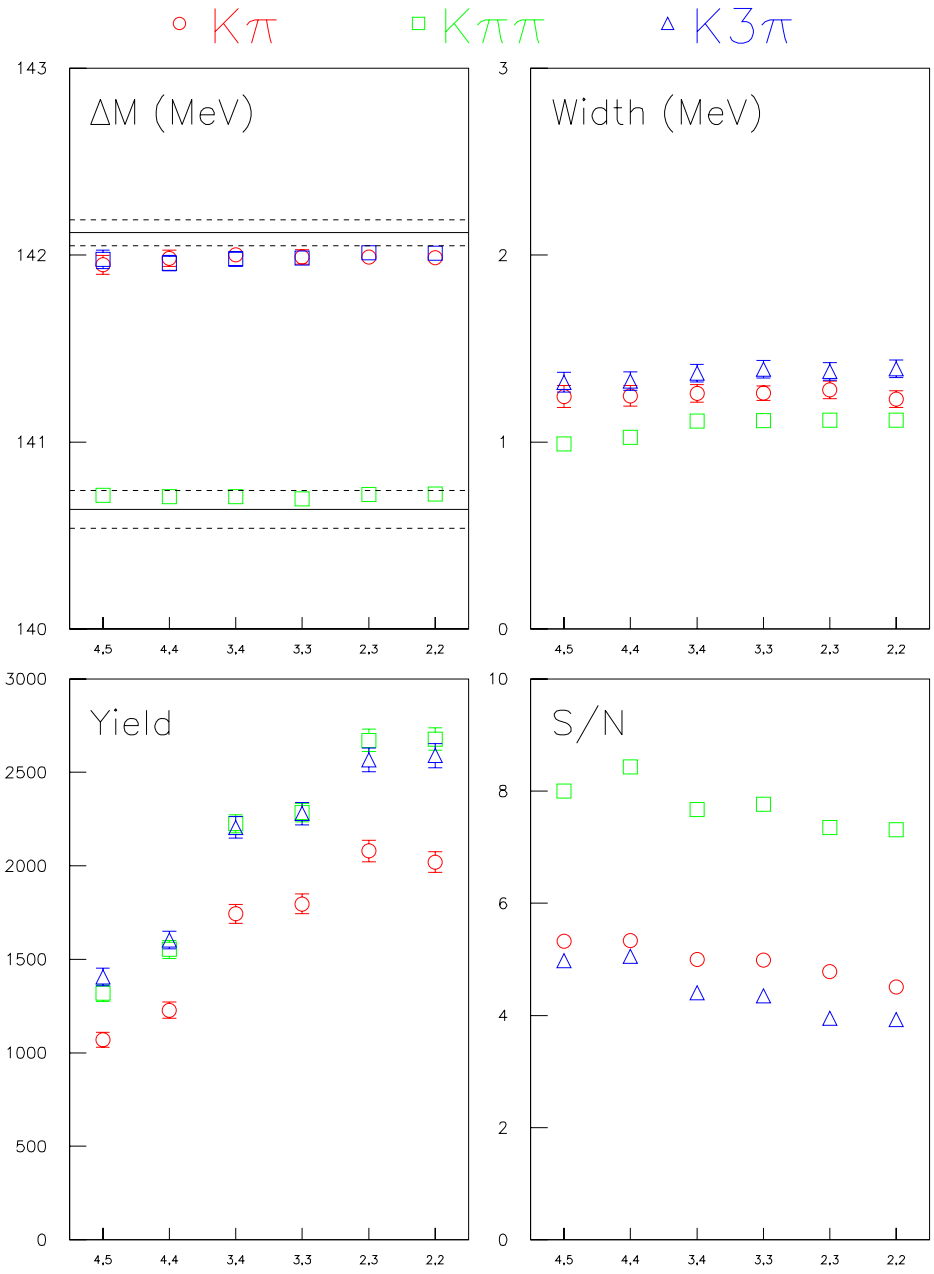

Figure A.4: Summary of π^0 size cuts. Shown are mass difference, width, yield, and signal-to-noise for the D^* signals in each Golden Mode final state. The first point *excludes* π^0's with less than 4 blocks in one cluster and 5 blocks in the other (denoted as **(4,5)**). Successive points *allow* **(4,4)**, **(3,4)**, **(3,3)**, **(2,3)**, and **(2,2)**. The horizontal lines represent the PDG averages and errors on the mass.

A.4 Momentum and mass cuts

While cuts on the π^0 momentum have been shown to improve the quality of the overall π^0 signal, they are disastrous for soft π^0's. The momentum requirement quickly cuts into the phase space of the $D^* \to D\pi^0$ decay. This effect is shown in Figure A.5. We see that while signal to noise increases, the yield drops off even more dramatically.

In the standard π^0 reconstruction ΔM, the difference between the reconstructed and nominal π^0 masses, is required to be less than 15 MeV/c^2. For soft π^0's, the mass resolution is significantly worse so we investigate changing this cut. Figure A.6 shows the results of this study as we vary the ΔM cut from 10–40 MeV/c^2. In all the other studies we use 25 MeV as our ΔM cut. Useful cuts appear to be in the 10–25 MeV range, which decrease background events with a corresponding decrease in yield.

A.5 Other π^0 cuts

Studies of high-momentum π^0's have shown the π^0 energy asymmetry, defined as

$$A \equiv \frac{|E_1 - E_2|}{E_1 + E_2}, \tag{A.1}$$

to be a useful variable to cut on. Small values of A are associated with cleaner π^0's. We have investigated this cut for soft π^0's and find the results to be less than encouraging. The results are shown in Figure A.7, where from left to right we cut on smaller and smaller values of A. There is no significant increase in signal-to-noise for any asymmetry cut, but the yield drops precipitously.

The π^0 fitting routine **PI0FIT** returns a χ^2 which measures the goodness of the fit (how easily the energy and position values can be adjusted within their errors to form the nominal π^0 mass). We have examined cutting on this variable; results are shown in Figure A.8. We can see that this cut works as expected; as we cut tighter and tighter, yield decreases and signal-to-noise increases; cutting at $\chi^2 < 1$ appears to give good results: an increase in purity with small losses in yield.

A.6 π^0 Arbitration

Finally, we study an arbitration method when more than one π^0 combinations are found in an event. The method we choose is to require that when a photon is shared between two or more π^0's that meet all of the other requirements, the π^0 combination

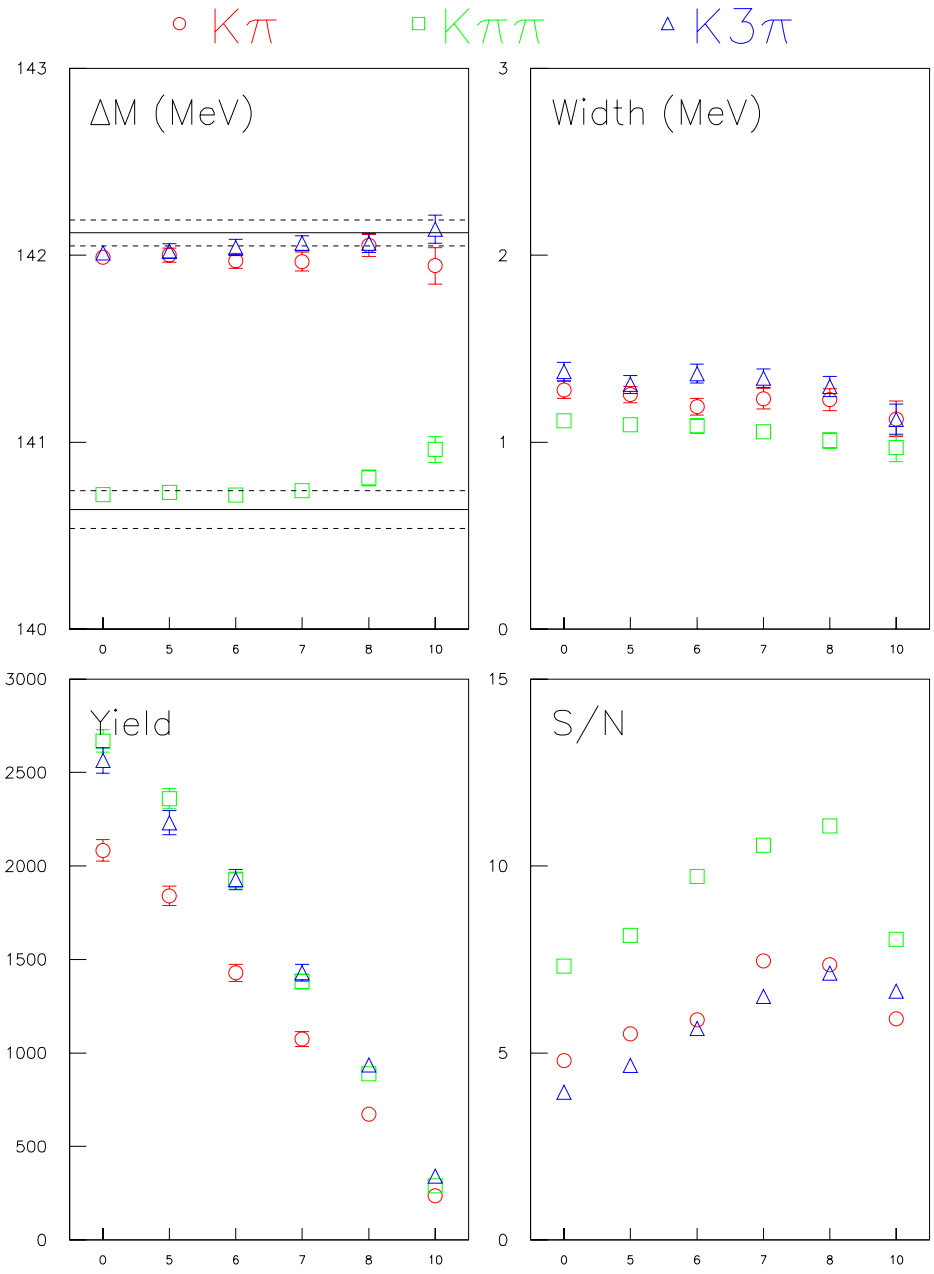

Figure A.5: Effect of a π^0 momentum cut on the D^* signals. The six points are $p > 0, 5, 6, 7, 8, 10$ GeV/c respectively.

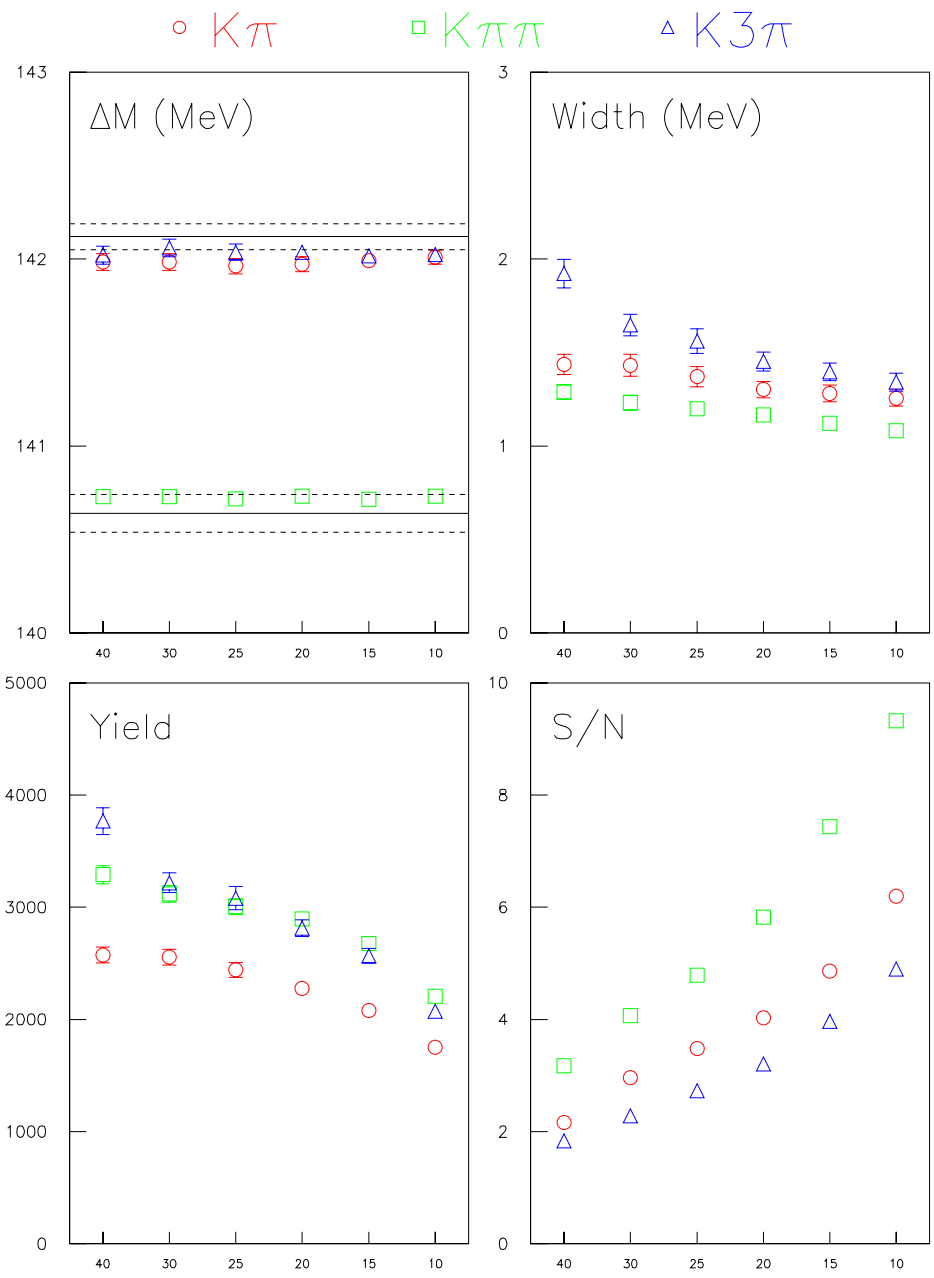

Figure A.6: Summary of mass difference cuts. We cut on the difference between the reconstructed π^0 mass and the nominal mass. The six points are $|\Delta M| < 40, 30, 20, 15, 10, 5$ MeV/c^2.

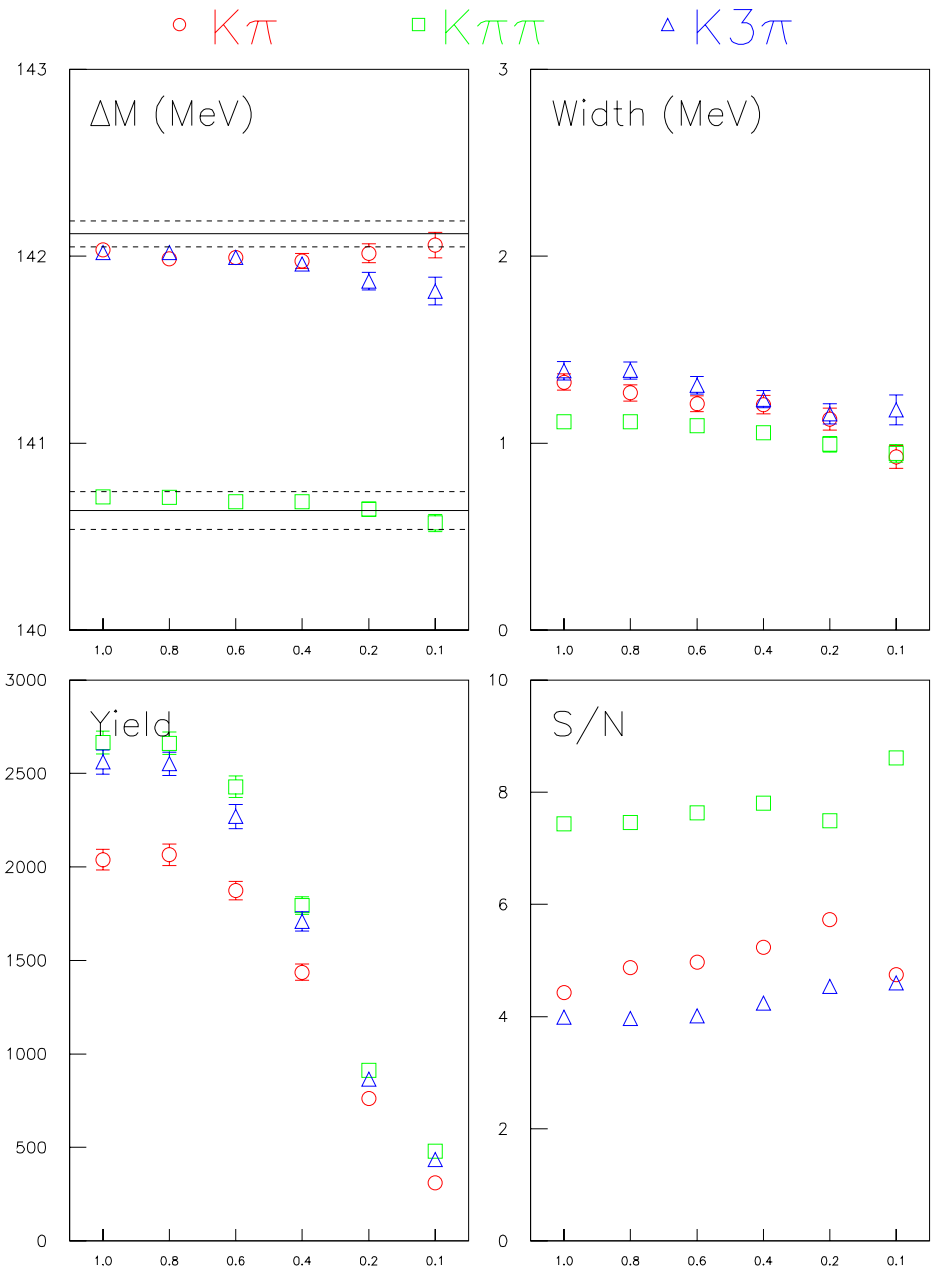

Figure A.7: Effect of asymmetry cuts. From left to right we cut on the asymmetry, $A < 1.0, 0.8, 0.6, 0.4, 0.2, 0.1$

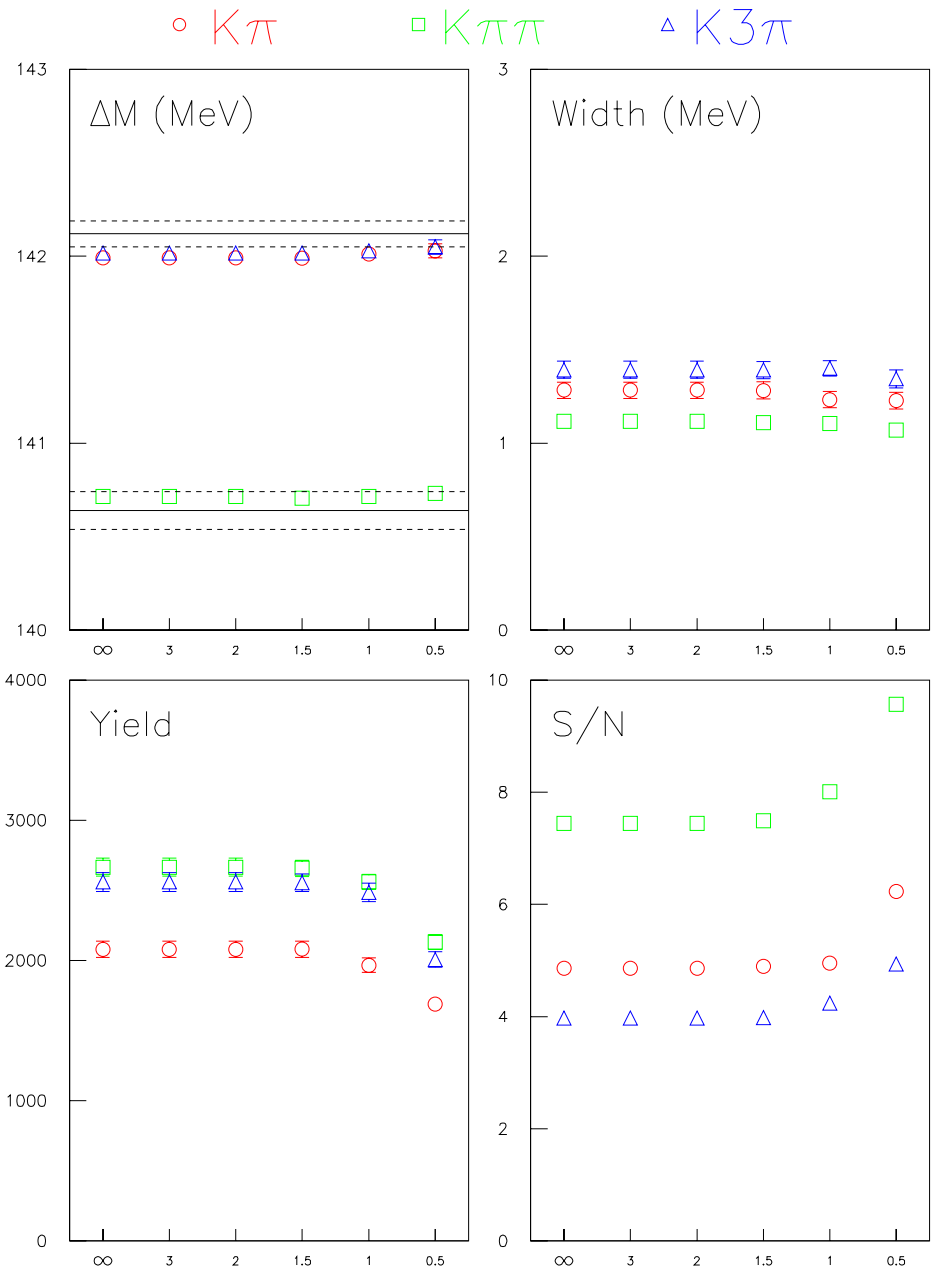

Figure A.8: Effect of a cut on χ^2 from **PI0FIT**. From left to right, we cut at $\chi^2 < \infty, 4, 3, 2, 1, 0.5$.

with the lowest χ^2 is used [86]. The other combinations are disregarded. This will usually keep only one π^0 per event, but two π^0's, each of which have two distinct photons, can also be kept. Since the χ^2 depends on how well the reconstructed mass matches the nominal mass, this requirement is more effective as the mass cut window is enlarged. The D^* signals which pass and fail this arbitration requirement are shown in Figure A.9.

A.7 Conclusions

First, since the D^*'s are about 20 MeV/c^2 closer to the π^0 threshold than the Σ_c^+, these results may not be directly applicable to Σ_c^+ decays, but they do give valuable guidance. Second, this study tells us that we are required to redo the π^0 reconstruction for each event with a Λ_c^+ if we want to have the best possible soft π^0 reconstruction. Fortunately, we had the foresight to save the raw information which allows us to redo this reconstruction.

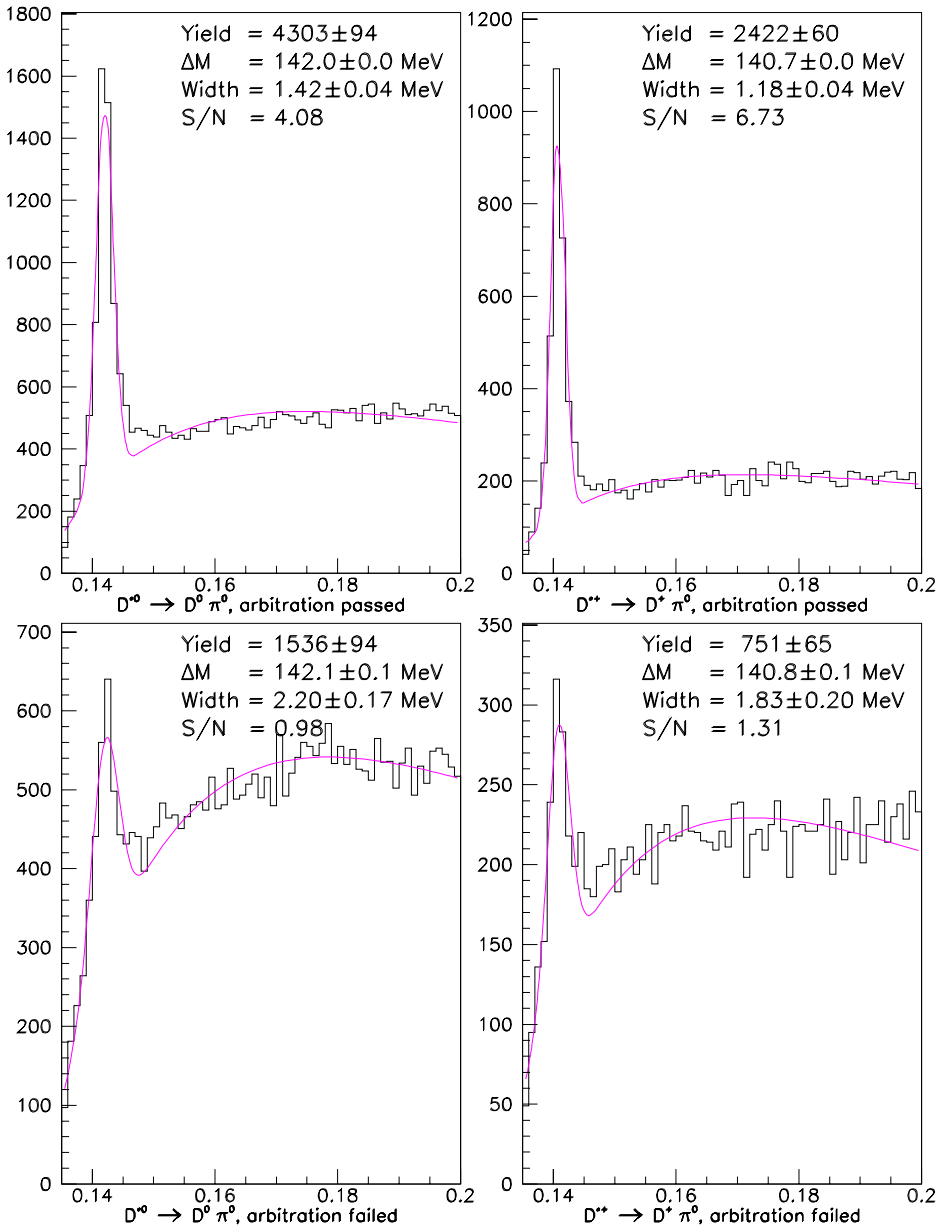

Figure A.9: Effect of π^0 arbitration.

Appendix B

Calculation of systematic errors

Typically there are three types of systematic errors in an analysis:

1. The case where there is a known systematic problem in the reconstruction. In this case, we calculate, estimate, or even correct the systematic error.

2. The case where we examine the stability of a measurement as a function of variables which may cause a shift in the measured value. This is known as the "split sample" technique where we split the signal into two or more roughly equal parts based on some variable, for instance high or low L/σ_L or particle/antiparticle where one might expect a bias to appear.

3. The case where we use different reconstruction or fitting methods, such as varying the fit function or the histogram binning.

Because of the different statistical properties of the second and third cases, we use two different methods to estimate the systematic errors in these cases.

B.1 Split Sample Systematics

A simplistic method of determining systematic errors when the sample has been split into several parts is to take the spread of the measured values and divide by 2. Many such systematic errors can then be added in quadrature. However, since the measured values will fluctuate within the statistical errors, we end up with a situation where $\sigma_{\text{syst}} \propto \sqrt{\text{number of splits}}$. In other words, as we test more and more hypotheses, we are *guaranteed* to get a larger value for the systematic error.

To more correctly determine systematic errors in the split sample case, we would like to know which differences in fitted values are significant and which are not. In order to treat these split samples more correctly, we use a more complicated statistical method.

If we have N measurements, each from an independent data sample, we can form a χ^2 of the form

$$\chi^2 = \sum_{i=1}^{N} \frac{\left(x_i - \langle x \rangle\right)^2}{\sigma_i^2} \tag{B.1}$$

where x_i and σ_i are the individual measurements and errors, respectively and

$$\langle x \rangle \equiv \frac{\sum_{i=1}^{N} x_i/\sigma_i^2}{\sum_{i=1}^{N} 1/\sigma_i^2}\,. \tag{B.2}$$

If $\chi^2/(N-1) \leq 1$, then our measurements are consistent with each other within their errors. However, if $\chi^2/(N-1) \geq 1$, then we assume that the statistical error is underestimating the true error. If we scale each sub-sample statistical error σ_i to

$$\sigma_i \sqrt{\frac{\chi^2}{(N-1)}} \tag{B.3}$$

then we are guaranteed that $\chi^2/(N-1) = 1$ for the new values of σ_i. The weighted average of the subsample errors

$$\bar{\sigma} \equiv \frac{1}{\sqrt{\sum_{i=1}^{N} 1/\sigma_i^2}} \tag{B.4}$$

will be increased by the same amount.

We can then calculated a scaled error

$$\tilde{\sigma} = \bar{\sigma} \sqrt{\frac{\chi^2}{(N-1)}} = \sqrt{\frac{\langle x^2 \rangle - \langle x \rangle^2}{N-1}} \tag{B.5}$$

where $\langle x^2 \rangle$ is defined as

$$\langle x^2 \rangle \equiv \frac{\sum_{i=1}^{N} x_i^2/\sigma_i^2}{\sum_{i=1}^{N} 1/\sigma_i^2}\,. \tag{B.6}$$

When this scaled error is smaller than the statistical error from the fit of the full sample (σ_{stat}), any difference between the split samples can be interpreted as being compatible with a statistical fluctuation.

To determine the final systematic error for a split sample, we calculate

$$\sigma_{\rm sys} = \sqrt{\tilde{\sigma}^2 - \sigma_{\rm stat}^2} \qquad \text{If } \tilde{\sigma} > \sigma_{\rm stat} \tag{B.7}$$

$$\sigma_{\rm sys} = 0 \qquad \text{If } \tilde{\sigma} < \sigma_{\rm stat} \tag{B.8}$$

where $\sigma_{\rm sys}$ denotes the final systematic error.

This process is repeated for each of several split sample checks. In this way, we are able to discern, somewhat arbitrarily, between systematic effects which cannot be explained by statistical fluctuations and those that can.

B.2 Fit Variant Systematics

In this case the results from each different fitting or reconstruction method are considered to be equally valid. (No method is more likely to give the correct answer than another.) In addition, the statistical errors on the measurement should be correlated.

Because each measurement is equally valid, each measurement is given equal weight and the estimate of the systematic error is simply the standard deviation on the set of measurements. In other words, the systematic error is

$$\sigma_{\rm sys} = \sqrt{\frac{\sum_{i=1}^{N} x_i^2 - N\bar{x}^2}{N-1}} \tag{B.9}$$

where the quantities x_i are the individual measurements and $\bar{x}$ is the mean.

This method makes the assumption that each method produces a result of equal "goodness." A measurement that is far from the others, even with a large error, can inflate the overall systematic error.

A more detailed description and derivation of these methods is presented in Reference 87.

Appendix C

Glossary of terms

Most of these terms are defined in the text of the thesis. They are collected here for ease of reference.

CITADL: Čerenkov Identification Through A Digital Likelihood technique. The primary Čerenkov identification algorithm used in FOCUS. See Section 4.2.1.

DVERT: D (meson) VERTexer. The candidate driven vertex finder. Also calculates direction vectors which include target silicon information.

Golden Modes: The D decay modes $D^0 \to K^-\pi^+$, $D^0 \to K^-\pi^+\pi^+\pi^-$, and $D^+ \to K^-\pi^+\pi^+$. So called because they have large branching ratios and charged final states.

HC: The Hadron Calorimeter

IE: The Inner Electromagnetic calorimeter

OE: The Outer Electromagnetic calorimeter

PI0FIT: A fitting routine which adjusts photon shower energies and positions to form a constrained π^0 mass.

π_{con}: Pion consistency. A **CITADL** cut which measures the difference between the π hypothesis and the most likely hypothesis.

PMT: Photomultiplier Tube.

PWC: Multi-wire proportional chambers. There are five such detectors in FOCUS labeled P0, P1, ... P4.

Silver Modes:
The decays $D^+ \to K^-K^+\pi^+$, $D_s^+ \to K^-K^+\pi^+$, and $\Lambda_c^+ \to pK^-\pi^+$. These are the decays modes in which the D_s^+ and Λ_c^+ are most prevalent.

SSD: Silicon Strip Detector. The downstream stations of silicon microstrip detectors.

Stub: A track with hits in three or fewer PWC stations.

SuperEZD:
A reconstruction and skimming package. **SuperEZD** was used to find many of the known or postulated D^+, D^0, D_s^+, and Λ_c^+ modes with a consistent set of requirements. It is the basis for many of the physics skims.

TRACCE: Track parameters (direction only) which come from the downstream silicon stations.

Track: Generally, a calculation of the path taken by a particle. More specifically, this term is often used to refer to a track with hits in five PWC stations.

TRKFIT: An algorithm to improve the momentum determination of tracks by fitting the bend angles of the track in M1 and M2.

TSSD: Target Silicon Strip Detector. The embedded stations of silicon microstrip detectors.